Motility-Induced Patterning in Quorum Sensing Bacteria

Wesley J. M. Ridgway

Somerville College

University of Oxford

A thesis submitted for the degree of

Doctor of Philosophy

Summer 2024

Acknowledgements

This thesis would not have been possible without several people whom I wish to acknowledge.

Psalm 23.

I thank my supervisors Jon Chapman, Mohit Dalwadi, and Philip Pearce for their guidance, advice, time, and effort. They have taught me many essential research skills. I am incredibly grateful for their patience throughout my DPhil.

I wholeheartedly thank my parents and brother for their invaluable support.

I am eternally grateful to my future wife Lavie for her support, encouragement, and companionship throughout my DPhil.

Abstract

Populations of bacteria regulate motility through chemical signalling to control emergent self-organisation. We investigate emergent behaviour in a population of bacteria whose motility is controlled through a type of chemical signalling called quorum sensing (QS). We develop a cell-level mathematical model that accounts for both QS and genetic regulation of motility. By systematically upscaling our model with the Fokker–Planck equation, we derive two multi-scale continuum models that describe the system at the population level. Our first model uses chemical structuring to capture genetic regulation of motility. We derive our second model by effectively averaging out the chemical structure, leading to a simpler reaction-diffusion system. Through analysis and simulation of both models, we characterise different types of emergent behaviour for various broad classes of gene-regulatory networks. Examples of emergent behaviour include motility-induced phase separation, spatio-temporal oscillations, and oscillator synchronisation. We investigate qualitative and quantitative differences between the two models in order to characterise situations where chemical structure is important. This comparison provides insight on the reliability of reaction-diffusion models for motile signalling bacteria, which should benefit future modelling efforts.

Contents

List of Figures

Chapter 1

Introduction

1.1 Bacterial Motility and Active Matter

Motility is crucial for the successful operation of cells. It allows colonies of bacteria to locate valuable resources or avoid noxious ones, and is an integral part of antimicrobial resistance development [73], as well as tissue remodelling in morphogenesis, wound healing, and cancer invasion [31]. Cells exhibit several methods of locomotion, but in this thesis we focus on flagella-driven motility, which is used by many bacterial species [12, 67, 88].

Escherichia coli is a model organism for which flagella-driven motility is well-studied. Individual *E. coli* perform so-called run-and-tumble motion [12] (Ch. 4). Broadly, this motion consists of straight line trajectories at a constant speed, punctuated by 'tumbles' wherein the cell randomly chooses a new direction of travel. Locomotion during runs is achieved through the counterclockwise rotation of a flagella bundle. The flagella become unbundled when one or more individual flagella reverse direction, thereby triggering a tumbling event. The reversal of flagella is controlled by intracellular biochemical circuitry, the specifics of which are outside the scope of this work (see [67, 88] for details).

We outline some of the quantitative details of run-and-tumble motion since they are relevant to our modelling in Chapter 2. The time between tumbles follows an exponential distribution with an average of roughly one second while the average duration of a tumble is approximately 0.1 seconds (see [11], Ch. 6). Because cells typically exist in low-Reynold's number environments ($\sim 10^{-5}$), they are effectively stationary during tumbling events when the propulsion mechanism ceases [75]. In reality, the movement of *E. coli* is only approximated by run-and-tumble motion. The trajectories during runs differ slightly from straight lines due to rotational and

passive diffusion, and the short duration of tumbles results in a slight bias towards the previous orientation (see [11], Ch. 6).

By sensing and responding to chemical concentrations in their surrounding environment, *E. coli* modulate their run-and-tumble motion so as to bias their net motion in a desirable direction — this is called chemotaxis. Through biochemical regulation of the tumbling frequency, cells can bias their motion either up (chemoattractant) or down (chemorepellent) spatial gradients of an external chemical signal [88]. Because cells are too small to directly measure spatial gradients, they direct their motion by tumbling more frequently when they encounter lower concentrations of chemoattractant, and *vice versa* for chemorepellent.

Colonies of motile bacteria are an example of active matter, defined as a collection of interacting self-propelled particles. Examples of active matter range from chemically propelled Janus particles that interact through steric forces [10, 17], to flocks of birds and schools of fish where individuals align themselves relative to their neighbours [87]. These systems display complex emergent behaviour such as motility-induced phase separation [20], macroscopic orientational ordering [21,37,87], and other complex spatio-temporal dynamics [85]. Motility-induced phase separation (MIPS) occurs when a system of active particles phase separates in the absence of attractive forces, leading to a two-phase system comprising a dense phase of immotile particles surrounded by a dilute phase of motile particles. For motile bacteria, the inter-particle interactions include physical forces such as collisions and hydrodynamic effects [10], as well as chemical interactions such as quorum sensing [90].

1.1.1 Mathematical Modelling of Active Matter

There are two broad approaches to modelling active systems: microscopic particle-level models and macroscopic population-level models. Macroscopic models are commonly upscaled from a microscopic model, but can also be phenomenological. One method of describing particle motion on the microscale is with a set of SDEs for the positional and orientational degrees of freedom. Lattice-based models provide another approach (see, e.g., [16]).

Two types of particles are commonly studied in active systems: run-and-tumble particles and active Brownian particles (for a review see, e.g., [10]). For run-and-tumble particles in 2D, the position $\mathbf{x}_i$ and orientation $\mathbf{e}_i := (\cos\phi_i, \sin\phi_i)^T$ of each

particle are governed by

$$\frac{d\mathbf{x}_i}{dt} = v\mathbf{e}_i + \mathbf{F}_i, \tag{1.1a}$$

$$\frac{d\phi_i}{dt} = 0, \tag{1.1b}$$

where v is a constant self-propulsion speed and $\mathbf{F}_i$ is the net external force acting on the i^{th} particle. Instantaneous tumbling events can be modelled by selecting a random new orientation ϕ_i after a random time interval; the new orientation and time interval are chosen from uniform and exponential distributions, respectively [10]. These modelling assumptions are in line with our description of run-and-tumble motion above. For active Brownian particles, the equations of motion are

$$\frac{d\mathbf{x}_i}{dt} = v\mathbf{e}_i + \mathbf{F}_i, \tag{1.2a}$$

$$\frac{d\phi_i}{dt} = \sqrt{2D_r}\eta(t), \tag{1.2b}$$

where D_r is a rotational diffusion coefficient, and η is zero-mean, unit-variance white noise [10]. In other words, the orientation angle ϕ_i undergoes standard Brownian motion. We note that inertial forces have already been neglected in (1.1)–(1.2), which is appropriate in small Reynold's number regimes.

For systems of active Brownian or run-and-tumble particles, the force $\mathbf{F}_i$ crucially includes particle interactions. Examples include steric repulsion [39] and electrostatic interactions [96]. Alignment interactions or rules can also be included in either (1.1b) or (1.2b) (see, e.g., [87,96]). Hydrodynamic effects can be included by supplementing (1.1) or (1.2) with a flow field [51, 78]. In this thesis, we choose to neglect hydrodynamic effects and instead focus on the role of chemical interactions.

1.1.1.1 Continuum Models

While agent-based microscopic models are useful for investigating emergent behaviour, they can be computationally intensive for large numbers of particles. This is usually due to the expensive evaluation of pairwise summations in the interaction term $\mathbf{F}_i$. An alternative approach is to derive macroscopic models through a formal upscaling. These models have the added benefit that they are amenable to mathematical analysis. We now review several continuum models of active matter and later provide a brief overview of upscaling strategies in Section 1.4.

The result of upscaling either of the microscopic systems (1.1) or (1.2) is a set of governing equations that describe the system at the macroscale. The key macroscale

quantity is the cell density $\rho(\mathbf{x}, t)$. A hallmark of these models is effective density-dependent transport coefficients that describe the effect of particle interactions on motility.

The system of active Brownian particles with pairwise interactions in (1.2) is upscaled in [13]. They obtain

$$\frac{\partial \rho}{\partial t} = \nabla \cdot (\mathcal{D}(\rho)\nabla\rho), \quad \mathcal{D}(\rho) = D + \frac{(v - \zeta\rho)(v - 2\zeta\rho)}{2D_r}, \tag{1.3}$$

where D is the long-time diffusion coefficient of the passive system (with $v = 0$) and ζ is a constant. Both D and ζ can in principle be measured from numerical simulation of the microscopic system. The quantity $\mathcal{D}(\rho)$ is an effective diffusion coefficient representing cell motility at the macroscale. Similar continuum models are obtained in [39, 81].

Another approach to continuum modelling uses stochastic PDEs to describe the cell density. As we will see in Section 1.4, the cell density in (1.3) derives from a probability density function (PDF). As such, it is not completely accurate to refer to ρ as a cell density. The actual density field evolves stochastically due to the randomness at the microscale. It is given by $\sum_{i=1}^{N} \delta(\mathbf{x} - \mathbf{x}_i(t))$, where $\mathbf{x}_i$ are the particle positions, and δ is the Dirac-delta function [30]. A slightly different approach to upscaling the microscale system (1.2) results in a stochastic PDE of the form [20, 30]

$$\frac{\partial \tilde{\rho}}{\partial t} = -\nabla \cdot \left[\mathbf{V}[\tilde{\rho}]\tilde{\rho} - \mathcal{D}[\tilde{\rho}]\nabla\tilde{\rho} + (2\mathcal{D}[\tilde{\rho}]\tilde{\rho})^{1/2}\boldsymbol{\eta}(\mathbf{x}, t)\right] \tag{1.4}$$

where $\tilde{\rho}(\mathbf{x}, t)$ is a coarse-grained density field (sometimes referred to as the empirical density), $\boldsymbol{\eta}$ is white noise, and the transport coefficients $\mathcal{D}[\tilde{\rho}]$ and $V[\tilde{\rho}]$ are density dependent functionals given by

$$\mathcal{D}[\tilde{\rho}] = \frac{v^2[\tilde{\rho}]}{2D_r[\tilde{\rho}]}, \quad \mathbf{V}[\tilde{\rho}] = \frac{-v[\tilde{\rho}]\nabla v[\tilde{\rho}]}{2D_r[\tilde{\rho}]}. \tag{1.5}$$

The cell-level motility parameters $v[\tilde{\rho}]$ and $D_r[\tilde{\rho}]$ are now also effective functionals of the density due to the interaction. Their precise form depends on the type of interaction and is not particularly relevant here. Equation (1.4) describes the stochastic evolution of the density field $\tilde{\rho}$, rather than the PDF ρ.

Motility-induced phase separation is well-studied in active systems [20]. An advantage of continuum models is that often one can derive criteria for the onset of MIPS from the spatially uniform state $\rho = \text{const}$. For example, in [13] it was shown that MIPS occurs when $\mathcal{D}(\rho) < 0$ in (1.3), which is a condition for the continuum model to become ill-posed. As another example, when the functionals v and D_r in

(1.5) are local functions of the density, the criteria for the onset of MIPS in the homogeneous state is given by [20]

$$\rho\frac{v'}{v} < -1. \tag{1.6}$$

According to (1.6), MIPS is caused by a density-dependent self-propulsion; density-dependent tumbling frequency or rotational diffusion cannot cause MIPS. We note that this only applies to systems in a specific large lengthscale and timescale regime where the upscaling leading to (1.4)–(1.5) is valid; outside of this regime, MIPS can be caused by variations in rotational diffusion (see, e.g., [16]). In Chapter 3 we show that variations in rotational diffusion or tumbling frequency can cause MIPS in living active systems in the large lengthscale and timescale regime where MIPS is classically forbidden according to (1.6). We have published this result in [77]. Before discussing chemical interactions in active systems in Section 1.3, we briefly introduce quorum sensing (QS).

1.2 Bacterial Quorum Sensing

Quorum sensing is a method of chemical signalling that enables colonies of bacteria to alter their collective behaviour in response to environmental queues. Examples of collective behaviour where quorum sensing has been implicated include virulence factor production [29, 80], biofilm formation [48, 59], and bioluminescence [70]. Quorum sensing circuitry is often used as a building block in synthetic biology applications as it allows the engineering of tunable coordinated behaviour at the population scale [15]. This has been exploited in the design of toggle switches [56] and oscillators [28, 74], as well as industrial metabolite production [5, 47]. Quorum sensing also regulates motility in both natural [82] and synthetic [91] biological systems.

Quorum sensing works in bacteria through gene regulatory networks (GRNs), which alter production of molecules such as proteins, and ultimately emergent behaviours, in response to the local concentration of a chemical signal. In certain QS systems in bacteria, the chemical signal is self-generated in the form of diffusible signalling molecules called autoinducers (AI). AI molecules can freely diffuse through the cell membrane and be detected by intracellular transcription factors or gene-regulatory proteins [70,93]. Termed the LuxIR circuit, the QS circuitry in the marine bacterium *Vibrio fischeri* stands as a canonical example since many other bacterial species possess variants thereof [9,92]. A hallmark of this system is a positive feedback loop, the core of which has two steps [90]. In step one, AI binds to an intracellular

protein called LuxR to form a LuxR-AI complex. Second, the LuxR-AI complex triggers production of AI, which re-initiates step one provided that LuxR is present. The feedback loop requires a threshold level of AI in order to begin, and it saturates when LuxR is no longer abundant. A more nuanced explanation of the details in each step can be found in [70, 93].

The effect of the chemical signalling and positive feedback in the GRN is a switch-like change in behaviour [90]. At low cell densities the AI concentration is small, so the positive feedback loop is inactive. As cell density increases (e.g. by bacterial growth and division), the AI concentration also increases, which eventually initiates the feedback loop, thereby flooding the extracellular space with AI. The higher levels of internal LuxR and AI, in the case of *V. fischeri*, lead to transcription of genes that control bioluminescence. On the population scale, the result is a spontaneous change in behaviour.

1.2.1 Mathematical Modelling of Quorum Sensing

Several mathematical models of QS have been developed independently from active systems. These models tend to represent the GRN and chemical signalling in more detail, but do not focus on motility. The biochemical aspects of these models will be relevant to our model formulation in Chapter 2.

A mathematical model of QS was developed in [89] for the canonical LuxIR circuit. Here the population is treated as a continuum and consists of subpopulations of up-regulated and down-regulated cells. Each cell is in either of the two states depending on whether the QS switch is active or inactive. The concentration of AI is modelled as a well-mixed field that permeates the population. Signal production, uptake, and natural decay are incorporated. Broadly, they demonstrate that an initially down-regulated population undergoes a colony-wide transition to the up-regulated state as the population increases, in line with real biological systems. They additionally quantify the timescale over which the up-regulation occurs.

Another approach to modelling QS is to treat cells as fixed immotile 'compartments' [24, 46]. In [46], the concentration field of AI permeates the intercellular space only. Cells are modelled as small immotile 'holes' in the domain with Robin boundary conditions that mediate influx and efflux of AI. Inside each cell, ODEs govern the (well-mixed) chemical reactions involved in the QS genetic circuitry, while in the extracellular space AI molecules diffusive passively with a natural decay rate. Using the method of matched asymptotic expansions in the limit of small cell radius, they demonstrate the onset of synchronous collective oscillations at a critical population.

A similar modelling framework is used in [24], but the cell positions are periodic in space and they do not assume well-mixed internal concentrations. Through a systematic upscaling *via* homogenisation theory (method of multiple scales in space), they derive a set of averaged governing equations which is valid on the macroscale. Upscaling QS has paved the way for recent studies that investigate QS in e.g. the presence of fluid flow [25] and morphogens [26].

When the GRN reaction kinetics admit oscillatory solutions (limit cycles) QS can trigger synchronous collective oscillations [46, 53]. These systems of chemically coupled oscillators are relevant in biological contexts such as collective migration of *Dictyostelium* (see, e.g., [41] and references therein). Using the general framework of [46], a quantitative criterion for the onset of collective oscillations is derived in [53]. Although we will be primarily focused on studying motility-induced patterning in this thesis, we study a class of GRN kinetics in Section 4.3 that is directly relevant to the problem of characterising oscillator synchronisation by QS.

1.3 Regulation of Bacterial Motility through Quorum Sensing

Quorum sensing regulation of motility has been achieved in synthetic biological systems to generate tunable patterns *in vitro*. In [58] a population of *E. coli* was engineered with the LuxIR circuitry from *V. fischeri* and coupled to genes that regulate tumbling frequency (rather than bioluminescence). They demonstrated the emergence of concentric ring patterns of high and low cell density in an expanding population and that these patterns could be switched on or off by modulating the expression of a single gene. A similar system exhibiting ring patterns was engineered in [23] where the population consists of two different strains of engineered *E. coli*. Each strain regulates the motility of its counterpart. The LuxIR QS circuitry from *V. fischeri* and the LasI QS circuitry from *Pseudomonas aeruginosa* was engineered into the two strains and coupled with motility genes.

Quorum sensing interactions in active matter have been represented mathematically through effective physical interactions. At the macroscopic level, this has been done with effective density-dependent transport coefficients [84]. At the microscopic level, QS interactions have been modelled as effective forces [2, 45, 54] or rule-based collisions [69]. These studies have demonstrated clustering and phase-separation behaviour, similar to active systems with physical interactions (hereafter referred to as classical active matter). However, it is not known how well these existing models

predict emergent patterning since they represent QS through effective terms rather than accounting for gene regulation and chemical signalling explicitly.

Recent studies have supplemented active systems with a concentration field of signalling molecules that mediate the interactions [3, 18, 57, 60, 76, 98]. The concentration field in these models is self-generated and detectable by cells, in line with our description of QS in Section 1.2. At the population level, interactions are modelled by posing transport coefficients that depend on the local concentration of AI, rather than the local cell density. Similarly, microscale models assume AI dependent motility parameters. These studies have shown that, broadly, repression of motility through QS tends to promote emergent patterning. However, the effect of the GRN remains unclear in general since an explicit model of gene regulation is absent in these studies.

Recent studies have begun to address this issue by incorporating phenomenological reaction-diffusion models of gene regulation [99], or through a structured model [52, 94, 97]. In [99], a reaction-diffusion system represents the concentration of intracellular gene-regulatory proteins or transcription factors through an effective macroscopic field. A range of dynamic emergent behaviours was found through numerical simulation. In [94], a detailed model incorporating gene-regulated motility, bacterial growth, and nutrient concentration was developed and shown (numerically) to successfully reproduce the experimentally observed stripe patterns in [58]. Similarly, in [52, 97] models incorporating gene-regulated motility were studied for simple gene-regulatory networks and found to exhibit clustering behaviour. While these models have made progress in exploring the role of the GRN, they have several important limitations, which we will discuss at the end of this chapter in Section 1.6.

1.4 Approaches to Upscaling

Upscaling microscopic models of active systems is a challenging problem in general. We briefly review some general strategies for upscaling the SDE models of the form (1.1)–(1.2), omitting most of the technical details. We use similar techniques in our continuum model formulation in Chapter 2.

One formal method of upscaling is to reformulate the SDEs (1.1)–(1.2) in terms of a probability density function (PDF) with the many-particle Fokker–Planck (Smoluchowski) equation. This is the approach that we will use for our upscaling in Chapter 2. In [13] they consider active Brownian particles that undergo passive diffusion (with diffusion coefficient equal to one) and pairwise interactions. The particles are confined

to a periodic domain Ω and the Fokker–Planck equation reads

$$\frac{\partial \psi_N}{\partial t} = \sum_{i=1}^{N} \nabla_{\mathbf{x}_i} \cdot [\nabla_{\mathbf{x}_i} \mathcal{U} - v\mathbf{e}_i + \nabla_{\mathbf{x}_i}] \, \psi_N + D_r \sum_{i=1}^{N} \frac{\partial^2 \psi_N}{\partial {\phi_i}^2}, \quad \mathbf{x}_i \in \Omega, \quad \phi_i \in [0, 2\pi), \quad t > 0, \tag{1.7}$$

where N is the number of particles, $\mathcal{U} = \sum_{i<j} U(|\mathbf{x}_i - \mathbf{x}_j|)$ is the interaction potential, and $\psi_N(\{\mathbf{x}_i, \mathbf{e}_i\}, t)$ is the PDF for the system to be in the configuration $\{\mathbf{x}_i, \mathbf{e}_i\}$ at time t. Although Eq. (1.7) is used for the specific system in [13], the upscaling approaches in other models have similar starting points [7, 19, 39, 81]. Eq. (1.7) has has a dimension of $(3N + 1)$, making it impractical to study directly. A series of approximations, broadly involving two steps, is used to reduce the dimension. First, an effective equation for the marginal one-particle PDF is derived. The dimension is usually still too large to be tractable, so the second step is to eliminate or approximate the orientational degrees of freedom.

A challenge arises due to the pairwise interaction potential $\mathcal{U}$. This causes the governing equation for the one-particle PDF to depend on the (unknown) two-particle PDF, which in turn depends on the three-particle PDF, and so on. For (1.7), the one-particle PDF $\psi_1(\mathbf{x}_1, \phi_1, t)$ satisfies [13]

$$\frac{\partial \psi_1}{\partial t} = -\nabla_{\mathbf{x}_1} \cdot [\mathbf{G} + v\mathbf{e}\psi_1 - \nabla_{\mathbf{x}_1} \psi_1] + D_r \frac{\partial^2 \psi_1}{\partial {\phi_1}^2}, \tag{1.8}$$

where $\mathbf{G}(\mathbf{x}, t)$ depends on the two-particle PDF $\psi_2(\mathbf{x}_1, \mathbf{x}_2, \phi_1, \phi_2, t)$. There are a few methods to eliminate the two-particle PDF. For example, in [13, 81] they introduce a phenomenological model for the interaction term $\mathbf{G}$ assuming a strong, short-ranged interaction potential. In [16], two additional (off-lattice) methods are presented which are suitable for weak, long-range interactions and strong, very-short-range interactions. The first is a mean-field approximation where the one-particle PDF for any two particles are effectively assumed independent as

$$\psi_2(\mathbf{x}_1, \mathbf{x}_2, \phi_1, \phi_2, t) \approx \psi_1(\mathbf{x}_1, \phi_1, t) \psi_1(\mathbf{x}_2, \phi_2, t), \tag{1.9}$$

resulting in a closed equation for the one-particle PDF. The second off-lattice method in [16] uses the fact that for strong very-short range potentials, particles cannot overlap, i.e. $|\mathbf{x}_i - \mathbf{x}_j| > \varepsilon$ with ε being the particle diameter. Thus the space of allowed particle positions becomes a 'perforated' domain with small circular holes of radius ε. They obtain approximations for the two-particle PDF using matched asymptotics in the regime $\varepsilon \ll 1$, which enables a closure for the one-particle PDF.

The governing equation for the one-particle PDF depends on the state variables $\mathbf{x}_1$ and ϕ_1 as well as time. It is therefore sometimes desirable to reduce the dimension by eliminating the orientational degrees of freedom. One way to accomplish this is to derive equations for the angular moments of the one-particle PDF (see, e.g., [13, 19, 84]). The cell density ρ is defined as the zeroth angular moment of the one-particle PDF:

$$\rho(\mathbf{x}, t) := \int_0^{2\pi} \psi_1(\mathbf{x}, \phi, t)\, \mathrm{d}\phi, \tag{1.10}$$

where the subscript '1' is dropped on the independent variables for convenience. The first angular moment, defined by

$$\mathbf{p}(\mathbf{x}, t) := \int_0^{2\pi} \psi_1(\mathbf{x}, \phi, t)\mathbf{e}\, \mathrm{d}\phi, \tag{1.11}$$

describes the local average orientation of the particles. Governing equations for ρ and $\mathbf{p}$ can be obtained by integrating (1.8). This moment expansion technique again leads to closure issues because the governing equations for ρ and $\mathbf{p}$ depend on higher order moments. This has been addressed with macroscopic scaling arguments [13, 19, 39] as well as truncating higher-order moments [7]. Other methods of reducing the dimension of the equation for the one-particle PDF have been employed for active suspensions, such as generalised Taylor dispersion theory [63] and recently an operator inversion method [42]. We will not use these methods in this thesis and therefore omit a detailed review.

1.5 Structured Population Models

Throughout this thesis we will make use of a 'chemically structured' model. This model is similar to an age-structured model (see, e.g., the book by Murray [66]), but the 'age' variable will be the concentration of an internal gene-regulatory protein or transcription factor. Structured models are relevant here because upscaling *via* the Fokker–Planck equation 'transforms' *dependent* state variables into *independent* state variables. These macroscopic models are therefore structured in terms of any state variables that are posed at the microscale. A few studies mentioned above use structured models to describe the intracellular gene-regulatory network [52,94,97]. We remark that kinetic transport models are another example of structured population models (see, e.g., [36, 61]). In these models, the governing equations are structured in terms of cell/particle velocity.

1.6 Thesis Goals and Structure

Mathematical models of motile bacteria with QS regulated motility have typically been placed within the framework of active matter [2, 45, 54, 69, 84]. In line with classical active systems, these models broadly predict clustering and phase separation behaviour when motility is effectively decreased by the interactions. These studies represent the GRN and QS through effective terms rather than explicitly. Several recent studies have supplemented models of classical active matter with concentration fields of signalling molecules [3, 18, 57, 60, 76, 98], as well as reaction-diffusion systems to represent the GRN [99]. While these models can be studied to predict emergent behaviour, their phenomenological nature makes it difficult to relate model parameters to measurable cell-level quantities. Additionally, they may contain hidden or uncontrolled assumptions. Only a few studies have explicitly modelled the genetic regulation of motility using a structured modelling framework [52, 94, 97]. However, they either focus on specific experimental setups or do not explicitly account for chemical signalling. Additionally, some of these models are too complex to be amenable to mathematical analysis. Models of QS tend to represent the GRN and chemical signalling in more detail [24, 46, 53, 89]. However, the cells are usually immotile or well-mixed. Overall, we conclude from this Introduction that the role of the GRN and QS in emergent motility-induced patterning remains poorly understood. In particular, it is not known whether physical forces in classical active systems can accurately represent chemical signalling, or how different types of GRN affect emergent motility-induced patterning.

We aim to address this gap by systematically investigating the role of QS and the GRN in motility-induced patterning. To this end, we develop two continuum mathematical models of motile bacteria that explicitly incorporate genetic regulation of motility through QS. Both models are derived through systematic upscaling of a microscopic system so that the assumptions underlying our continuum model are clear. Our first model retains as much information as possible about the GRN while remaining analytically tractable. In this model, the internal GRN reaction kinetics are modelled through chemical structuring, in principle retaining the full distribution of internal states. By effectively replacing the full distribution in this structured model with a discrete set of effective states, we are able to derive a significantly simpler set of reaction-diffusion equations. This reaction-diffusion system constitutes our second model, which we hereafter refer to as an internal mean-field (IMF) model. Our formal

upscaling sheds light on hidden assumptions associated with approximating the GRN kinetics through a reaction-diffusion system, rather than a structured model.

In order to better understand how the GRN affects emergent behaviour, we systematically analyse both models for various broad classes of GRN reaction kinetics. We are then able to compare the predictions of both models in order to clarify situations where the IMF model is qualitatively and/or quantitatively inaccurate. To concretely illustrate both models, we also consider a simple model of the canonical LuxIR QS system and characterise motility-induced patterning therein.

The structure of the remainder of this thesis is as follows. First, we formulate the cell-level model in Chapter 2 and perform a systematic upscaling. This leads to our structured and IMF models which we analyse in chapters 3–5. In Chapter 3 we develop a WKBJ (Louiville-Green)-like framework for analysing the structured model for the canonical LuxIR QS circuit. In Chapter 4, we extend our analytical techniques to three broad classes of reaction kinetics. Specifically, we consider kinetics that admit multiple equilibria, kinetics with multiple internal chemical species, and kinetics that admit a stable limit cycle. This last case poses significant analytical and numerical challenges, so we restrict our attention to the spatially uniform case. Even so, our system is directly relevant to the problem of QS-induced oscillator synchronisation discussed above. It is also a situation in which the predictions of the IMF model differ significantly from those of the structured model. In Chapter 5, we analyse the IMF model and perform qualitative and quantitative comparisons with the structured model. Finally, we summarise the key results of this work in Chapter 6 and discuss potentially fruitful directions for future work.

Chapter 2

Model Formulation and Derivation of Continuum Equations

We have published a simplified version of this chapter for one internal chemical in [77].

2.1 Cell-level Model

To investigate emergent pattering in motile signalling bacteria, we begin by formulating a mathematical model at the cell level. We then derive two continuum models through a systematic upscaling of our cell-level model in a biologically realistic scaling regime.

We consider a population of N chemically interacting bacteria and neglect physical interactions in order to focus on the role of chemical signalling. We model each bacterium as a motile agent in two spatial dimensions with an internal chemical state. For each cell, we specify an index $i = 1, \ldots, N$ and assign a position $\mathbf{x}_i$, orientation $\mathbf{e}_i = (\cos\phi_i, \sin\phi_i)^T$, and a set of internal concentrations $\mathbf{u}_i$. In deriving the model, we consider M internal species where $\mathbf{u}_i = (u_{1i}, \ldots, u_{Mi})^T$, but later specialise to the cases $M = 1, 2$. Each cell is therefore characterised by the state $\{\mathbf{x}_i, \phi_i, \mathbf{u}_i\}$. The chemical interactions between cells are mediated by a global concentration field $c(\mathbf{x}, t)$ of autoinducer (AI), which depends on position $\mathbf{x}$ and time t. The full system is therefore characterised by the state variables $\{\mathbf{x}_i, \phi_i, \mathbf{u}_i\}_{i=1}^N$ and AI concentration field $c(\mathbf{x}, t)$.

Next we specify the dynamics for the state variables $\mathbf{x}_i$, ϕ_i, and $\mathbf{u}_i$. In terms of motility, we consider cells that undergo both run-and-tumble and active Brownian motion for generality. We also allow the cells to undergo passive diffusion. We model the genetic regulation of motility by allowing all active motility parameters

to depend on the internal concentrations $\mathbf{u}_i$. Between tumbles, the particle positions and orientations therefore obey

$$\frac{d\mathbf{x}_i}{dt} = v(\mathbf{u}_i)\mathbf{e}_i + \sqrt{2D_t}\boldsymbol{\zeta}_i(t), \tag{2.1a}$$

$$\frac{d\phi_i}{dt} = \sqrt{2D_r(\mathbf{u}_i)}\eta_i(t), \tag{2.1b}$$

where $\mathbf{e}_i := (\cos\phi_i, \sin\phi_i)^T$, while $v(\mathbf{u}_i)$ and $D_r(\mathbf{u}_i)$ are the respective gene-regulated self-propulsion speed and rotational diffusion coefficient. The passive translational diffusion coefficient is denoted by D_t. The quantities $\boldsymbol{\zeta}_i$ and η_i are independent, zero-mean, unit-variance Gaussian white noise terms associated with the translational diffusion and rotational diffusion, respectively. The motion of each cell, characterised by (2.1a)–(2.1b), is punctuated by tumbling events in which the cell attains a new orientation angle. In *E. coli*, the average duration of a tumble is roughly ten-times smaller than the average duration of a run, while the actual run time and new orientation are chosen from exponential and (approximate) uniform distributions, respectively [11] (Ch. 6). We therefore treat tumbling events as instantaneous and use exponential and uniform distributions for the run times and new orientations. To model gene-regulated motility, we pose a gene-regulated rate parameter (tumbling frequency) $\gamma(\mathbf{u}_i)$ for the exponential distribution. We omit a chemotactic term proportional to the gradient of a concentration field in (2.1a)–(2.1b) because many species of bacteria, including *E. coli*, are too small to sense spatial gradients directly. They instead bias their motion along gradients by adjusting their tumbling frequency to the local signal concentration *via* intracellular biochemical pathways (see [11], Ch. 2), which we model here by allowing a $\mathbf{u}_i$-dependent tumbling frequency γ. The cells are assumed to occupy a physical (2D) domain Ω that has reflecting boundaries $\partial\Omega$.

The internal state $\mathbf{u}_i$ represents the intracellular concentrations of gene-regulatory proteins or transcription factors, as well as any intermediate proteins involved in the reactions. Biochemical reactions are known to have a stochastic component, especially when the reagents are present in small amounts [44]. We model this by including a noise term in the reaction kinetics. As we will show, the noise term has the additional benefit that it regularises the resulting continuum equations. We thus have

$$\frac{d\mathbf{u}_i}{dt} = \mathbf{f}(\mathbf{u}_i, c(\mathbf{x}_i, t)) + \sqrt{2\varepsilon}\boldsymbol{\xi}_i(t), \tag{2.1c}$$

where $\mathbf{f} = (f_1, \ldots, f_M)^T$ describes the reaction kinetics, which depend on the local AI concentration $c(\mathbf{x}, t)$. We will introduce the governing equation for c directly in terms of continuum quantities in our formal upscaling in the following section; for

now we assume that c is prescribed. The quantity ε is the strength of the zero-mean, unit-variance Gaussian white noise $\boldsymbol{\xi}_i$. We consider generic reaction kinetics $\mathbf{f}$ in developing the model, but in later chapters specialise to various classes. Eq. (2.1c) assumes a common noise strength ε for each chemical species. In general, this can be accomplished through a rescaling of the components of $\mathbf{u}_i$. In later chapters we will work in the regime of small noise, so it is important that the noise strengths prior to the rescaling are on the same order of magnitude. In the linear noise approximation (LNA) of a stochastic reaction network, the coefficient ε should be a function of $\mathbf{u}_i$ in general (see e.g. [35], Ch. 3). We make ε constant in (2.1c) for simplicity, which we expect to have no affect on any of our results since we consider the limit of small ε (after non-dimensionalising). In reality, the concentration $\mathbf{u}_i$ of each reagent is discrete and the reaction network is accurately described by the chemical master equation [35], Ch. 3. However, it is known that in the LNA, the system is well-approximated by a Langevin equation (see [43]), as assumed in (2.1c).

Before continuing, we state here some generic assumptions on $\mathbf{f}$ to ensure physically realistic (i.e. bounded and non-negative) chemical concentrations. These assumptions will be important in our formal upscaling. Let us write $\mathbf{u} = (u_1, \ldots, u_M)$, where we drop the cell index for convenience. Non-negative concentrations require that $\mathbf{u}$ lies in the positive orthant of state space, which we denote by $\mathbb{R}^M_+$. To ensure non-negative concentrations in the absence of noise ($\varepsilon = 0$), it is sufficient to impose that the components of $\mathbf{f}$ satisfy $f_j(\mathbf{u}, c) \geq 0$ on the boundary $\partial\mathbb{R}^M_+$. For finite ε, we additionally impose that $\partial\mathbb{R}^M_+$ is reflecting. To ensure bounded concentrations, we also impose $f_j(\mathbf{u}, c) < 0$ as $|\mathbf{u}| \to \infty$ in the positive orthant.

Our cell-level model consists of the equations of motion (2.1). The motility of each cell is determined by the internal concentration $\mathbf{u}_i$, which evolves according to prescribed gene-regulatory reaction kinetics $\mathbf{f}(\mathbf{u}_i, c)$. The cells interact through the global concentration field $c(\mathbf{x}, t)$, which couples the reaction kinetics in each cell. Our system therefore describes a population of motile bacteria whose motility is effectively controlled by chemical signalling in combination with the gene-regulatory network.

2.2 Formal Upscaling and Continuum Model

Our starting point for the upscaling is to reformulate the SDEs (2.1) in terms of a probability density function. In this alternative description, the probability of the population being in the state $\{\mathbf{x}_i, \phi_i, \mathbf{u}_i\}_{i=1}^N$ at time t is given by $\psi_N(\{\mathbf{x}_i, \phi_i, \mathbf{u}_i\}_{i=1}^N, t)$.

Our approach is similar to the methodology of [13,19] wherein they upscale a system of active particles that have pairwise physical interactions, but no chemical interaction.

The evolution of ψ_N is governed by the Fokker–Planck equation. For our system of SDEs (2.1), we have

$$\begin{aligned}\frac{\partial \psi_N}{\partial t} =& \sum_{i=1}^{N} \nabla_{\mathbf{x}_i} \cdot \left(-v(\mathbf{u}_i)\mathbf{e}_i + D_t \nabla_{\mathbf{x}_i}\right) \psi_N + \sum_{i=1}^{N} D_r(\mathbf{u}_i) \frac{\partial^2 \psi_N}{\partial {\phi_i}^2} \\ &+ \sum_{i=1}^{N} \left(\frac{\gamma(\mathbf{u}_i)}{2\pi} \int_0^{2\pi} \psi_N \, \mathrm{d}\phi_i - \gamma(\mathbf{u}_i)\psi_N \right) + \sum_{i=1}^{N} \nabla_{\mathbf{u}_i} \cdot \left[\varepsilon \nabla_{\mathbf{u}_i} \psi_N - \mathbf{f}(\mathbf{u}_i, c(\mathbf{x}_i, t))\psi_N \right], \\ &\mathbf{x}_i \in \Omega, \quad \mathbf{u}_i \in \mathbb{R}_+^M, \quad \phi_i \in [0, 2\pi). \end{aligned} \tag{2.2}$$

Since probability is conserved, (2.2) has the form of a conservation equation where each term on the RHS is the divergence of a flux. The fluxes can be interpreted as follows. The fluxes in the first sum are due to self-propulsion and translational diffusion, respectively. In the second sum, the diffusive flux (in orientation space) is due to the rotational diffusion. In the third sum, the respective fluxes describe tumbles into and out of the orientation ϕ_i. Since we previously assumed that tumbling events occur instantaneously, the flux into angle ϕ_i is non-local. The form of the integral also implies that all orientations are equally probable, in line with our earlier assumption. The decay term describing tumbles out of orientation ϕ_i is due to our assumption that the run times are exponentially distributed. Finally, the diffusive and advective fluxes in the last sum are due to the internal noise and reaction kinetics. The form of these terms follows directly from (2.1c).

Next we impose appropriate boundary conditions on ψ_N. In our cell-level model, we confined the cells in both physical space and state space with reflecting boundaries. Hence, no-flux conditions are appropriate. These read

$$\left[D_t \nabla_{\mathbf{x}_i} \psi_N - v(\mathbf{u}_i)\mathbf{e}_i \psi_N\right] \cdot \mathbf{N}_{\mathbf{x}} = 0, \quad \mathbf{x}_i \in \partial\Omega, \tag{2.3a}$$

$$\left[\varepsilon \nabla_{\mathbf{u}_i} \psi_N - \mathbf{f}(\mathbf{u}_i, c)\psi_N\right] \cdot \mathbf{N}_{\mathbf{u}} = 0, \quad \mathbf{u}_i \in \partial\mathbb{R}_+^M, \quad |\mathbf{u}_i| \to \infty, \tag{2.3b}$$

for $i = 1, \ldots, N$, where $\mathbf{N}_{\mathbf{x}}$ and $\mathbf{N}_{\mathbf{u}}$ are the unit normals on the relevant domain boundary. We also impose periodic boundary conditions in the orientation variables ϕ_i.

Eq. (2.2) is a deterministic PDE that governs the evolution of the full probability density ψ_N. However, it is too complicated to study directly since it has $N \cdot (M + 3)$ independent variables. Moreover, it describes the system in full detail at the microscopic level, and we are interested in a macroscopic description. Our next step

therefore is to simplify (2.2)–(2.3) through a formal upscaling in which we effectively average out most of the independent variables.

Following [13], our next step is to derive a governing equation for the one-particle probability density. This is the conditional probability of finding a given cell in a given state, and we denote this quantity by ψ_1. Since the particles are identical, we consider the conditional probability for the first particle without loss of generality, so ψ_1 is determined by averaging over the other particles' state variables:

$$\psi_1(\mathbf{x}, \phi, \mathbf{u}, t) := \int \psi_N \, \mathrm{d}\phi_2 \ldots \mathrm{d}\phi_N \mathrm{d}\mathbf{x}_2 \ldots \mathrm{d}\mathbf{x}_N \mathrm{d}\mathbf{u}_2 \ldots \mathrm{d}\mathbf{u}_N. \tag{2.4}$$

Here the subscript '1' has been dropped on the independent variables to ease notation. By integrating (2.2) over positions, orientations, and internal concentrations of particles $2, \ldots, N$, we obtain an equation for ψ_1, which reads

$$\begin{aligned} \frac{\partial \psi_1}{\partial t} =& \nabla_{\mathbf{x}} \cdot (D_t \nabla_{\mathbf{x}} \psi_1 - v\mathbf{e}\psi_1) + D_r \frac{\partial^2 \psi_1}{\partial \phi^2} + \frac{\gamma}{2\pi} \int_0^{2\pi} \psi_1 \, \mathrm{d}\phi - \gamma \psi_1 \\ &+ \nabla_{\mathbf{u}} \cdot \left[\varepsilon \nabla_{\mathbf{u}} \psi_1 - \mathbf{f}(\mathbf{u}, c(\mathbf{x}, t)) \psi_1 \right], \end{aligned} \tag{2.5}$$

where we have used the no-flux boundary conditions in (2.3), as well as periodic boundary conditions in ϕ.

Next we employ a moment expansion technique with respect to the orientation ϕ (cf. [13, 19]). We denote the zeroth and first angular moments of ψ_1 as n and $\mathbf{p}$, which we refer to as the chemically structured cell density and orientation field. These quantities are defined by

$$n(\mathbf{x}, \mathbf{u}, t) := N \int_0^{2\pi} \psi_1 \, \mathrm{d}\phi, \tag{2.6a}$$

$$\mathbf{p}(\mathbf{x}, \mathbf{u}, t) := N \int_0^{2\pi} \mathbf{e}\psi_1 \, \mathrm{d}\phi. \tag{2.6b}$$

We emphasize here that the structured cell density n will be one of the main quantities of interest throughout the remainder of this thesis. The governing equations for n and $\mathbf{p}$ are found by computing zeroth and first angular moments of (2.5). These equations read

$$\frac{\partial n}{\partial t} = \nabla_{\mathbf{x}} \cdot (D_t \nabla_{\mathbf{x}} n - v\mathbf{p}) + \nabla_{\mathbf{u}} \cdot (\varepsilon \nabla_{\mathbf{u}} n - \mathbf{f} n), \tag{2.7a}$$

$$\frac{\partial \mathbf{p}}{\partial t} = D_t \nabla_{\mathbf{x}}^2 \mathbf{p} - \frac{v}{2} \nabla_{\mathbf{x}} n - (D_r + \gamma)\mathbf{p} + \varepsilon \nabla_{\mathbf{u}}^2 \mathbf{p} - \nabla_{\mathbf{u}} \cdot \left(\mathbf{f}\mathbf{p}^T \right) + v \nabla_{\mathbf{x}} \cdot \mathbf{Q}, \tag{2.7b}$$

where $\mathbf{Q}$ is the second angular moment of ψ_1, defined by

$$\mathbf{Q}(\mathbf{x}, \mathbf{u}, t) := N \int_0^{2\pi} \left(\frac{\mathbf{I}}{2} - \mathbf{e}\mathbf{e}^T \right) \psi_1 \, \mathrm{d}\phi, \tag{2.8}$$

where $\mathbf{I}$ is the identity matrix. We remark that the term $\mathbf{I}/2$ must be present so that the matrix $\mathbf{I}/2 - \mathbf{e}\mathbf{e}^T$ contains only the second-order harmonics $\cos(2\phi)$ and $\sin(2\phi)$. Otherwise the integral in (2.8) would have a contribution from n. We remark that since $\mathbf{f}\mathbf{p}^T$ is not square in general, the divergence term in (2.7b) is performed column-wise. In contrast $\mathbf{Q}$ is symmetric, so row-wise and column-wise divergence are equivalent.

Each of the terms on the RHS of (2.7) has physical meaning. On the RHS of the equation for n, the terms inside the first divergence represent the flux of cells through physical space, consisting of translational diffusion and advection in the direction of the orientation field $\mathbf{p}$ (cf. the corresponding terms in (2.2) in the first set of brackets). The flux through state space in the second set of brackets in (2.7a) is also similar to the corresponding fluxes in (2.2); the internal noise appears as a diffusion, and the reaction kinetics as an advection. In (2.7b), we see that orientational order is lost due to translational diffusion (first term), but produced by spatial gradients in the structured density (second term). The third term on the RHS of (2.7b) states that orientational order decays at the rate of reorientation $D_r + \gamma$. The final two terms represent the flux through chemical space, which have the same interpretation as in (2.7a).

The system (2.7) constitutes our upscaled version of the cell-level equations (2.1). However, even if we prescribe the AI concentration c, the system (2.7) is not closed due to the term involving the second-order moment $\mathbf{Q}$. It is possible in principle to derive a governing equation for $\mathbf{Q}$, but it will depend on the third-order moment. In general, the governing equation for each moment will have contributions from the next higher moment. In order to proceed with our upscaling, we will introduce a closure for $\mathbf{p}$ in (2.7). We accomplish this by exploiting a suitable macroscopic scaling regime, as detailed in the following subsection.

Before introducing our closure of (2.7), we describe our modelling choices for the AI concentration field $c(\mathbf{x}, t)$. We assume that AI molecules passively diffuse with coefficient D_c, decay with rate β, and are generated through cell secretion at a rate $\alpha(\mathbf{u})$. We therefore have

$$\frac{\partial c}{\partial t} = D_c \nabla_{\mathbf{x}}^2 c - \beta c + \int_{\mathbb{R}_+^M} \alpha(\mathbf{u}) n(\mathbf{x}, \mathbf{u}, t) \, \mathrm{d}\mathbf{u}, \tag{2.9}$$

where $\mathbb{R}_+^M$ is the positive orthant of $\mathbb{R}^M$. The final term on the RHS is the secretion term, which is non-local in $\mathbf{u}$ as it encodes the contribution from all internal concentrations in a locally averaged region of space. By allowing for a non-constant secretion

rate $\alpha(\mathbf{u})$, we retain the details of the reaction kinetics that generate c within each cell. In posing a secretion term proportional to the marginal probability density n, we implicitly assume a mean-field approximation for c and that the system comprises a large number of cells ($N \gg 1$) for which a continuum description is appropriate. Our continuum model so far consists of Eqs. (2.7) and (2.9).

2.2.1 Macroscopic Scaling Regime

Our goal now is to close the moment equations (2.7) using a suitable macroscopic scaling regime. To this end, we introduce the dimensionless quantities

$$\begin{aligned}
\tilde{\mathbf{x}} &= \frac{\mathbf{x}}{\mathcal{L}}, \quad \tilde{t} = \frac{t}{\mathcal{T}_d}, \quad \tilde{u} = \frac{u}{\mathcal{U}}, \\
\tilde{n}(\tilde{\mathbf{x}}, \tilde{u}, \tilde{t}) &= \frac{n(\mathbf{x}, u, t)}{\mathcal{N}}, \quad \tilde{\mathbf{p}}(\tilde{\mathbf{x}}, \tilde{u}, \tilde{t}) = \frac{\mathbf{p}(\mathbf{x}, \mathbf{u}, t)}{\mathcal{P}}, \quad \tilde{\mathbf{Q}}(\tilde{\mathbf{x}}, \tilde{\mathbf{u}}, \tilde{\mathbf{t}}) = \frac{\mathbf{Q}(\mathbf{x}, \mathbf{u}, t)}{\mathcal{Q}} \\
\tilde{c}(\tilde{\mathbf{x}}, \tilde{t}) &= \frac{c(\mathbf{x}, t)}{\mathcal{C}}, \quad \tilde{\mathbf{f}}(\tilde{\mathbf{u}}, \tilde{c}) = \frac{\mathcal{T}_k}{\mathcal{U}} \mathbf{f}(\mathbf{u}, c)
\end{aligned} \tag{2.10a}$$

as well as the dimensionless parameters

$$\begin{aligned}
&\tilde{D}_r(\tilde{\mathbf{u}}) = D_r(\mathbf{u})\mathcal{T}_r, \quad \tilde{\gamma}(\tilde{\mathbf{u}}) = \gamma(\mathbf{u})\mathcal{T}_r \quad \tilde{v}(\tilde{u}) = \frac{v(u)}{V} \quad \tilde{D}_t = \frac{D_t \mathcal{T}_d}{\mathcal{L}^2}, \quad \tilde{D}_c = \frac{D_c \mathcal{T}_d}{\mathcal{L}^2}, \\
&\tilde{\alpha}(\tilde{\mathbf{u}}) = \frac{\alpha(\mathbf{u})\mathcal{T}_d \mathcal{U}^M \mathcal{N}}{\mathcal{C}}, \quad \tilde{\beta} = \mathcal{T}_d \beta, \qquad \tilde{\varepsilon} = \frac{\varepsilon \mathcal{T}_k}{\mathcal{U}^2},
\end{aligned} \tag{2.10b}$$

where tildes denote dimensionless quantities. Here $\mathcal{L}$ is a characteristic lengthscale while $\mathcal{T}_d$, $\mathcal{T}_r$, and $\mathcal{T}_k$ are respective characteristic diffusive, rotational, and kinetic timescales. The quantities $\mathcal{U}$ and $\mathcal{C}$ are characteristic concentrations of internal chemical and AI. The quantities $\mathcal{N}$, $\mathcal{P}$, and $\mathcal{Q}$ are typical values of the structured cell density, orientation field magnitude, and $|\mathbf{Q}|$ respectively. Finally, V is a typical cell speed between tumbling events. We additionally define the dimensionless parameters

$$\chi := \frac{\mathcal{T}_d}{\mathcal{T}_r}, \quad \Gamma := \frac{\mathcal{T}_d}{\mathcal{T}_k}, \tag{2.10c}$$

and fix the ratio

$$\frac{\mathcal{L}^2}{\mathcal{T}_d} = V^2 \mathcal{T}_r, \tag{2.10d}$$

where the RHS of (2.10d) is the long-time, large-length diffusion coefficient of an individual active Brownian particle (cf. [13, 14, 19]); hence $\mathcal{L}$ and $\mathcal{T}_d$ are diffusive length and timescales characteristic of the active motion. We also fix $\mathcal{P}/\mathcal{N} = V\mathcal{T}_r/\mathcal{L}$ and $\mathcal{Q}/\mathcal{N} = (V\mathcal{T}_r/\mathcal{L})^2$. The quantity $V\mathcal{T}_r/\mathcal{L}$ is the ratio of the persistence length to the diffusive lengthscale and will turn out to be small in our macroscopic scaling

regime, implying that we consider systems whose (dimensional) orientation $|\mathbf{p}|$ and second moment $|\mathbf{Q}|$ are small compared to n. Inserting the non-dimensionalisation (2.10) into the governing equations for n and $\mathbf{p}$ (2.7) yields

$$\frac{\partial \tilde{n}}{\partial \tilde{t}} = \tilde{D}_t \nabla^2_{\tilde{\mathbf{x}}} \tilde{n} - \tilde{v} \nabla_{\tilde{\mathbf{x}}} \cdot \tilde{\mathbf{p}} + \Gamma \nabla_{\tilde{\mathbf{u}}} \cdot \left(\tilde{\varepsilon} \nabla_{\tilde{\mathbf{u}}} \tilde{n} - \tilde{\mathbf{f}}(\tilde{\mathbf{u}}, \tilde{c}) \tilde{n} \right), \tag{2.11a}$$

$$\begin{aligned} \frac{\partial \tilde{\mathbf{p}}}{\partial \tilde{t}} =& \tilde{D}_t \nabla^2_{\tilde{\mathbf{x}}} \tilde{\mathbf{p}} - \chi \left(\frac{\tilde{v}}{2} \nabla_{\tilde{\mathbf{x}}} \tilde{n} + (\tilde{D}_r + \tilde{\gamma}) \tilde{\mathbf{p}} \right) + \Gamma \left(\tilde{\varepsilon} \nabla^2_{\tilde{\mathbf{u}}} \tilde{\mathbf{p}} - \nabla_{\tilde{\mathbf{u}}} \cdot \left[\tilde{\mathbf{f}}(\tilde{\mathbf{u}}, \tilde{c}) \tilde{\mathbf{p}}^T \right] \right) \\ &+ \tilde{v} \nabla_{\tilde{\mathbf{x}}} \cdot \tilde{\mathbf{Q}}. \end{aligned} \tag{2.11b}$$

Eqs. (2.11) constitute dimensionless versions of (2.7).

We now close (2.11) using scaling arguments. We consider a macroscopic scaling regime in which the reorientation timescale $\mathcal{T}_r$ is much shorter than both the diffusive timescale $\mathcal{T}_d$ and kinetic timescale $\mathcal{T}_k$. Mathematically, this regime is given by $\chi \gg 1$ and $\chi \gg \Gamma$; we make no assumption on the size of Γ. We consider an alternative scaling regime in the following section in which our system reduces to an effective active system with physical interactions (a classical active system).

Since $\chi \gg 1$ and $\chi \gg \Gamma$, the $\mathcal{O}(\chi)$ terms dominate in (2.11b). Hence $\mathbf{p}$ has the following quasi-steady state to leading order in χ:

$$\mathbf{p} \sim -\frac{v}{2\left[\gamma + D_r\right]} \nabla_{\mathbf{x}} n, \tag{2.12}$$

where we drop the tilde notation as well as neglect the second-order moment, assuming $|\mathbf{Q}| \ll \chi$. In [13, 19, 61] they argue that $\mathbf{Q}$ is negligible for 1) timescales much longer than the tumbling/reorientation timescale and 2) lengthscales much larger than the persistence length $V\mathcal{T}_r$. In our case, the first condition is satisfied in the regime $\chi \gg 1$, while the second is satisfied due to the diffusive scaling (2.10d), i.e. $(V\mathcal{T}_r)^2 = \mathcal{L}^2 \mathcal{T}_r / \mathcal{T}_d \ll \mathcal{L}^2$. Next, we substitute the quasi-steady orientation field (2.12) into the density equation (2.11a) to obtain

$$\frac{\partial n}{\partial t} = \left(D_t + \frac{v^2(\mathbf{u})}{2(D_r(\mathbf{u}) + \gamma(\mathbf{u}))} \right) \nabla^2_{\mathbf{x}} n + \Gamma \nabla_{\mathbf{u}} \cdot \left(\varepsilon \nabla_{\mathbf{u}} n - \mathbf{f}(\mathbf{u}, c) n \right). \tag{2.13}$$

We now absorb the factor of Γ into our definition of $\mathbf{f}$ and ε. As this factor will not reappear in our subsequent analysis, we remark here that our small-ε asymptotics in the following chapters requires that $\Gamma\varepsilon \ll 1$ in addition to $\varepsilon \ll 1$. Physically, this means that the chemical noise is small on the diffusive timescale $\mathcal{T}_d$. Our dimensionless

continuum model is therefore

$$\frac{\partial n}{\partial t} = \mathcal{D}(\mathbf{u})\nabla_{\mathbf{x}}^2 n + \nabla_{\mathbf{u}} \cdot (\varepsilon \nabla_{\mathbf{u}} n - \mathbf{f}(\mathbf{u}, c)n)\,, \tag{2.14a}$$

$$\frac{\partial c}{\partial t} = D_c \nabla_{\mathbf{x}}^2 c - \beta c + \int_{\mathbb{R}_+^M} \alpha(\mathbf{u}) n(\mathbf{x}, \mathbf{u}, t)\, \mathrm{d}\mathbf{u}, \tag{2.14b}$$

$$\mathcal{D}(\mathbf{u}) := D_t + \frac{v^2(\mathbf{u})}{2\left[\gamma(\mathbf{u}) + D_r(\mathbf{u})\right]}. \tag{2.14c}$$

Here, $\mathcal{D}(\mathbf{u})$ is an effective gene-regulated diffusion coefficient resulting from the upscaled run-and-tumble/active Brownian motion. Eq. (2.14c) agrees with the effective diffusion coefficient derived previously in the parameter regime where our model and previous models in [13,19] overlap. This regime is given by no gene-regulated motility ($v, \gamma =$ const. in (2.14c)) and no physical interaction ($\zeta = 0$ in (1.3)). This agreement is expected since we consider a similar diffusive scaling regime (2.10d) with $\chi \gg 1$.

In summary, we have derived the simplified governing equation (2.14a) by upscaling the cell-level equations of motion (2.1) in a suitable macroscopic scaling regime. In this scaling regime, the timescale of particle tumbling and reorientation is much faster than the kinetic and diffusive timescales. With the diffusive scaling (2.10d), this is equivalent to considering lengthscales larger than the particle persistence length. We emphasize that the relationship between the kinetic and diffusive timescales remains general as we have made no assumption on the size of Γ. Our continuum model is expected to hold for populations with large numbers of cells, as are typically present in natural [27] and synthetic [58] biological systems. In the continuum equations (2.14), the intracellular chemical concentrations $\mathbf{u}$ become independent variables, whereas they began as dependent variables in the cell-level model (2.1). That is, the population-level equations are structured in terms of the GRN inside cells; we refer to these multiscale equations as GRN-structured.

We now deduce the boundary conditions on n. We accomplish this by integrating the boundary conditions for ψ_N in (2.3) over the state variables of particles $2, \ldots, N$ as well as the orientation of particle 1. By integrating (2.3a) in this way and using the definition (2.6b) as well as the quasi-steady orientation (2.12), we obtain

$$\nabla_{\mathbf{x}} n \cdot \mathbf{N}_{\mathbf{x}} = 0, \quad \mathbf{x} \in \partial\Omega. \tag{2.14d}$$

We integrate (2.3b) in the same fashion and obtain

$$[\varepsilon \nabla_{\mathbf{u}} n - \mathbf{f}(\mathbf{u}, c)n] \cdot \mathbf{N}_{\mathbf{u}} = 0, \quad \mathbf{u} \in \partial\mathbb{R}_+^M, \quad |\mathbf{u}| \to \infty. \tag{2.14e}$$

Finally, we assume that the AI molecules are confined to the domain Ω, just as the cells. We therefore impose no-flux boundary conditions on c as

$$\nabla_{\mathbf{x}} c \cdot \mathbf{N}_{\mathbf{x}} = 0, \quad \mathbf{x} \in \partial\Omega. \tag{2.14f}$$

Our full continuum model consists of the governing equations (2.14a)–(2.14c) as well as the no-flux boundary conditions (2.14d)–(2.14f). A schematic of the model illustrating its multiscale nature is given in Figure 2.1. We remark that that the physical cell density $\rho(\mathbf{x}, t)$ is related to the GRN-structured cell density n through (cf. (1.10))

$$\rho(\mathbf{x}, t) = \int_{\mathbb{R}_+^M} n \, \mathrm{d}\mathbf{u}. \tag{2.15}$$

Importantly, we note that (2.14a) is a conservation equation as the RHS is the total divergence (with respect to $\mathbf{u}$ and $\mathbf{x}$) of a flux. As such, there is an associated conserved quantity given by

$$\int_{\mathbb{R}_+^M} \int_{\Omega} n(\mathbf{x}, \mathbf{u}, t) \, \mathrm{d}\mathbf{x}\mathrm{d}\mathbf{u} := \rho^* |\Omega| = \text{const.}, \tag{2.16}$$

where ρ^* is the global cell density and can be considered an additional model parameter while $|\Omega|$ the area of Ω. When expressed in dimensional quantities using (2.10a), the constant on the RHS of (2.16) is equal to N, the total number of cells. In principle, we could fix the scaling $\mathcal{N}$ in (2.10a) so that the RHS of (2.16) is equal to one; however, it will be convenient to keep ρ^* as a parameter to explore the effect of varying the total number of cells in our system.

Finally, we check that our scaling regime is biologically relevant. We estimate $\chi \approx 900$ and $\Gamma \approx 15$ for run-and-tumble bacteria (no rotational diffusion) with a canonical LuxIR gene-regulatory network (see Chapter 3) and a lengthscale of $\mathcal{L} = 1\text{mm}$. These values are in line with the scaling regime $\chi \gg 1$ and $\chi \gg \Gamma$. On a lengthscale comparable to a Petri dish ($\mathcal{L} \approx 1\text{cm}$), we obtain even more favourable estimates of $\chi \approx 9 \times 10^4$ and $\Gamma \approx 1.5 \times 10^3$. These values are estimated with (2.10c)–(2.10d) and with a tumble rate of $\mathcal{T}_r^{-1} \approx 0.6\text{s}^{-1}$ and run speed of $V \approx 20\mu\text{m/s}$ (see the paragraph below Eq. (12) and bottom of page 6 of [94]). We also use $\mathcal{T}_k^{-1} \approx 0.01\text{s}^{-1}$ as the natural decay rate of the LuxR-AI dimer in the canonical LuxIR system (see the parameter $\tilde{k}_-$ in Table S1 of [25]). We note that other possible choices for $\mathcal{T}_k$ based on the parameter values given in [25] yield even more favourable estimates for Γ.

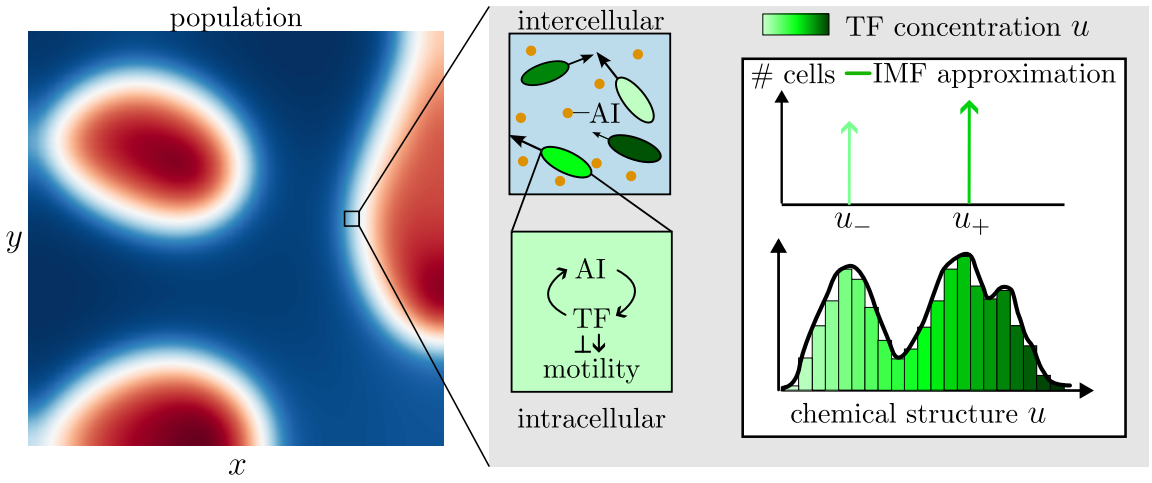

Figure 2.1: Schematic illustration of our multiscale models of chemically interacting cells. We represent the cell density (left panel) by a continuum field $n(\mathbf{x}, \mathbf{u}, t)$. The motility of individual cells depends on their internal concentrations $\mathbf{u}$. The various gene-regulatory proteins or transcription factors can either repress or promote motility. The GRN-structured model in (2.14) retains the distribution of internal chemical while the internal mean-field (IMF) model in (2.36) and (2.38) approximates the distribution of each chemical species as a superposition of Dirac-delta functions (two shown here).

2.2.2 Alternative Scaling Regime: Reduction to a Classical System

In this section, we give an alternative scaling regime in which our upscaling instead leads to an effective classical system. In particular, the chemical interaction is replaced by an effective physical interaction. Our analysis therefore clarifies the conditions under which chemical interaction can be accurately represented by an effective physical force, as is often done in the literature [2, 45, 54].

We aim to show that on a diffusive timescale the full system (2.11) is dynamically equivalent to a classical active matter system when the following scaling assumptions are satisfied:

1. fast reaction kinetics with respect to the tumbling and reorientation timescales ($\Gamma \gg \chi$),

2. fast AI secretion and decay timescales as compared to AI diffusion timescales ($\beta \sim |\alpha| = \mathcal{O}(\Gamma) \gg D_c$),

3. fast tumbling and reorientation with respect to cell diffusion ($\chi \gg 1$),

4. the kinetics have a unique, linearly stable equilibrium in the sense that for any fixed c, there is a unique $\mathbf{u}^*$ such that $\mathbf{f}(\mathbf{u}^*, c) = \mathbf{0}$ for which the eigenvalues of the Jacobian of $\mathbf{f}$ are negative.

At the continuum level, physical inter-particle interactions generally appear as a density dependence in the motility parameters [13, 38, 83]. For pure active Brownian particles, the self-propulsion speed is approximately linear over a wide range of cell densities and several pairwise interaction potentials [39]. Below, we describe a further special case where the gene-regulated motility in our model reduces to a linear density-dependent motility, thereby effectively representing repulsive active Brownian particles.

We begin by considering (2.11) in the regime characterised by assumptions 1 – 4 above. For simplicity, we set $\varepsilon = D_t = 0$. Eq. (2.11) thus becomes

$$\frac{\partial n}{\partial t} = -v\nabla_{\mathbf{x}} \cdot \mathbf{p} - \Gamma \nabla_{\mathbf{u}} \cdot [\mathbf{f}(\mathbf{u}, c)n], \tag{2.17a}$$

$$\frac{\partial \mathbf{p}}{\partial t} = -\chi \left[\frac{v}{2}\nabla_{\mathbf{x}} n + (D_r + \gamma)\mathbf{p}\right] - \Gamma \nabla_{\mathbf{u}} \cdot \left[\mathbf{f}(\mathbf{u}, c)\mathbf{p}^T\right] + v\nabla_{\mathbf{x}} \cdot \mathbf{Q}. \tag{2.17b}$$

When $\Gamma \gg \chi \gg 1$, the reaction terms dominate in both (2.17a) and (2.17b), so the internal reactions equilibrate on an $\mathcal{O}(\Gamma^{-1})$ timescale. To account for both the fast $\mathcal{O}(\Gamma^{-1})$ kinetic timescale and the slow $\mathcal{O}(1)$ diffusive timescale, we use a formal multiple scales approach and introduce fast and slow time variables τ and T as

$$\tau = \Gamma t, \qquad T = t, \tag{2.18}$$

respectively. We then separate the two scales in the field variables as

$$n(\mathbf{x}, \mathbf{u}, t) = n(\mathbf{x}, \mathbf{u}, \tau, T), \qquad \mathbf{p}(\mathbf{x}, \mathbf{u}, t) = \mathbf{p}(\mathbf{x}, \mathbf{u}, \tau, T), \qquad c(\mathbf{x}, t) = c(\mathbf{x}, \tau, T). \tag{2.19}$$

The leading order $\mathcal{O}(\Gamma)$ terms in (2.17) describe the dynamics on the fast scale as

$$\frac{\partial n}{\partial \tau} = -\nabla_{\mathbf{u}} \cdot [\mathbf{f}(\mathbf{u}, c)n], \tag{2.20a}$$

$$\frac{\partial \mathbf{p}}{\partial \tau} = -\nabla_{\mathbf{u}} \cdot \left[\mathbf{f}(\mathbf{u}, c)\mathbf{p}^T\right], \tag{2.20b}$$

where we assume that the higher-order moment is $o(\Gamma)$. Similarly, the leading order $\mathcal{O}(\Gamma)$ terms in (2.14b) yield

$$\frac{\partial c}{\partial \tau} = -\beta c + \int_{\mathbb{R}_+^M} \alpha(\mathbf{u}) n(\mathbf{x}, \mathbf{u}, \tau), \tag{2.20c}$$

where we have implicitly rescaled α and β in accordance with assumption 2 above.

Since our aim is to simplify our system for $t = \mathcal{O}(1)$, we are interested in the limit $\tau \to \infty$ of (2.20). To this end, we note that Eqs.(2.20a) and (2.20b) are first order PDEs that have characteristic curves $\mathbf{u}(\mathbf{x}, \tau, T)$, $n(\mathbf{x}, \tau, T)$, $\mathbf{p}(\mathbf{x}, \tau, T)$ defined by

$$\frac{d\mathbf{u}}{d\tau} = \mathbf{f}(\mathbf{u}, c), \tag{2.21a}$$

$$\frac{dn}{d\tau} = -\left(\nabla_{\mathbf{u}} \cdot \mathbf{f}\right) n, \tag{2.21b}$$

$$\frac{d\mathbf{p}}{d\tau} = -\left(\nabla_{\mathbf{u}} \cdot \mathbf{f}\right) \mathbf{p}, \tag{2.21c}$$

where $\mathbf{x}$ and T appear as parameters. From (2.20c) and (2.21a), $\mathbf{u}$ and c have quasi-steady states $\mathbf{u} = \mathbf{u}^*(\mathbf{x}, T)$, $c = c^*(\mathbf{x}, T)$ where

$$\mathbf{f}(\mathbf{u}^*(\mathbf{x}, T), c^*(\mathbf{x}, T)) = \mathbf{0}, \tag{2.22a}$$

$$\beta c^* - \int_{\mathbb{R}^M_+} \alpha(\mathbf{u}) n(\mathbf{x}, \mathbf{u}, T)\, \mathrm{d}\mathbf{u} = 0. \tag{2.22b}$$

From assumption 4, we have that $\nabla_{\mathbf{u}} \cdot \mathbf{f} < 0$ at $\mathbf{u} = \mathbf{u}^*$, so we deduce from (2.21b) that $n(\mathbf{x}, \mathbf{u}^*, \tau, T) \to \infty$ as $\tau \to \infty$. The boundary conditions (2.14e) with $\varepsilon = 0$ imply that n vanishes on the boundary $\partial\mathbb{R}^M_+$. Since the components of $\mathbf{f}$ are positive on the boundary and negative as $|\mathbf{u}| \to \infty$ (by our earlier assumptions at the end of Section 2.1 to ensure bounded, non-negative concentrations), the characteristics $\mathbf{u}(\mathbf{x}, \tau, T)$ sweep inwards into $\mathbb{R}^M_+$. As such we have that that $n(\mathbf{x}, \mathbf{u}, \tau, T) \to 0$ as $\tau \to \infty$ for $\mathbf{u} \neq \mathbf{u}^*$. The same reasoning applies to $\mathbf{p}$ in (2.21c). There may be multiple solutions of (2.22) in general, but assumption 4 implies that (2.22a) determines $\mathbf{u}^*$ uniquely in terms of c^*. This implies that $n(\mathbf{x}, \mathbf{u}, \tau, T)$ diverges at only a single point as $\tau \to \infty$. Overall for n and $\mathbf{p}$, we formally have

$$n(\mathbf{x}, \mathbf{u}, \tau, T) = \rho(\mathbf{x}, T)\delta(\mathbf{u} - \mathbf{u}^*(\mathbf{x}, T)), \quad \text{as } \tau \to \infty, \tag{2.23a}$$

$$\mathbf{p}(\mathbf{x}, \mathbf{u}, \tau, T) = \mathbf{P}(\mathbf{x}, T)\delta(\mathbf{u} - \mathbf{u}^*(\mathbf{x}, T)), \quad \text{as } \tau \to \infty, \tag{2.23b}$$

where δ is the Dirac-delta function, while ρ and $\mathbf{P}$ are the unknown cell density and orientation field that vary on the diffusive timescale. We note that (2.23) is a steady solution of (2.20) in the weak sense. That is, if we require $\int_0^\infty \nabla_{\mathbf{u}} \cdot [\mathbf{f}(\mathbf{u}, c^*)n]\, \Psi(u)\, \mathrm{d}u = 0$ for all smooth test functions Ψ, then after integration by parts we see that (2.23a) is a solution by the sifting property of the Dirac-delta function. Again by the sifting property, Eq. (2.22b) now becomes

$$\beta c^* = \alpha(\mathbf{u}^*(\mathbf{x}, T))\rho(\mathbf{x}, T). \tag{2.24}$$

Eqs. (2.22a) and (2.24) constitute an algebraic system that can in principle be solved for $\mathbf{u}^*(\mathbf{x}, T)$ and $c^*(\mathbf{x}, T)$ as a function of $\rho(\mathbf{x}, T)$. We therefore make use of the shorthand $\mathbf{u}^*(\rho) := \mathbf{u}^*(\rho(\mathbf{x}, T))$.

Next we determine the unknown cell density and orientation field ρ and $\mathbf{P}$ in (2.23). We integrate (2.17b) over $\mathbf{u}$ and make use of assumption 3 ($\chi \gg 1$). This yields

$$\mathbf{P} \sim -\frac{1}{2\left(D_r(\rho) + \gamma(\rho)\right)} \nabla_{\mathbf{x}} \left(\rho \int_{\mathbb{R}_+^M} v(\mathbf{u}) \delta(\mathbf{u} - \mathbf{u}^*(\rho)) \, \mathrm{d}\mathbf{u} \right) = -\frac{1}{2} \nabla_{\mathbf{x}} \left(v(\rho)\rho \right), \quad (2.25)$$

where we have assumed that the higher order moment is $o(\chi)$. Integrating (2.17a) over $\mathbf{u}$ and substituting (2.25) yields

$$\frac{\partial \rho}{\partial T} = \nabla_{\mathbf{x}} \cdot \left[\left(\frac{v^2 + v v'}{2(D_r + \gamma)} \right) \nabla_{\mathbf{x}} \rho \right], \quad (2.26)$$

where the motility parameters v, γ, and D_r are now functions of ρ, and $v' = \mathrm{d}v/\mathrm{d}\rho$. Eq. (2.26) is equivalent to a continuum description of classical active matter in which the particles interact through physical forces. Eq. (2.26) has a linear instability when $v'/v < -\rho^{-1}$, consistent with classical active matter in the large lengthscale and timescale regime considered in [19, 20]; also cf. Eq. (1.6). This large lengthscale and timescale regime in our notation is given by (2.10d) and $\chi \gg 1$ (note that there is no kinetic timescale and hence no parameter Γ in classical systems).

We remark that assumption 2 can be relaxed to simply $\beta \sim |\alpha| \gg D_c$, in which the AI concentration still equilibrates on a timescale faster than diffusion, but possibly on a different timescale than the internal kinetics. We would find that n is still highly localised in $\mathbf{u}$ and the system reduces to classical active matter.

Finally, we give an example where our system is equivalent to a collection of interacting active Brownian particles, which is characterised by a linear self-propulsion $v(\rho)$. In the very-fast-chemical-timescale limit ($\Gamma \gg \chi \gg 1$), our self-propulsion $v(\mathbf{u}^*(\rho^*))$ will in general be nonlinear in the density. A linear motility arises as a special case when

1. the secretion rate is constant ($\alpha(\mathbf{u}) = \alpha_0$),

2. there is one internal species and the kinetics are linear in both the internal concentration $\mathbf{u} = u$ and the AI concentration c (cf. [40]), e.g. $f(u, c) = a + Lc - \lambda u$, for some constants a, L, and λ,

3. $v(u)$ is linear in the internal chemical u.

The first two of these assumptions imply that (2.22a) and (2.24) reduce to

$$a + Lc - \lambda u^* = 0, \quad \beta c = \alpha_0 \rho(\mathbf{x}, t). \tag{2.27}$$

Then assumption 3 gives a linear $v(\rho)$:

$$v(u^*(\rho)) = v_0 - \zeta u^*(\rho) = \bar{v}_0 - \bar{\zeta}\rho(\mathbf{x}, t), \tag{2.28}$$

where we absorb the intermediate coefficients.

2.3 The Internal Mean-Field Approximation

In this section, we return to our chemically structured system (2.14) and introduce an approximation for the cells' internal state, which reduces our model to a reaction-diffusion system. We hereafter refer to this model as the internal mean-field (IMF) model. The purpose of introducing an IMF model is to clarify situations in which the full chemical structure is important. We present the model in this chapter, but defer the analysis thereof to Chapter 5. We remark that a natural starting point for modelling of our system could have been to simply write down a phenomenological reaction-diffusion model. The derivation in this section formalises the relationship between the two modelling approaches. The IMF model also benefits from being much simpler to treat both analytically and numerically.

The main idea in the IMF approximation is to replace the full distribution of internal states with a finite set of effective states. Here we demonstrate the approximation for two internal states, but we emphasize that our analysis is generally applicable to any finite number of states. In the case of only one internal state, our approach effectively replaces the distribution with the mean. We again defer discussion of how to fix the number of internal states to Chapter 5 at which point our analysis of the structured model will provide a natural choice.

We begin by looking for solutions in which the cells are effectively in one of two states $\mathbf{u}_-$ or $\mathbf{u}_+$. We therefore impose an exponentially localised (in $\mathbf{u}$) distribution of internal chemical as

$$n(\mathbf{x}, \mathbf{u}, t) = (\pi\delta)^{-M/2} \sum_{j=\pm} \rho_j(\mathbf{x}, t) \exp\left(-\frac{|\mathbf{u} - \mathbf{u}_j(\mathbf{x}, t)|^2}{\delta}\right), \tag{2.29}$$

and seek functions $\mathbf{u}_\pm$ and $\rho_\pm$ such that (2.29) satisfies the governing equations (2.14) in an average sense (to be clarified below). Here $\rho_\pm$ are the cell densities for the respective internal states $\mathbf{u}_\pm$. The free parameter δ is chosen small (i.e. $0 < \delta \ll 1$)

so that it makes sense to classify the cells into two effective states. Importantly, we assume that the two states are well-separated in the sense $|\mathbf{u}_+ - \mathbf{u}_-| = \mathcal{O}(1)$ for all $\mathbf{x}$ and t. We remark that n has been normalised such that

$$\int_{\mathbb{R}^M_+} n(\mathbf{x}, \mathbf{u}, t)\,\mathrm{d}\mathbf{u} = \rho_+(\mathbf{x}, t) + \rho_-(\mathbf{x}, t) + \text{E.S.T.}, \tag{2.30}$$

where here E.S.T. denotes exponentially small terms with respect to δ. The goal of the following analysis is to derive approximate governing equations for $\rho_\pm$ and $\mathbf{u}_\pm$.

The natural next step of substituting (2.29) into the governing equations (2.14a) fails because exact solutions do not have a $\mathbf{u}$-dependence in the form (2.29). Instead, we integrate the governing equations in neighbourhoods $\mathbb{B}_+$ of $\mathbf{u}_+$ and $\mathbb{B}_-$ of $\mathbf{u}_-$. For concreteness, we let these neighbourhoods be balls of radius R, where $\delta \ll R^2 \ll 1$. This choice guarantees that $\mathbf{u}_\mp \notin \mathbb{B}_\pm$ as $\mathbf{u}_\pm$ are well-separated and crucially allows us to employ Laplace's method to eventually evaluate the integrals. Next, we integrate (2.14a) over $\mathbb{B}_+$ and apply the divergence theorem to obtain

$$\int_{\mathbb{B}_+} \partial_t n\,\mathrm{d}\mathbf{u} = \int_{\mathbb{B}_+} \mathcal{D}\nabla^2_{\mathbf{x}} n\,\mathrm{d}\mathbf{u} + \int_{\partial\mathbb{B}_+} (\varepsilon\nabla_{\mathbf{u}} n - \mathbf{f}n)\cdot \mathrm{d}\mathbf{S}, \tag{2.31a}$$

where $\mathrm{d}\mathbf{S}$ is the surface element on $\partial\mathbb{B}_+$. Similarly, multiplying (2.14a) by $\mathbf{u}$ and integrating leads to

$$\int_{\mathbb{B}_+} \mathbf{u}\partial_t n\,\mathrm{d}\mathbf{u} = \int_{\mathbb{B}_+} \mathbf{u}\mathcal{D}\nabla^2_{\mathbf{x}} n\,\mathrm{d}\mathbf{u} - \int_{\mathbb{B}_+} (\varepsilon\nabla_{\mathbf{u}} n - \mathbf{f}n)\;\mathrm{d}\mathbf{u} + \int_{\partial\mathbb{B}_+} \mathbf{u}\,(\varepsilon\nabla_{\mathbf{u}} n - \mathbf{f}n)\cdot \mathrm{d}\mathbf{S}. \tag{2.31b}$$

Next we want to use (2.29) and apply Laplace's method to simplify the integrals. It is convenient to use Reynold's Transport Theorem to interchange the order of integration over $\mathbf{u}$ and differentiation with respect to $\mathbf{x}$ and t. For example, the volume integrals in (2.31a) can be rewritten as

$$\int_{\mathbb{B}_+} \partial_t n\,\mathrm{d}\mathbf{u} = \partial_t \int_{\mathbb{B}_+} n\,\mathrm{d}\mathbf{u} - \int_{\partial\mathbb{B}_+} n\partial_t \mathbf{u}_+ \cdot \mathrm{d}\mathbf{S}, \tag{2.32}$$

and

$$\int_{\mathbb{B}_+} \mathcal{D}\nabla^2_{\mathbf{x}} n\,\mathrm{d}\mathbf{u} = \nabla^2_{\mathbf{x}} \int_{\mathbb{B}_+} \mathcal{D}n\,\mathrm{d}\mathbf{u} - 2\int_{\partial\mathbb{B}_+} \mathcal{D}(\nabla_{\mathbf{x}} n)^T \nabla_{\mathbf{x}} \mathbf{u}_+\,\mathrm{d}\mathbf{S} - \nabla_{\mathbf{x}} \cdot \int_{\partial\mathbb{B}_+} \mathcal{D}n\nabla_{\mathbf{x}}\mathbf{u}_+\,\mathrm{d}\mathbf{S}. \tag{2.33}$$

We rewrite the volume integrals in (2.31b) in a similar fashion so that (2.31) becomes

$$\begin{aligned}\partial_t \int_{\mathbb{B}_+} n\,\mathrm{d}\mathbf{u} - \nabla^2_{\mathbf{x}} \int_{\mathbb{B}_+} \mathcal{D}n\,\mathrm{d}\mathbf{u} = \int_{\partial\mathbb{B}_+} \left(n\partial_t \mathbf{u}_+ - 2\mathcal{D}(\nabla_{\mathbf{x}} n)^T \nabla_{\mathbf{x}}\mathbf{u}_+\right)\,\mathrm{d}\mathbf{S} \\ - \nabla_{\mathbf{x}} \cdot \int_{\partial\mathbb{B}_+} \mathcal{D}n\nabla_{\mathbf{x}}\mathbf{u}_+\,\mathrm{d}\mathbf{S},\end{aligned} \tag{2.34a}$$

$$\partial_t \int_{\mathbb{B}_+} \mathbf{u} n \, \mathrm{d}\mathbf{u} - \nabla_{\mathbf{x}}^2 \int_{\mathbb{B}_+} \mathbf{u}\mathcal{D} n \, \mathrm{d}\mathbf{u} + \int_{\mathbb{B}_+} \left(\varepsilon \nabla_{\mathbf{u}} n - \mathbf{f} n\right) \, \mathrm{d}\mathbf{u} = \int_{\partial\mathbb{B}_+} \mathbf{u} \left(n \partial_t \mathbf{u}_+ - 2\mathcal{D}(\nabla_{\mathbf{x}} n)^T \nabla_{\mathbf{x}} \mathbf{u}_+\right) \, \mathrm{d}\mathbf{S} - \nabla_{\mathbf{x}} \cdot \int_{\partial\mathbb{B}_+} \mathbf{u}\mathcal{D} n \nabla_{\mathbf{x}} \mathbf{u}_+ \, \mathrm{d}\mathbf{S}. \tag{2.34b}$$

By repeating the above procedure for $\mathbb{B}_-$, we derive a similar set of equations for ρ_- and $\mathbf{u}_-$. From (2.29), and assuming that spatial and temporal gradients of ρ_+ and $\mathbf{u}_+$ are $\mathcal{O}(1)$, the integrands in each of the boundary integrals above are proportional to $R^{M-1}\delta^{-M/2}\exp(-R^2/\delta) = \text{E.S.T.}$ In principle this holds independently of M. As such, the leading order contribution comes from the volume integrals, which we evaluate using Laplace's method (see (A.21) in Appendix A). We obtain

$$\partial_t \rho_\pm - \nabla_{\mathbf{x}}^2 \left[\mathcal{D}(\mathbf{u}_\pm)\rho_\pm\right] = \mathcal{O}(\delta), \tag{2.35a}$$

$$\partial_t (\rho_\pm \mathbf{u}_\pm) - \nabla_{\mathbf{x}}^2 \left[\mathcal{D}(\mathbf{u}_\pm)\mathbf{u}_\pm \rho_\pm\right] - \mathbf{f}(\mathbf{u}_\pm, c)\rho_\pm = \mathcal{O}(\delta), \tag{2.35b}$$

where the $\mathcal{O}(\delta)$ terms arise from Laplace's method. Note also that the $\mathcal{O}(\varepsilon)$ term in (2.34b) integrates to zero due to symmetry. As δ is a free parameter, we take the limit $\delta \to 0$ in (2.35) so that we are left with

$$\partial_t \rho_\pm = \nabla_{\mathbf{x}}^2 \left[\mathcal{D}(\mathbf{u}_\pm)\rho_\pm\right], \tag{2.36a}$$

$$\partial_t (\rho_\pm \mathbf{u}_\pm) = \nabla_{\mathbf{x}}^2 \left[\mathcal{D}(\mathbf{u}_\pm)\mathbf{u}_\pm \rho_\pm\right] + \mathbf{f}(\mathbf{u}_\pm, c)\rho_\pm. \tag{2.36b}$$

Eqs. (2.36) are the approximate governing equations for $\rho_\pm$ and $\mathbf{u}_\pm$, which constitute a system of reaction-diffusion equations. It remains to determine boundary conditions, as well as an effective equation for the AI concentration c.

We deduce boundary conditions for $\rho_\pm$ and $\mathbf{u}_\pm$ by integrating (2.14d) separately over $\mathbb{B}_+$ and $\mathbb{B}_-$. Using Laplace's method, we obtain the no-flux conditions

$$\nabla_{\mathbf{x}} \rho_\pm \cdot \mathbf{N}_{\mathbf{x}} = 0, \qquad \mathbf{x} \in \partial\Omega, \tag{2.37a}$$

$$\nabla_{\mathbf{x}} (\mathbf{u}_\pm) \mathbf{N}_{\mathbf{x}} = \mathbf{0}, \qquad \mathbf{x} \in \partial\Omega, \tag{2.37b}$$

where recall that $\mathbf{N}_{\mathbf{x}}$ is the unit normal to the boundary of the *spatial* domain Ω, not the ball $\mathbb{B}_+$ in $\mathbf{u}$-space.

Finally, we eliminate the structured density n from the governing equation (2.14b) for c. We substitute (2.29) into (2.14b) and use Laplace's method again to obtain

$$\partial_t c = D_c \nabla_{\mathbf{x}}^2 c - \beta c + \sum_{j=\pm} \alpha(\mathbf{u}_j)\rho_j. \tag{2.38}$$

We have again used the assumption that $\mathbf{u}_\pm$ are well-separated in order to divide the domain of integration into local contributions around $\mathbf{u}_\pm$. The boundary conditions on c remain unchanged, specifically

$$\nabla_{\mathbf{x}} c \cdot \mathbf{N}_{\mathbf{x}} = 0, \qquad \mathbf{x} \in \partial\Omega. \tag{2.39}$$

Our IMF model consists of the governing equations (2.36) and (2.38), together with the no-flux boundary conditions (2.37) and (2.39). A schematic illustration of the IMF model is given in Figure 2.1. We emphasize again that although we have assumed two internal states $\mathbf{u}_\pm$, the above derivation straightforwardly generalises to any finite number of states, provided that they satisfy the well-separated condition.

In the following two chapters, we investigate motility-induced patterning in the structured model. This will provide insight on the connection between the states $\mathbf{u}_\pm$ and the reaction kinetics $\mathbf{f}$. We then return to the IMF model in Chapter 5 where we explore this connection and compare the predictions of two models qualitatively and quantitatively.

Chapter 3

Analysis of a Canonical Quorum Sensing Circuit

In this chapter, we use our structured modelling framework that we developed in Chapter 2 to study a canonical quorum sensing circuit in a population of motile bacteria. We have published the steady-state and linear stability analyses from Sections 3.1 and 3.2, as well as some of the numerical results from Section 3.4 in [77]. The weakly nonlinear analysis in Section 3.3 has not been published nor submitted for publication.

3.1 Model Setup

Throughout this chapter, we consider a simple representation of the canonical LuxIR quorum sensing (QS) circuit [70]. A key feature of this system, and many other QS gene-regulatory networks (GRNs) in other bacterial species, is positive feedback [25, 70]. We pose the following specific functional form for the (scalar) kinetics $\mathbf{f} = f$ in the governing equations (2.14), which incorporate positive feedback

$$f(u, c) = a + \frac{Lc}{K + c} - \lambda u, \tag{3.1}$$

where $\mathbf{u} = u$ is the single internal chemical species and c is the local autoinducer (AI) concentration. Here a represents a constant base production rate of the intracellular chemical u, and λ is a natural decay rate. The second term on the RHS of (3.1) represents the production of internal chemical induced by the local AI concentration, which constitutes one half of the positive feedback. This term saturates at a maximal production rate of L and has a 'threshold' concentration at $c = K$ at which the production rate is half-maximal. Here we can interpret u as the concentration of the LuxR-AI dimer in the canonical system [25]. All parameters are positive.

The second half of the positive feedback enters through the secretion of AI in the final term on the RHS of (2.14b). For simplicity, we pose a secretion rate which increases linearly with the internal concentration:

$$\alpha(u) = \alpha_0 u, \tag{3.2}$$

where $\alpha_0 > 0$ is a constant. The positive feedback can be intuitively understood by considering the relationship between the AI concentration c and internal chemical u. From (3.1), larger values of c increase the production of internal chemical u, which in turn increases the local AI concentration c as seen from the governing equation (3.3b) below. We note that a gene-regulated (u-dependent) secretion rate is required to model positive feedback. If α constant, then the secretion would only be proportional to the cell density, so the internal GRN would not directly affect the AI concentration.

Our governing equations for the remainder of the chapter are, from (2.14),

$$\frac{\partial n}{\partial t} = \mathcal{D}(u)\nabla_{\mathbf{x}}^2 n + \varepsilon\frac{\partial^2 n}{\partial u^2} - \frac{\partial}{\partial u}\big(f(u,c)n\big), \tag{3.3a}$$

$$\frac{\partial c}{\partial t} = D_c\nabla_{\mathbf{x}}^2 c - \beta c + \alpha_0\int_0^\infty u\, n(\mathbf{x},u,t)\,\mathrm{d}u. \tag{3.3b}$$

We recall that D_c and β are the diffusion coefficient and natural decay rate of AI, $\mathcal{D}$ is the effective gene-regulated diffusion coefficient of the cells, and ε measures the strength of the noise in the GRN kinetics; all are positive. The boundary conditions read

$$\varepsilon\frac{\partial n}{\partial u} - f(u,c)n \to 0, \quad u \to 0,\infty, \tag{3.4a}$$

$$\nabla_{\mathbf{x}} n\cdot\mathbf{N}_{\mathbf{x}} = \nabla_{\mathbf{x}} c\cdot\mathbf{N}_{\mathbf{x}} = 0, \quad \mathbf{x}\in\partial\Omega, \tag{3.4b}$$

where we take Ω to be a rectangle with side lengths $\mathcal{L}_x$ and $\mathcal{L}_y$.

3.2 Steady-State and Linear Stability Analysis

3.2.1 Spatially Uniform Steady-State

To study the emergence of motility-induced patterning, we look for instabilities in the spatially uniform steady-state. We emphasize that this steady-state is not independent of the internal concentration u. We denote this steady-state by $n^*(u)$ and c^*, which together satisfy

$$\varepsilon\frac{d^2 n^*}{du^2} - \frac{d}{du}\left[f(u,c^*)n^*\right] = 0, \tag{3.5a}$$

$$\beta c^* - \alpha_0\int_0^\infty u\, n^*(u)\,\mathrm{d}u = 0. \tag{3.5b}$$

As c^* is constant, we can solve (3.5a) immediately to obtain

$$n^*(u) = A \exp\left[-\frac{\lambda}{2\varepsilon}(u-u^*)^2\right], \tag{3.6}$$

where A is an integration constant and the mean internal concentration u^* satisfies

$$f(u^*, c^*) = a + \frac{Lc^*}{K+c^*} - \lambda u^* = 0. \tag{3.7}$$

In (3.6) we have utilized the boundary condition (3.4a) to fix one of the integration constants. We calculate the constant A from (2.16) and find

$$A = \rho^* \sqrt{\frac{\lambda}{2\pi\varepsilon}} + \text{E.S.T.}, \tag{3.8}$$

where here and henceforth E.S.T. denotes exponentially small terms in ε. Next, we substitute (3.6) into (3.5b), and utilize Laplace's method (see (A.9) in Appendix A) to deduce that

$$\beta c^* = \alpha_0 \rho^* u^* + \text{E.S.T.} \tag{3.9}$$

The leading order terms in Eq. (3.9), together with Eq. (3.7), constitute an algebraic system that we can solve for the steady concentrations c^* and u^*. Although not explicitly required in the analysis that follows, we provide the (positive) solution for completeness:

$$c^* = \frac{1}{2}\left[\frac{\alpha_0\rho^*}{\beta\lambda}(a+L) - K\right] + \frac{1}{2}\sqrt{\left[K - \frac{\alpha_0\rho^*}{\beta\lambda}(a+L)\right]^2 + \frac{4\alpha_0\rho^* aK}{\beta\lambda}} + \text{E.S.T.}, \tag{3.10a}$$

$$u^* = \frac{\beta c^*}{\alpha_0 \rho^*} + \text{E.S.T.} \tag{3.10b}$$

The leading order spatially uniform steady-state of the system (3.1)–(3.4) is given by Eqs. (3.6) and (3.10).

3.2.2 Linear Stability Analysis

We now perform a linear stability analysis to detect the onset of patterning. First, we introduce small perturbations around the spatially uniform steady-state in the form

$$n(\mathbf{x}, u, t) = n^*(u) + \eta(u) e^{i\mathbf{k}\cdot\mathbf{x}+\sigma t}, \qquad c(\mathbf{x}, t) = c^* + C e^{i\mathbf{k}\cdot\mathbf{x}+\sigma t}, \tag{3.11}$$

where $\mathbf{k}$ is the spatial wavenumber of the perturbation and σ the growth rate. The quantities $\eta(u)$ and C are unknowns to be determined in combination with σ. The

spatially uniform steady solution given in (3.6) and (3.10) is linearly stable whenever $\mathrm{Re}(\sigma) < 0$ and linearly unstable whenever $\mathrm{Re}(\sigma) > 0$. The goal of the following analysis is to determine σ in terms of the model parameters. Setting $\mathrm{Re}(\sigma) = 0$ will therefore define a boundary in parameter space between stable (patterning) and unstable (no patterning) regimes.

To start the analysis, we substitute the perturbations (3.11) into the governing equation (3.3) and assume that the perturbations are small, i.e. $|\eta|, |C| \ll 1$, so that we can retain only the terms linear in η and C. This yields the following eigenvalue problem for the eigenfunctions η, C and eigenvalue σ:

$$\varepsilon \frac{d^2\eta}{du^2} + \frac{d}{du}\left[\lambda(u-u^*)\eta\right] - (\sigma + \mathcal{D}(u)k^2)\eta - f_c^* \frac{dn^*}{du} C = 0, \tag{3.12a}$$

$$(\sigma + \beta + D_c k^2)C - \alpha_0 \int_0^\infty u\eta(u)\,\mathrm{d}u = 0, \tag{3.12b}$$

where we define $k^2 := |\mathbf{k}|^2$ and f_c^* as

$$f_c^* := \frac{\partial f}{\partial c}(u, c^*). \tag{3.13}$$

Using (3.4a), we deduce that the perturbation η satisfies the no-flux (in u) boundary condition

$$\varepsilon \frac{d\eta}{du} - f(u, c^*)\eta \to 0, \quad u \to 0, \infty. \tag{3.14}$$

The no-flux (in $\mathbf{x}$) boundary conditions (3.4b) imply that $\mathbf{k}$ can only take on certain values

$$\mathbf{k} = \left(\frac{\pi\ell}{\mathcal{L}_x}, \frac{\pi m}{\mathcal{L}_y}\right)^T, \tag{3.15}$$

where ℓ and m are non-negative integers. Since we focus on studying spatial patterning, we do not allow $\ell = m = 0$.

The unperturbed solution $n^*(u)$ is exponentially localised near $u = u^*$ for small ε; in order for the perturbation to remain small compared to the steady-state, the same must be true for η. We therefore look for a WKBJ (Liouville-Green) approximation to η in the form

$$\eta(u) = \varepsilon^{-\frac{3}{2}} q(u) \exp\left[-\frac{\lambda(u-u^*)^2}{2\varepsilon}\right], \tag{3.16}$$

for an amplitude $q(u)$ to be determined. The $\varepsilon^{-3/2}$ prefactor is included for convenience so that $q = \mathcal{O}(C)$, as seen in (3.17) below. Inserting the WKBJ solution (3.16) and steady-state (3.6) into the governing equation for η in (3.12a), we obtain the amplitude equation for q, which reads

$$\varepsilon \frac{d^2 q}{du^2} - \lambda(u-u^*)\frac{dq}{du} - \left(\sigma + \mathcal{D}k^2\right) q = -\sqrt{\frac{\lambda^3}{2\pi}} \rho^* f_c^* C (u-u^*). \tag{3.17}$$

Since η is exponentially small as $u \to 0, \infty$, the amplitude q must be polynomially bounded as $u \to 0, \infty$.

We proceed by expanding the amplitude in a regular asymptotic series as

$$q(u) \sim \sum_{j=0}^{\infty} q_j(u)\varepsilon^j, \tag{3.18}$$

where each q_j must also be polynomially bounded as $u \to 0, \infty$. The goal now is to calculate q_0 and q_1 in order to obtain a leading order evaluation of the integral in (3.12b). We cannot ignore q_1 because we will find that $q_0(u^*) = 0$, which means that the contributions from the q_0 and q_1 terms to the integral will be comparable. Substituting the asymptotic series (3.18) into the amplitude equation (3.17) and equating coefficients of powers of ε gives

$$\lambda(u-u^*)q_0' + \left[\sigma + \mathcal{D}(u)k^2\right] q_0 = \sqrt{\frac{\lambda^3}{2\pi}}\rho^* f_c^* C(u-u^*), \tag{3.19a}$$

$$\lambda(u-u^*)q_j' + \left[\sigma + \mathcal{D}(u)k^2\right] q_j = q_{j-1}'', \qquad j = 1, \ldots, \tag{3.19b}$$

where we note from the definition of f in (3.1) that f_c^* is independent of u.

In general, solutions of (3.19) are non-smooth at u^*, even though solutions of the full amplitude equation (3.17) are smooth. This is because u^* is a singular point for the ODEs in (3.19), but not for (3.17). However, we show in Section 3.2.3 that any non-smooth solution of (3.19) cannot satisfy the boundary condition that q is polynomially bounded as $u \to 0, \infty$. We therefore proceed under the assumption that q_0 and q_1 must be smooth at $u = u^*$ without loss of generality, justifying this assumption later in Section 3.2.3.

Under the assumption that q_0 and q_1 are smooth at u^*, we look for solutions of (3.19) in the form of a regular power series centred at $u = u^*$. We therefore expand q_0 and q_1 as

$$q_j(u) = \sum_{\ell=0}^{\infty} q_j^{(\ell)}(u-u^*)^\ell, \tag{3.20}$$

and additionally Taylor expand $\mathcal{D}$ as

$$\mathcal{D}(u) = \sum_{\ell=0}^{\infty} \frac{\mathcal{D}_*^{(\ell)}}{\ell!}(u-u^*)^\ell, \quad \mathcal{D}_*^{(\ell)} := \left.\frac{d^\ell}{du^\ell}\right|_{u=u^*} \mathcal{D}(u). \tag{3.21}$$

We emphasize that the power series solution (3.20) does not introduce additional error in our calculation of the eigenvalue σ. This is because the form of the integrand in (3.12b) with the WKBJ solution (3.16) is such that the local behaviour of q_0

and q_1 is sufficient to evaluate the leading order contribution *via* Laplace's method. To calculate the coefficients $q_j^{(\ell)}$, we substitute (3.20)–(3.21) into (3.19) and equate powers of $u - u^*$ to obtain the following recursion relations

$$q_0^{(0)} = 0, \tag{3.22a}$$

$$q_0^{(\ell)} = \frac{1}{\sigma + \mathcal{D}_* k^2 + \ell\lambda} \left[\delta_{\ell 1} \sqrt{\frac{\lambda^3}{2\pi}} \rho^* f_c^* C - k^2 \sum_{m=1}^{\ell} \frac{\mathcal{D}_*^{(m)}}{m!} q_0^{(\ell-m)} \right], \quad \ell = 1, \ldots, \tag{3.22b}$$

$$q_1^{(0)} = \frac{2q_0^{(2)}}{\sigma + \mathcal{D}_* k^2}, \tag{3.22c}$$

$$q_1^{(\ell)} = \frac{1}{\sigma + \mathcal{D}_* k^2 + \ell\lambda} \left[(\ell+1)(\ell+2) q_0^{(\ell+2)} - k^2 \sum_{m=1}^{\ell} q_1^{(\ell-m)} \frac{\mathcal{D}_*^{(m)}}{m!} \right], \quad \ell = 1 \ldots, \tag{3.22d}$$

where δ_{ij} is the Kronecker delta. We note that $q_0(u^*) = 0$ as anticipated. The first few terms in the power series solutions for q_0 and q_1 read

$$q_0(u) = \sqrt{\frac{\lambda^3}{2\pi}} \frac{C\rho^* f_c^*}{\sigma + \mathcal{D}_* k^2 + \lambda} (u - u^*) \left[1 - \frac{\mathcal{D}_*' k^2}{\sigma + \mathcal{D}_* k^2 + 2\lambda} (u - u^*) + \ldots \right], \tag{3.23a}$$

$$q_1(u) = -\sqrt{\frac{\lambda^3}{2\pi}} \frac{2C\rho^* f_c^* \mathcal{D}_*' k^2}{(\sigma + \mathcal{D}_* k^2)(\sigma + \mathcal{D}_* k^2 + \lambda)(\sigma + \mathcal{D}_* k^2 + 2\lambda)} + \ldots, \tag{3.23b}$$

where we show only the terms required for a leading order evaluation of (3.12b).

We can now evaluate the integral in (3.12b) using Laplace's method. We are able to use this method because η is exponentially localised around u^*, as seen from (3.16) and (3.18). Using the version of Laplace's method in Eq. (A.9) of Appendix A gives

$$\begin{aligned} \int_0^\infty u\eta(u)\,\mathrm{d}u &= \sqrt{\frac{\pi}{2\lambda^3}} \frac{d^2}{du^2}\bigg|_{u=u^*} \Big(u q_0(u) \Big) + \sqrt{\frac{2\pi}{\lambda}} u^* q_1(u^*) + \mathcal{O}(\varepsilon) \\ &= \rho^* f_c^* C \frac{\sigma + (\mathcal{D}_* - u^* \mathcal{D}_*')\, k^2}{(\sigma + \mathcal{D}_* k^2)(\sigma + \mathcal{D}_* k^2 + \lambda)} + \mathcal{O}(\varepsilon). \end{aligned} \tag{3.24}$$

Finally, we put (3.24) into (3.12b) and rearrange, imposing that $C \neq 0$, to obtain the algebraic equation

$$\sigma + D_c k^2 + \beta - \alpha_0 f_c^* \rho^* \frac{\sigma + (\mathcal{D}_* - u^* \mathcal{D}_*')\, k^2}{(\sigma + \mathcal{D}_* k^2)(\sigma + \mathcal{D}_* k^2 + \lambda)} = 0. \tag{3.25}$$

Eq. (3.25) represents the key result of our linear stability analysis; it is a cubic equation for the eigenvalue σ in terms of a given wavenumber k. The solutions of Eq. (3.25) therefore define a discrete family of eigenvalues $\sigma = \sigma(k)$; the eigenvalue with the largest real part determines the linear stability of the spatially uniform steady-state

(3.6)–(3.10). In Section 3.2.4 we will derive criteria for the onset of patterning, signified by solutions of (3.25) with $\mathrm{Re}(\sigma) > 0$. Before deriving these criteria, we provide formal justification for our earlier assumption that q_0 and q_1 in (3.19) are smooth.

3.2.3 Stokes Phenomenon Implies no Inner Region around u^*

We now justify our earlier assumption that solutions of (3.17) have no inner region around u^*. In other words, we show that the terms in the naïve outer expansion (3.18) must be smooth. Our analysis in this section requires the calculation of exponentially small terms in the asymptotic expansion of the solutions of (3.19). These techniques were developed in [22, 68] to investigate Stokes phenomenon in linear and non-linear ODEs. Our contribution here is to apply these techniques to (3.19) in order to rule out non-smooth solutions. If such solutions were possible, they could lead to instabilities in the eigenvalue problem (3.12) that would otherwise result in pattern formation.

To give a brief overview of our approach before getting into the details, we demonstrate that q_j must be regular at u^* as follows. First, we show that the naïve asymptotic expansion (3.18) is divergent when any one of the q_j's are non-smooth at u^*. Then we optimally truncate the expansion and show that the remainder exhibits Stokes phenomenon (see, e.g., [50], p.26) whereby different asymptotic expansions for q are needed in the regions $u < u^*$ and $u > u^*$. We will find that a term proportional to $\exp(\lambda(u-u^*)^2/2\varepsilon)$ in the remainder is switched on across a Stokes line characterised by purely imaginary values of $u - u^*$, on which the contribution is exponentially small. However, for real-valued u the contribution from this Stokes switching is exponentially large. We show that the exponentially large term cannot be simultaneously eliminated from the expansion in both $u > u^*$ and $u < u^*$. If it were present in the expansion, q could not be polynomially bounded as required by the boundary conditions. Hence we conclude that q_j must be smooth.

As a final remark before we start, Stokes lines generally lie in the complex plane so it will be necessary to consider complex-valued u. Therefore, in this subsection we interpret the ODEs (3.19) as complex-valued, even though we ultimately restrict the solutions to the real axis.

We start by showing that if q_0 is non-smooth at u^*, then the expansion (3.18) is divergent in the form factorial/power. In order to do this, we must determine the behaviour of q_j for large j. Let us suppose that q_{j-1} has a singularity of strength p at u^*. Then q_j will be singular with strength $p+2$. Roughly speaking, this is because in (3.19b) we obtain q_j by differentiating q_{j-1} twice, dividing by $u - u^*$ once, and

integrating once. Thus if $q_0 \sim a_0(u-u^*)^{-p}$ as $u \to u^*$ for some constant a_0, then $q_j \sim a_j(u-u^*)^{-(p+2j)}$ as $u \to u^*$ for all j for some other constant a_j. Motivated by this observation, as well as similar calculations in [22, 68], we look for a solution as $j \to \infty$ in the form

$$q_j(u) \sim Q\frac{\Gamma(j+\gamma(u)+1)}{\lambda^j\big(v(u)\big)^{j+\kappa(u)}}, \tag{3.26}$$

where λ is the same as in the equations for q_j in (3.19), Γ is the Gamma function, while $v(u)$, $\gamma(u)$, and $\kappa(u)$ are functions independent of j. The constant Q, known as the connection coefficient [68], will not be relevant for our analysis. The goal now is to determine v, γ, and κ by substituting (3.26) into (3.19b). As there are three unknowns in (3.26), we must retain three orders of dominant terms in (3.19b). To make progress we use a generalised form of Stirling's approximation of the Gamma function (see, e.g., [50], p. 34):

$$\Gamma(z) = \sqrt{\frac{2\pi}{z}}\left(\frac{z}{e}\right)^z\left(1+\frac{1}{12z}+\mathcal{O}(z^{-2})\right), \qquad \mathrm{Re}(z)>0. \tag{3.27}$$

Even though three orders of dominant terms are required in (3.19b) to determine the three unknowns v, γ, and κ, the two-term expansion of Γ is sufficient as the derivatives of Γ introduce successively larger terms, e.g. $\Gamma'(z) \sim \mathcal{O}(\Gamma(z)\log z)$, so the $\mathcal{O}(z^{-2})$ terms in (3.27) can be safely neglected for our purposes.

We substitute the ansatz (3.26) into the equations for q_j (3.19b), and use the approximation (3.27) to simplify the Gamma function. After some algebra, we obtain

$$\begin{aligned}-(sv'+(v')^2)j^3 + (sv+2vv')\,\gamma' j^2\log j - \Big[(sv+2vv')\log v\kappa' + \big(sv'+2(v')^2\big)\,\kappa \\ - hv + sv'\left(2\gamma+\frac{25}{12}\right) + (v')^2\left(\gamma+\frac{11}{12}\right) - vv''\Big]j^2 = o(j^2),\end{aligned} \tag{3.28}$$

where we introduce $s := u-u^*$ and

$$h(u) := \frac{\sigma+\mathcal{D}(u)k^2}{\lambda}, \tag{3.29}$$

to ease notation. Collecting the leading order $\mathcal{O}(j^3)$ terms yields either $v'=0$ or $v'=-s$. Since we seek non-smooth q_0 at u^*, the same must be true of q_j for all j. We therefore require $v(u^*)=0$ and v not identically zero, leading to

$$v(u) = -\frac{(u-u^*)^2}{2}. \tag{3.30}$$

From the $\mathcal{O}(j^2 \log j)$ terms in (3.28) we deduce $\gamma' = 0$, so γ is a constant which we determine below. Then the $\mathcal{O}(j^2)$ terms at next order lead to the following ODE for κ

$$s\kappa' \log v + 2\kappa + h - 2\gamma - 3 = 0, \tag{3.31}$$

which we solve by standard methods to deduce that

$$\kappa(u) = \gamma + \frac{3}{2} + \frac{\log q_h(u) + \tilde{C}}{\log\left(-\frac{(u-u^*)^2}{2}\right)}. \tag{3.32}$$

Here $\tilde{C}$ is a constant of integration and q_h solves the homogeneous version of (3.19), and is given by

$$q_h(u) := \exp\left[-\int_1^u \frac{h(\bar{u})}{\bar{u} - u^*}\,\mathrm{d}\bar{u}\right], \tag{3.33}$$

where the arbitrary lower bound of integration is fixed for concreteness. Any non-zero value of $\tilde{C}$ can be absorbed into Q in (3.26) since

$$\left(-\frac{s^2}{2}\right)^{\tilde{C}/\log(-s^2/2)} = e^{\tilde{C}} = \text{const.} \tag{3.34}$$

We therefore set $\tilde{C} = 0$ without loss of generality.

It remains to determine the constant value of γ. Although the expansion (3.26) is valid only for $j \gg 1$, the singularity structure of q_j is known for all j. As discussed above, if $q_0 \sim (u - u^*)^{-p}$ as $u \to u^*$, then $q_j \sim (u - u^*)^{-(p+2j)}$. Demanding that the singularity structure in (3.26) is consistent with this fact will determine γ. To do this, we must determine the exponent p. In general, q_0 is a sum of a homogeneous solution q_h and a particular solution q_p of (3.19a). From (3.19a), we can see that the local behaviour of q_p is given by

$$q_p(u) = \sqrt{\frac{\lambda^3}{2\pi}} \frac{\rho^* f_c^* C(u - u^*)}{\sigma + \mathcal{D}(u^*)k^2 + \lambda} + \mathcal{O}\left((u - u^*)^2\right), \quad \text{as } u \to u^*, \tag{3.35}$$

which is smooth at u^*. As such, the homogeneous solution q_h must determine the singularity structure of q_0. From (3.33) we have

$$q_h(u) \sim a(u - u^*)^{-h_0}, \quad h_0 := h(u^*), \quad \text{as } u \to u^*, \tag{3.36}$$

for some constant a. Thus (3.36) allows us to deduce from (3.26) and (3.32) that

$$\gamma = h_0 - \frac{3}{2}. \tag{3.37}$$

Putting together the solutions for v, κ, and γ in Eqs. (3.30), (3.32), and (3.37), as well as the ansatz for q_j in (3.26), we find that overall q_j has the asymptotic behaviour

$$q_j(u) \sim Q\frac{(-1)^j\Gamma\left(j+h_0-\frac{1}{2}\right)}{(u-u^*)^{2j+2h_0}q_h(u)}\left(\frac{2}{\lambda}\right)^j, \quad \text{as } j\to\infty. \tag{3.38}$$

By inserting (3.38) into the asymptotic expansion (3.18), we observe that (3.18) exhibits the expected factorial/power divergence. Since our goal is to show that it is impossible to have non-smooth q_j, we assume that h_0 in (3.36) is not a negative integer[1]. We expect that all non-smooth solutions of (3.19) have the large j behaviour in (3.38) (up to a finite shift in j as we argue below) since any contribution to q_j from the homogeneous solution q_h is subdominant as $j\to\infty$. Additionally, the smooth particular solution for q_0 in (3.35) should generate terms in q_j that grow more slowly than factorial/power, and would therefore also be subdominant in (3.26) as $j\to\infty$.

So far we have shown that if q_0 is non-smooth, then the expansion (3.18) exhibits factorial/power divergence. Since the particular solution of (3.19) is smooth (see (3.35)), it is the non-smooth homogeneous solution q_h that 'sets off' the factorial/power divergence. If q_0 were smooth (with no contribution from q_h), and instead the first non-smooth term in the series (3.18) occurred at $j=j'>0$, then the only change to our analysis would be in the calculation of γ. Instead of demanding that q_0 has a singularity of strength h_0, we would impose that $q_{j'}$ has a singularity of strength h_0. This would shift γ by j', effectively delaying the index j in (3.26) since the divergent behaviour is set off by q_h deeper in the series. We therefore conclude that if any of the q_j's are non-smooth, then the naïve expansion (3.18) is divergent in the form factorial/power. Since the analysis that follows does not crucially depend on γ, we assume for simplicity that q_0 is non-smooth.

The next step is to truncate the divergent series (3.18), (3.38) so that we can detect Stokes switching in the exponentially small terms. Thus we introduce the remainder R_N through

$$q(u)=\sum_{j=0}^{N-1}q_j(u)\varepsilon^j+R_N(u). \tag{3.39}$$

Substituting (3.39) into (3.17), we deduce that R_N exactly satisfies

$$\varepsilon R_N''-\lambda(u-u^*)R_N'-(\sigma+\mathcal{D}(u)k^2)R_N=-\varepsilon^N q_{N-1}''. \tag{3.40}$$

[1]If h_0 is a negative integer, then necessarily $\mathrm{Re}(\sigma)<0$ and there would be no linearly unstable solutions.

Following [22], we expect a multiple of a homogeneous solution of (3.40) to be switched on across a Stokes line. It is therefore helpful to determine the leading order (in ε) behaviour of the homogeneous solutions.

One family of homogeneous solutions of (3.40) has $R_N \sim q_h(u)$ as $\varepsilon \to 0$. This is a consequence of the fact that Eq. (3.17) for q is linear; every term in the expansion can potentially contain a term proportional to q_h. We may therefore assume without loss of generality that only q_0 has this term, and simply reject this as a solution to R_N. The second family of linearly independent homogeneous solutions varies rapidly around u^*, so we seek a WKBJ solution of the form

$$R_N(u) = \tilde{R}_N(u) \exp\left(\frac{\psi(u)}{\varepsilon}\right). \tag{3.41}$$

Inserting the ansatz (3.41) into (3.40) and equating the leading order power of ε leads to

$$\psi' = \lambda(u - u^*). \tag{3.42}$$

So $2\psi = \lambda(u-u^*)^2$ and the terms at next order in ε yield

$$\lambda(u-u^*)\tilde{R}_N' - \left(\sigma + \mathcal{D}k^2 - \lambda\right)\tilde{R}_N = 0. \tag{3.43}$$

Solving (3.43), we find that the homogeneous solutions of (3.40) have the leading order behaviour

$$R_N = \frac{1}{(u-u^*)q_h(u)}\left(1 + \mathcal{O}(\varepsilon)\right)\exp\left(\frac{\lambda(u-u^*)^2}{2\varepsilon}\right), \tag{3.44}$$

as $\varepsilon \to 0$. We will show that a contribution proportional to (3.44) is switched on across a Stokes line. We expect the Stokes line to be located in the region of the complex plane in which this term is subdominant in the expansion (3.39).

Before determining the location of the Stokes line, it is helpful to first deduce the optimal truncation N in (3.39). To this end we introduce complex polar coordinates as

$$u - u^* = re^{i\theta}. \tag{3.45}$$

Successive terms in the expansion become disordered (asymptotically larger) after N terms when $\varepsilon^N|q_N| \sim \varepsilon^{N+1}|q_{N+1}|$. Using (3.38), this gives $N \sim \lambda r^2/2\varepsilon$. Thus we set

$$N = \frac{\lambda r^2}{2\varepsilon} + N_0(\varepsilon), \tag{3.46}$$

where N_0 is $\mathcal{O}(1)$ as $\varepsilon \to 0$. We emphasize that the optimal truncation depends on ε and the distance from u^*, but not the angle θ.

To detect the Stokes switching, we seek a particular solution of (3.40) of the form

$$R_N(u) = \frac{S(u)}{(u-u^*)q_h(u)} \exp\left(\frac{\lambda(u-u^*)^2}{2\varepsilon}\right), \tag{3.47}$$

where S is the new dependent variable. We expect S to be approximately constant, except across the Stokes line. Thus, we effectively search for solutions proportional to the homogeneous solution in (3.44). Using (3.47) and (3.46) in (3.40), and expanding in the regime $\varepsilon \ll 1$, we find that at leading order S satisfies

$$\begin{aligned}\frac{dS}{du} :=& -\frac{ie^{-i\theta}}{r}\frac{dS}{d\theta} \\ =& \frac{Q}{\varepsilon^{h_0}} \exp\left[-\frac{\lambda r^2}{2\varepsilon}(1+e^{2i\theta}) - i\left(\frac{\lambda r^2}{2\varepsilon}+N_0\right)(2\theta-\pi) - 2ih_0\theta\right][1+\mathcal{O}(\varepsilon)],\end{aligned} \tag{3.48}$$

where we have expressed the derivative in (complex) polar coordinates. For convenience, we have also absorbed the constant prefactors that do not depend on N_0 or ε into Q. We observe from the RHS of (3.48) that S' is exponentially small in ε everywhere except when $1+e^{2i\theta}=0$. Hence there is a Stokes line along the imaginary axis, across which S changes algebraically in ε. Away from the imaginary axis, S is approximately constant. On $\theta = 3\pi/2$, the sign of the RHS oscillates rapidly as $\varepsilon \to 0$. Although this rapid oscillation with ε can be a complication in similar calculations (see, e.g., [68]), here it is sufficient to consider only the behaviour of S across $\theta = \pi/2$. This analysis is simpler because the sign of the RHS is independent of the truncation in this region.

In order to examine the behaviour across the Stokes line $\theta = \pi/2$, we consider a local inner region. To this end, we rescale S and θ as

$$\theta = \frac{\pi}{2} + \sqrt{\varepsilon}\tilde{\theta}, \qquad S = \frac{\tilde{S}}{\varepsilon^{h_0-\frac{1}{2}}}, \tag{3.49}$$

where $\tilde{\theta}$ and $\tilde{S}$ are the inner variables and the scalings are chosen to balance appropriate terms in (3.48). At leading order we find from (3.48)

$$\frac{\partial \tilde{S}}{\partial \theta} \sim -\frac{Qr}{e^{i\pi(h_0-\frac{1}{2})}} e^{-\lambda r^2 \tilde{\theta}^2}, \tag{3.50}$$

justifying our scalings in (3.49). Solving (3.50) and absorbing constants into Q, we obtain

$$\tilde{S}(\tilde{\theta}) \sim Q\left[\mathcal{S} - \operatorname{erf}\left(\sqrt{\lambda} r\tilde{\theta}\right)\right], \tag{3.51}$$

where $\operatorname{erf}(\cdot)$ is the error function and $\mathcal{S}$ is an integration constant.

Lastly, we must select the constant $\mathcal{S}$ such that q satisfies the boundary conditions. Overall, for R_N we have the leading order behaviour

$$R_N \sim \frac{Q\varepsilon^{\frac{1}{2}-h_0}}{(u-u^*)q_h(u)} \exp\left[\frac{\lambda(u-u^*)^2}{2\varepsilon}\right]\left[\mathcal{S} - \operatorname{erf}\left(\sqrt{\frac{\lambda}{\varepsilon}} r\left(\frac{\pi}{2}-\theta\right)\right)\right], \tag{3.52}$$

with $u - u^* := re^{i\theta}$. This expansion is valid in the outer region $|u-u^*| = \mathcal{O}(1)$. In order for q to satisfy the boundary conditions, we require the remainder to be polynomially bounded as $u \to 0, \infty$. This requires the bracketed term containing the error function to be exponentially small in order to counteract the exponentially large factor. Since we only have one free constant $\mathcal{S}$, we can eliminate the exponential growth in either $u < u^*$ or $u > u^*$ (i.e. by taking $\mathcal{S} = \pm 1$), but not both. The only way to satisfy the boundary conditions is therefore to take $Q = 0$, which is equivalent to demanding that no terms in (3.39) contain q_h, as otherwise this would set off the divergent expansion (3.18), (3.26), leading again to Stokes phenomenon. This in turn implies that we must demand a smooth particular solution $q_0 = q_p$ of (3.19a), where q_p locally is given by (3.35) (also cf. Eq. (3.23a)).

In summary, we have effectively linked the behaviour of q at infinity with the local behaviour at u^*, which allows for exchanging the boundary conditions on q for a regularity condition at u^*. Specifically, we have shown that if a solution of (3.19) is non-smooth at u^*, then it is not polynomially bounded as $u \to 0, \infty$. We therefore conclude that any solution of (3.19) that is polynomially bounded as $u \to 0, \infty$ must be smooth at u^*. This rules out the possibility of an inner region near u^*. In other words, the 'outer' solution q_j must have the local representation (3.20), as assumed in the analysis of the previous section. Overall, our analysis in this section implies that the only solution of (3.17) satisfying the boundary conditions that q is polynomially bounded as $u \to 0, \infty$ is given locally by (3.20), (3.23) to leading order in ε.

3.2.4 Criteria for Motility-Induced Patterning

We now return to our algebraic equation for the eigenvalue σ, which is given in (3.25). To determine criteria for motility-induced patterning, we now translate the instability condition $\operatorname{Re}(\sigma) > 0$ into one involving only the original parameters in the system (3.1)–(3.4). We will find that there are two possibilities depending on the sign of the derivative $\mathcal{D}_*'$. Throughout the rest of this chapter we will use $\mathcal{D}_*'$ as a bifurcation parameter.

At the onset of instability we have the bifurcation condition $\operatorname{Re}(\sigma) = 0$ so that one of two cases occurs: either $\sigma = 0$ is a root, or there is a complex conjugate

pair of purely imaginary roots (i.e. a Hopf bifurcation). We consider these two cases separately below, starting with the former.

If $\sigma = 0$ is a solution of (3.25), then

$$\frac{\mathcal{D}'_*}{\mathcal{D}_*} = -\frac{1}{u^*}\left[\frac{(D_c k^2 + \beta)\,(\mathcal{D}_* k^2 + \lambda)}{\alpha_0 \rho^* f_c^*} - 1\right]. \tag{3.53}$$

Thus the eigenvalue has exactly one zero-crossing as $\mathcal{D}'_*$ is varied from ∞ to $-\infty$, with all other quantities fixed. Because the RHS of (3.53) is a decreasing function of k^2, the first mode to satisfy (3.53) as $\mathcal{D}'_*$ is decreased corresponds to the smallest allowed value of k^2, as determined from (3.15). We therefore set $k = \pi/\mathcal{L}_m$, where $\mathcal{L}_m = \max(\mathcal{L}_x, \mathcal{L}_y)$ is the largest side length of the domain. The condition for instability is therefore

$$\frac{\mathcal{D}'_*}{\mathcal{D}_*} < -\frac{A}{u^*}, \quad A := \frac{1}{\alpha_0 \rho^* f_c^*}\left(\frac{D_c \pi^2}{\mathcal{L}_m^2} + \beta\right)\left(\frac{\mathcal{D}_* \pi^2}{\mathcal{L}_m^2} + \lambda\right) - 1, \tag{3.54}$$

where we deduce the direction of the inequality from the observation that real solutions of (3.25) have $\sigma > 0$ as $\mathcal{D}'_* \to -\infty$ with all other parameters fixed.

Next we determine the condition for a Hopf bifurcation from (3.25). In this case, there is a purely imaginary pair of eigenvalues $\sigma = \pm i\omega$, where ω is real. Substituting this into (3.25), the real and imaginary components satisfy

$$\omega^2 - [\nu_0\nu_\lambda + \nu(\nu_0 + \nu_\lambda) - \alpha_0 \rho^* f_c^*] = 0, \tag{3.55a}$$

$$(\nu_0 + \nu_\lambda + \nu)\omega^2 + \nu_0\nu_\lambda\nu - \alpha_0\rho^* f_c^*(\nu_0 - u^*\mathcal{D}'_* k^2) = 0, \tag{3.55b}$$

where we define

$$\nu_j := \mathcal{D}_* k^2 + j, \quad \nu := D_c k^2 + \beta. \tag{3.56}$$

The two equations for ω in (3.55) are consistent if, and only if,

$$\nu_0\nu_\lambda + \nu(\nu_0 + \nu_\lambda) - \alpha_0\rho^* f_c^* = -\frac{\nu_0\nu_\lambda\nu_\beta - \alpha_0 f_c^* \rho^*(\nu_0 - u^*\mathcal{D}'_* k^2)}{\nu_0 + \nu_\lambda + \nu}. \tag{3.57}$$

After rearranging (3.57), we obtain

$$\frac{\mathcal{D}'_*}{\mathcal{D}_*} > \frac{B}{u^*}, \quad B := \frac{\nu_\lambda + \nu}{\nu_0}\left[\frac{(\nu_0 + \nu_\lambda)(\nu_0 + \nu)}{\alpha_0 \rho^* f_c^*} - 1\right], \tag{3.58}$$

where we again deduce the direction of the inequality from the observation that the pair of complex conjugate solutions of (3.25) have $\mathrm{Re}(\sigma) > 0$ as $\mathcal{D}'_* \to \infty$. Note that in contrast to the previous case, the RHS of (3.58) tends to ∞ as $k \to 0$ and as $k \to \infty$ and is therefore non-monotonic in k^2 (this requires knowing that $B > 0$,

which we show shortly). Thus, in general, the first mode to lose stability as $\mathcal{D}'_*$ is increased corresponds to an intermediate wavenumber.

Next, we demonstrate that the two classes of instability characterised by (3.54) and (3.58) can only occur when $\mathcal{D}'_* < 0$ and $\mathcal{D}'_* > 0$, respectively. This requires showing that the constants A and B are strictly positive. Noting that $\nu_j > j$ and $\nu > \beta$, we see from (3.54) and (3.58)

$$A > \frac{\lambda\beta}{\alpha_0\rho^* f_c^*} - 1, \quad B > \frac{\nu_\lambda + \nu}{\nu_0}\left(\frac{\lambda\beta}{\alpha_0\rho^* f_c^*} - 1\right). \tag{3.59}$$

Since ν_λ, ν, and ν_0 are positive, we only need to show that the RHS of the first inequality in (3.59) is positive. Using the definition of f in (3.1), we calculate

$$f_c^* = \frac{LK}{(K + c^*)^2}. \tag{3.60}$$

Then since $(K + c^*)^2 > K^2 + 2Kc^*$, we have

$$\frac{\lambda\beta}{\alpha_0\rho^* f_c^*} - 1 > \frac{\lambda\beta(2c^* + K)}{\alpha_0\rho^* L} - 1. \tag{3.61}$$

Upon substituting the steady AI concentration c^* from (3.10a) into the above, we find

$$\frac{\lambda\beta(2c^* + K)}{\alpha_0\rho^* L} - 1 > 0. \tag{3.62}$$

Thus A and B in (3.54) and (3.58) are positive.

In summary, we have derived the criteria in (3.54) and (3.58) for the onset of pattern formation in the spatially uniform steady-state (3.6)–(3.10). The first of these criteria can only occur when $\mathcal{D}'_* < 0$, while the second can only occur when $\mathcal{D}'_* > 0$. Neither instability is possible when $\mathcal{D}'_* = 0$, which implies that genetic regulation of motility is crucial for this type of pattern formation. In Section 3.4, we compare our theory with full numerical solutions of the governing equations (3.3)–(3.4) and investigate emergent patterning arising from the two instabilities. Although we have performed our analysis for the specific functional form (3.1) for the gene-regulatory kinetics, in subsequent chapters we consider more generic classes.

3.3 Characterisation of the Bifurcation when QS Represses Motility

In this section, we characterise the type of bifurcation that occurs when $\mathcal{D}'_* := \mathcal{D}'(u^*) < 0$, as well as determine the local bifurcating branches of the steady-states.

We additionally determine a condition for the switch between a supercritical and subcritical bifurcation. We accomplish this through a weakly nonlinear analysis near the bifurcation point. We recall that the criterion for the bifurcation is given in (3.54), and the corresponding eigenvalue that becomes unstable is real-valued. We continue to use $\mathcal{D}'_*$ as the bifurcation parameter. We also work in one spatial dimension for mathematical convenience (i.e. $\mathbf{x} = x$), although our analysis straightforwardly generalises.

The general approach in this analysis is to consider the behaviour of small perturbations about the spatially uniform steady-state near the bifurcation point. This is similar to the linear stability analysis in the previous section in which we considered perturbations of the form (3.11). The key idea here is that near the bifurcation point, the bifurcating branch of steady-states is 'close' to the spatially uniform branch. By expanding the solution near the bifurcation point and retaining terms beyond only the linear terms in (3.11), we are able to detect this branch and characterise its local properties.

In order to study the local behaviour near the bifurcation point, we introduce a perturbation to the bifurcation parameter $\mathcal{D}'_*$ as follows

$$\mathcal{D}(u) = \mathcal{D}_0(u) + \delta^r d(u), \tag{3.63}$$

where $d(u)$ is a perturbing function and $0 < \delta \ll 1$ is a small parameter measuring the distance from the bifurcation point. The scaling $r > 0$ will be determined in the course of our analysis and the unperturbed diffusion coefficient $\mathcal{D}_0(u)$ is such that there is a bifurcation when $\delta = 0$, as clarified in detail below. Since we take $\mathcal{D}'_*$ as the bifurcation parameter, it is convenient to have $\mathcal{D}_*$ independent of the perturbation $d(u)$. We therefore require

$$d(u^*) = 0. \tag{3.64}$$

Explicitly, the perturbation to the bifurcation parameter $\mathcal{D}'_*$ is

$$\mathcal{D}'_* = \mathcal{D}'_{0*} + \delta^r d'_*, \tag{3.65}$$

where $d'_* := d'(u^*)$. We remark that $d(u)$ also perturbs the higher-order derivatives of $\mathcal{D}$, but this will not affect our final result.

Since we work in the regime $\varepsilon \ll 1$, there is a choice as to exactly how we define $\mathcal{D}'_{0*}$ in relation to the bifurcation point. We can either take $\mathcal{D}'_{0*}$ such that the bifurcation point occurs exactly at $\delta = 0$, i.e. without approximation in ε, or we can take $\mathcal{D}'_{0*}$ to coincide with the leading order result (3.53), in which case the bifurcation occurs at

some $\delta = \mathcal{O}(\varepsilon)$. Both choices are possible to analyse, but we opt for the former as this avoids technical complications with an $\mathcal{O}(\varepsilon)$ eigenvalue that would otherwise appear in our analysis at linear order in δ. As such we have the leading order behaviour

$$\frac{\mathcal{D}'_{0*}}{\mathcal{D}_{0*}} \sim -\frac{1}{u^*}\left[\frac{(D_c k^2+\beta)\left(\mathcal{D}_{0*}k^2+\lambda\right)}{\alpha_0\rho^* f_c^*} - 1\right], \tag{3.66}$$

as $\varepsilon \to 0$, where we emphasize that equality does not hold for finite ε. We further emphasize that the wavenumber k that appears in (3.66), and the remainder of this section, corresponds to the critical wavenumber of the instability, i.e. $k = \pi/\mathcal{L}_x$. Our analysis straightforwardly generalises to instabilities in any of the other spatial modes.

In general, small perturbations around the uniform steady-state will vary over an $\mathcal{O}(1)$ timescale. However, near a bifurcation the timescales involved are much longer. This can be intuitively understood from the fact that the timescales scale with the reciprocal of the eigenvalue, and this eigenvalue is close to zero near the bifurcation. With this in mind, we rescale time as

$$t = \delta^{-p}\tau, \tag{3.67}$$

where τ is slow time and $p > 0$ is an unknown scaling to be determined.

We then look for solutions of the governing equations (3.1)–(3.4) in the form

$$n(x,u,\tau) = n^*(u) + \delta\eta_1(x,u,\tau) + \delta^2\eta_2(x,u,\tau) + \delta^3\eta_3(x,u,\tau) + \mathcal{O}(\delta^4), \tag{3.68a}$$

$$c(x,\tau) = c^* + \delta c_1(x,\tau) + \delta^2 c_2(x,\tau) + \delta^3 c_3(x,\tau) + \mathcal{O}(\delta^4), \tag{3.68b}$$

up to and including the powers of δ required to characterise the bifurcation. Here n^* and c^* are the spatially uniform steady-states given in (3.6)–(3.9). Next we substitute the scalings (3.63) and (3.67), and expansions (3.68) into the governing equations (3.3)–(3.4) and expand in powers of δ to obtain governing equations for the unknown functions η_j and c_j, $j = 1\ldots,3$. In order to be clear about our small ε and δ approximations, we first perform this expansion without approximation in ε. We then analyse the governing equations for the unknowns in (3.68) in the limit $\varepsilon \ll 1$. The next subsection is concerned with the leading order $\mathcal{O}(1)$ and linear $\mathcal{O}(\delta)$ terms, similar to the analysis in Section 3.2, while the following subsection is devoted to the weakly nonlinear analysis proper at orders $\mathcal{O}(\delta^2)$ and $\mathcal{O}(\delta^3)$.

3.3.1 Leading Order and Linear Analysis

We insert the scalings (3.63), (3.67) and expansions (3.68) into the governing equations (3.1)–(3.4) and collect terms at powers of δ. At $\mathcal{O}(1)$ we recover the steady-state

system in (3.5). At $\mathcal{O}(\delta)$, we obtain

$$\mathcal{D}_0(u)\frac{\partial^2\eta_1}{\partial x^2} + \varepsilon\frac{\partial^2\eta_1}{\partial u^2} - \frac{\partial}{\partial u}\left[f(u,c^*)\eta_1\right] - c_1 f_c^*\frac{dn^*}{du} = 0, \tag{3.69a}$$

$$D_c\frac{\partial^2 c_1}{\partial x^2} - \beta c_1 + \alpha_0\int_0^\infty u\eta_1(x,u,t)\,\mathrm{d}u = 0, \tag{3.69b}$$

with the no-flux boundary conditions

$$\varepsilon\frac{\partial\eta_1}{\partial u} - f(u,c^*)\eta_1 \to 0, \quad u\to 0,\infty, \tag{3.69c}$$

$$\frac{\partial\eta_1}{\partial x} = \frac{\partial c_1}{\partial x} = 0, \quad x = 0,\mathcal{L}_x. \tag{3.69d}$$

The system (3.69) is linear and separable. We therefore look for non-trivial solutions in the form

$$\eta_1(x,u,\tau) = C(\tau)\eta(u)\cos(kx), \qquad c_1(x) = C(\tau)\cos(kx), \tag{3.70}$$

where η and C are functions that we seek to determine. The function C will turn out to be the quantity controlling the bifurcation. We remark that since the system is linear, homogeneous, and independent of τ, both η_1 and c_1 must have the same functional dependence on τ, as implicitly assumed in (3.70). Substituting (3.70) into (3.69) leads to the following system for η

$$\varepsilon\frac{d^2\eta}{du^2} + \frac{d}{du}\left[\lambda(u-u^*)\eta\right] - \mathcal{D}_0(u)k^2\eta = f_c^*\frac{dn^*}{du}, \tag{3.71a}$$

$$D_c k^2 + \beta - \alpha_0\int_0^\infty u\eta(u)\,\mathrm{d}u = 0, \tag{3.71b}$$

$$\varepsilon\frac{d\eta}{du} - f(u,c^*)\eta \to 0, \quad u\to 0,\infty, \tag{3.71c}$$

where we recall that $f_c^* := \frac{\partial f}{\partial c}(u,c^*)$. Since η is the only unknown and there are two equations in (3.71), one might assume that there is no solution in general. However, we recall that we are seeking solutions near a bifurcation, and so Eq. (3.71) is equivalent to the condition for zero to be an eigenvalue of the linear problem (3.12). That is, since we have defined $\mathcal{D}_0$ such there is a bifurcation at $\delta = 0$, zero is an eigenvalue for (3.71) and we conclude that (3.71) has a solution. As such, our analysis at linear order in $\mathcal{O}(\delta)$ is similar to that considered previously; subsequently our exposition here is slightly more brief. We recall that (3.66) is the leading order (in ε) condition on $\mathcal{D}'_{0*}$ for zero to be an eigenvalue. Therefore, in the regime $\varepsilon \ll 1$, we look for the solution η using a WKBJ ansatz

$$\eta(u) = \varepsilon^{-3/2}q(u)\exp\left(-\frac{\lambda(u-u^*)^2}{2\varepsilon}\right). \tag{3.72}$$

Then following the analysis from the previous section, we expand q in a regular asymptotic series and seek formal power series solutions at each order in ε (see Eqs. (3.18)–(3.22), but with $\sigma = 0$ and $C = 1$). Explicitly,

$$q_0^{(0)} = 0, \tag{3.73a}$$

$$q_0^{(\ell)} = \frac{1}{\mathcal{D}_* k^2 + \ell\lambda}\left[\delta_{\ell 1}\sqrt{\frac{\lambda^3}{2\pi}}\rho^* f_c^* - k^2 \sum_{m=1}^{\ell} \frac{\mathcal{D}_*^{(m)}}{m!} q_0^{(\ell-m)}\right], \quad \ell = 1, \ldots, \tag{3.73b}$$

$$q_j^{(0)} = \frac{2q_{j-1}^{(\ell+2)}}{\mathcal{D}^* k^2}, \quad j = 1, \ldots, \tag{3.73c}$$

$$q_j^{(\ell)} = \frac{1}{\mathcal{D}_* k^2 + \ell\lambda}\left[(\ell+1)(\ell+2)q_{j-1}^{(\ell+2)} - k^2 \sum_{m=1}^{\ell} q_j^{(\ell-m)} \frac{\mathcal{D}_*^{(m)}}{m!}\right], \quad j, \ell = 1 \ldots, \tag{3.73d}$$

where we have included all the higher-order coefficients for completeness. The sequence of coefficients in the recursion is in ascending order of the upper index, nested in ascending order of the lower index, i.e. $q_0^{(0)}, q_0^{(1)}, q_0^{(2)}, \ldots, q_1^{(0)}, q_1^{(1)}, q_1^{(2)}, \ldots$. In principle, the recursion relations determine η up to all algebraic orders of ε. For the purpose of this analysis, we will find that the first few terms are sufficient.

The goal for the remainder of this section is to determine a governing equation for the time-dependent factor $C(\tau)$ in (3.70). This equation will determine the type of bifurcation as well as the stability of the bifurcating branch of steady-states.

3.3.2 Weakly Nonlinear Analysis

Next, we obtain governing equations for the $\mathcal{O}(\delta^2)$ terms in (3.68). In principle, the goal is to derive a solvability condition for these governing equations, which will yield a relationship between $C(\tau)$ and d_*'. However, we will find this condition yields no additional information beyond the linear analysis at $\mathcal{O}(\delta)$. Consequently, we will have to consider terms at $\mathcal{O}(\delta^3)$. The solutions at $\mathcal{O}(\delta^2)$ feed into the solvability condition at next order. In order to explicitly show that the analysis at order $\mathcal{O}(\delta^2)$ yields no additional information, we take the scalings in (3.63) and (3.67) as $r = p = 1$ so that both the time derivative and the perturbation to $\mathcal{D}$ appear at $\mathcal{O}(\delta^2)$.

After substituting (3.63), (3.67), and (3.68), into the governing equations (3.1)–(3.4) and collecting terms at $\mathcal{O}(\delta^2)$, we obtain

$$\begin{aligned}\mathcal{D}_0\frac{\partial^2\eta_2}{\partial x^2} + \varepsilon\frac{\partial^2\eta_2}{\partial u^2} - \frac{\partial}{\partial u}\left[f(u,c^*)\eta_2\right] - c_2 f_c^*\frac{dn^*}{du} =& c_1^2\frac{f_{cc}^*}{2}\frac{dn^*}{du} + c_1 f_c^*\frac{\partial\eta_1}{\partial u} \\ &+ \frac{\partial\eta_1}{\partial\tau} - d(u)\frac{\partial^2\eta_1}{\partial x^2},\end{aligned} \tag{3.74a}$$

$$D_c\frac{\partial^2 c_2}{\partial x^2} - \beta c_2 + \alpha_0\int_0^\infty u\eta_2\,\mathrm{d}u = \frac{\partial c_1}{\partial\tau}, \tag{3.74b}$$

and the boundary conditions

$$\varepsilon\frac{\partial\eta_2}{\partial u} - f(u,c^*)\eta_2 \to 0, \quad u \to 0,\infty, \tag{3.74c}$$

$$\frac{\partial\eta_2}{\partial x} = \frac{\partial c_2}{\partial x} = 0, \quad x = 0,\mathcal{L}_x, \tag{3.74d}$$

where we have ignored exponentially small terms in the boundary conditions. We define the quantity f^*_{cc} as

$$f^*_{cc} := \frac{\partial^2 f}{\partial c^2}(u,c^*). \tag{3.75}$$

We observe that the differential operator on the LHS of (3.74) is the same as the linear problem in (3.69). Since Eq. (3.74) is inhomogeneous, the Fredholm Alternative implies that there is no solution unless the inhomogeneous terms satisfy a solvability condition. More specifically, the RHS must be orthogonal to the nullspace of the adjoint operator (details below). Therefore, our next task is to determine the adjoint operator and calculate its nullspace.

3.3.2.1 Analysis of the Adjoint Problem

In this subsection we derive the adjoint of the operator on the LHS of (3.69) and (3.74). We further obtain leading order in ε expressions for the nullspace.

Let us denote the LHS operator in (3.69) and (3.74) by $\mathcal{L}$. For a vector function $\mathbf{v} = (v_1(x,u), v_2(x))^T$, we have

$$\mathcal{L}(\mathbf{v}) = \begin{pmatrix} \mathcal{L}_1 & \mathcal{L}_2 \\ \mathcal{L}_3 & \mathcal{L}_4 \end{pmatrix} \begin{pmatrix} v_1 \\ v_2 \end{pmatrix}, \tag{3.76a}$$

where the components $\mathcal{L}_j$, $j = 1,...4$ satisfy

$$\mathcal{L}_1(v_1) := \mathcal{D}_0\frac{\partial^2 v_1}{\partial x^2} + \varepsilon\frac{\partial^2 v_1}{\partial u^2} - \frac{\partial}{\partial u}\left[f(u,c^*)v_1\right], \tag{3.76b}$$

$$\mathcal{L}_2(v_2) := -f^*_c\frac{dn^*}{du}v_2, \tag{3.76c}$$

$$\mathcal{L}_3(v_1) := \alpha_0\int_0^\infty uv_1\,\mathrm{d}u, \tag{3.76d}$$

$$\mathcal{L}_4(v_2) := D_c\frac{\partial^2 v_2}{\partial x^2} - \beta v_2. \tag{3.76e}$$

We emphasize that the domains and ranges of each $\mathcal{L}_j$ are different. For example, $\mathcal{L}_2$ takes a function of x only and produces a function of both x and u. In contrast, $\mathcal{L}_3$ takes a function of x and u and produces a function of x. With this notation, the

governing equations at $\mathcal{O}(\delta)$ in (3.69) and at $\mathcal{O}(\delta^2)$ in (3.74) can be rewritten as

$$\mathcal{L}\begin{pmatrix}\eta_1\\ c_1\end{pmatrix} = \begin{pmatrix}0\\ 0\end{pmatrix}, \tag{3.77a}$$

$$\mathcal{L}\begin{pmatrix}\eta_2\\ c_2\end{pmatrix} = \begin{pmatrix}c_1^2\frac{f^*_{cc}}{2}\frac{dn^*}{du} + c_1 f^*_c\frac{\partial\eta_1}{\partial u} + \frac{\partial\eta_1}{\partial\tau} - d(u)\frac{\partial^2\eta_1}{\partial x^2}\\ \frac{\partial c_1}{\partial\tau}\end{pmatrix}. \tag{3.77b}$$

In order to determine the adjoint operator, we must define an inner product. To this end, we observe that $\mathcal{L}$ is a linear operator that acts on the product vector space of functions of (x,u) and functions of x. A natural inner product is therefore a sum of inner products on these spaces, i.e

$$(\mathbf{v},\mathbf{w}) := \int_{\Omega\times\mathbb{R}_+} v_1(x,u)w_1(x,u)\,\mathrm{d}u\mathrm{d}x + \int_\Omega v_2(x)w_2(x)\,\mathrm{d}x, \tag{3.78}$$

where the subscripts denote components of $\mathbf{v}$ and $\mathbf{w}$. This definition meets the requirements of an inner product (see, e.g., chapters 6–7 in the book by Axler [8]).

Now suppose that $\mathbf{v}$ satisfies the no-flux boundary conditions (cf. (3.69))

$$\varepsilon\frac{\partial v_1}{\partial u} - f(u,c^*)v_1 \to 0, \quad u\to 0,\infty, \tag{3.79a}$$

$$\frac{\partial v_1}{\partial x} = \frac{\partial v_2}{\partial x} = 0, \quad x = 0,\mathcal{L}_x. \tag{3.79b}$$

Then the adjoint operator $\mathcal{L}^*$ is defined uniquely through

$$(\mathcal{L}(\mathbf{v}),\mathbf{w}) = (\mathbf{v},\mathcal{L}^*(\mathbf{w}))\,, \tag{3.80}$$

along with the adjoint boundary conditions

$$\exp\left(-\frac{\lambda(u-u^*)^2}{2\varepsilon}\right)\frac{\partial w_1}{\partial u} \to 0, \quad u\to 0,\infty, \tag{3.81a}$$

$$\frac{\partial w_1}{\partial x} = \frac{\partial w_2}{\partial x} = 0, \quad x = 0,\mathcal{L}_x. \tag{3.81b}$$

In (3.81a) it is sufficient to require w_1 to be polynomially bounded. Inserting the definition of $\mathcal{L}$ in (3.76) into the inner product (3.80), we integrate by parts and use the adjoint boundary conditions (3.81) to find that $\mathcal{L}^*$ is given by

$$\mathcal{L}^* = \begin{pmatrix}\mathcal{L}_1^* & \mathcal{L}_3^*\\ \mathcal{L}_2^* & \mathcal{L}_4^*\end{pmatrix}, \tag{3.82a}$$

with the components $\mathcal{L}_j^*$, $j = 1, \ldots, 4$ given by

$$\mathcal{L}_1^*(w_1) = \mathcal{D}_0 \frac{\partial^2 w_1}{\partial x^2} + \varepsilon \frac{\partial^2 w_1}{\partial u^2} + f(u, c^*) \frac{\partial w_1}{\partial u}, \tag{3.82b}$$

$$\mathcal{L}_2^*(w_1) = -f_c^* \int_0^\infty \frac{dn^*}{du} w_1(x, u)\, \mathrm{d}u, \tag{3.82c}$$

$$\mathcal{L}_3^*(w_2) = \alpha_0 u w_2(x), \tag{3.82d}$$

$$\mathcal{L}_4^*(w_2) = D_c \frac{\partial^2 w_2}{\partial x^2} - \beta w_2. \tag{3.82e}$$

Next, we obtain solvability conditions for the inhomogeneous problem. Suppose that we want to solve $\mathcal{L}(\mathbf{v}) = \mathbf{g}$, with the boundary conditions (3.79) for some $\mathbf{g} = (g_1, g_2)^T$ not identically zero. We note that Eq. (3.74) is one such example. The Fredholm Alternative states that there is a solution of this problem if, and only if, $\mathbf{g}$ satisfies the solvability condition

$$(\mathbf{g}, \mathbf{w}) = \int_{\Omega \times \mathbb{R}_+} g_1(x, u) w_1(x, u)\, \mathrm{d}u\mathrm{d}x + \int_\Omega g_2(x) w_2(x)\, \mathrm{d}x = 0, \tag{3.83}$$

for all solutions $\mathbf{w}$ of the homogeneous adjoint problem $\mathcal{L}^*(\mathbf{w}) = \mathbf{0}$, with $\mathbf{w}$ satisfying the adjoint boundary conditions (3.81). This condition is a consequence of (3.80), with $\mathcal{L}(\mathbf{v}) = \mathbf{g}$ and $\mathcal{L}^*(\mathbf{w}) = \mathbf{0}$. Our next goal therefore is to calculate all solutions of the homogeneous adjoint problem $\mathcal{L}^*(\mathbf{w}) = \mathbf{0}$, which is analytically tractable in the limit $\varepsilon \ll 1$. Explicitly, our homogeneous adjoint problem reads

$$\mathcal{D}_0 \frac{\partial^2 w_1}{\partial x^2} + \varepsilon \frac{\partial^2 w_1}{\partial u^2} + f(u, c^*) \frac{\partial w_1}{\partial u} + \alpha_0 u w_2 = 0, \tag{3.84a}$$

$$D_c \frac{\partial^2 w_2}{\partial x^2} - \beta w_2 - \int_0^\infty f_c^* \frac{dn^*}{du} w_1(x, u)\, \mathrm{d}u = 0, \tag{3.84b}$$

with the adjoint boundary conditions in (3.81). If there are multiple linearly independent solutions of $\mathcal{L}^*(\mathbf{w}) = \mathbf{0}$, then each linearly independent solution provides a unique solvability condition.

By inspection, we see that that $w_1 = 1$ and $w_2 = 0$ satisfies (3.84a) exactly and (3.84b) up to all algebraic orders of ε since the integral is exponentially small:

$$\int_0^\infty f_c^* \frac{dn^*}{du}\, \mathrm{d}x = -\rho^* f_c^* \sqrt{\frac{\lambda}{2\pi\varepsilon}} \exp\left(-\frac{\lambda (u^*)^2}{2\varepsilon}\right). \tag{3.85}$$

Using (3.83), the corresponding solvability condition on $\mathbf{g}$ reads

$$\int_0^\infty \int_\Omega g_1(x, u)\, \mathrm{d}x\mathrm{d}u = \text{E.S.T.} \tag{3.86}$$

We argue that this solvability condition is unrelated to the bifurcation, but is rather a consequence of the fact that the original governing equation for $n(x,u,t)$ in (3.3a) is a conservation equation. As such, every constituent term in g_1 must be either a pure divergence or a pure time-derivative, both of which trivially integrate to zero. The divergence terms individually integrate to zero due to the no-flux boundary conditions, whereas the time derivatives integrate to zero because the perturbation in (3.68a) must contain zero mass in order for the total mass (i.e. number of cells) to be conserved over time.

The above discussion motivates the existence of a second solvability condition, one that is a consequence of the underlying bifurcation and not conservation of cells. We therefore seek a solution of the homogeneous adjoint problem (3.81) and (3.84) in the form

$$w_1(x,u) = W(u)\cos(kx), \qquad w_2(x) = \cos(kx), \tag{3.87}$$

where, because (3.84) is homogeneous, we fix the scaling of w_2 without loss of generality. As before, we take k to be the (non-zero) wavenumber corresponding to the bifurcation in the linear problem (3.71). Substituting (3.87) into (3.84) leads to

$$\varepsilon\frac{d^2W}{du^2} - \lambda(u-u^*)\frac{dW}{du} - \mathcal{D}_0(u)k^2W = -\alpha_0 u, \tag{3.88a}$$

$$D_c k^2 + \beta + \int_0^\infty f_c^*\frac{dn^*}{du}W(u)\,\mathrm{d}u = 0. \tag{3.88b}$$

The adjoint boundary conditions (3.81) become

$$\exp\left(-\frac{\lambda(u-u^*)^2}{2\varepsilon}\right)\frac{dW}{du} \to 0, \quad u \to 0,\infty. \tag{3.88c}$$

In general, the system (3.88) is overdetermined as W is the only unknown. However, we now show that whenever W satisfies (3.88a), then (3.88b) is automatically satisfied. We accomplish this by showing that (3.88b) is exactly equivalent to (3.71b). To show this, we multiply (3.88a) by $\eta(u)$, which satisfies the linear problem (3.71), and integrate over u. After integrating by parts and using the boundary conditions for η and W (without approximation in ε). We obtain

$$\begin{aligned}\alpha_0\int_0^\infty u\eta(u)\,\mathrm{d}u &= \int_0^\infty\left[\varepsilon\frac{d^2\eta}{du^2} + \frac{d}{du}\left[\lambda(u-u^*)\eta\right] - \mathcal{D}_0k^2\eta\right]W\,\mathrm{d}u \\ &= -\int_0^\infty f_c^*\frac{dn^*}{du}W(u)\,\mathrm{d}u,\end{aligned} \tag{3.89}$$

which states that the integral terms (3.88b) and (3.71b) are exactly equal and the two equations are equivalent. The equivalence implies that (3.88) has a solution only at the bifurcation point, and hence the second solvability condition that we seek can only be present at the bifurcation, as expected.

We now obtain a solution of (3.88a) in the regime $\varepsilon \ll 1$. The only difference between (3.88a) and the equation for $q(u)$ in (3.17) is the inhomogeneous term. We therefore proceed in the same fashion and expand W in a regular asymptotic series as

$$W(u) \sim \sum_{j=0}^{\infty} W_j(u)\varepsilon^j. \tag{3.90}$$

Substituting into (3.88a) and collecting terms at powers of ε, we obtain

$$\lambda(u-u^*)W_0' + \mathcal{D}_0(u)k^2 W_0 = \alpha_0 u, \tag{3.91a}$$

$$\lambda(u-u^*)W_j' + \mathcal{D}_0(u)k^2 W_j = W_{j-1}'', \quad j = 1, \ldots. \tag{3.91b}$$

We deduce that W must be smooth at u^* by the same argument that we used to show that q must be smooth at u^*. We therefore seek formal power series solutions in the form

$$W_j(u) = \sum_{\ell=0}^{\infty} W_j^{(\ell)}(u-u^*)^\ell. \tag{3.92}$$

By substituting (3.92) into (3.91), we obtain the following recurrence relations for the coefficients:

$$W_0^{(0)} = \frac{\alpha_0 u^*}{\mathcal{D}_{0*}k^2}, \tag{3.93a}$$

$$W_0^{(1)} = \frac{\alpha_0 - W_0^{(0)}\mathcal{D}_{0*}'k^2}{\mathcal{D}_{0*}k^2 + \lambda}, \tag{3.93b}$$

$$W_0^{(\ell)} = -\frac{k^2}{\mathcal{D}_{0*}k^2 + \ell\lambda}\sum_{m=1}^{\ell} W_0^{(\ell-m)}\frac{\mathcal{D}_{0*}^{(m)}}{m!}, \quad \ell = 2, \ldots, \tag{3.93c}$$

$$W_j^{(\ell)} = \frac{(\ell+2)(\ell+1)W_{j-1}^{(\ell+2)} - k^2\sum_{m=1}^{\ell} W_j^{(\ell-m)}\frac{\mathcal{D}_{0*}^{(m)}}{m!}}{\mathcal{D}_{0*}k^2 + \ell\lambda}, \quad j = 1, \ldots, \quad \ell = 0, \ldots. \tag{3.93d}$$

In principle, the recurrence relations above allow us to determine $w_1(x,u)$ in (3.87) locally to all algebraic orders of ε. Only the first several coefficients will be needed in the final result.

We are now in a position to state the second solvability condition, which we obtain by substituting (3.87) into (3.83). This gives

$$\int_{\Omega\times\mathbb{R}_+} g_1(x,u)W(u)\cos(kx)\,\mathrm{d}u\mathrm{d}x + \int_{\Omega} g_2(x)\cos(kx)\,\mathrm{d}x = 0. \tag{3.94}$$

Our task now is to impose the solvability conditions (3.86) and (3.94) on (3.74), which is the subject of the following subsection. We will find that both solvability conditions yield no additional information, which implies that the required information must be obtained from an analysis of terms at order $\mathcal{O}(\delta^3)$ in the perturbation (3.68).

3.3.2.2 Analysis at $\mathcal{O}(\delta^2)$

We now return to our analysis of the $\mathcal{O}(\delta^2)$ problem (3.74). First, we impose the solvability condition (3.86), where we recall that $g_1(x,u)$ is the RHS of (3.74a). After substituting η_1 in (3.70) into (3.86), we find

$$C^2(\tau)\left(\frac{f_{cc}^*}{2}n^*(u)+f_c^*\eta(u)\right)\Big|_{u=0}\int_\Omega \cos^2(kx)\,\mathrm{d}x = \text{E.S.T.} \tag{3.95}$$

Since $n^*(0)$ and $\eta(0)$ are exponentially small in ε, as seen from (3.6) and (3.72), this condition is trivially satisfied. The second solvability condition (3.94) gives

$$\frac{dC}{d\tau} = -\frac{k^2\int_0^\infty d(u)\eta(u)W(u)\,\mathrm{d}u}{1+\int_0^\infty \eta(u)W(u)\,\mathrm{d}u}C, \tag{3.96}$$

where we have used the forms (3.70) and (3.87) for η_1, w_1, and w_2. The contributions to the above solvability condition only involve the last two terms on the RHS of (3.74a). This is because the other terms, when multiplied by $w_1(x,u)$, are proportional to $\cos^3(kx)$ and hence their integrals (over x) are exactly zero. We evaluate the leading order in ε contribution to the integrals using the WKBJ solution for η (3.72) in combination with Laplace's method. Then using the expansions (3.18) and (3.20) for q, and the expansions in (3.90) and (3.92) for W, we find

$$\frac{\int_0^\infty d(u)\eta(u)W(u)\,\mathrm{d}u}{1+\int_0^\infty \eta(u)W(u)\,\mathrm{d}u} = \frac{d'(u^*)q_0^{(2)}W_0^{(0)}}{1+\left(\lambda q_1^{(0)}+q_2^{(0)}\right)W_0^{(0)}+q_0^{(1)}W_0^{(1)}}+\mathcal{O}(\varepsilon). \tag{3.97}$$

We further simplify the above using the recursion relations (3.73) and (3.93) for the coefficients, which yields

$$\frac{dC}{d\tau} \sim -\frac{\alpha_0\rho^* f_c^* u^*\left(\mathcal{D}_{0*}k^2+\lambda\right)d'_*k^2}{\mathcal{D}_{0*}k^2\left(\mathcal{D}_{0*}k^2+\lambda\right)^2+\alpha_0\rho^* f_c^*\left[\mathcal{D}_{0*}k^2-\left(2\mathcal{D}_{0*}k^2+\lambda\right)u^*\frac{\mathcal{D}'_{0*}}{\mathcal{D}_{0*}}\right]}C, \tag{3.98}$$

where we have dropped the $\mathcal{O}(\varepsilon)$ terms. Since $\mathcal{D}'_{0*}<0$, the sign of the RHS coefficient is the opposite of the sign of d'_*, where we recall that d'_* is the local bifurcation parameter as defined in (3.63) and (3.65). We therefore deduce that as $\tau\to\infty$, either $C\to 0$ when $d'_*>0$ or $C\to\infty$ when $d'_*<0$. This implies that the uniform

steady-state $n^*(u)$ is unstable when $\mathcal{D}'_* < \mathcal{D}'_{0*}$, and stable when $\mathcal{D}'_* > \mathcal{D}'_{0*}$, which is consistent with the leading order linear instability criterion (3.54).

Since (3.96) is linear, it yields no information beyond that of the linear stability analysis. This implies that the choice of scalings $r = p = 1$ in (3.63) and (3.67) is not appropriate, as expected. We should therefore choose r and p such that perturbation to $\mathcal{D}_0$ and the time-derivative term appear at next order in δ, i.e. $r = p = 2$. This also ensures that the solvability conditions at $\mathcal{O}(\delta^2)$ are trivially satisfied. We remark that our analysis at $\mathcal{O}(\delta^2)$ effectively rules out the possibility of a transcritical bifurcation. This is because the terms proportional to C^2 in (3.74a), i.e. the first two terms on the RHS, do not contribute to (3.98). The analysis at next order in δ will yield an equation for C that contains a term proportional to C^3; hence we anticipate a pitchfork bifurcation at $d'_* = 0$.

Before proceeding with our analysis of the $\mathcal{O}(\delta^3)$ terms, we require solutions of (3.74). This is a necessary step as the solvability conditions at next order in δ will depend on η_2 and c_2. To this end, we rewrite the RHS (3.74a)–(3.74b) using (3.70) to obtain

$$\mathcal{L}\begin{pmatrix}\eta_2(x,u,\tau)\\ c_2(x,\tau)\end{pmatrix} = \begin{pmatrix} C^2\left(\frac{f^*_{cc}}{2}\frac{dn^*}{du} + f^*_c\frac{d\eta}{du}\right)\cos^2(kx)\\ 0\end{pmatrix}, \tag{3.99}$$

where $\mathcal{L}$ is defined in (3.76) and the final two terms on the RHS of (3.74a) do not appear in the above due to our new choice of scalings $r = p = 2$ in (3.63) and (3.67). As the RHS is proportional to $C^2\cos^2(kx)$ we seek solutions in the form

$$\eta_2(x,u,\tau) = C^2(\tau)\big(\eta_{20}(u) + \eta_{22}(u)\cos(2kx)\big), \quad c_2(x,\tau) = C^2(\tau)\big(c_{20} + c_{22}\cos(2kx)\big), \tag{3.100}$$

where η_{20}, η_{22}, c_{20} and c_{22} are unknowns to be determined. We note that since $\mathbf{v} = (\eta_1, c_1)^T$ is a non-trivial solution to $\mathcal{L}(\mathbf{v}) = \mathbf{0}$, any combination of η_1 and c_1 can be added to η_2 and c_2 above. However, these terms can be absorbed into the $\mathcal{O}(\delta)$ terms in the expansion (3.68). Moreover, we show below that any such contribution will not affect the final result.

We obtain governing equations for the unknowns η_{20}, η_{22}, c_{20} and c_{22} by substituting (3.100) into (3.99) and using the linear independence of the Fourier modes 1 and $\cos(2kx)$ to equate coefficients. This results in a system for η_{20} and c_{20}, given by

$$\varepsilon\frac{d^2\eta_{20}}{du^2} - \frac{d}{du}\left[f(u,c^*)\eta_{20}\right] - c_{20}f^*_c\frac{dn^*}{du} = \frac{1}{2}\left[\frac{f^*_{cc}}{2}\frac{dn^*}{du} + f^*_c\frac{d\eta}{du}\right], \tag{3.101a}$$

$$\beta c_{20} - \alpha_0\int_0^\infty u\eta_{20}(u)\,\mathrm{d}u = 0, \tag{3.101b}$$

and a similar system for η_{22} and c_{22}:

$$\varepsilon\frac{d^2\eta_{22}}{du^2} - \frac{d}{du}\left[f(u,c^*)\eta_{22}\right] - c_{22}f_c^*\frac{dn^*}{du} - 4\mathcal{D}_0k^2\eta_{22} = \frac{1}{2}\left[\frac{f_{cc}^*}{2}\frac{dn^*}{du} + f_c^*\frac{d\eta}{du}\right], \quad (3.102a)$$

$$\left(4D_ck^2+\beta\right)c_{22} - \alpha_0\int_0^\infty u\eta_{22}(u)\,\mathrm{d}u = 0. \quad (3.102b)$$

Here η_{20} and η_{22} are subject to the same no-flux boundary conditions as η_2, cf. (3.74c)–(3.74d).

We now obtain solutions of (3.101) and (3.102), beginning with the former. Since the RHS of (3.101a) is proportional to $\exp\left(-\lambda(u-u^*)^2/2\varepsilon\right)$, we again seek a WKBJ solution in the form

$$\eta_{20}(u) = r(u)\exp\left(-\frac{\lambda(u-u^*)^2}{2\varepsilon}\right). \quad (3.103)$$

However, here we are able to obtain an exact solution owing to the fact that (3.101a) can be directly integrated. Integrating and substituting (3.103), we obtain the first-order equation

$$\varepsilon r' = \left(c_{20}f_c^* + \frac{f_{cc}^*}{4}\right)\rho^*\sqrt{\frac{\lambda}{2\pi\varepsilon}} + \varepsilon^{-3/2}\frac{f_c^*}{2}q(u), \quad (3.104)$$

where we recall that q is the amplitude in the WKBJ solution for $\eta(u)$, as given in (3.72). Integrating a second time, we obtain

$$r(u) = \left(c_{20}f_c^* + \frac{f_{cc}^*}{4}\right)\rho^*\sqrt{\frac{\lambda}{2\pi\varepsilon^3}}(u-u^*) + \varepsilon^{-5/2}\frac{f_c^*}{2}\int_{u^*}^u q(u)\mathrm{d}u + \bar{r}\sqrt{\frac{\lambda}{2\pi\varepsilon}}, \quad (3.105)$$

where $\bar{r}$ is a constant to be determined. To deduce its value, we observe that if the mass $\int_\Omega\int_0^\infty \eta_{20}\,\mathrm{d}u\mathrm{d}x$ is non-zero, then the expansion (3.68) effectively adds a perturbation of order $\mathcal{O}(\delta^2)$ to the global cell density ρ^*. To avoid this, we must select $\bar{r}$ using (3.103) such that the perturbation to the mass vanishes. Hence

$$\bar{r} = -\varepsilon^{-5/2}\frac{f_c^*}{2}\int_0^\infty Q(u)\exp\left(-\frac{\lambda(u-u^*)^2}{2\varepsilon}\right) + \text{E.S.T.}, \quad Q(u) := \int_{u^*}^u q(u)\,\mathrm{d}u. \quad (3.106)$$

We approximate the integral asymptotically using Laplace's method (Eq. (A.10) in Appendix A) in combination with a power series representation for $Q(u)$, which is obtained *via* term-by-term integration of the power series for $q(u)$. The resulting expression is shown below in (3.108a). We remark that the above procedure of explicitly enforcing zero-mass perturbations is only necessary for η_{20} because its integral over x does not trivially integrate to zero; it is not necessary for the linear term η_1 nor the quadratic term η_{22} as their integrals over x vanish.

Before considering (3.102), we calculate c_{20} from (3.101b). We again use Laplace's method to calculate c_{20} to leading order in ε. This leads to

$$\beta c_{20} = \alpha_0 \sqrt{\frac{2\pi\varepsilon}{\lambda}} \left[ur(u) + \frac{\varepsilon}{2\lambda}(ur(u))'' + \frac{\varepsilon^2}{8\lambda^2}(ur(u))'''' + \mathcal{O}(\varepsilon^3) \right] \Bigg|_{u=u^*}. \tag{3.107}$$

We now simplify the RHS using (3.105) and (3.106) for r, as well as (3.18) and (3.20) for q. The required derivatives read

$$r(u^*) = \bar{r}\sqrt{\frac{\lambda}{2\pi\varepsilon}} \sim -\varepsilon^{-3/2}\frac{f_c^*}{2}\left[\frac{1}{2\lambda}(q_0^{(1)} + \varepsilon q_1^{(1)}) + \frac{3\varepsilon}{8\lambda^2}q_0^{(3)} + \mathcal{O}(\varepsilon^2)\right], \tag{3.108a}$$

$$r'(u^*) = \left(c_{20}f_c^* + \frac{f_{cc}^*}{4}\right)\rho^*\sqrt{\frac{\lambda}{2\pi\varepsilon^3}} + \varepsilon^{-3/2}\frac{f_c^*}{2}\left(q_1^{(0)} + \varepsilon q_2^{(0)} + \mathcal{O}(\varepsilon^2)\right), \tag{3.108b}$$

$$r''(u^*) = \varepsilon^{-5/2}\frac{f_c^*}{2}\left(q_0^{(1)} + \varepsilon q_1^{(1)} + \mathcal{O}(\varepsilon^2)\right), \tag{3.108c}$$

$$r'''(u^*) = \varepsilon^{-5/2}f_c^*\left(q_0^{(2)} + \mathcal{O}(\varepsilon)\right), \tag{3.108d}$$

$$r''''(u^*) = 3\varepsilon^{-5/2}f_c^*\left(q_0^{(3)} + \mathcal{O}(\varepsilon)\right), \tag{3.108e}$$

where we have shown only the terms required for a leading order calculation of c_{20}. Substituting into (3.107), we obtain

$$c_{20} = \frac{\alpha_0\left(\rho^* f_{cc}^* + \sqrt{\frac{8\pi}{\lambda^3}}f_c^*\left(\lambda q_1^{(0)} + q_0^{(2)}\right)\right)}{4\left(\lambda\beta - \alpha_0\rho^* f_c^*\right)} + \mathcal{O}(\varepsilon). \tag{3.109}$$

In principle, we can use (3.73) to eliminate the coefficients $q_0^{(2)}$ and $q_1^{(0)}$. We remark that there is no $\mathcal{O}(\varepsilon^{-1})$ term in (3.109) as might be expected from the fact that the terms $u^*r(u^*)$ and $\varepsilon u^* r''(u^*)/2\lambda$ in (3.107) are individually $\mathcal{O}(\varepsilon^{-1})$. Their contributions exactly cancel as can be seen from (3.108a) and (3.108c).

Next, we work out η_{22} and c_{22} from (3.102). We again seek a solution in the form

$$\eta_{22}(u) = \varepsilon^{-5/2}s(u)\exp\left(-\frac{\lambda(u-u^*)^2}{2\varepsilon}\right), \tag{3.110}$$

where the $\varepsilon^{-5/2}$ scaling is introduced for convenience so that $s = \mathcal{O}(1)$, as seen from (3.111) below. With (3.110), the governing equation (3.102a) becomes

$$\varepsilon s'' - \lambda(u-u^*)s' - 4\mathcal{D}_0 k^2 s = \frac{f_c^*}{2}\left(\varepsilon q' - \lambda(u-u^*)q\right) - \varepsilon\rho^*\sqrt{\frac{\lambda^3}{2\pi}}\left(f_c^* c_{22} + \frac{f_{cc}^*}{4}\right). \tag{3.111}$$

Since the largest term on the RHS is $\mathcal{O}(1)$, we expand s in a regular asymptotic series as

$$s(u) \sim \sum_{j=0}^{\infty} s_j(u)\varepsilon^j, \tag{3.112}$$

and substitute into (3.111). Collecting powers of ε leads to the hierarchy of equations for each s_j given by

$$\lambda(u-u^*)s_0' + 4\mathcal{D}_0 k^2 s_0 = \frac{f_c^*}{2}\lambda(u-u^*)q_0(u), \tag{3.113a}$$

$$\begin{aligned}\lambda(u-u^*)s_j' + 4\mathcal{D}_0 k^2 s_j =& s_{j-1}'' - \frac{f_c^*}{2}\left(q_{j-1}' - \lambda(u-u^*)q_j\right) \\ &+ \delta_{j1}\rho^*\sqrt{\frac{\lambda^3}{2\pi}}\left(f_c^* c_{22} + \frac{f_{cc}^*}{4}\right)(u-u^*), \quad j=1,\dots\end{aligned} \tag{3.113b}$$

In general, solutions of (3.113) will not be regular at u^*. However, the form of the LHS is the same as in (3.19), only with k replaced with $2k$. As such, we deduce that each s_j is regular at u^* by the same argument that we used to show that q_j is regular at u^*. We note that our argument applies despite the fact that the RHS contains contributions from q_j for arbitrarily large j. Specifically, if any of the terms in the expansion for s are singular at u^*, then this switches on a divergent expansion of the form factorial/power. As a result, the inhomogeneous terms at large j are dominated by the s_{j-1}'' term, rather than the terms involving q_j, which necessarily grow slower than factorial/power because q_j is smooth at u^* for all j.

We now use standard power series methods to obtain solutions of (3.113) in the form

$$s_j(u) = \sum_{\ell=0}^{\infty} s_j^{(\ell)}(u-u^*)^\ell, \qquad j=0,\dots. \tag{3.114}$$

After some algebra, we find

$$s_0^{(0)} = s_0^{(1)} = 0, \tag{3.115a}$$

$$s_0^{(\ell)} = \frac{\frac{1}{2}f_c^* q_0^{(\ell-1)} - 4k^2\sum_{m=1}^{\ell}\frac{\mathcal{D}_{0*}^{(m)}}{m!}s_0^{(\ell-m)}}{4\mathcal{D}_{0*}k^2 + \ell\lambda}, \quad \ell=2,\dots, \tag{3.115b}$$

$$s_j^{(0)} = \frac{2s_{j-1}^{(2)}}{4\mathcal{D}_{0*}k^2}, \quad j=1,\dots, \tag{3.115c}$$

$$\begin{aligned}s_j^{(\ell)} =& \left[(\ell+1)(\ell+2)s_{j-1}^{(\ell)} - 4k^2\sum_{m=1}^{\ell}\frac{\mathcal{D}_{0*}}{m!}s_j^{(\ell-m)} - \frac{f_c^*}{2}\left[(\ell+1)q_{j-1}^{(\ell+1)} - \lambda q_j^{(\ell-1)}\right]\right. \\ &\left. + \delta_{\ell 1}\delta_{j1}\rho^*\sqrt{\frac{\lambda^3}{2\pi}}\left(f_c^* c_{22} + \frac{f_{cc}^*}{4}\right)\right]\left(4\mathcal{D}_{0*}k^2 + \ell\lambda\right)^{-1}, \quad \ell, j = 1,\dots,\end{aligned} \tag{3.115d}$$

where we have used the expansions for q_j in (3.20) in order to write the coefficients in terms of those for q_j. Although the above recursion relations allow us to compute arbitrarily many coefficients, in practice we will only need to compute a few to obtain a leading order final result.

The next step is to compute c_{22}. In principle, we can substitute (3.110) into (3.102b) and evaluate the integral using Laplace's method. However, since $s_1^{(1)}$ explicitly depends on c_{22}, all coefficients that recursively depend on $s_1^{(1)}$ also depend on c_{22}. In order to simplify the calculation, we can completely eliminate η_{22} from the integrand. In particular, we observe that the adjoint of (3.102a) is given by (3.88a), but with k replaced by $2k$. As such, we multiply (3.88a) by η_{22}, set $k \mapsto 2k$, and integrate by parts to transfer all derivatives to η_{22}. This results in

$$\begin{aligned}\alpha_0 \int_0^\infty u\eta_{22}\,\mathrm{d}u &= -\int_0^\infty \left(\varepsilon\eta_{22}'' - [f(u,c^*)\eta_{22}]' - 4\mathcal{D}_{0*}k^2\right)\tilde{W}\,\mathrm{d}u \\ &= \int_0^\infty \left[\left(c_{22}f_c^* + \frac{f_{cc}^*}{4}\right)n^* + \frac{f_c^*}{2}\eta\right]\tilde{W}'\,\mathrm{d}u, \end{aligned} \tag{3.116}$$

where $\tilde{W}$ denotes W, but with the replacement $k \mapsto 2k$. This replacement allows for a straightforward calculation of $\tilde{W}$ from (3.92)–(3.93). The boundary terms arising from integration by parts in (3.116) vanish due to the no-flux boundary conditions on η_{22} and W. We have also used (3.102a) to eliminate terms containing η_{22}. Since η and $\tilde{W}$ do not depend on c_{22}, we rearrange (3.116) and use Laplace's method (see (A.10) in Appendix A) to evaluate the integrals. We find

$$c_{22} = \frac{\rho^* f_{cc}^* \tilde{W}_0^{(1)} + 2f_c^*\sqrt{\frac{2\pi}{\lambda^3}}\left[\left(\lambda q_1^{(0)} + q_0^{(2)}\right)\tilde{W}_0^{(1)} + +2q_0^{(1)}\tilde{W}_0^{(2)}\right]}{4\left(4D_c k^2 + \beta - \rho^* f_c^* \tilde{W}_0^{(1)}\right)} + \mathcal{O}(\varepsilon). \tag{3.117}$$

We have now determined c_{20} and c_{22} in Eqs. (3.109) and (3.117) as well as η_{20} and η_{22} in Eqs. (3.103) and (3.110). The amplitude r for η_{20} is given in (3.105)–(3.106) while the amplitude s for η_{22} is given in (3.112) and (3.114). In principle, the coefficients $q_j^{(\ell)}$, $W_j^{(\ell)}$, and $s_j^{(\ell)}$ that appear in these formulas can be eliminated using (3.73), (3.93), and (3.115). This completes our analysis at $\mathcal{O}(\delta^2)$ and we proceed to next (and final) order in δ. We recall that the solvability conditions at $\mathcal{O}(\delta^2)$ yielded no additional information beyond that of the linear stability analysis (see (3.98)).

3.3.2.3 Analysis at $\mathcal{O}(\delta^3)$

To obtain governing equations for η_3 and c_3 in the expansion (3.68), we substitute (3.68), as well as the scalings (3.63) and (3.67), into the governing equations (3.1)–

(3.4) and equate terms at $\mathcal{O}(\delta^3)$. This leads to

$$\mathcal{D}_0\frac{\partial^2\eta_3}{\partial x^2}+\varepsilon\frac{\partial^2\eta_3}{\partial u^2}-\frac{\partial}{\partial u}\left[f(u,c^*)\eta_3\right]-c_3f_c^*\frac{dn^*}{du}=\left(c_1c_2f_{cc}^*+c_1^3\frac{f_{ccc}^*}{6}\right)\frac{dn^*}{du}$$
$$+\left(c_2f_c^*+c_1^2\frac{f_{cc}^*}{2}\right)\frac{\partial\eta_1}{\partial u}$$
$$+c_1f_c^*\frac{\partial\eta_2}{\partial u}+\frac{\partial\eta_1}{\partial\tau}-d\frac{\partial^2\eta_1}{\partial x^2}, \quad (3.118a)$$

$$D_c\frac{\partial^2c_3}{\partial x^2}-\beta c_3+\alpha_0\int_0^\infty\eta_3\,\mathrm{d}u=\frac{\partial c_1}{\partial\tau}, \quad (3.118b)$$

with the no-flux boundary conditions

$$\frac{\partial c_3}{\partial x}=\frac{\partial\eta_3}{\partial x}=0, \quad x=0,\mathcal{L}_x, \quad (3.118c)$$

$$\varepsilon\frac{\partial\eta_3}{\partial u}-f(u,c^*)\eta_3\to 0, \quad \text{as } u\to 0,\infty. \quad (3.118d)$$

In line with our notation, we define f_{ccc}^* as

$$f_{ccc}^*:=\frac{\partial^3 f}{\partial c^3}(u,c^*). \quad (3.119)$$

We now impose the two solvability conditions (3.86) and (3.94), where we recall that g_1 and g_2 are the RHS of (3.118a) and (3.118b), respectively. The first states that the RHS of (3.118a) must integrate to zero up to exponentially small terms. Hence

$$\int_0^\infty\int_\Omega\left(c_1c_2f_{cc}^*+c_1^3\frac{f_{ccc}^*}{6}\right)\frac{dn^*}{du}+\left(c_2f_c^*+c_1^2\frac{f_{cc}^*}{2}\right)\frac{\partial\eta_1}{\partial u}$$
$$+c_1f_c^*\frac{\partial\eta_2}{\partial u}+\frac{\partial\eta_1}{\partial\tau}-d\frac{\partial^2\eta_1}{\partial x^2}\,\mathrm{d}x\mathrm{d}u=\text{E.S.T.} \quad (3.120)$$

To evaluate the integral, we observe from (3.70) and (3.100) that c_1 and η_1 are proportional to $\cos(kx)$, while c_2 and η_2 are a linear combination of terms that are either independent of x or proportional to $\cos(2kx)$. As a result, every term in the integrand is proportional to either $\cos(kx)$, $\cos(kx)\cdot\cos(2kx)$, or $\cos^3(kx)$. Since these terms integrate to zero, the solvability condition (3.120) is satisfied automatically. We note that had we included terms in η_2 and c_2 proportional to $\cos(kx)$ in (3.100), then (3.120) would contain terms proportional to $\cos^2(kx)$, which do not integrate to zero. However, these terms are exponentially small when integrated over u, so the solvability condition is still satisfied.

We now consider the second solvability condition (3.94). Using the forms (3.70) for η_1 and c_1, (3.87) for w_1 and w_2, and (3.100) for η_2 and c_2, we explicitly evaluate

the integral over x in (3.94) to obtain the weakly nonlinear form for the bifurcation

$$\frac{dC}{d\tau} = -\frac{I_1}{I_0+1}k^2 C - \frac{\mu}{I_0+1}C^3, \tag{3.121a}$$

$$\mu := \left[\left(c_{20}+\frac{c_{22}}{2}\right)f^*_{cc} + \frac{f^*_{ccc}}{8}\right]I_2 + \left[\left(c_{20}+\frac{c_{22}}{2}\right)f^*_c + \frac{3}{8}f^*_{cc}\right]I_3 + f^*_c\left(I_4+\frac{I_5}{2}\right), \tag{3.121b}$$

where the integrals $I_0, \ldots, I_5$ are given by

$$I_0 := \int_0^\infty \eta(u)W(u)\,\mathrm{d}u, \tag{3.121c}$$

$$I_1 := \int_0^\infty d(u)\eta(u)W(u)\,\mathrm{d}u, \tag{3.121d}$$

$$I_2 := \int_0^\infty \frac{dn^*}{du}W\,\mathrm{d}u, \tag{3.121e}$$

$$I_3 := \int_0^\infty \frac{d\eta}{du}W\,\mathrm{d}u, \tag{3.121f}$$

$$I_4 := \int_0^\infty \frac{d\eta_{20}}{du}W\,\mathrm{d}u, \tag{3.121g}$$

$$I_5 := \int_0^\infty \frac{d\eta_{22}}{du}W\,\mathrm{d}u. \tag{3.121h}$$

As expected the bifurcation ODE (3.121a) has terms proportional to C^3, and essentially describes a pitchfork bifurcation at $I_1 = 0$.

In order to write (3.121a) in terms of the local bifurcation parameter d'_*, we evaluate the leading order contribution to the integrals *via* Laplace's method owing to the fact that n^*, η, η_{20}, and η_{22} are exponentially localised at u^*. We use the version of Laplace's method in Eq. (A.10) in Appendix A. A lengthy but straightforward

calculation results in

$$I_0 \sim \frac{\alpha_0 \rho^* f_c^* \left[\mathcal{D}_{0*} k^2 - \left(2\mathcal{D}_{0*} k^2 + \lambda\right) u^* \frac{\mathcal{D}'_{0*}}{\mathcal{D}_{0*}}\right]}{\left(\mathcal{D}_{0*} k^2 + \lambda\right)^2 \mathcal{D}_{0*} k^2}, \tag{3.122a}$$

$$I_1 \sim \frac{\alpha_0 \rho^* u^* f_c^*}{\mathcal{D}_{0*} k^2 \left(\mathcal{D}_{0*} k^2 + \lambda\right)} d'_*, \tag{3.122b}$$

$$I_2 \sim \frac{\alpha_0 \rho^* \left(u^* \frac{\mathcal{D}'_{0*}}{\mathcal{D}_{0*}} - 1\right)}{\mathcal{D}_{0*} k^2 + \lambda}, \tag{3.122c}$$

$$I_3 \sim -\sqrt{\frac{2\pi}{\lambda}} \left[\left(q_1^{(0)} + \frac{q_0^{(2)}}{\lambda}\right) W_0^{(1)} + \frac{2}{\lambda} q_0^{(1)} W_0^{(2)}\right], \tag{3.122d}$$

$$I_4 \sim -\sqrt{\frac{2\pi}{\lambda^5}} f_c^* \left[\left(q_0^{(2)} + \lambda q_1^{(0)}\right) W_0^{(2)} + \frac{3}{2} q_0^{(1)} W_0^{(3)}\right] - \frac{\rho^*}{\lambda} \left(2c_{20} f_c^* + \frac{f_{cc}^*}{2}\right) W_0^{(2)}, \tag{3.122e}$$

$$I_5 \sim -\sqrt{\frac{2\pi}{\lambda}} \left[\left(s_2^{(0)} + \frac{s_1^{(2)}}{\lambda} + \frac{3s_0^{(4)}}{\lambda^2}\right) W_0^{(1)} + \frac{2}{\lambda} \left(s_1^{(1)} + \frac{3s_0^{(3)}}{\lambda}\right) W_0^{(2)} + \frac{3}{\lambda} \left(s_1^{(0)} + \frac{3s_0^{(2)}}{\lambda}\right) W_0^{(3)}\right], \tag{3.122f}$$

where we have neglected $\mathcal{O}(\varepsilon)$ terms and used Eq. (3.6) for n^*, Eqs. (3.16), (3.18), and (3.20) for η, Eqs. (3.90), and (3.92) for W, Eqs. (3.103), (3.105), and (3.108) for η_{20}, and finally (3.110), (3.112), and (3.114) for η_{22}. For the sake of brevity, we have written the results in terms of the power series coefficients of W, η, η_{20}, and η_{22}, except in cases where the resulting formulas are short enough to write explicitly in terms of the basic parameters of the model. In these cases, we used (3.73) and (3.93) to eliminate the coefficients. In principle, the recursion relations (3.73), (3.93), and (3.115), together with the results (3.109) and (3.117) for c_{20} and c_{22} can be used to eliminate the remaining coefficients, thereby expressing $I_0, \ldots, I_5$ in terms of the original model parameters. Then Eq. (3.121a) fully determines $C(\tau)$ in terms of the model parameters. Putting this together with a final simplification of the linear term using (3.122a) and (3.122b), we may rewrite (3.121a) as

$$\frac{dC}{d\tau} \sim -\frac{\alpha_0 \rho^* f_c^* u^* \left(\mathcal{D}_{0*} k^2 + \lambda\right) d'^* k^2}{\mathcal{D}_{0*} k^2 \left(\mathcal{D}_{0*} k^2 + \lambda\right)^2 + \alpha_0 \rho^* f_c^* \left[\mathcal{D}_{0*} k^2 - \left(2\mathcal{D}_{0*} k^2 + \lambda\right) u^* \frac{\mathcal{D}'_{0*}}{\mathcal{D}_{0*}}\right]} C - \frac{\mu}{I_0 + 1} C^3. \tag{3.123}$$

The local solution structure near the bifurcation point is determined by the steady-states of (3.123) and their stability. We recall that d'_* is our local bifurcation parameter in the neighbourhood of the bifurcation point at $\mathcal{D}'_* = \mathcal{D}'_{0*}$, cf. (3.65). The

linear term is identical to what we obtained in (3.98) (since it must be consistent with the linear stability analysis), and by the same reasoning we conclude that the trivial steady-state is stable when $d'_* > 0$ and unstable when $d'_* < 0$, consistent with our linear stability analysis. A key upside of our weakly nonlinear analysis is in understanding the role of the local nonlinearity. Since $I_0 > 0$, whenever d'_* and μ have opposite signs, the system has non-trivial steady-states near the bifurcation given by

$$C \sim \pm\sqrt{-d'_* \frac{\alpha_0 \rho^* f_c^* u^*}{\mu \mathcal{D}_{0*} \left(\mathcal{D}_{0*} k^2 + \lambda\right)}}. \tag{3.124}$$

The stability of these steady-states is determined by the sign of μ. Specifically, they are stable (supercritical) if $\mu > 0$ and unstable (subcritical) if $\mu < 0$. These two possibilities are illustrated in Figure 3.1 for specific parameters. The condition $\mu = 0$ can be expressed in terms of the integrals I_j using (3.121b) as

$$\left[\left(c_{20} + \frac{c_{22}}{2}\right) f_{cc}^* + \frac{f_{ccc}^*}{8}\right] I_2 + \left[\left(c_{20} + \frac{c_{22}}{2}\right) f_c^* + \frac{3}{8} f_{cc}^*\right] I_3 + f_c^* \left(I_4 + \frac{I_5}{2}\right) = 0. \tag{3.125}$$

As explained above, the I_j's, as well as c_{20} and c_{22}, can be expressed in terms of the original model parameters. Eq. (3.125) is the first key result of this section; it quantifies the condition for a switch between a subcritical and supercritical pitchfork bifurcation when QS represses motility.

In the following section, it will be more convenient to construct bifurcation diagrams for the density $\rho(x)$, rather than the AI concentration $c(x)$. It will be helpful therefore to rewrite the non-trivial states (3.124) as a relationship between ρ and d'_*. Since $\rho(x) := \int_0^\infty n \, \mathrm{d}u$, using (3.68a) and (3.70) we have

$$\rho(x) = \rho^* + \delta C \cos(kx) \int_0^\infty \eta(u) \, \mathrm{d}u + \mathcal{O}(\delta^2). \tag{3.126}$$

Then utilizing our WKBJ ansatz (3.72), we apply Laplace's method to evaluate the leading order (in ε) contribution to the integral. Subsequently eliminating d'_* and δ in favour of the original variable $\mathcal{D}'_*$ in (3.65) leads to

$$\rho(x) = \rho^* \pm \mathcal{D}'_{0*} \sqrt{-\frac{\alpha_0 u^* (\rho^* f_c^*)^3 \left(\mathcal{D}'_* - \mathcal{D}'_{0*}\right)}{\mu \mathcal{D}_{0*}^3 \left(\mathcal{D}_{0*} k^2 + \lambda\right)^3}} \cos(kx) + \mathcal{O}\left(\varepsilon, \mathcal{D}'_* - \mathcal{D}'_{0*}\right), \tag{3.127}$$

as $\mathcal{D}'_* \to \mathcal{D}'_{0*}$. Eq. (3.127) is the second and final key result of this section. It constitutes an explicit representation for the spatially non-uniform steady cell density $\rho(x)$, in the neighbourhood of the bifurcation point $\mathcal{D}'_{0*}$. Similar expressions can also be derived for $c(x)$ and $n(x, u)$.

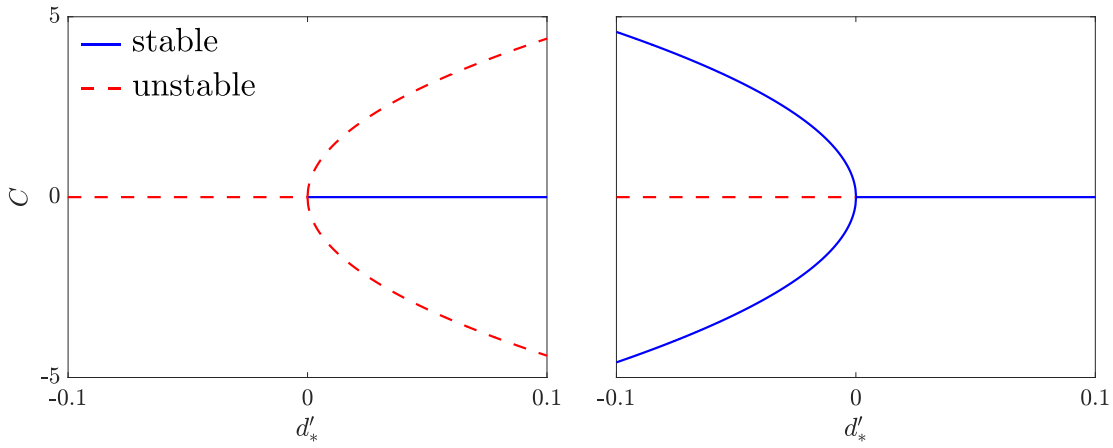

Figure 3.1: Local bifurcation diagrams for C in (3.123) showing a pitchfork bifurcation. The subcritical case has $\mu < 0$ (left) and the supercritical case (right) has $\mu > 0$. Red dashed lines denote unstable equilibria, while blue solid lines denote stable. Here we used a domain length of $\mathcal{L}_x = 10$, diffusion coefficient $\mathcal{D}_* = 0.03$, as well as $K = 0.9$ for the subcritical case and $K = 0.1$ for the supercritical case. All other parameters are set to one for convenience. A comparison with full numerical solutions of the governing equations is performed in Section 3.4.

Before continuing with numerical results and discussion in the next section, we make a few remarks about our analysis. First, we have taken $\mathcal{D}'_*$ and $\mathcal{D}_*$ to be parameters that can be varied independently, which is explicitly assumed in (3.64). Importantly, our analysis does not crucially depend on this assumption and, in fact, the only part of our analysis affected by relaxing this assumption is the evaluation of the integral I_1 in (3.122b), which in turn only affects the behaviour of the non-uniform steady-states near the bifurcation in (3.127). The linear stability criteria (3.54) and (3.58) can generically incorporate any choice of $\mathcal{D}(u)$. Notably, the type of bifurcation (either a subcritical or supercritical pitchfork) does not depend on the specific form of $\mathcal{D}(u)$, only its local behaviour near the bifurcation point.

We also remark that our theoretical results are generalisable in several ways. First, it is straightforward to make $\alpha(u)$ in (3.2) a generic function of u and $f(u, c)$ in (3.1) a generic function of c provided that f is still linear in u. A caveat here is that the steady-state may not be unique. However, as long as n^* is exponentially localised at a single point u^*, the analysis is nearly identical. We will explore this in more detail in the next chapter. In principle, it is also possible to choose kinetics that are nonlinear in u. In this case, the prolific amount of terms that arise from Laplace's method renders the algebra significantly more complicated, especially the evaluation of integrals I_4 and I_5 in (3.122) above and the underlying recursion relations for

the coefficients. Finally, we remark that it may be interesting to perform a similar weakly nonlinear analysis for the Hopf bifurcation, characterised by (3.58), in order to classify it as either subcritical or supercritical. We anticipate that the method of multiple timescales would be needed to capture the $\mathcal{O}(1)$ oscillation timescale and the asymptotically longer growth or decay timescales (likely $\mathcal{O}(\delta^{-2})$). In the following section, we verify the predictions of our theory *via* full numerical solutions of the governing equations (3.1)–(3.4).

3.4 Comparison with Numerical Results and Discussion

In this section, we compare the predictions of our asymptotic theory with full numerical solutions of the governing equations (3.1)–(3.4). We also characterise the emergent patterning that arises from the linear instabilities. The remainder of this chapter is organised into two sections. First, we consider the case where the QS circuit represses motility ($\mathcal{D}'_* < 0$). We then consider the case where QS promotes motility ($\mathcal{D}'_* > 0$).

The numerical solution of the governing equations (3.1)–(3.4) in this section, and for the remainder of this thesis, are performed with `oomph-lib`, an open-source finite-element software library for C++ [49]. This package facilitates computationally intensive numerics as well as the implementation of the non-local coupling and nonlinear boundary condition (3.4a). Broadly, we use a Galerkin finite element method with quadratic Lagrange elements on a rectangular grid and the BDF2 scheme for time-stepping. We emphasize that several custom codes were needed to handle the non-local secretion term in (3.3b) as well as the fact that the domains for (3.3a) and (3.3b) have different dimension. The methodology is described in more detail in Appendix C. We also emphasize that the governing equations for our model are computational intensive due to the high dimension and the strongly localised solution structure arising from its singular nature, i.e. $\varepsilon \ll 1$. The finite-element calculations in this section and the remainder of this thesis were therefore performed on several high-performance machines including the Oxford Advanced Research Computing (ARC) high-performance cluster, the High Performance Cluster (HPC) machines at UCL, and the Mathematics Department cluster also at UCL.

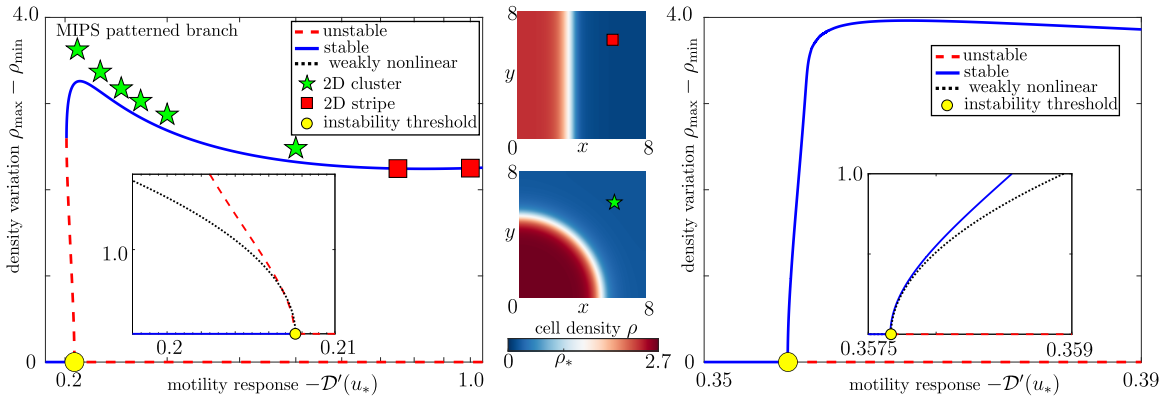

Figure 3.2: Bifurcation diagrams when QS represses motility showing the predicted subcritical (left) and supercritical (right) pitchfork bifurcations. Theoretical bifurcation points given by (3.66) are denoted by yellow circles. The trivial branches, given by (3.6), (3.8), and (3.10), are spatially uniform and therefore have $\rho = \text{const.}$, while the non-trivial branches are spatially non-uniform and are computed numerically from the governing equations (3.1)–(3.4) and (3.128)–(3.129). Near the bifurcation (insets), the local behaviour of the non-trivial branches agree well with the theoretical local behaviour in (3.127). Numerical results in 2D are shown for the subcritical case as green stars and red squares, where the steady-state profiles correspond to spot and stripe patterns, respectively. The solid blue line in both panels corresponds to stripe patterns. To facilitate computationally intensive numerics in 2D, we choose $\varepsilon = 0.04$ on the left, whereas on the right we use a smaller value of $\varepsilon = 0.001$. All other parameter values here and for the rest of this Chapter are given in Table D.1 of Appendix D.

3.4.1 Quorum Sensing Represses Motility: $\mathcal{D}'_* < 0$

First we consider the case where QS represses motility. To perform numerical calculations, we fix a convenient form for the diffusion coefficient $\mathcal{D}$ as

$$\mathcal{D}(u) = \begin{cases} \mathcal{D}'_*(u - u^*) + \mathcal{D}_*, & 0 \le u \le u_0, \\ \mathcal{D}_\infty, & u > u_0, \end{cases} \tag{3.128}$$

where $\mathcal{D}_\infty$ is a parameter and u_0 is chosen such that $\mathcal{D}$ is continuous. In the above, $\mathcal{D}(u^*) = \mathcal{D}_*$ and $\mathcal{D}'(u^*) = \mathcal{D}'_* < 0$, in line with our previous definitions of $\mathcal{D}_*$ and $\mathcal{D}'_*$. As before, we take $\mathcal{D}'_*$ to be our bifurcation parameter. We recall from (2.15) that the cell density is computed from

$$\rho(\mathbf{x}, t) = \int_0^\infty n(\mathbf{x}, u, t)\, \mathrm{d}u. \tag{3.129}$$

We begin by comparing our theory with numerically computed bifurcation diagrams. We show results for both the subcritical case and supercritical case in Figure

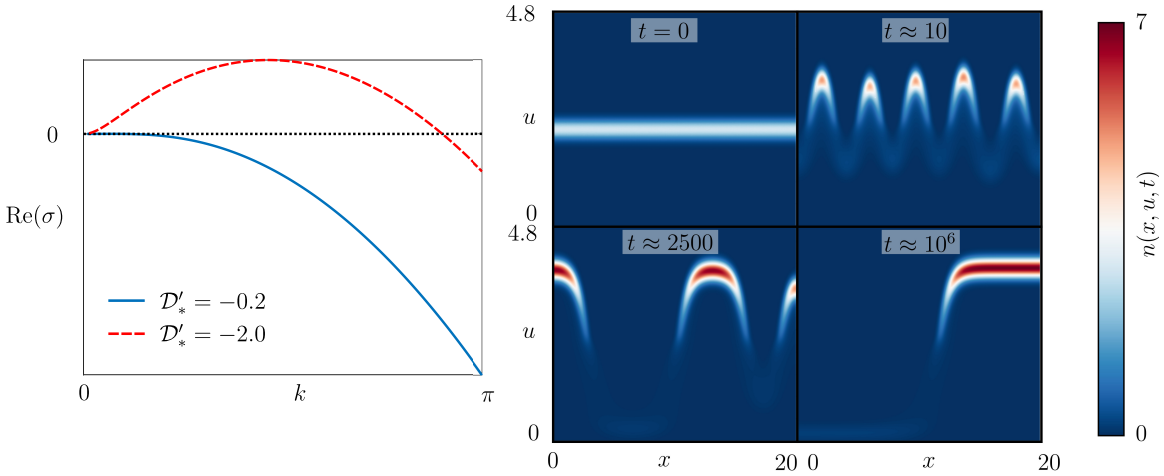

Figure 3.3: Left: theoretically predicted dispersion relations for the dominant eigenvalue σ, computed from (3.25), close to the onset of instability ($\mathcal{D}'_* = -0.2$) and well within the unstable regime ($\mathcal{D}'_* = -2$). The longest wavelength mode is the first to lose stability as $\mathcal{D}'_*$ is varied through the bifurcation point, but inside the linearly unstable regime the most unstable mode in general has an intermediate wavelength. Right: snapshots of a 1D solution of the governing equations (3.1)–(3.4) and (3.128)–(3.129) for $\mathcal{D}'_* = -2.0$. The lengthscale of the instability at early times is in agreement with the most unstable mode of $k \approx \pi/2$.

3.2. In both cases, the linear stability of the uniform state predicted from theory in Eq. (3.54) agrees well with numerical results. The behaviour of the non-trivial branch of equilibria near the bifurcation, as predicted by our weakly nonlinear analysis, is also in good agreement with numerics. In the subcritical case, we also show 2D steady-states, which we find can either be spots or stripes. Since stripe patterns are effectively 1D, they lie on the same solution branch as the 1D results.

Next, we consider the time evolution following the linear instability. Figure 3.3 shows typical dispersion relations near the bifurcation point and well into the unstable regime. As predicted by (3.54), the first mode to lose stability has the longest wavelength (i.e. closest to $k = 0$), but the most unstable mode inside the unstable regime has an intermediate wavelength (i.e. away from $k = 0$) in general. Snapshots of the solution in Figure 3.3 show the formation of clusters of high density at early times. The wavelength of the most unstable mode gives an approximation of the typical cluster size. As time progresses, the clusters coarsen into a single cluster, which then migrates to one of the boundaries. We observe that $n(x, u, t)$ is localised at larger values of u inside the cluster, implying that clusters consist primarily of lower motility cells. In contrast, cells outside the clusters have lower values of u, or higher motility. Snapshots of the cell density for a 2D simulation are shown in Figure 3.4

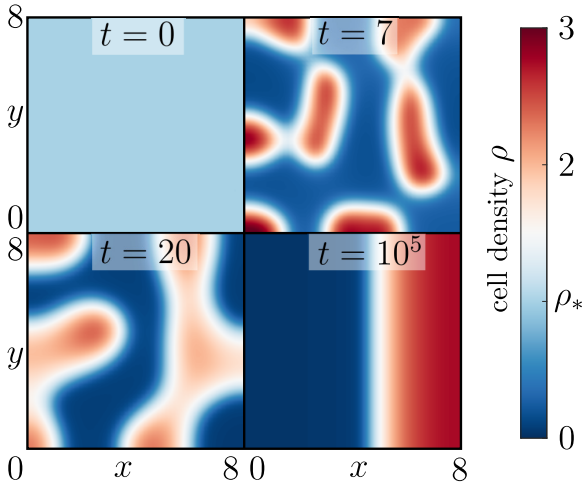

Figure 3.4: Snapshots of a 2D numerical solution of (3.1)–(3.4) and (3.128)–(3.129) showing phase separation behaviour for the cell density. Here the system eventually reaches a stripe pattern, but a spot pattern is also possible (intermediate states are similar). The AI concentration profiles are qualitatively similar to the cell density and therefore omitted.

where we observe similar clustering behaviour.

We illustrate the physical mechanism underlying the instability schematically in Figure 3.5a. A small localised increase to the cell density induces a local increase in the AI concentration through the secretion term in (3.3b). This in turn leads to a 'chemical flux' in the u-coordinate due to the GRN kinetics, which is denoted by the blue arrows in Figure 3.5. This flux acts to achieve an internal concentration for which $f(u, c) = 0$, so locally higher values of c result in higher internal concentrations. In effect, the chemical fluxes convert high motility cells to low motility cells inside the cluster, and *vice versa* outside the cluster. The higher internal concentrations inside the cluster reduce the motility through the gene-regulated diffusion coefficient $\mathcal{D}(u)$, which affects the diffusive fluxes into and out of the cluster (purple arrows in Figure 3.5). Perturbations grow if the inward flux overcomes the outward flux. This can happen if the motility is sufficiently reduced inside the cluster, which is quantified by the bifurcation parameter $\mathcal{D}'_*$.

The above-described mechanism is different in principle, but similar in outcome, to the mechanism behind the well-known motility induced phase separation (MIPS) in classical active matter. We recall our definition of classical active matter as an active system with physical interactions and no QS nor gene-regulated motility. Broadly, the classical mechanism operates as follows [20]. Physical interaction between particles acts to effectively reduce motility at high density. Since particles naturally

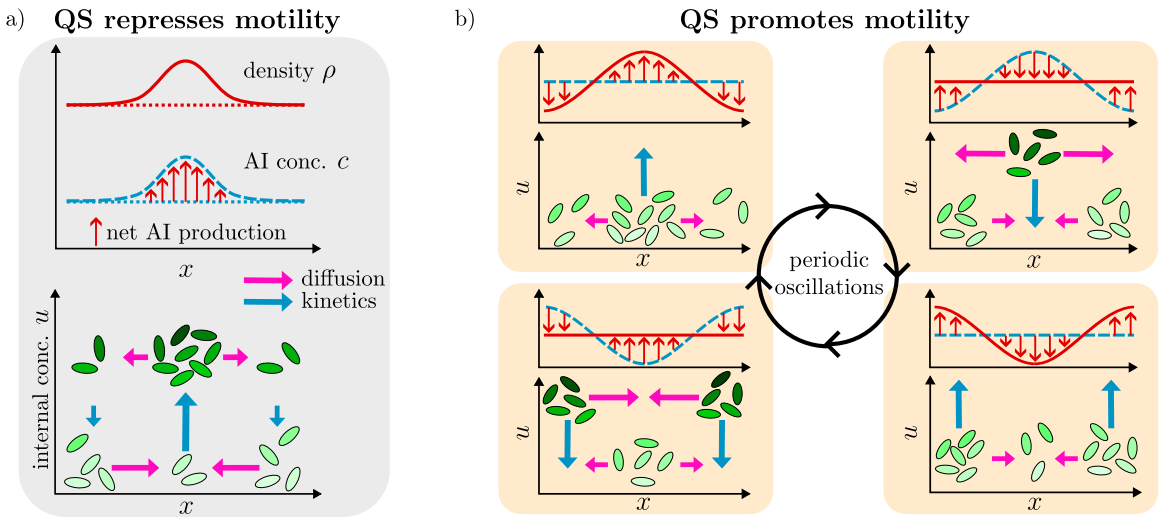

Figure 3.5: Simplified illustrations of the instability mechanisms. a) Small density/AI perturbation from the unstable uniform equilibrium when QS represses motility. Perturbations grow when the diffusive flux of high motility (low u) cells into the cluster is greater than the diffusive flux of low motility (high u) cells out of the cluster. b) Periodic spatio-temporal oscillations when QS promotes motility (right).

accumulate in regions where they slow down, they accumulate in regions of high density. This further reduces motility, leading to MIPS. The outcome is a dense cluster of immotile particles surrounded by a dilute phase of motile particles. This is exactly the outcome that we observe in Figure 3.3. Some qualitative features such as the transient behaviour and the possibility of either continuous (supercritical) or discontinuous (subcritical) phase transitions are similar to their counterparts in classical active systems [81]. The cluster behaviour that we observe when QS represses motility can therefore be thought of as a chemical analogue of MIPS.

Another key difference between classical MIPS and our chemical analogue is that our results predict a new route to MIPS. Here MIPS can be triggered by genetic regulation of any one of the motility functions that make up the effective diffusion coefficient. We recall that the effective diffusion coefficient $\mathcal{D}(u)$ is given in terms of cell-level quantities by (2.14c), which reads

$$\mathcal{D}(u) = D_t + \frac{v^2(u)}{2(D_r(u) + \gamma(u))}, \tag{3.130}$$

where v is the self-propulsion speed, D_r the rotational diffusion coefficient, and γ the tumbling frequency. In classical active systems in the large lengthscale and timescale regime (2.10d) with $\chi \gg 1$, only variations in the self-propulsion speed v (due to physical interaction) can trigger MIPS (see (1.6) and [19, 20]).

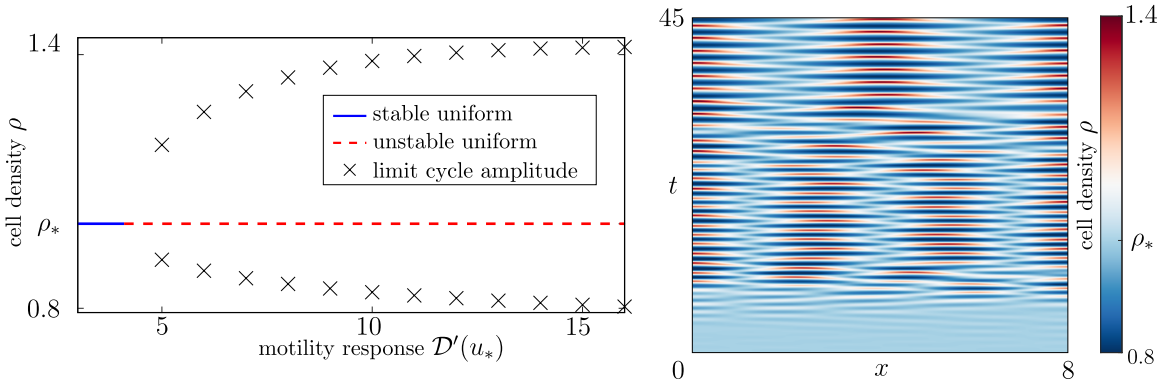

Figure 3.6: Left: bifurcation diagram when QS promotes motility showing a Hopf bifurcation and the numerically computed branch of stable limit cycles. The linear stability of the uniform branch as predicted from asymptotic theory is indicated. Right: spacetime diagram of the cell density ρ for $\mathcal{D}'_* = 16$, computed from (3.1)–(3.4), (3.129), and (3.131).

3.4.2 Quorum Sensing Promotes Motility: $\mathcal{D}'_* > 0$

Next, we consider the case where QS promotes motility. In this case, we fix the effective diffusion coefficient $\mathcal{D}$ as

$$\mathcal{D}(u) = \begin{cases} \mathcal{D}_0, & 0 \leq u < u_0, \\ \mathcal{D}'_*(u - u^*) + \mathcal{D}_*, & u_0 \leq u < \infty, \end{cases} \tag{3.131}$$

where now $\mathcal{D}_0$ is a parameter and u_0 is again fixed such that $\mathcal{D}$ is continuous. The parameter $\mathcal{D}'_*$ is now positive.

We begin by comparing our theoretical predictions with numerical results. We show a bifurcation diagram in Figure 3.6 where the spatially non-uniform solutions are computed numerically. We observe that the Hopf bifurcation predicted from the linear stability analysis is supercritical; a branch of stable limit cycles bifurcates from the uniform state. To illustrate the transient dynamics and convergence to periodic behaviour, we provide a typical spacetime diagram in Figure 3.6. As we illustrate in Figure 3.7, the qualitative behaviour of unstable solutions at early times agrees well with our theoretically predicted behaviour for the dominant eigenvalue $\sigma(k)$ in (3.25).

To help understand the limit cycle behaviour physically, we plot snapshots of the full numerical solution for n, c, and ρ in Figure 3.8. We observe that the oscillations of n correspond to oscillations in both the cell density and internal concentrations. These oscillations are out of phase with each other and out of phase with the AI concentration. The phase differences correspond to effective time delays between changes in cell density, changes in AI concentration, and changes in internal concentrations (motility).

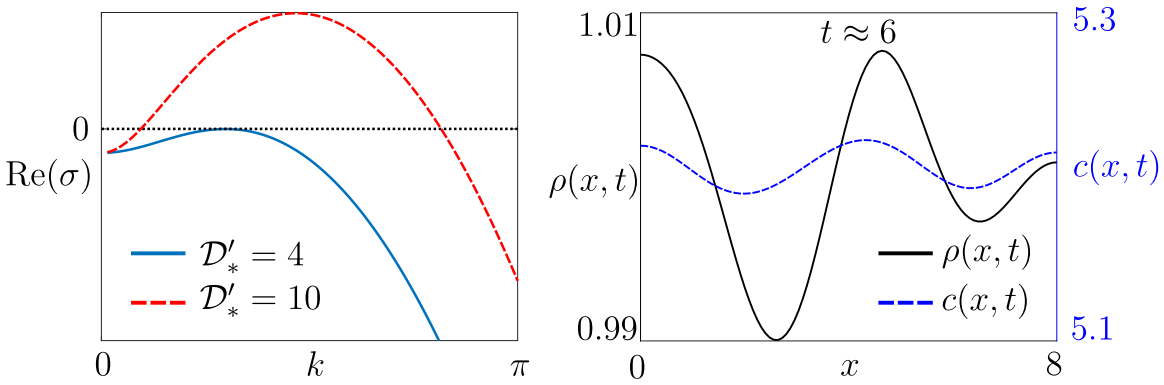

Figure 3.7: Left: theoretically predicted dispersion relations for the dominant eigenvalue σ, computed from (3.25), close to the onset of instability ($\mathcal{D}'_* = 4$) and well within the unstable regime ($\mathcal{D}'_* = 10$). In general, an intermediate wavelength mode is the first to lose stability as $\mathcal{D}'_*$ is varied through the bifurcation point. Inside the unstable region, there is a band of unstable modes since the system is stable for $k \to 0$ and $k \to \infty$. The most unstable wavenumber for $\mathcal{D}'_* = 10$ is approximately $\pi/2$. Right: snapshot of the cell density and AI concentration for $\mathcal{D}'_* = 10$ at an early time showing that the most unstable wavenumber is approximately $\pi/2$. The snapshot is calculated from a numerical solution of (3.1)–(3.4), (3.129), and (3.131).

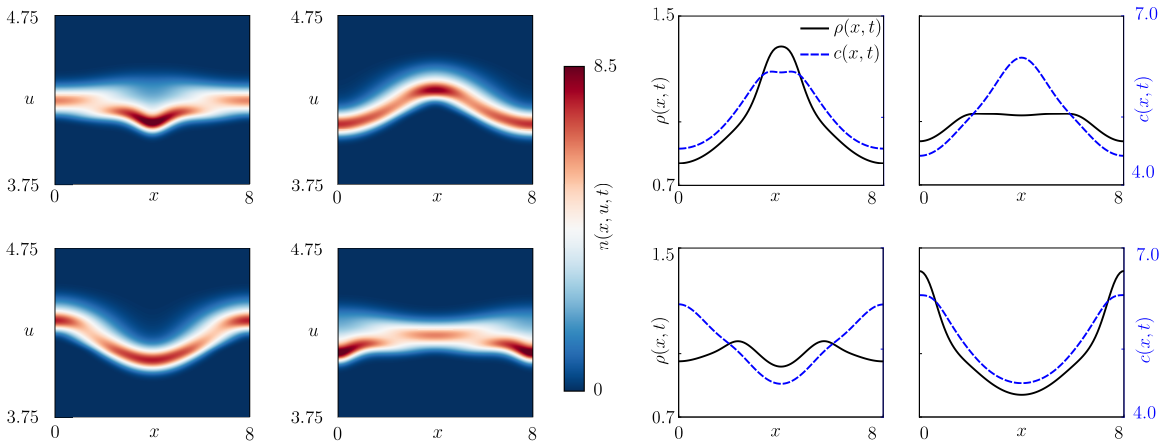

Figure 3.8: Snapshots of the limit cycle behaviour for $n(x,u,t)$ (left) as well as profiles of the AI concentration $c(x,t)$ and cell density $\rho(x,t)$ (right). The snapshots are computed from a numerical solution of (3.1)–(3.4), (3.129), and (3.131). The oscillations in density, AI concentration, and internal chemical are out of phase due to an effective time delay caused by finite chemical timescales. The temporal ordering of the snapshots is consistent with Figure 3.5b, i.e. top-left, top-right, bottom-right, bottom-left.

We give a simplified schematic of the limit cycle in Figure 3.5b. To illustrate the main idea behind the physical mechanism, we neglect the effective time delay between the AI concentration and internal concentration. First, let us consider a region of locally higher cell density. As the density fluctuation begins to relax due to diffusion, the AI concentration field increases locally in response to the higher density. This in turn leads to locally higher internal concentrations due to the reaction kinetics, which leads to locally increased cellular motility (as quantified by the effective diffusion coefficient $\mathcal{D}(u)$). As the local density returns to the equilibrium value, the locally higher motility persists and the region begins to deplete of cells, thereby forming a region of lower density. This forms the first half of the periodic cycle, with the second half having equivalent reasoning. This description ignores the effective time delay between the AI concentration and internal concentration. A more accurate description includes additional steps during which the internal concentrations respond to changes in the AI concentration. However, the principle of operation remains unchanged; finite chemical timescales induce effective time delays between changes in cell density and changes in motility, which leads to spatio-temporal oscillations.

The effective time delay is a critical aspect of the mechanism because the instability disappears as the effective time delay tends to zero. This can be seen mathematically by considering the location of the Hopf bifurcation in the limit of fast chemical timescales, given by the parameter regime $a \sim L \sim \lambda \sim \alpha_0 \sim \beta \gg 1$. We recall that the condition for instability is given in Eq. (3.58), which we repeat here for convenience:

$$\frac{\mathcal{D}_*'}{\mathcal{D}_*} > \frac{B}{u^*}, \quad B := \frac{\nu_\lambda + \nu}{\nu_0}\left[\frac{(\nu_0+\nu_\lambda)(\nu_0+\nu)}{\alpha_0 \rho^* f_c^*} - 1\right], \quad \nu_j := \mathcal{D}_* k^2 + j, \quad \nu := D_c k^2 + \beta. \tag{3.132}$$

In the limit of fast chemical timescales, we find that $B \gg 1$, and hence the criterion cannot be satisfied unless $\mathcal{D}_*'$ is large. This favours a stable uniform population.

In this chapter, we have characterised motility-induced patterning for simple reaction kinetics f that model the canonical LuxIR system. In the following chapter, we extend our theory and results to a few general classes of reaction kinetics.

Chapter 4

Motility-Induced Patterning for General Reaction Kinetics

In this chapter, we aim to characterise motility-induced patterning for more general reaction kinetics using our structured modelling framework. We divide this work into four sections, the first of which considers reaction kinetics that have multiple stable equilibria. The second deals with multiple internal chemicals. The third deals with kinetics that have a stable limit cycle, but no stable equilibrium. Finally, we compare the results of our theory with full numerical calculations.

4.1 General One-Component Kinetics

In this section, we consider scalar reaction kinetics with multiple equilibria. Examples of GRN kinetics with multiple equilibria can be found in detailed models of the canonical LuxIR quorum sensing circuit [25,65,89], the *las*/*rhl* circuit in *Pseudomonas aeruginosa* [33], as well as Fitzhugh–Nagumo kinetics in some parameter regimes (see, e.g., [46]).

Our governing equations for the remainder of this section are

$$\frac{\partial n}{\partial t} = \mathcal{D}(u)\nabla^2 n + \varepsilon\frac{\partial^2 n}{\partial u^2} - \frac{\partial}{\partial u}\left[f(u,c)n\right], \quad \mathbf{x}\in\Omega, \quad u\in\mathbb{R}_+, \tag{4.1a}$$

$$\frac{\partial c}{\partial t} = D_c\nabla^2 c - \beta c - \int_0^\infty \alpha(u)n\,\mathrm{d}u, \quad \mathbf{x}\in\Omega, \tag{4.1b}$$

where we take Ω to be a rectangle with side lengths $\mathcal{L}_x$ and $\mathcal{L}_y$. We impose no-flux boundary conditions in $\mathbf{x}$ and u, which read

$$\varepsilon\frac{\partial n}{\partial u} - f(u,c)n \to 0, \quad u\to 0,\infty, \tag{4.2a}$$

$$\nabla_{\mathbf{x}} n\cdot\mathbf{N}_{\mathbf{x}} = \nabla_{\mathbf{x}} c\cdot\mathbf{N}_{\mathbf{x}} = 0, \quad \mathbf{x}\in\partial\Omega, \tag{4.2b}$$

where $\mathbf{N}_\mathbf{x}$ is the unit normal on Ω.

In order for the reaction kinetics to represent physically and biologically realistic systems, we impose some restrictions on f. First, we disallow infinite and negative internal concentrations by requiring

$$f(u,c) < 0 \quad \text{as } u \to \infty, \tag{4.3a}$$

$$f(0,c) > 0, \tag{4.3b}$$

for all positive values of c (we also disallow $c < 0$). We also assume that f has multiple equilibria, as clarified below. By continuity of f, Eq. (4.3) guarantees that there is at least one value of u such that $f(u,c) = 0$.

Our general approach is similar to that of the previous chapter: we determine the spatially uniform steady-state and perform a stability analysis in order to detect patterning. A key difference here is that when f has multiple equilibria, then there are spatially uniform, quasi-steady solutions of (4.1) as we show below. We extend our linear stability analysis from the previous chapter to account for perturbations around a slowly varying base state.

4.1.1 Spatially Uniform Quasi-Steady States

In order to motivate our analysis of quasi-steady states, we begin by calculating true steady-states. Let us denote one of the (possibly many) spatially uniform steady-states of (4.1)–(4.2) by $n^*(u)$ and c^*. They satisfy

$$\varepsilon \frac{d^2 n^*}{du^2} - \frac{d}{du}\left[f(u,c^*)n^*\right] = 0, \tag{4.4a}$$

$$\beta c^* - \int_0^\infty \alpha(u) n^*(u)\,\mathrm{d}u = 0. \tag{4.4b}$$

Since c^* is constant, we directly integrate (4.4a) and use the no-flux condition (4.2a) to fix the integration constant. Integrating again then yields

$$n^*(u) = A \exp\left[-\frac{F(u,c^*)}{\varepsilon}\right], \tag{4.5}$$

where the constant A is determined from the normalisation condition $\rho^* = \int_0^\infty n^*(u)\,\mathrm{d}u$ and we recall that ρ^* is the global cell density. The quantity $F(u,c)$ in (4.5) is defined by

$$F(u,c) := -\int_{u^*}^{u} f(\bar{u},c)\,\mathrm{d}\bar{u}. \tag{4.6}$$

The lower bound of integration is arbitrary as it can always be absorbed into the constant A. For convenience, we choose u^* to be the point at which $F(u,c^*)$ has a

global minimum, so that the global minimum is $F = 0$. The point u^* is also a linearly stable equilibrium of f in the sense

$$0 = \frac{\partial F}{\partial u}(u^*, c^*) = -f(u^*, c^*), \tag{4.7a}$$

$$0 > \frac{\partial^2 F}{\partial u^2}(u^*, c^*) = -\frac{\partial f}{\partial u}(u^*, c^*). \tag{4.7b}$$

We remark that a global minimum is guaranteed to exist since F is increasing as $u \to \infty$, decreasing at $u = 0$ by virtue of (4.3), and continuous. We assume for now that u^* is unique; however, we will later drop this assumption when considering quasi-steady states. We note that (4.5) is exact; no approximations have been made.

In the limit $\varepsilon \to 0$, the steady-state (4.5) is exponentially localised around each local minimum of F. However, the dominant contribution to n^* is from the global minimum since

$$\frac{n^*(u_0)}{n^*(u^*)} = \exp\left[-\frac{F(u_0, c^*)}{\varepsilon}\right] = \text{E.S.T.}, \tag{4.8}$$

where u_0 is any other local minimiser of $F(u, c^*)$ and E.S.T. denotes exponentially small terms. We therefore ignore the exponentially small contribution from the local minima and calculate A from $\rho^* = \int_0^\infty n^*(u)\,\mathrm{d}u$ using Laplace's method. Using Eq. (A.9) from Appendix A, we find

$$n^*(u) = \rho^* \sqrt{-\frac{f_u(u^*, c^*)}{2\pi\varepsilon}}\left[1 + \mathcal{O}(\varepsilon)\right] \exp\left[-\frac{F(u, c^*)}{\varepsilon}\right], \tag{4.9}$$

where $f_u := \frac{\partial f}{\partial u}$. The $\mathcal{O}(\varepsilon)$ terms in the above are due to the fact that $F(u, c^*)$ is not a quadratic in u as was the case for the kinetics in the previous chapter, cf. (3.6)–(3.8).

Our next task is to determine u^* and c^*. To this end, we substitute (4.9) into (4.4b) and apply Laplace's method to the integral term, which yields

$$c^* = \frac{\alpha(u^*)\rho^*}{\beta} + \mathcal{O}(\varepsilon), \tag{4.10}$$

where again the $\mathcal{O}(\varepsilon)$ terms are due to non-quadratic F and nonlinear α. Eqs. (4.7a) and (4.10) constitute an algebraic system that can in principle be solved for u^* and c^*. We restrict our attention to reaction kinetics for which there are $M > 1$ distinct solutions of Eqs. (4.7a) and (4.10). For a steady-state, we emphasize that solutions u^* that do not correspond to the global minimum of $F(u, c^*)$ must be discarded since (4.10) was derived under this assumption.

Even though the system (4.7a) and (4.10) has multiple solutions, the steady-state density n^* is exponentially localised around a single point[1]. Physically this

[1]This is due to our earlier assumption below Eq. (4.7) that u^* is unique.

corresponds to all cells effectively having the same internal state. In principle, each steady-state can be analysed separately through a linear stability analysis, which is qualitatively similar to the analysis from the previous chapter. We therefore ask whether it is possible to have a quasi-steady (slowly varying in time) solution in which n^* is localised around multiple points.

With this in mind, we observe that ε effectively fixes the relative number of cells in each local minimum of $F(u, c^*)$, as seen from (4.8). However, when $\varepsilon = 0$ there is a solution of (4.4a) of the form

$$n^*(u) = \sum_{\ell=1}^{M} \rho_\ell \delta(u - u_\ell), \tag{4.11a}$$

where the constants $\rho_1, \ldots, \rho_M$ satisfy $\sum_\ell \rho_\ell = \rho^*$ but are otherwise arbitrary and can be considered additional model parameters. We note that Eq. (4.11a) is a solution of (4.4a) in the weak sense[2]. The concentrations $u_1, \ldots, u_M$, in combination with c^*, satisfy the algebraic system

$$f(u_\ell, c^*) = 0, \quad \ell = 1, \ldots, M, \tag{4.11b}$$

$$\beta c^* = \sum_{\ell=1}^{M} \alpha(u_\ell)\rho_\ell, \tag{4.11c}$$

where the u_ℓ's are taken to be distinct. The steady-state (4.11) has M parameters $(\rho_1, \ldots, \rho_M)$ that control the number of cells in each state. We seek to construct an analog of (4.11) for finite ε so that our analytical techniques from the previous chapter are available. Such a construction cannot be a steady-state since it is not of the form (4.5), which is exact.

Motivated by the above discussion, we now seek quasi-steady solutions of (4.4). We construct the state $n_q(u)$ and c_q as follows

$$n_q(u) = A_\ell \exp\left[-\frac{F_\ell(u, c_q)}{\varepsilon}\right] + \text{E.S.T.}, \qquad U_\ell \le u < U_{\ell+1}, \quad \ell = 0, \ldots, M-1, \tag{4.12a}$$

$$c_q = \frac{1}{\beta}\int_0^\infty \alpha(u) n_q(u, t)\,\mathrm{d}u + \text{E.S.T}, \tag{4.12b}$$

where F_ℓ is defined analogously to F as

$$F_\ell(u, c) := -\int_{u_\ell}^{u} f(\bar{u}, c)\,\mathrm{d}\bar{u}, \tag{4.13}$$

[2]That is, if we require $\int_0^\infty \frac{d}{du}\left[f(u, c^*)n^*\right]\Psi(u)\,\mathrm{d}u = 0$ for all smooth test functions Ψ, then after integration by parts we see that (4.11a) is a solution by the sifting property of the Dirac-delta function.

and $U_1, \ldots, U_{M-1}$ are the $M-1$ local maxima[3] of F_ℓ, while $U_0 = 0$ and $U_M = \infty$. We assume that the U_ℓ's and u_ℓ's are well-separated in the sense $|U_{\ell+1} - U_\ell| \sim |u_\ell - U_\ell| \gg \mathcal{O}(\sqrt{\varepsilon})$ so that the discontinuities in the leading-order term of n_q are exponentially small. Consequently, we include exponentially small terms in (4.12) so that overall n_q is continuous. The constants A_ℓ determine the fraction of the population in each of the piecewise states, and are defined through

$$\rho_\ell := \int_{U_\ell}^{U_{\ell+1}} n_q(u)\,\mathrm{d}u, \tag{4.14}$$

which can be evaluated using Laplace's method to give

$$A_\ell = \rho_\ell \sqrt{-\frac{f_u(c_q, u_\ell)}{2\pi\varepsilon}}\left[1 + \mathcal{O}(\varepsilon)\right]. \tag{4.15}$$

A further application of Laplace's method to the integral in (4.12b) leads to

$$\beta c_q = \sum_{\ell=1}^{M} \alpha(u_\ell)\rho_\ell + \mathcal{O}(\varepsilon). \tag{4.16}$$

As flagged above, we no longer require that the global minimum of $F_\ell(u, c_q)$ is unique since we include the $\mathcal{O}(1)$ contributions to (4.16) from all local minima; the global minimum now has no special significance. Next, the fact that u_ℓ are local minima of $F(u, c_q)$ requires

$$f(u_\ell, c_q) = 0, \quad \ell = 1, \ldots, M, \tag{4.17}$$

so that in principle (4.16) and (4.17) can be solved for u_ℓ and c. Eqs. (4.12a) and (4.16)–(4.17) are consistent with (4.11) in the formal limit $\varepsilon \to 0$, as desired.

We now observe that on each of the intervals $(U_\ell, U_{\ell+1})$, Eq. (4.12) satisfies the steady-state problem (4.4) up to all algebraic orders of ε. However, there is clearly a large disagreement with the exact steady-state (4.5) because $n^*(u)$ is exponentially small near u_ℓ, but $n_q(u)$ is $\mathcal{O}(\varepsilon^{-1/2})$. We therefore conclude that (4.12) is a quasi-steady state in which A_ℓ's are slowly varying functions of time. We expect that the A_ℓ's vary over an exponentially long timescale since (4.12) fails to satisfy the steady-state problem (4.4) by an exponentially small amount.

Before continuing, we remark that M in (4.11) is not necessarily the same as our previous definition as the number of solutions of the algebraic system (4.7a) and

[3]Since the F_ℓ's differ by a constant, they share critical points. Moreover, there are exactly $M-1$ local maxima of $F_\ell(u, c_q)$ since the M local minima must be separated by exactly one local maximum. Additionally F is decreasing at $u = 0$ and increasing as $u \to \infty$.

(4.10). In fact, depending on the specific functional form of f, it may be fairly non-trivial to work out since it can in principle depend on the choice of ρ_ℓ (which in turn depend on M). We will assume $M = 2$ for the linear stability analysis, however our asymptotic theory does not crucially depend on M and can in principle be generalised. We illustrate how to work out M by way of a simple example in the final section of this chapter.

4.1.2 Stability Analysis

In the previous section, we constructed spatially uniform, quasi-steady solutions of (4.1). In order to detect the onset of motility-induced patterning, we seek to understand how these states respond to small spatially-dependent perturbations. Since the quasi-steady solutions vary over an exponentially long timescale, we restrict our attention to instabilities that arise on a much faster $\mathcal{O}(1)$ timescale.

As mentioned above, we consider the case $M = 2$ for which n_q is exponentially localised around two distinct states, which we denote by u_- and u_+. In this case, the quasi-steady solution (4.12a) and (4.15)–(4.17) can be written as

$$n_q(u) = \begin{cases} \rho_- \sqrt{\dfrac{f_u^-}{2\pi\varepsilon}} \left[1 + \mathcal{O}(\varepsilon)\right] \exp\left[-\dfrac{F_-(u, c_q)}{\varepsilon}\right] + \text{E.S.T.}, & 0 \le u < U, \\ \rho_+ \sqrt{\dfrac{f_u^+}{2\pi\varepsilon}} \left[1 + \mathcal{O}(\varepsilon)\right] \exp\left[-\dfrac{F_+(u, c_q)}{\varepsilon}\right] + \text{E.S.T.}, & U \le u < \infty, \end{cases} \tag{4.18a}$$

$$c_q = \frac{1}{\beta}\left(\alpha_- \rho_- + \alpha_+ \rho_+\right) + \mathcal{O}(\varepsilon), \tag{4.18b}$$

$$f(u_\pm, c_q) = 0, \tag{4.18c}$$

where $\alpha_\pm := \alpha(u_\pm)$, $f_u^\pm := f_u(u_\pm, c_q)$, and $F_\pm$ is defined by

$$F_\pm(u, c) := -\int_{u_\pm}^{u} f(\bar{u}, c)\, \mathrm{d}\bar{u}. \tag{4.19}$$

Here $U \in (u_-, u_+)$ is the unique local maximum of $F_\pm$ and we recall that $u_- < u_+$ are the local minima. The quantities $\rho_\pm$ are defined by

$$\rho_- := \int_0^U n_q(u)\, \mathrm{d}u, \quad \rho_+ := \int_U^\infty n_q(u)\, \mathrm{d}u, \tag{4.20}$$

and satisfy $\rho_- + \rho_+ = \rho^*$. They vary exponentially slowly in time, but we suppress the time-dependence for convenience.

We now introduce perturbations to the quasi-steady state (4.18) in the form

$$n(\mathbf{x},u,t) = n_q(u) + \delta\eta(u)e^{i\mathbf{k}\cdot\mathbf{x}+\sigma t}, \qquad c(\mathbf{x},t) = c_q + \delta C e^{i\mathbf{k}\cdot\mathbf{x}+\sigma t}. \tag{4.21}$$

Here, $\mathbf{k}$ is the wavenumber of the perturbation and σ the growth rate. Here $0 < \delta \ll 1$ measures the size of the perturbation. Similar to our analysis from the previous chapter, $\mathbf{k}$ has only the allowed values

$$\mathbf{k} = \left(\frac{\pi\ell}{\mathcal{L}_x}, \frac{\pi m}{\mathcal{L}_y}\right)^T, \tag{4.22}$$

where ℓ and m are non-negatives integers not both equal to zero. Next, we substitute (4.21) into (4.1) and neglect $\mathcal{O}(\delta^2)$ terms. Since n_q and c_q satisfy (4.4) only up to exponentially small terms (in ε), the coefficient of δ^0 is not exactly zero as it would be for a perturbation around a true steady-state. There is a contribution from the exponentially small terms in (4.18) as well as from the time-derivatives of n_q and c_q, all of which are exponentially small. We therefore choose δ much larger than these exponentially small terms (but still $\delta \ll 1$) so that the $\mathcal{O}(\delta)$ terms are dominant. At leading-order we therefore obtain

$$\varepsilon\frac{d^2\eta}{du^2} - \frac{d}{du}\left[f(u,c_q)\eta\right] - (\sigma + \mathcal{D}(u)k^2)\eta - \frac{d}{du}\left[f_c(u,c_q)n^*(u)\right]C = 0, \tag{4.23a}$$

$$(\sigma + \beta + D_c k^2)C - \int_0^\infty \alpha(u)\eta(u)\,\mathrm{d}u = 0, \tag{4.23b}$$

where $f_c := \frac{\partial f}{\partial c}(u,c_q)$. We note that in contrast to the kinetics from the previous chapter, both partial derivatives $\frac{\partial f}{\partial u}$ and $\frac{\partial f}{\partial c}$ in general depend on u.

The unperturbed state is exponentially localised near $u = u_\pm$ for small ε; we expect the same to be true for the perturbation η. We therefore use a WKBJ-(Liouville-Green) type method in which we seek solutions of the form

$$\eta(u) \sim \begin{cases} \varepsilon^{-3/2} q_-(u) \exp\left[-\dfrac{F_-(u,c_q)}{\varepsilon}\right], & 0 \le u < U, \\ \varepsilon^{-3/2} q_+(u) \exp\left[-\dfrac{F_+(u,c_q)}{\varepsilon}\right], & U \le u < \infty, \end{cases} \tag{4.24}$$

where we neglect exponentially small terms and the $\varepsilon^{-3/2}$ prefactor is introduced for convenience so that $q_\pm = \mathcal{O}(C)$ as seen in (4.25) below. By substituting (4.24) into (4.23a), we obtain the following two equations for $q_\pm$

$$\varepsilon q_\pm'' + q_\pm' f(u,c_q) - \left(\sigma + \mathcal{D}(u)k^2\right) q_\pm = C\sqrt{\frac{-f_u^\pm}{2\pi}}\left[\rho_\pm f(u,c_q)f_c(u,c_q) + \varepsilon\rho_\pm\frac{\partial^2 f}{\partial u \partial c}(u,c_q)\right], \tag{4.25}$$

where the domain for the '$-$' equation is $u \in (0, U)$, and $u \in (U, \infty)$ for the '$+$' equation. We remark that the bracketed $\mathcal{O}(\varepsilon)$ terms in (4.18a) are constant and hence effectively perturb $\rho_\pm$ by $\mathcal{O}(\varepsilon)$. For simplicity, we have incorporated these terms into $\rho_\pm$ in (4.25) above. The boundary conditions that η must be exponentially small as $u \to 0, \infty$ imply that q_- is polynomially bounded as $u \to 0$ and that q_+ is polynomially bounded as $u \to \infty$. An additional boundary condition is needed for $q_\pm$ at $u = U$, which comes from imposing smoothness of η. We therefore require that both $q_\pm$ are polynomially bounded as $u \to U$, so that (4.24) is smooth at all algebraic orders of ε.

Following our methodology from the previous chapter, we seek solutions for the amplitudes $q_\pm$ in the form of a regular asymptotic series as follows

$$q_\pm(u) \sim \sum_{j=0}^{\infty} q_{j\pm}(u)\varepsilon^j, \tag{4.26}$$

where again the boundary conditions are that each $q_{j\pm}$ is polynomially bounded. To obtain governing equations for $q_{j\pm}$, we substitute (4.26) into (4.25) and equate terms at $\mathcal{O}(1)$ and $\mathcal{O}(\varepsilon)$, which gives

$$f(u, c_q)q'_{0\pm} - \left(\sigma + \mathcal{D}(u)k^2\right) q_{0\pm} = C\rho_\pm \sqrt{\frac{-f_u^\pm}{2\pi}} f(u, c_q) f_c(u, c_q), \tag{4.27a}$$

$$f(u, c_q)q'_{1\pm} - \left(\sigma + \mathcal{D}(u)k^2\right) q_{1\pm} = -q''_{0\pm} + C\rho_\pm \sqrt{\frac{-f_u^\pm}{2\pi}} \frac{\partial^2 f}{\partial u \partial c}(u, c_q). \tag{4.27b}$$

The counterpart of (4.27) for the canonical kinetics in the previous chapter is given in (3.19). Since $f(u_\pm, c_q) = 0$, solutions of (4.27) are non-smooth at $u_\pm$ in general. However, we argue that $q_{j\pm}$ are smooth due to the boundary conditions that $q_\pm$ are polynomially bounded. We base this argument on the Stokes' line calculation of the previous chapter for which it was found that solutions of (3.19) must be smooth in order for q to be polynomially bounded as $u \to 0, \infty$. We expect a similar calculation to yield an analogous result here. Namely, that each term in the expansion of q_- must be smooth in order for q_- to be polynomially bounded as $u \to 0, U$, and similarly for q_+. We expect that such an analysis would be slightly more complicated as the two Stokes' lines originating from $u_\pm$ would be curved in general (cf. [22]).

Motivated by the above discussion, we look for smooth solutions for $q_{0\pm}$ and $q_{1\pm}$ in the form of regular power series centred at $u = u_\pm$. We therefore expand $q_{0\pm}$ and $q_{1\pm}$ as

$$q_{j\pm} = \sum_{\ell=0}^{\infty} q_{j\pm}^{(\ell)}(u - u_\pm)^\ell, \tag{4.28}$$

and additionally Taylor expand $f(u, c_q)$ as well as $\mathcal{D}$ as

$$\mathcal{D}(u) = \sum_{\ell=0}^{\infty} \frac{\mathcal{D}_{\pm}^{(\ell)}}{\ell!}(u - u_{\pm})^{\ell}, \quad \mathcal{D}_{\pm}^{(\ell)} := \left.\frac{d^{\ell}}{du^{\ell}}\right|_{u=u_{\pm}} \mathcal{D}(u). \tag{4.29}$$

To calculate the coefficients $q_{j\pm}^{(\ell)}$, we substitute (4.28)–(4.29) into (4.27) and use standard power series methods to obtain the following recursion relations

$$q_{0\pm}^{(0)} = 0, \tag{4.30a}$$

$$q_{0\pm}^{(1)} = \rho_{\pm}\sqrt{-\frac{(f_u^{\pm})^3}{2\pi}}\frac{Cf_c^{\pm}}{\sigma + \mathcal{D}_{\pm}k^2 - f_u^{\pm}}, \tag{4.30b}$$

$$q_{0\pm}^{(2)} = \frac{-\rho_{\pm}\sqrt{\frac{-f_u^{\pm}}{2\pi}}\left(f_u^{\pm}f_{cu}^{\pm} + \frac{f_{uu}^{\pm}f_c^{\pm}}{2}\right)C - \left(\mathcal{D}_{\pm}'k^2 - \frac{f_{uu}^{\pm}}{2}\right)q_{0\pm}^{(1)}}{\sigma + \mathcal{D}_{\pm}k^2 - 2f_u^{\pm}}, \tag{4.30c}$$

$$q_{1\pm}^{(0)} = \frac{2q_{0\pm}^{(2)} - \rho_{\pm}\sqrt{\frac{-f_u^{\pm}}{2\pi}}f_{cu}^{\pm}C}{\sigma + \mathcal{D}_{\pm}k^2}, \tag{4.30d}$$

where $f_c^{\pm}$, $f_{uu}^{\pm}$, and $f_{cu}^{\pm}$ denote derivatives of f evaluated at $(u_{\pm}, c_q)$. We have shown only the coefficients required for a leading-order evaluation of the integral in (4.23b), but in principle we can straightforwardly calculate higher-order terms in both (4.26) and (4.28).

We now evaluate the integral in (4.23b) to leading-order in ε using Laplace's method. Using (A.9) from Appendix A, we obtain after some algebra

$$\begin{aligned}\int_0^{\infty} \alpha(u)\eta(u)\,\mathrm{d}u &= \sum_{j=\pm}\sqrt{\frac{2\pi}{-f_u}}\left[\alpha q_j - \frac{1}{2f_u}\frac{d^2}{du^2}(\alpha q_j) - \frac{f_{uu}}{(f_u)^2}\frac{d}{du}(\alpha q_j) + \mathcal{O}(\varepsilon)\right]\Bigg|_{u=u_j} \\ &= \sum_{j=\pm}\left[\rho_j f_c C\frac{\alpha'(\sigma + \mathcal{D}k^2) - \alpha\mathcal{D}'k^2}{(\sigma + \mathcal{D}k^2)(\sigma + \mathcal{D}k^2 - f_u)} + \mathcal{O}(\varepsilon)\right]\Bigg|_{u=u_j}. \end{aligned} \tag{4.31}$$

Finally, we put (4.31) into (4.23b) and collect terms at $\mathcal{O}(1)$, imposing that $C \neq 0$, to obtain the following algebraic equation for σ

$$\sigma + D_c k^2 + \beta = \sum_{j=\pm}\left[\rho_j f_c\frac{\alpha'(\sigma + \mathcal{D}k^2) - \alpha\mathcal{D}'k^2}{(\sigma + \mathcal{D}k^2)(\sigma + \mathcal{D}k^2 - f_u)}\right]\Bigg|_{u=u_j}. \tag{4.32}$$

Eq. (4.32) has five solutions in general since it can be rearranged into a fifth-order polynomial equation. If there are any solutions with $\mathrm{Re}(\sigma) > 0$, then the quasi-steady solution (4.18) is unstable to spatial perturbations on an $\mathcal{O}(1)$ timescale. We emphasize that the quasi-steady solution is always 'unstable' on an exponentially long timescale by virtue of it not being a true steady-state.

We emphasize that our analysis is valid for perturbations that are not exponentially small. This has the important implication that if the quasi-steady solution crosses through an instability threshold exponentially slowly, then the instability may not immediately manifest. This is due to the well-known phenomenon of slow passage through a bifurcation, or 'delayed' bifurcations [62]. The key idea is that if the system is initially perturbed at $t = 0$ in a stable parameter regime, where $\mathrm{Re}(\sigma) < 0$, then perturbations will decay exponentially in time. As n and c continuously transition between quasi-steady states with different ρ_+ and ρ_-, the system may move through a state in which $\mathrm{Re}(\sigma) = 0$ at some large time t. At this point, the initial perturbation has become exponentially small and our assumption on δ in (4.21) is no longer valid. The system however is still unstable and the perturbation will grow, provided that we remain in an unstable parameter regime. In the final section of this chapter, we illustrate this point by way of example.

We remark here that the second derivatives of f appeared at many intermediate stages of our analysis, but dropped out of the leading-order result for the eigenvalue (4.32). This is typical of linear stability analyses for ODEs and PDEs in general. We therefore could have initially assumed vanishing second derivatives of f and still obtained the correct eigenvalues; we will use this observation to simplify our analysis in the next section. It is noteworthy that the same is not true for the eigenfunction η, whose amplitude q depends on second derivatives of f at leading-order in ε, as can be seen from the quadratic coefficients for q_0 in (4.30c).

4.2 Two-Component Kinetics with Stable Equilibria

In this section, we consider another generalisation of our system to the case where the reaction kinetics involve multiple internal chemicals. Similar to kinetics with multiple equilibria, this is also a common feature of quorum sensing GRNs [25, 65, 89]. For simplicity, we will restrict our attention to the case of two internal species, i.e. $\mathbf{u} := (u_1, u_2)^T$, and reaction kinetics $\mathbf{f}(\mathbf{u}, c) := (f_1(\mathbf{u}, c), f_2(\mathbf{u}, c))^T$.

The governing equations for $n(\mathbf{x}, \mathbf{u}, t)$ and $c(\mathbf{x}, t)$ are

$$\frac{\partial n}{\partial t} = \mathcal{D}(\mathbf{u})\nabla^2_{\mathbf{x}} n + \varepsilon \nabla^2_{\mathbf{u}} n - \nabla_{\mathbf{u}} \cdot [\mathbf{f}(\mathbf{u}, c) n] \,, \tag{4.33a}$$

$$\frac{\partial c}{\partial t} = D_c \nabla^2_{\mathbf{x}} c - \beta c - \int_{\mathbb{R}^2_+} \alpha(\mathbf{u}) n(\mathbf{x}, \mathbf{u}, t) \, \mathrm{d}\mathbf{u}, \tag{4.33b}$$

where the domain of integration $\mathbb{R}^2_+$ in (4.33b) is the positive quadrant. We again impose no-flux boundary conditions, which read

$$[\varepsilon\nabla_{\mathbf{u}} n - \mathbf{f}(\mathbf{u}, c)n] \cdot \mathbf{N}_u \to 0, \quad \mathbf{u} \in \partial\mathbb{R}^2_+, \quad |\mathbf{u}| \to \infty, \tag{4.34a}$$

$$\nabla_{\mathbf{x}} n \cdot \mathbf{N}_x = \nabla_{\mathbf{x}} c \cdot \mathbf{N}_x = 0, \quad \mathbf{x} \in \partial\Omega, \tag{4.34b}$$

where $\partial\mathbb{R}^2_+$ denotes the boundary segments of $\mathbb{R}^2_+$ on $u_1 = 0$ and $u_2 = 0$, while $\mathbf{N}_u$ and $\mathbf{N}_x$ are respective unit normals on $\partial\mathbb{R}^2_+$ and $\partial\Omega$.

As before, the general approach is to determine spatially uniform steady-states and perform a linear stability analysis to detect the onset of patterning. We begin with the steady-state analysis. In general, there are quasi-steady solutions of (4.33); however, we restrict our analysis to the true steady-state for simplicity.

4.2.1 Spatially Uniform Steady-States

Let us denote the spatially uniform steady-states of (4.33) by $n^*(\mathbf{u})$ and c^*. Together, they satisfy

$$\varepsilon\nabla^2_{\mathbf{u}} n^* - \nabla_u \cdot [\mathbf{f}(\mathbf{u}, c^*)n^*] = 0, \tag{4.35a}$$

$$\beta c^* - \int_{\mathbb{R}^2_+} \alpha(\mathbf{u}) n^*(\mathbf{u}) \, \mathrm{d}\mathbf{u} = 0. \tag{4.35b}$$

In contrast to our previous analysis, we cannot find an exact solution of (4.35a) for $n^*(\mathbf{u})$. However, we still expect solutions to be exponentially localised near the point $\mathbf{u}^*$ where $\mathbf{f}(\mathbf{u}^*, c^*) = \mathbf{0}$. This is motivated from the observation that when $\varepsilon = 0$, Eq. (4.35a) has a solution (in a distributional sense) of the form $n^*(\mathbf{u}) = \rho^*\delta(\mathbf{u} - \mathbf{u}^*)$. As such, we seek a WKBJ solution in the regime $\varepsilon \ll 1$ of the form

$$n^*(\mathbf{u}) = S(\mathbf{u}) \exp\left(\frac{\phi(\mathbf{u})}{\varepsilon}\right), \tag{4.36}$$

where the amplitude S and phase ϕ are functions to be determined.

Next, we obtain governing equations for S and ϕ. We substitute (4.36) into (4.35a) and obtain

$$\frac{S}{\varepsilon}\left[\nabla_{\mathbf{u}}\phi \cdot (\nabla_{\mathbf{u}}\phi - \mathbf{f})\right] + \nabla_{\mathbf{u}} S \cdot (2\nabla_{\mathbf{u}}\phi - \mathbf{f}) + S\left(\nabla^2_{\mathbf{u}}\phi - \nabla_{\mathbf{u}} \cdot \mathbf{f}\right) + \varepsilon\nabla^2_{\mathbf{u}} S = 0. \tag{4.37}$$

The leading order $\mathcal{O}(\varepsilon^{-1})$ terms yield an equation for the phase given by

$$\nabla_{\mathbf{u}}\phi \cdot (\nabla_{\mathbf{u}}\phi - \mathbf{f}) = 0, \tag{4.38}$$

and the remaining terms constitute the amplitude equation:

$$\nabla_{\mathbf{u}} S \cdot (2\nabla_{\mathbf{u}}\phi - \mathbf{f}) + S\left(\nabla_{\mathbf{u}}^2\phi - \nabla_{\mathbf{u}} \cdot \mathbf{f}\right) + \varepsilon\nabla_{\mathbf{u}}^2 S = 0. \tag{4.39}$$

In contrast to the case with one internal chemical where $\mathbf{f}$ and $\mathbf{u}$ were scalars, in general there is no solution for ϕ that satisfies $\nabla_{\mathbf{u}}\phi = \mathbf{f}$. However, since n^* is exponentially localised around the local maximizers of ϕ, we only need a local representation of ϕ. Since the zeros of $\mathbf{f}$ are critical points of ϕ, as seen from (4.38), we have

$$\nabla_{\mathbf{u}}\phi(\mathbf{u}^*) = \mathbf{f}(\mathbf{u}^*, c^*) = \mathbf{0}. \tag{4.40}$$

Moreover, we can take the global maximum of ϕ to be zero without loss of generality since any non-zero value can be absorbed into S. We therefore seek a local quadratic form for ϕ as

$$\phi(\mathbf{u}) = \tilde{\mathbf{u}}^T \Phi \tilde{\mathbf{u}} + \mathcal{O}(|\tilde{\mathbf{u}}|^3), \quad \Phi := \begin{pmatrix} \phi_1 & \phi_2 \\ \phi_2 & \phi_3 \end{pmatrix}, \tag{4.41}$$

where we have introduced the shifted variable $\tilde{\mathbf{u}} := \mathbf{u} - \mathbf{u}^*$. Our next task is to determine the entries in the matrix Φ. To this end, we Taylor expand $\mathbf{f}$ as

$$\mathbf{f}(\mathbf{u}, c^*) = \mathbf{J}\tilde{\mathbf{u}} + \mathcal{O}(|\tilde{\mathbf{u}}|^2), \quad \mathbf{J} := \begin{pmatrix} \mu_{11} & \mu_{12} \\ \mu_{21} & \mu_{22} \end{pmatrix}, \tag{4.42}$$

where the Jacobian matrix $\mathbf{J}$ has entries $\mu_{ij} = \partial f_i/\partial u_j(\mathbf{u}^*, c^*)$. Substituting (4.41) and (4.42) into (4.38) and equating powers of $\mathbf{u}$ yields the following system of coupled quadratic equations

$$2\phi_1^2 + 2\phi_2^2 - \mu_{11}\phi_1 - \mu_{21}\phi_2 = 0, \tag{4.43a}$$

$$4\phi_2(\phi_1 + \phi_3) - \mu_{12}\phi_1 - (\mu_{11} + \mu_{22})\phi_2 - \mu_{21}\phi_3 = 0, \tag{4.43b}$$

$$2\phi_2^2 + 2\phi_3^2 - \mu_{12}\phi_2 - \mu_{22}\phi_3 = 0. \tag{4.43c}$$

For a system of coupled polynomial equations, Bézout's theorem states that the number of (complex-valued) solutions is equal to the product of the degrees of the polynomials, which for (4.43) is eight. Here we discard non-real solutions for ϕ since they correspond to rapid sign changes of n^*, and we demand physically realistic solutions where $n^*(u) > 0$. As we argue in Appendix B, seven of the solutions (including the trivial solution), are either complex-valued or have $\det\Phi = 0$ and require that $S(\mathbf{u})$ is non-smooth at $\mathbf{u}^*$ as we later show.

Fortunately, the relevant solution of (4.43) can be obtain analytically. We intuitively expect that that the local properties of n^* are related to the coefficients of the Jacobian $\mathbf{J}$. In the case where $\mu_{12} = \mu_{21}$, we would have a solution of (4.43) for

which $\phi_1 = \mu_{11}/2$ and $\phi_3 = \mu_{22}/2$. It turns out that if we guess a solution in the form $2(\phi_1 + \phi_3) = \operatorname{Tr}\mathbf{J}$ for the general case $\mu_{12} \neq \mu_{21}$, we can find one solution:

$$\phi_1 = \frac{\mu_{11}+\mu_{22}}{2}\left[\frac{\mu_{11}\left(\mu_{11}+\mu_{22}\right)+\mu_{21}(\mu_{21}-\mu_{12})}{\left(\mu_{11}+\mu_{22}\right)^2+\left(\mu_{21}-\mu_{12}\right)^2}\right], \tag{4.44a}$$

$$\phi_2 = \frac{\mu_{11}+\mu_{22}}{2}\left[\frac{\left(\mu_{11}\mu_{12}+\mu_{21}\mu_{22}\right)}{\left(\mu_{11}+\mu_{22}\right)^2+\left(\mu_{21}-\mu_{12}\right)^2}\right], \tag{4.44b}$$

$$\phi_3 = \frac{\mu_{11}+\mu_{22}}{2}\left[\frac{\mu_{22}\left(\mu_{11}+\mu_{22}\right)+\mu_{12}(\mu_{12}-\mu_{21})}{\left(\mu_{11}+\mu_{22}\right)^2+\left(\mu_{21}-\mu_{12}\right)^2}\right]. \tag{4.44c}$$

For this solution, the trace and determinant of Φ are related to the Jacobian as

$$\operatorname{Tr}\Phi := \phi_1 + \phi_3 = \frac{\operatorname{Tr}\mathbf{J}}{2}, \tag{4.45a}$$

$$\det\Phi := \phi_1\phi_3 - \phi_2^2 = \frac{(\operatorname{Tr}\mathbf{J})^2 \det\mathbf{J}}{4\left[(\operatorname{Tr}\mathbf{J})^2 + \Delta^2\right]}, \quad \Delta := \mu_{21} - \mu_{12}. \tag{4.45b}$$

This implies that the trace and determinant of Φ have the same respective signs as the trace and determinant of $\mathbf{J}$. Thus for $\mathbf{u}^*$ to be a local maximizer of $\phi(\mathbf{u})$, we must have

$$\operatorname{Tr}\mathbf{J} < 0, \quad \det\mathbf{J} > 0, \tag{4.46}$$

which is just the condition for $\mathbf{u}^*$ to be a stable steady-state of the ODE $\dot{\mathbf{u}} = \mathbf{f}(\mathbf{u}, c^*)$. In contrast, unstable steady-states do not maximise ϕ since they have one or both inequalities in (4.46) reversed.

Next, we determine the amplitude S in (4.36). We begin by expanding S in a regular asymptotic series as

$$S(\mathbf{u}) = S_0(\mathbf{u}) + \mathcal{O}(\varepsilon). \tag{4.47}$$

Now we substitute (4.47) into (4.39) and collect the leading-order terms, which yields

$$\nabla_{\mathbf{u}} S_0 \cdot (2\nabla_{\mathbf{u}}\phi - \mathbf{f}) + \left(\nabla_{\mathbf{u}}^2\phi - \nabla_{\mathbf{u}}\cdot\mathbf{f}\right) S_0 = 0. \tag{4.48}$$

Since n^* is exponentially small except near $\mathbf{u}^*$ where it is algebraic in ε, it is sufficient to also seek a local approximation for S_0. Thus we seek power series solutions of the form

$$S_0(\tilde{\mathbf{u}}) = S_0^{(0)} + \tilde{\mathbf{u}}^T\mathbf{S}_0^{(1)} + \mathcal{O}(|\tilde{\mathbf{u}}|^2), \tag{4.49}$$

where the coefficients $S_0^{(0)}$ and $\mathbf{S}_0^{(1)}$ are unknowns to be determined. We then substitute the local approximations (4.41) and (4.42) for ϕ and $\mathbf{f}$ into (4.48) and use standard methods to obtain equations for the coefficients. We find

$$\left(2\operatorname{Tr}\Phi - \operatorname{Tr}\mathbf{J}\right) S_0^{(0)} = 0, \tag{4.50a}$$

$$(4\Phi - \mathbf{J})\mathbf{S}_0^{(1)} = S_0^{(0)}\boldsymbol{\chi}, \tag{4.50b}$$

where the terms proportional to the third derivatives of ϕ and second derivatives of $\mathbf{f}$ have been denoted by $\boldsymbol{\chi}$ whose precise form will not be important for our subsequent analysis. Since $2\,\mathrm{Tr}\,\Phi = \mathrm{Tr}\,\mathbf{J}$, the first equation above is trivially satisfied, so $S_0^{(0)}$ is arbitrary. This is expected since (4.35a) only determines n^* (and hence S) up to a multiplicative constant; this constant is determined by the normalisation condition $\rho^* = \int_{\mathbb{R}^2_+} n^*(\mathbf{u})\,\mathrm{d}\mathbf{u}$. Eq. (4.50b) has a unique solution provided that the matrix $4\Phi - \mathbf{J}$ is non-singular. Using (4.44) we calculate that

$$\det(4\Phi - \mathbf{J}) = \det \mathbf{J} > 0, \tag{4.51}$$

so in principle $\mathbf{S}_0^{(1)}$ is uniquely determined once $S_0^{(0)}$ is fixed. We remark that $2\,\mathrm{Tr}\,\Phi - \mathrm{Tr}\,\mathbf{J}$ vanishes only for the solution in (4.44); for all other solutions (4.50) implies that $S_0 \equiv 0$ and consequently $S \equiv 0$. In order to obtain a non-trivial solution for S, we would then need to incorporate singular terms into (4.49).

We now determine $S_0^{(0)}$ using the normalisation condition

$$\rho^* = \int_{\mathbb{R}^2_+} n^*(\mathbf{u})\,\mathrm{d}\mathbf{u} = \int_{\mathbb{R}^2_+} S(\mathbf{u}) \exp\left(\frac{\phi(\mathbf{u})}{\varepsilon}\right)\,\mathrm{d}\mathbf{u}. \tag{4.52}$$

The form of the integrand again suggests an application of Laplace's method. Since ϕ is locally quadratic near its global maximum, we apply the version of Laplace's method given in Eq. (A.21) of Appendix A to evaluate the leading-order contribution to the integral. The dominant contribution to the integral is due to the local behaviour of n^* near the local maximum of ϕ, which we have taken to be zero in (4.41) without loss of generality. As such, the contributions from the the other local maxima are exponentially small. Laplace's method therefore yields

$$S_0^{(0)} = \frac{\rho^* \sqrt{\det \Phi}}{\pi\varepsilon} + \mathcal{O}(1), \tag{4.53}$$

and hence

$$n^*(\mathbf{u}) = \frac{\rho^* \sqrt{\det \Phi}}{\pi\varepsilon}\left(1 + \tilde{\mathbf{u}}^T(4\Phi - \mathbf{J})^{-1}\boldsymbol{\chi} + \mathcal{O}(|\tilde{\mathbf{u}}|^2, \varepsilon)\right) \exp\left(-\frac{\phi(\mathbf{u})}{\varepsilon}\right), \tag{4.54}$$

where ϕ is given in (4.41) and (4.44). We remark that (4.54) is valid for $\tilde{\mathbf{u}}$ in an inner region of $\mathcal{O}(\varepsilon^{1/2})$ thickness near the origin; everywhere else n^* is exponentially small.

Our next task is to determine $\mathbf{u}^*$ and c^*. To this end, we apply Laplace's method to the integral in (4.35b) to obtain

$$\beta c^* = \rho^* \alpha(\mathbf{u}^*) + \mathcal{O}(\varepsilon). \tag{4.55}$$

Eqs. (4.40) and (4.55) constitute an algebraic system that in principle can be solved for $\mathbf{u}^*$ and c^*. We note that there may be multiple solutions of this system, but they all correspond to true steady-states (rather than quasi-steady solutions).

4.2.2 Linear Stability Analysis

Next, we perform a linear stability analysis for the steady-states given in (4.40) and (4.54)–(4.55). Since there may be multiple solutions of the algebraic system (4.40) and (4.55), in principle our system admits quasi-steady solutions. Here we focus on the linear stability of the true steady-states.

As mentioned in the previous section, we expect that the second derivatives of $\mathbf{f}$ do not contribute to the linear stability. We therefore assume that the reaction kinetics $\mathbf{f}(\mathbf{u}, c)$ are linear in $\mathbf{u}$, which significantly simplifies the algebra throughout, as we shall see. We still allow $\mathbf{f}$ to be nonlinear in c. This assumption implies that all second derivatives of $\mathbf{f}$, except the mixed partial derivatives involving c are equal to zero.

When the reaction kinetics are linear in $\mathbf{u}$, our local approximation for the phase ϕ in our steady-state analysis is actually valid globally. In particular, the leading-order term in (4.41), with (4.44), is an exact solution of (4.38). This in turn implies that $S(\mathbf{u}) = \text{const.}$ is a exact solution of the amplitude equation (4.39) since by (4.45a),

$$\nabla_{\mathbf{u}}^2 \phi - \nabla_{\mathbf{u}} \cdot \mathbf{f} = 2 \operatorname{Tr} \Phi - \operatorname{Tr} \mathbf{J} = 0. \tag{4.56}$$

Overall, the steady-states are given by

$$n^*(\mathbf{u}) = \frac{\rho^* \sqrt{\det \Phi}}{\pi \varepsilon} \exp\left(-\frac{\phi(\mathbf{u})}{\varepsilon}\right) + \text{E.S.T.}, \tag{4.57a}$$

$$c^* = \frac{\rho^* \alpha(\mathbf{u}^*)}{\beta} + \mathcal{O}(\varepsilon), \tag{4.57b}$$

$$\mathbf{f}(\mathbf{u}^*, c^*) = \mathbf{0}, \tag{4.57c}$$

where ϕ is given by

$$\phi(\mathbf{u}) = \tilde{\mathbf{u}}^T \Phi \tilde{\mathbf{u}}, \quad \Phi := \begin{pmatrix} \phi_1 & \phi_2 \\ \phi_2 & \phi_3 \end{pmatrix}, \tag{4.57d}$$

with the entries ϕ_1, ϕ_2, and ϕ_3 given in (4.44). Note that the neglected terms in (4.57a), which come from the normalisation condition (4.52), are now exponentially small since ϕ is exactly quadratic. We remark that there still may be multiple solutions of the algebraic system (4.57b)–(4.57c) since $\mathbf{f}$ can be nonlinear in c. For the remainder of this section, we take c^* and $\mathbf{u}^*$ to be any one of these solutions.

We introduce perturbations to the steady-state (4.57) in the form

$$n(\mathbf{x}, \mathbf{u}, t) = n^*(\mathbf{u}) + \eta(\mathbf{u}) e^{i\mathbf{k}\cdot\mathbf{x} + \sigma t}, \quad c(\mathbf{x}, t) = c^* + C e^{i\mathbf{k}\cdot\mathbf{x} + \sigma t}. \tag{4.58}$$

Next, we substitute (4.58) into the governing equations (4.33) and retain up to linear terms in η and C. This yields

$$\varepsilon\nabla_{\mathbf{u}}^2\eta - \nabla_{\mathbf{u}}\cdot(\mathbf{f}(\mathbf{u},c^*)\eta) - \left(\sigma+\mathcal{D}k^2\right)\eta = C\nabla_{\mathbf{u}}\cdot\left(n^*\left.\frac{\partial\mathbf{f}}{\partial c}\right|_{c=c^*}\right), \tag{4.59a}$$

$$\left(\sigma + D_c k^2 + \beta\right)C - \int_{\mathbb{R}^2_+}\alpha(\mathbf{u})\eta(\mathbf{u})\,\mathrm{d}\mathbf{u} = 0. \tag{4.59b}$$

Since the unperturbed solution is exponentially localised near $\mathbf{u}^*$, we expect the same to be true of the perturbation η, so we seek WKBJ solutions of the form

$$\eta(\mathbf{u}) = \varepsilon^{-2}q(\mathbf{u})\exp\left(\frac{\phi(\mathbf{u})}{\varepsilon}\right), \tag{4.60}$$

where the phase ϕ is the same as for the steady-state. Substituting (4.60) into (4.59a) leads to

$$\varepsilon\nabla_{\mathbf{u}}^2 q + \nabla_{\mathbf{u}}q\cdot(2\nabla_{\mathbf{u}}\phi - \mathbf{f}) - \left(\sigma+\mathcal{D}k^2\right)q = \frac{C\rho^*\sqrt{\det\Phi}}{\pi}\left(\nabla_{\mathbf{u}}\phi\cdot\frac{\partial\mathbf{f}}{\partial c} + \varepsilon\nabla_{\mathbf{u}}\cdot\frac{\partial\mathbf{f}}{\partial c}\right), \tag{4.61a}$$

$$\left(\sigma + D_c k^2 + \beta\right)C = \varepsilon^{-2}\int_{\mathbb{R}^2_+}\alpha(\mathbf{u})q(\mathbf{u})\exp\left(\frac{\phi(\mathbf{u})}{\varepsilon}\right)\,\mathrm{d}\mathbf{u}. \tag{4.61b}$$

The boundary condition (4.34a) implies that q must be polynomially bounded for $\mathbf{u}\in\partial\mathbb{R}^2_+$ and $|\mathbf{u}|\to\infty$.

The goal now is to determine $q(\mathbf{u})$ so that we can evaluate the integral in (4.61b), and obtain an algebraic equation for the eigenvalue σ. To this end, we expand q in a regular asymptotic expansion in the form

$$q(\mathbf{u}) = q_0(\mathbf{u}) + \varepsilon q_1(\mathbf{u}) + \mathcal{O}(\varepsilon^2). \tag{4.62}$$

We obtain governing equations for q_0 and q_1 by inserting (4.62) into (4.61a) and collecting the $\mathcal{O}(1)$ and $\mathcal{O}(\varepsilon)$ terms; they read

$$\nabla_{\mathbf{u}}q_0\cdot(2\nabla_{\mathbf{u}}\phi - \mathbf{f}) - \left(\sigma+\mathcal{D}k^2\right)q_0 = \varepsilon C S_0\nabla_{\mathbf{u}}\phi\cdot\frac{\partial\mathbf{f}}{\partial c}, \tag{4.63a}$$

$$\nabla_{\mathbf{u}}q_1\cdot(2\nabla_{\mathbf{u}}\phi - \mathbf{f}) - \left(\sigma+\mathcal{D}k^2\right)q_1 = -\nabla_{\mathbf{u}}^2 q_0 + \frac{C\rho^*\sqrt{\det\Phi}}{\pi}\nabla_{\mathbf{u}}\cdot\frac{\partial\mathbf{f}}{\partial c}. \tag{4.63b}$$

In our previous analysis with a single internal chemical, we obtained analogous equations for q_0 and q_1, cf. Eq. (4.25). In those cases, we argued that q_0 and q_1 must be

smooth so that q was polynomially bounded, thereby satisfying the boundary conditions. We expect that the current situation is similar and therefore demand smooth solutions of (4.63) at $\mathbf{u}^*$. We therefore seek formal power series solutions of the form

$$q_0(\mathbf{u}) = c_0^{(0)} + \tilde{\mathbf{u}}^T \mathbf{c}_0^{(1)} + \tilde{\mathbf{u}} \mathbf{c}_0^{(2)} \tilde{\mathbf{u}} + \mathcal{O}(|\tilde{\mathbf{u}}|^3), \tag{4.64a}$$

$$q_1(\mathbf{u}) = c_1^{(0)} + \mathcal{O}(|\tilde{\mathbf{u}}|), \tag{4.64b}$$

where

$$\mathbf{c}_0^{(1)} := \begin{pmatrix} c_0^{(10)} \\ c_0^{(01)} \end{pmatrix}, \quad \mathbf{c}_0^{(2)} := \begin{pmatrix} c_0^{(20)} & \frac{1}{2} c_0^{(11)} \\ \frac{1}{2} c_0^{(11)} & c_0^{(02)} \end{pmatrix}, \tag{4.64c}$$

and we show only the terms required for a leading order evaluation of the integral in (4.61b). We now substitute (4.64) into (4.63) and collect powers of the components of $\tilde{\mathbf{u}}$. This yields the following recursion relations for the coefficients

$$c_0^{(0)} = 0, \tag{4.65a}$$

$$\left[\left(\sigma + \mathcal{D}_* k^2 \right) I_2 + \mathbf{J} - 4\Phi \right] \mathbf{c}_0^{(1)} = -\frac{2\rho^* C \sqrt{\det \Phi}}{\pi} \Phi \mathbf{f}_c^*, \tag{4.65b}$$

$$\left[\left(\sigma + \mathcal{D}_* k^2 \right) I_3 + \mathcal{J} \right] \tilde{\mathbf{c}}_0^{(2)} = -\frac{2\rho^* C \sqrt{\det \Phi}}{\pi} \tilde{\Phi} \boldsymbol{\mu}_c - \mathbf{B} \mathbf{c}_0^{(1)}, \tag{4.65c}$$

where I_k is the $k \times k$ identity matrix, the matrices $\mathcal{J}$, $\tilde{\Phi}$, and $\mathbf{B}$ are given by

$$\mathcal{J} := \begin{pmatrix} 2\mu_{11} - 8\phi_1 & \mu_{21} - 4\phi_2 & 0 \\ 2\mu_{12} - 8\phi_2 & -\mu_{11} - \mu_{22} & 2\mu_{21} - 8\phi_2 \\ 0 & \mu_{12} - 4\phi_2 & 2\mu_{22} - 8\phi_3 \end{pmatrix}, \tag{4.65d}$$

$$\tilde{\Phi} := \begin{pmatrix} \phi_1 & \phi_2 & 0 & 0 \\ \phi_2 & \phi_1 & \phi_3 & \phi_2 \\ 0 & 0 & \phi_2 & \phi_3 \end{pmatrix}, \tag{4.65e}$$

$$\mathbf{B} := \begin{pmatrix} \mathcal{D}_{u_1}^* k^2 & 0 \\ \mathcal{D}_{u_2}^* k^2 & \mathcal{D}_{u_1}^* k^2 \\ 0 & \mathcal{D}_{u_2}^* k^2 \end{pmatrix}, \tag{4.65f}$$

where $\mathcal{D}_{u_j}^* := \frac{\partial \mathcal{D}}{\partial u_j}(\mathbf{u}^*)$, and finally the vectors $\tilde{\mathbf{c}}_0^{(2)}$ and $\boldsymbol{\mu}_c$ are defined by

$$\tilde{\mathbf{c}}_0^{(2)} := \begin{pmatrix} c_0^{(20)} & c_0^{(11)} & c_0^{(02)} \end{pmatrix}^T, \quad \boldsymbol{\mu}_c := \frac{\partial}{\partial c} \begin{pmatrix} \frac{\partial f_1}{\partial u_1} & \frac{\partial f_1}{\partial u_2} & \frac{\partial f_2}{\partial u_1} & \frac{\partial f_2}{\partial u_2} \end{pmatrix}^T \Big|_{(\mathbf{u}^*, c^*)}. \tag{4.65g}$$

The linear systems (4.65b)–(4.65c) have a unique solution provided that the coefficient matrices on the LHS are non-singular. In the case of (4.65b), the determinant of the coefficient matrix vanishes if, and only if, $\sigma + \mathcal{D}_* k^2$ is an eigenvalue of $4\Phi - \mathbf{J}$. Using (4.44), we find

$$\operatorname{Tr}(4\Phi - \mathbf{J}) = \operatorname{Tr} \mathbf{J}, \quad \det(4\Phi - \mathbf{J}) = \det \mathbf{J}. \tag{4.66}$$

This implies that $4\Phi - \mathbf{J}$ has the same eigenvalues as $\mathbf{J}$, which we denote as $\lambda_{\mathbf{J}}^{\pm}$. It follows that the determinant of the coefficient matrix on the LHS of (4.65b) vanishes if, and only if, $\sigma = \lambda_{\mathbf{J}}^{\pm} - \mathcal{D}_* k^2$, which has a negative real part. A similar argument applies for (4.65c) where we find that the three eigenvalues of $\mathcal{J}$ are $\operatorname{Tr}\mathbf{J} \pm \sqrt{(\operatorname{Tr}\mathbf{J})^2 - 4\det\mathbf{J}}$ and $\operatorname{Tr}\mathbf{J}$, all of which have a negative real part. In all cases, singular coefficient matrices require $\operatorname{Re}(\sigma) < 0$. In order to detect linear instabilities, we proceed under the assumption that the coefficient matrices in (4.65b)–(4.65c) are non-singular. The linear systems in (4.65) therefore uniquely determine $\mathbf{c}_0^{(1)}$ and $\mathbf{c}_0^{(2)}$, but we omit explicit formulas for brevity.

Next, we evaluate the leading-order contribution to the integral in (4.61b) using Laplace's method. We use the variant (A.17) from Appendix A since the phase ϕ is exactly quadratic. We obtain

$$\begin{aligned}\int_{\mathbb{R}^2_+} \alpha(\mathbf{u})\eta(\mathbf{u})\,\mathrm{d}\mathbf{u} =& \varepsilon^{-2}\int_{\mathbb{R}^2_+} \alpha(\mathbf{u})q(\mathbf{u})\exp\left(\frac{\phi(\mathbf{u})}{\varepsilon}\right)\mathrm{d}\mathbf{u} \\ =& \frac{\pi}{\sqrt{\det\Phi}}\left[\alpha(\mathbf{u}^*)q_1(\mathbf{u}^*) + \frac{1}{4}\left(\frac{\partial^2}{\partial{\xi_1}^2} + \frac{\partial^2}{\partial{\xi_2}^2}\right)\Big(\alpha(\mathbf{u}(\boldsymbol{\xi}))q_0(\mathbf{u}(\boldsymbol{\xi}))\Big)\right]\Bigg|_{\boldsymbol{\xi}=0} \\ &+ \mathcal{O}(\varepsilon),\end{aligned} \tag{4.67}$$

where $\boldsymbol{\xi} = (\xi_1, \xi_2)^T$ is defined through the linear transformation

$$\mathbf{u}(\boldsymbol{\xi}) = \mathbf{u}^* + V\operatorname{diag}\left(-\frac{1}{\lambda_1}, -\frac{1}{\lambda_2}\right)\boldsymbol{\xi}, \tag{4.68}$$

with $\lambda_{1,2}$ being the eigenvalues of Φ and the corresponding columns of the matrix V being the orthonormal eigenvectors of Φ (which must be ordered so they form a right-handed basis). We can rewrite the RHS of (4.67) in terms of the coefficients of q_0 and q_1 using (4.64a)–(4.64b). We additionally eliminate $\boldsymbol{\xi}$ with (4.68) and the quantities related to Φ using (4.44). After some algebra, we find that the $\mathcal{O}(1)$ term in (4.67) simplifies to

$$\begin{aligned}\frac{\pi}{\sqrt{(\det\mathbf{J})^3}\operatorname{Tr}\mathbf{J}}\Bigg[&\alpha^*\Big(\operatorname{Tr}\mathbf{J}\det\mathbf{J}c_1^{(0)} - (\mu_{22}\operatorname{Tr}\mathbf{J} + \mu_{12}\Delta)\,c_0^{(11)} + (\mu_{11}\mu_{12} + \mu_{21}\mu_{22})\,c_0^{(12)} \\ &- (\mu_{11}\operatorname{Tr}\mathbf{J} - \mu_{21}\Delta)\,c_0^{(22)}\Big) + \alpha_{u_1}^*\Big((\mu_{11}\mu_{12} + \mu_{21}\mu_{22})\,c_0^{(2)} \\ &- (\mu_{22}\operatorname{Tr}\mathbf{J} + \mu_{12}\Delta)\,c_0^{(1)}\Big) + \alpha_{u_2}^*\Big((\mu_{11}\mu_{12} + \mu_{21}\mu_{22})\,c_0^{(1)} \\ &- (\mu_{11}\operatorname{Tr}\mathbf{J} - \mu_{21}\Delta)\,c_0^{(1)}\Big)\Bigg],\end{aligned} \tag{4.69}$$

where we recall that $\Delta := \mu_{21} - \mu_{12}$, while $\alpha^*_{u_1}$ and $\alpha^*_{u_2}$ are given by

$$\alpha^*_{u_j} := \frac{\partial \alpha}{\partial u_j}(\mathbf{u}^*, c^*), \quad j = 1, 2. \tag{4.70}$$

We now solve the linear system (4.65b)–(4.65c) for the coefficients $c_j^{(\ell)}$ and substitute the result into (4.69). A straightforward, but lengthy calculation leads to

$$\begin{aligned}\int_{\mathbb{R}^2_+} \alpha(\mathbf{u})\eta(\mathbf{u})\,\mathrm{d}\mathbf{u} =& \frac{\rho^* \left(R_{\pi/2}\mathbf{f}_c^*\right)^T \left[(\sigma + \mathcal{D}_* k^2) I_2 - \mathbf{J}\right] R_{\pi/2}}{(\sigma + \mathcal{D}_* k^2)(\sigma + \mathcal{D}_* k^2 - \lambda_{\mathbf{J}}^-)(\sigma + \mathcal{D}_* k^2 - \lambda_{\mathbf{J}}^+)} \\ &\times \left[(\sigma + \mathcal{D}_* k^2)\nabla_{\mathbf{u}}\alpha^* - \alpha^* \nabla_{\mathbf{u}} \mathcal{D}^* k^2\right] + \mathcal{O}(\varepsilon),\end{aligned} \tag{4.71}$$

where the matrix $R_{\pi/2}$ is an anti-clockwise rotation by $\pi/2$ in the plane.

Finally, we impose that $C \neq 0$ and substitute (4.71) into (4.61b). After rearranging, we obtain at leading order in ε

$$\sigma + D_c k^2 + \beta = \frac{\rho^* \left(R_{\pi/2}\mathbf{f}_c^*\right)^T \left[(\sigma + \mathcal{D}_* k^2) I_2 - \mathbf{J}\right] R_{\pi/2} \left[(\sigma + \mathcal{D}_* k^2)\nabla_{\mathbf{u}}\alpha^* - \alpha^* \nabla_{\mathbf{u}} \mathcal{D}^* k^2\right]}{(\sigma + \mathcal{D}_* k^2)(\sigma + \mathcal{D}_* k^2 - \lambda_{\mathbf{J}}^-)(\sigma + \mathcal{D}_* k^2 - \lambda_{\mathbf{J}}^+)}, \tag{4.72}$$

which constitutes a fourth-order polynomial equation for the eigenvalue σ in terms of the basic model parameters. If there is any solution with $\mathrm{Re}(\sigma) > 0$, then the steady-state (4.57) is unstable to spatial perturbations.

We remark that even though the eigenvalues $\lambda_{\mathbf{J}}^{\pm}$ of $\mathbf{J}$ are complex-valued in general, solutions of (4.72) come in complex-conjugate pairs. Moreover, the denominator does not vanish since $\sigma + \mathcal{D}_* k^2$ is not an eigenvalue of $\mathbf{J}$ as we showed earlier, and we ignore the uninteresting case where $\sigma = -\mathcal{D}_* k^2 < 0$.

As expected, the non-zero second derivatives of $\mathbf{f}$ do not appear in the leading-order equation for the eigenvalue (4.72). Thus for the purpose of linear stability, we could have initially assumed without loss of generality that the mixed partials of $\mathbf{f}$ involving c are zero. We expect this to extend to all second derivatives of $\mathbf{f}$, which we did assume to be zero. Note that as expected, the eigenfunction η does depend on second derivatives, as seen from Eq. (4.65) for the quadratic coefficients of q_0.

4.3 Oscillatory Kinetics

In this section, we consider GRN reaction kinetics with oscillatory solutions (limit cycles). Examples include Fitzhugh-Nagumo and Sel'Kov kinetics [79], as well as populations of *Dictyostelium* where collective oscillations of chemical signal can occur [41] . As mentioned in the Introduction, this work is also related to the problem

of oscillator synchronisation in QS systems. For simplicity, we will restrict our attention to a well-mixed system, although it would be interesting to investigate spatial structure in the future. We comment on the modifications that would be necessary for such an analysis at the end of Chapter 6.

As we will see, our analysis for this class of kinetics is complicated by several factors. First, the spatially uniform steady-states have more structure than in previous sections. In particular, they are not exponentially localised at a single point. This in turn changes the form of the perturbations in the linear stability analysis. Secondly, we find that the spatially uniform state can be unstable to uniform perturbations, even when the underlying limit cycle is stable. Through numerical solution of the governing equations, we will show that this leads to partial oscillator synchronisation.

The setup for this section is similar to that of the previous section. We assume two internal species $\mathbf{u} = (u, v)^T$ and reaction kinetics $\mathbf{f}(\mathbf{u}, c)$. The governing equations for the structured density $n(\mathbf{u}, t)$ and AI concentration $c(t)$ are

$$\frac{\partial n}{\partial t} = \varepsilon \nabla_{\mathbf{u}}^2 n - \nabla_{\mathbf{u}} \cdot [\mathbf{f}(\mathbf{u}, c) n], \tag{4.73a}$$

$$\frac{dc}{dt} = -\beta c + \int_{\mathbb{R}_+^2} \alpha(\mathbf{u}) n(\mathbf{u}, t) \, \mathrm{d}\mathbf{u}, \tag{4.73b}$$

where we hereafter suppress the subscript $\mathbf{u}$ on the nabla operators. We also have no-flux boundary conditions in state space given by

$$[\varepsilon \nabla_{\mathbf{u}} n - \mathbf{f}(\mathbf{u}, c) n] \cdot \mathbf{N}_u \to 0, \quad \mathbf{u} \in \partial \mathbb{R}_+^2, \quad |\mathbf{u}| \to \infty. \tag{4.74}$$

For the reaction kinetics, we assume that there is a stable limit cycle, denoted $\mathbf{u}^*(t; c)$ of the ODE $\dot{\mathbf{u}} = \mathbf{f}(\mathbf{u}, c)$ for all fixed values of c. The properties of the limit cycle (period, shape in phase space, etc.) are allowed to depend on c. We further assume that all steady-states of $\mathbf{f}$ are unstable so that solutions of the form (4.57) are impossible. In order to develop some intuition about the solution structure, we briefly consider a simple example before proceeding to the general case.

4.3.1 Toy Example: Normal Form Kinetics without Quorum Sensing

As a first example, we consider the simplest possible choice of reaction kinetics that admits a unique, stable limit cycle. This is the normal form ODE for a Hopf bifurcation, which reads

$$\mathbf{f}(\mathbf{u}) = \begin{pmatrix} (\mu - \tilde{u}^2 - \tilde{v}^2)\tilde{u} - \omega\tilde{v} \\ (\mu - \tilde{u}^2 - \tilde{v}^2)\tilde{v} + \omega\tilde{u} \end{pmatrix}, \tag{4.75}$$

where μ and ω are positive constants, and $\tilde{\mathbf{u}} := \mathbf{u} - \mathbf{u}_0$ for some shift $\mathbf{u}_0$ such that the internal concentrations $\mathbf{u}$ are positive on the limit cycle. We hereafter drop the tilde notation for convenience. The limit cycle of the corresponding ODE $\dot{\mathbf{u}} = \mathbf{f}(\mathbf{u})$ lies on the circle $u^2 + v^2 = \mu$ and the period of oscillation is $2\pi/\omega$. For now we do not allow $\mathbf{f}$ to depend on c, so there is effectively no QS. Thus Eq. (4.73a) is decoupled from Eq. (4.73b), allowing us to focus on the solution structure for n as this will be crucial for the general case. We also impose the initial condition

$$n(\mathbf{u}, 0) = N_0(\mathbf{u}), \tag{4.76}$$

where we assume for simplicity that N_0 is smooth, which will be relevant shortly. We also require $n_0 \to 0$ sufficiently fast as $|\mathbf{u}| \to \infty$ so that n is normalisable.

It is convenient to change variables into polar coordinates as $u = r\cos\theta$ and $v = r\sin\theta$, as well as transform into a rotating frame

$$\psi = \theta - \omega t. \tag{4.77}$$

We also make use of the shorthand $n(r, \psi, t) = n(\mathbf{u}, t)$ and $N_0(r, \theta) = N_0(\mathbf{u})$. Changing variables to r and ψ in the governing equation (4.73a) yields

$$\frac{\partial n}{\partial t} + (\mu - r^2) r \frac{\partial n}{\partial r} = (4r^2 - 2\mu)n + \varepsilon \nabla^2_{\mathbf{u}} n, \tag{4.78}$$

where the Laplacian in the rotating frame is given by

$$\nabla^2_{\mathbf{u}} n = \frac{\partial^2 n}{\partial r^2} + \frac{1}{r}\frac{\partial n}{\partial r} + \frac{1}{r^2}\frac{\partial^2 n}{\partial \psi^2}. \tag{4.79}$$

For boundary conditions, we have from (4.74)

$$\varepsilon \frac{\partial n}{\partial r} - (\mu - r^2) r n \to 0, \quad r \to \infty, \tag{4.80}$$

as well as 2π-periodic boundary conditions in ψ. Eq. (4.78) has an (exact) axisymmetric steady-state $n^*(r)$ given by

$$n^*(r) = A \exp\left(\frac{\phi(r)}{\varepsilon}\right), \quad \phi(r) := -\frac{(r^2 - \mu)^2}{4}, \tag{4.81}$$

where the constant A is determined from normalisation. We see therefore that n^* is exponentially localised to $r = \sqrt{\mu}$, exactly the region in phase space occupied by the limit cycle.

The existence of a steady-state localised at $r = \sqrt{\mu}$ is somewhat surprising given that (4.75) has only the unstable steady-state at $r = 0$. The steady-state (4.81) represents a state in which the cells are individually oscillating such that the distribution

of internal states is constant, i.e. the cell-level oscillations are desynchronised. We refer to this state as asynchronous. In order to better understand the mechanism of desynchronisation, we now consider the general time-dependent solution of (4.78) in the limit of small noise $\varepsilon \ll 1$.

We begin by considering the unperturbed problem with $\varepsilon = 0$. It reads

$$\frac{\partial n_0}{\partial t} + (\mu - r^2) r \frac{\partial n_0}{\partial r} = (4r^2 - 2\mu) n_0. \tag{4.82}$$

Eq (4.78) is a linear PDE for n_0 which can be solved with the method of characteristics. The general solution is

$$n_0(r, \psi, t) = \begin{cases} N_0(r_0(r,t), \psi) \left(\frac{\mu e^{\mu t}}{r^2 + (\mu - r^2) e^{2\mu t}} \right)^2, & r < r_\infty(t), \\ 0, & r \geq r_\infty(t), \end{cases} \tag{4.83}$$

where $r_0(r,t)$ and $r_\infty(t)$ are given by

$$r_0(r,t) = \frac{\sqrt{\mu} r}{\sqrt{(\mu - r^2) e^{2\mu t} + r^2}}, \tag{4.84a}$$

$$r_\infty(t) = \sqrt{\frac{\mu}{1 - e^{-2\mu t}}}. \tag{4.84b}$$

Eq. (4.84a) defines a one-parameter family of characteristic curves $r = r(t)$ that sweep out the region of spacetime $r \leq r_\infty(t)$, and have $r(0) = r_0$. The curve $r_\infty(t)$ is the specific curve in this family satisfying $r \to \infty$ as $t \to 0^+$. Another one-parameter family of characteristic curves given by $r(t) = r_\infty(t - t_0)$, where $t \geq t_0 > 0$, sweep out the region $r > r_\infty(t)$. We plot the characteristic curves in Figure 4.1.

The solution (4.83) is smooth for all finite t since N_0 is smooth. However, we observe that n_0 grows exponentially in time on $r = \sqrt{\mu}$, and decays exponentially everywhere else. This causes large localised gradients to appear at long times. We therefore expect the perturbed problem (with finite ε) to develop an internal boundary layer in which the gradients are smoothed out *via* diffusion. This is consistent with the exponentially localised steady-state (4.81) where the width of the internal layer is $\mathcal{O}(\varepsilon^{1/2})$.

When ε is non-zero, (4.83) is the leading-order solution of the perturbed problem (4.78) in the outer region where $|r - \sqrt{\mu}|^2 \gg \mathcal{O}(\varepsilon)$. At large times n_0 is exponentially small in the outer region. We now show that the same is true for the correction terms. Let us expand the outer solution n in a regular asymptotic series as

$$n(r, \psi, t) = n_0(r, \psi, t) + \sqrt{\varepsilon} n_1(r, \psi, t) + \mathcal{O}(\varepsilon). \tag{4.85}$$

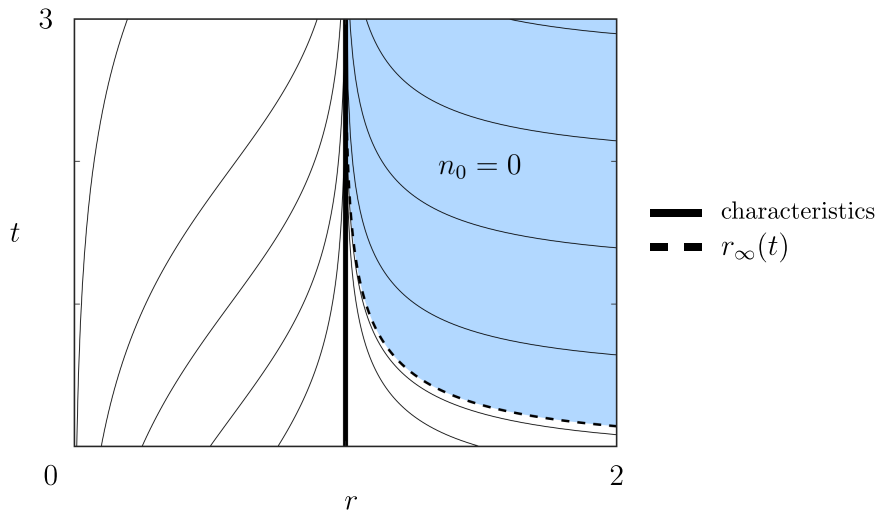

Figure 4.1: Characteristic curves for (4.82) with $\mu = 1$. The leading order outer solution n_0 is given by (4.83) in the unshaded region, and vanishes in the shaded. region. The dashed curve separating the two regions is $r_\infty(t)$, which satisfies $r_\infty \to \infty$ as $t \to 0^+$. The thick solid line is $r = \sqrt{\mu} = 1$.

Using the above in (4.78) leads to

$$\frac{\partial n_1}{\partial t} + (\mu - r^2) r \frac{\partial n_1}{\partial r} - (4r^2 - 2\mu) n_1 = \nabla^2 n_0. \tag{4.86}$$

The general solution for n_1 is a linear combination of a particular solution and a homogeneous solution n_0. Since n_0 is exponentially small away from $r = \sqrt{\mu}$ at long times, the same is true of both the homogeneous solution and the RHS of (4.86). Thus overall n_1 is exponentially small away from $r = \sqrt{\mu}$. Since the governing equation (4.78) is linear, the same will be true for higher order terms in the expansion (4.85).

We now consider an inner region near $r = \sqrt{\mu}$ at long times. From the steady-state solution (4.81), we know that the 'lengthscale' of the inner region is $\mathcal{O}(\varepsilon^{1/2})$. To deduce the long timescale, we note that the profile in r of the leading-order outer solution n_0 evolves on $\mathcal{O}(1)$ times, but the profile in ψ is constant. Since the lengthscale of ψ in the inner region is $\mathcal{O}(1)$, and the 'diffusion coefficient' in (4.78) is ε, we expect a timescale of $\mathcal{O}(\varepsilon^{-1})$ in order to balance the time-derivative and the diffusion term $\varepsilon \frac{\partial^2 n}{\partial \psi^2}$ from the Laplacian. We therefore define inner variables z and T through the scalings

$$t = \varepsilon^{-1} T, \quad z = \frac{r - \sqrt{\mu}}{\sqrt{\varepsilon}}, \tag{4.87}$$

and write the inner solution as

$$n(r, \theta, t) := \tilde{n}(z, \psi, T). \tag{4.88}$$

To obtain the inner problem, we insert the inner region quantities (4.87) and (4.88) into the governing equation (4.78). We obtain

$$\varepsilon\frac{\partial\tilde{n}}{\partial T}+\left(\sqrt{\frac{\mu}{\varepsilon}}+z\right)\left(\varepsilon z^2-2\sqrt{\mu\varepsilon}z\right)\frac{\partial\tilde{n}}{\partial z}=\left(2\mu+8\sqrt{\mu\varepsilon}z+\varepsilon z^2\right)\tilde{n}+\frac{\partial^2\tilde{n}}{\partial z^2}+\sqrt{\frac{\varepsilon}{\mu}}\frac{\partial\tilde{n}}{\partial z}+\frac{\varepsilon}{\mu}\left(\frac{\partial^2\tilde{n}}{\partial\psi^2}-\frac{\partial\tilde{n}}{\partial z}\right)+\mathcal{O}(\varepsilon^{3/2}), \tag{4.89}$$

which is valid for $z\in\mathbb{R}$, $\psi\in[0,2\pi)$, and $T>0$. Since the outer solution is exponentially small at long times, matching requires that the same is true of the inner solution as $|z|\to\infty$. The boundary conditions are therefore that $\tilde{n}\to 0$ as $|z|\to\infty$ for $T=\mathcal{O}(1)$ and that $\tilde{n}$ is 2π-periodic in ψ for all $T>0$. Next, we expand the inner solution as

$$\tilde{n}(z,\psi,T)\sim\tilde{n}_0(z,\psi,T)+\sqrt{\varepsilon}\tilde{n}_1(z,\psi,T)+\varepsilon\tilde{n}_2(z,\psi,T)+\mathcal{O}(\varepsilon^{3/2}), \tag{4.90}$$

and substitute into (4.89). Collecting the leading order terms at $\mathcal{O}(1)$ results in

$$\frac{\partial^2\tilde{n}_0}{\partial z^2}+2\mu\frac{\partial}{\partial z}(z\tilde{n}_0)=0, \tag{4.91}$$

which has the solution

$$\tilde{n}_0(z,\psi,T)=N(\psi,T)e^{-\mu z^2}, \tag{4.92}$$

where we have used the matching condition that $\tilde{n}_0\to 0$ as $|z|\to\infty$. The amplitude $N(\psi,T)$ is an unknown to be determined through consideration of higher order terms in (4.90).

Next we substitute (4.90) into (4.89) and collect terms at $\mathcal{O}(\varepsilon^{1/2})$. This leads to

$$\frac{\partial^2\tilde{n}_1}{\partial z^2}+2\mu\frac{\partial}{\partial z}(z\tilde{n}_1)=-\left(3z^2\sqrt{\mu}+\frac{1}{\sqrt{\mu}}\right)\frac{\partial\tilde{n}_0}{\partial z}-8\sqrt{\mu}z\tilde{n}_0. \tag{4.93}$$

Because the LHS operator has a non-trivial nullspace given by $\tilde{n}_0$, there is no solution for $\tilde{n}_1$ unless the RHS satisfies a solvability condition (by the Fredholm Alternative). In particular, the RHS must be orthogonal to the nullspace of the adjoint of the LHS operator. It is relatively straightforward to show that this nullspace is spanned by a constant; thus we must have

$$\int_{-\infty}^{\infty}\left[-\left(3z^2\sqrt{\mu}+\frac{1}{\sqrt{\mu}}\right)\frac{\partial\tilde{n}_0}{\partial z}-8\sqrt{\mu}z\tilde{n}_0\right]\mathrm{d}z=0, \tag{4.94}$$

for a solution $\tilde{n}_1$ to exist. Note that we have again used the matching condition that the inner solution be exponentially small as $|z|\to\infty$. For $\tilde{n}_0$ given in (4.92),

the integrand in (4.94) is odd so the solvability condition is trivially satisfied. We therefore proceed to next order to determine $N(\psi, T)$. To analyse this problem, we will need $\tilde{n}_1$ explicitly. Solving (4.93) yields

$$\tilde{n}_1(z, \psi, T) = \left[\hat{N}(\psi, T) - \sqrt{\mu} N(\psi, T) z^3\right] e^{-\mu z^2}, \tag{4.95}$$

where $\hat{N}(\psi, T)$ is an arbitrary function that will not be relevant in our analysis.

Now we collect terms at $\mathcal{O}(\varepsilon)$ in (4.89) after inserting the expansion (4.90) and obtain

$$\begin{aligned}\frac{\partial^2 \tilde{n}_2}{\partial z^2} + 2\mu \frac{\partial}{\partial z}\left(z\tilde{n}_2\right) = &- \frac{1}{\mu}\frac{\partial^2 \tilde{n}_0}{\partial \psi^2} + \frac{\partial \tilde{n}_0}{\partial T} - 4z^2\tilde{n}_0 + \left(\frac{z}{\mu} - z^3\right)\frac{\partial \tilde{n}_0}{\partial z} \\ &- \left(3\sqrt{\mu}z^2 + \frac{1}{\sqrt{\mu}}\right)\frac{\partial \tilde{n}_1}{\partial z} - 8\sqrt{\mu} z \tilde{n}_1.\end{aligned} \tag{4.96}$$

Invoking the solvability condition that the RHS integrates to zero results in

$$\mu \frac{\partial N}{\partial T} = \frac{\partial^2 N}{\partial \psi^2}, \tag{4.97}$$

which determines $N(\psi, T)$ once $N(\psi, 0)$ is known (with periodic boundary conditions). In principle, $N(\psi, 0)$ can be obtained by matching with the solution at earlier times. Here, we are only concerned with the evolution of N over the long $\mathcal{O}(\varepsilon^{-1})$ timescale. We therefore omit the calculation of $N(\psi, 0)$. Overall, we have that N smooths out over an $\mathcal{O}(\varepsilon^{-1})$ timescale so that at steady-state $\tilde{n}_0$ in (4.92) is independent of ψ. We note that the exact steady-state in (4.81) can be expressed in terms of the inner variable z as

$$n^*(\sqrt{\mu} + \sqrt{\varepsilon} z) = A e^{-\mu z^2} + \mathcal{O}(\sqrt{\varepsilon}), \tag{4.98}$$

consistent with the leading-order inner solution (4.92) as $T \to \infty$. This also justifies our earlier scalings in (4.87) for the inner variables.

The leading order outer and inner solutions in (4.83), (4.92), (4.97) can be used to understand desynchronisation in our toy system. Suppose initially that the system is partially synchronised with a (smooth) initial condition where the distribution of internal states is localised (with $\mathcal{O}(1)$ gradients) in state space (see Figure 4.2). Over a short $\mathcal{O}(1)$ time interval, the system evolves without desynchronising according to the outer solution in (4.83) and shown in Figure 4.2. Over long $\mathcal{O}(\varepsilon^{-1})$ times, the distribution n spreads out over the length of the limit cycle, representing desynchronisation. At steady-state the cells are uniformly distributed along the limit cycle, but still exponentially localised. Thus in the absence of QS, the system tends to

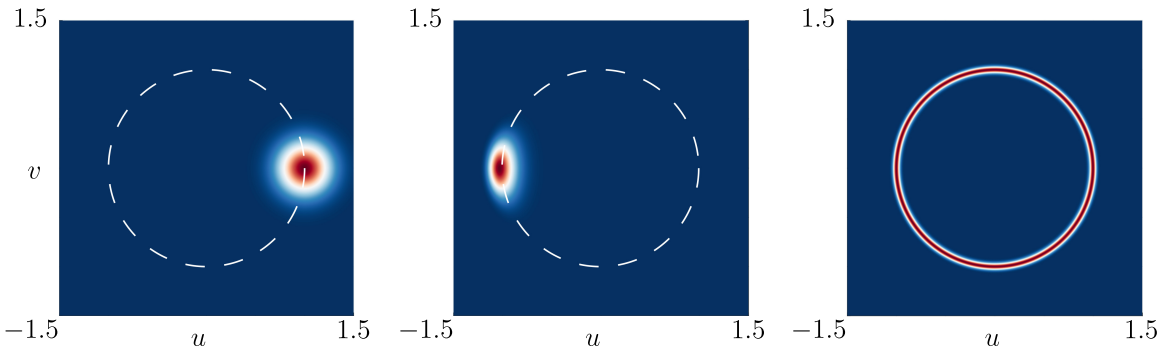

Figure 4.2: Evolution of the n for the normal form kinetics (4.75). Left: initial condition. Middle: outer solution in (4.83) after half of a period ($t = \pi/\omega$). Right: asynchronous steady-state (4.81). Initially, the distribution of internal states is chosen to be normally distributed in state space. Over short $\mathcal{O}(1)$ time intervals the distribution follows the state-space trajectories, eventually becoming localised to the limit cycle $r = \sqrt{\mu}$ (white dashed line). On long $\mathcal{O}(\varepsilon^{-1})$ timescales, state-space diffusion causes desynchronisation, represented by n spreading out in the θ-coordinate. Parameter values are $\mu = 1$, $\omega = 10$, and $\varepsilon = 10^{-3}$.

desynchronise due to the small noise in the GRN kinetics, represented by diffusion in state space (with diffusion coefficient ε). We note that the axial symmetry of the steady-state does not signify an asynchronous state, but is rather a consequence of axial symmetry in the reaction kinetics.

4.3.2 General Theory

In the previous section, we considered a toy example where the reaction kinetics are decoupled from QS. We saw that this leads to desynchronisation over a long timescale due to noise in the GRN. The goal now is to investigate whether QS can induce synchronisation for more general reaction kinetics with a limit cycle. We tackle this by investigating the linear stability of the desynchronised state, rather than considering the full time-dependent system as we did for our toy problem. If the steady-state is linearly unstable, we expect the system to synchronise, which we later verify through numerical simulation.

Before proceeding, we recall the assumptions about our general reaction kinetics $\mathbf{f}$. We assume $\mathbf{u}^*(t; c)$ to be a stable limit cycle of the ODE system $\dot{\mathbf{u}} = \mathbf{f}(\mathbf{u}, c)$ for fixed c. For simplicity we assume that the limit cycle exists for all c, but with properties (period, shape, etc.) that are c-dependent. Moreover, we take $\mathbf{u}^*$ to be a known quantity; determined either analytically or numerically from the cell-level ODE system. Finally, we assume that $\mathbf{f}$ has no stable steady-states.

In our toy example, we saw that the spatially uniform solution is exponentially localised to the limit cycle $r = \text{const}$. It is natural therefore to seek a coordinate system (ζ, s) for which the limit cycle lies on (say) $\zeta = \text{const}$. To this end, we parametrise the limit cycle $\mathbf{f}$ in terms of arc-length s. For convenience, we orient the curve such that it is consistent with the intracellular dynamics, i.e. increasing arc-length s corresponds to increasing time t in the trajectory $\mathbf{u}^*(t; c)$. We therefore introduce the shorthand $\mathbf{u}^*(t; c) = \mathbf{u}^*(s; c)$. Since the limit cycle forms a closed curve, $\mathbf{u}^*$ must be periodic in the arc-length coordinate. So $\mathbf{u}^*(s + S; c) = \mathbf{u}^*(s; c)$ where $S = S(c)$ is the perimeter of $\mathbf{u}^*$. The unit tangent vector to $\mathbf{u}^*$ is given by

$$\hat{\mathbf{T}}(s; c) = \frac{\partial \mathbf{u}^*}{\partial s}, \tag{4.99}$$

and we take the unit normal $\hat{\mathbf{N}}(s; c)$ such that $(\hat{\mathbf{T}}, \hat{\mathbf{N}})$ form a right-handed basis. The Serret-Frenet formulas for a plane curve relate $\hat{\mathbf{T}}$ and $\hat{\mathbf{N}}$ to their derivatives as

$$\frac{\partial \hat{\mathbf{T}}}{\partial s} = \kappa \hat{\mathbf{N}}, \quad \frac{\partial \hat{\mathbf{N}}}{\partial s} = -\kappa \hat{\mathbf{T}}, \tag{4.100}$$

where $\kappa = \kappa(s; c)$ is the (signed) curvature of $\mathbf{u}^*$. We assume that the limit cycle does not have sharp corners or kinks in the sense $\kappa = \mathcal{O}(1)$. We additionally assume that the limit cycle does not pass near to itself in the sense that $|\mathbf{u}^*(s, c) - \mathbf{u}^*(s', c)| = \mathcal{O}(1)$ when $|s - s'| = \mathcal{O}(1)$.

4.3.2.1 Asynchronous States

We begin our analysis by finding asynchronous states, which correspond to steady-state solutions of (4.73). We denote these states by $n^*(\mathbf{u})$ and c^*. Next we make the change of variables

$$\mathbf{u} = \mathbf{u}^*(s; c^*) + \zeta \hat{\mathbf{N}}(s; c^*), \tag{4.101}$$

where the arc-length coordinates (ζ, s) are the new independent variables. The coordinate ζ measures the signed distance from the limit cycle $\mathbf{u}^*(s; c^*)$, which lies on $\zeta = 0$. The change of variables (4.101) is only defined sufficiently close to the limit cycle, i.e. for $|\zeta| < 1/|\kappa(s; c^*)|$. Since we assume that $\kappa = \mathcal{O}(1)$, we expect n^* to be exponentially small outside of the domain where arc-length coordinates are valid. We remark that since $\mathbf{u}^*$ in general depends on c, we define the changes of variables (4.101) at steady-state only. Otherwise the transformation would be time-dependent, thereby posing problems for the linear stability analysis.

Next, we transform the steady version of (4.73a) using (4.101), which yields

$$\varepsilon \nabla^2 n^* - \nabla \cdot [\mathbf{f}(\zeta, s, c^*) n^*] = 0, \tag{4.102a}$$

where we calculate that the Laplacian ∇^2 and divergence $\nabla\cdot$ in arc-length coordinates are given by

$$\nabla^2 n^* = \frac{\partial^2 n^*}{\partial \zeta^2} + \frac{1}{(1-\zeta\kappa)^2}\frac{\partial^2 n^*}{\partial s^2} - \frac{\kappa}{1-\zeta\kappa}\frac{\partial n^*}{\partial \zeta} + \frac{\zeta\kappa'}{(1-\zeta\kappa)^3}\frac{\partial n^*}{\partial s}, \tag{4.102b}$$

$$\nabla\cdot\mathbf{f} = \hat{\mathbf{N}}\cdot\frac{\partial \mathbf{f}}{\partial \zeta} + \frac{\hat{\mathbf{T}}}{1-\zeta\kappa}\frac{\partial \mathbf{f}}{\partial s}. \tag{4.102c}$$

Here we again use the shorthand $\mathbf{f}(\mathbf{u}, c^*) = \mathbf{f}(\zeta, s, c^*)$ and $\kappa' = \frac{\partial \kappa}{\partial s}$. For boundary conditions, we require n^* to be S-periodic in s. The boundary conditions (4.74) cannot be imposed in arc-length coordinates since the boundaries lie in $|\zeta| > 1/|\kappa|$ in general. However, our analysis of the toy problem suggests that it is sufficient to impose that n^* is exponentially small away from the limit cycle, i.e. for $|\zeta| \gg \mathcal{O}(\varepsilon^{1/2})$.

Before proceeding, we derive some useful relations that are implied by $\mathbf{u}^*$ being a stable limit cycle. First, we rewrite the ODE system $\dot{\mathbf{u}} = \mathbf{f}(\mathbf{u}, c^*)$, which defines the limit cycle, in arc-length coordinates. That is, if $\mathbf{u}$, s and ζ depend on t in (4.101), then we differentiate with respect to t and obtain

$$\mathbf{f} = \dot{\mathbf{u}} = \left(\frac{\partial \mathbf{u}^*}{\partial s} + \zeta\frac{\partial \hat{\mathbf{N}}}{\partial s}\right)\dot{s} + \hat{\mathbf{N}}\dot{\zeta}. \tag{4.103}$$

As long as $\zeta \neq 1/\kappa$, we can invert this relation using the Serret-Frenet formulas (4.100) to obtain

$$\dot{s} = \frac{\hat{\mathbf{T}}(s; c^*)\cdot\mathbf{f}(\zeta, s, c^*)}{1-\zeta\kappa(s; c^*)}, \tag{4.104a}$$

$$\dot{\zeta} = \hat{\mathbf{N}}(s; c^*)\cdot\mathbf{f}(\zeta, s, c^*). \tag{4.104b}$$

Now from (4.101), we see that in order for $\mathbf{u}^*(t; c^*)$ to be a periodic solution of $\dot{\mathbf{u}} = \mathbf{f}(\mathbf{u}, c^*)$, we must have that $\dot{\zeta} = 0$ on $\zeta = 0$. That is, if we set the initial condition to be some point on the limit cycle $\mathbf{u}^*$, then the trajectory must remain on the limit cycle for all future times. Furthermore, there can be no point on $\mathbf{u}^*$ that is a steady-state. Thus we require $\dot{s} \neq 0$ on $\zeta = 0$. These two conditions can be stated as

$$\hat{\mathbf{N}}(s; c^*)\cdot\mathbf{f}(0, s, c^*) = 0, \quad \tilde{\omega}(s; c^*) := \hat{\mathbf{T}}(s; c^*)\cdot\mathbf{f}(0, s, c^*) \neq 0, \quad \forall s. \tag{4.105}$$

We note that $\tilde{\omega}$ is positive for all s since it cannot change sign and the arc-length coordinate increases with time on the limit cycle (i.e. $\dot{s} > 0$ on $\zeta = 0$). Additionally, for sufficiently small ζ, we can Taylor expand the RHS of (4.104b) to obtain

$$\hat{\mathbf{N}}(s; c^*)\cdot\mathbf{f}(\zeta, s, c^*) = \zeta\frac{\partial}{\partial \zeta}\bigg|_{\zeta=0}\left(\hat{\mathbf{N}}\cdot\mathbf{f}(\zeta, s, c^*)\right) + \mathcal{O}(\zeta^2) = \hat{\mathbf{N}}\cdot\mathbf{f}_\zeta\bigg|_{\zeta=0}\zeta + \mathcal{O}(\zeta^2), \tag{4.106}$$

where we use subscripts to denote derivatives. Since the limit cycle is assumed stable, it follows that

$$\hat{\mathbf{N}} \cdot \mathbf{f}_\zeta(0, s, c^*) < 0. \tag{4.107}$$

The identities (4.105), (4.107) will be useful in the following analysis.

Solutions of (4.102) cannot be computed analytically for general reaction kinetics. As such, we seek a WKBJ-type solution in the limit $\varepsilon \ll 1$. We therefore insert

$$n^*(\zeta, s) = Q(\zeta, s) \exp\left(\frac{\phi(\zeta, s)}{\varepsilon}\right), \tag{4.108}$$

into (4.102) and collect the leading-order $\mathcal{O}(\varepsilon^{-1})$ terms. This yields the following equation for the phase ϕ

$$\phi_\zeta^2 + \frac{\phi_s^2}{(1-\zeta\kappa)^2} - \left(\hat{\mathbf{N}} \cdot \mathbf{f}\right)\phi_\zeta - \frac{\hat{\mathbf{T}} \cdot \mathbf{f}\phi_s}{1-\zeta\kappa} = 0, \tag{4.109}$$

whereas the remaining terms give an equation for the amplitude Q

$$\varepsilon\nabla^2 Q + 2\left(Q_\zeta\phi_\zeta + \frac{Q_s\phi_s}{1-\zeta\kappa}\right) + Q\nabla^2\phi - \hat{\mathbf{N}} \cdot (\mathbf{f}Q)_\zeta - \frac{\hat{\mathbf{T}}}{1-\zeta\kappa} \cdot (\mathbf{f}Q)_s = 0. \tag{4.110}$$

Similar to the two-species kinetics from Section 4.2, we are not able to find an exact representation of the phase (cf. Eq. (4.38)). However, since we anticipate that n^* is exponentially localised around the curve $\zeta = 0$ (for all s), the phase ϕ must have a local maximum with respect to ζ. We therefore seek a local representation in the form

$$\phi(\zeta, s) = \phi_0(s)\zeta^2 + \phi_1(s)\zeta^3 + \dots, \tag{4.111}$$

where we absorb the constant term into the amplitude Q. The coefficients in (4.111) in general depend on s and cannot be expanded in Taylor series if we wish to find solutions which are uniformly valid along the limit cycle. We therefore insert the expansion (4.111) into (4.109) and Taylor expand the kinetics $\mathbf{f}$ in ζ only. After equating terms at powers of ζ, we obtain a Riccati ODE for ϕ_0

$$\tilde{\omega}\phi_0' - 4\phi_0^2 + 2\hat{\mathbf{N}} \cdot \mathbf{f}_\zeta\big|_{\zeta=0}\phi_0 = 0, \tag{4.112}$$

and a linear ODE for ϕ_1

$$\phi_1' - \frac{12\phi_0 - 3\hat{\mathbf{N}} \cdot \mathbf{f}_\zeta\big|_{\zeta=0}}{\tilde{\omega}}\phi_1 - \frac{\hat{\mathbf{T}} \cdot \mathbf{f}_\zeta\big|_{\zeta=0} + \kappa\hat{\mathbf{T}} \cdot \mathbf{f}\big|_{\zeta=0}}{\tilde{\omega}}\phi_0' - \frac{\hat{\mathbf{N}} \cdot \mathbf{f}_{\zeta\zeta}\big|_{\zeta=0}}{\tilde{\omega}}\phi_0 = 0, \tag{4.113}$$

where the identities in (4.105) have been used. To ease notation, we hereafter omit the evaluation bar at $\zeta = 0$. Because n^*, and hence ϕ, must be periodic in s, the

linear independence of terms in (4.111) implies that ϕ_0 and ϕ_1 must also be periodic. Moreover, we must have $\phi_0 < 0$ for all s in order for ϕ to have a local maximum at $\zeta = 0$.

Eq. (4.112) can be solved explicitly using the change of variables

$$v'(s) = -\frac{4v(s)}{\tilde{\omega}(s; c^*)}\phi_0(s). \tag{4.114}$$

This transforms (4.112) into the following second-order linear ODE for v

$$v'' = -\frac{2\hat{\mathbf{N}} \cdot \mathbf{f}_\zeta + \tilde{\omega}_s}{\tilde{\omega}} v'. \tag{4.115}$$

We solve (4.115) using standard methods and impose periodicity of $\phi_0(s)$ to fix one of the integration constants. Since $\phi_0 \propto v'/v$, the other constant of integration that controls the scaling of v does not affect ϕ_0. After solving for v, we use (4.114) to find ϕ_0. The result is

$$\phi_0(s) = -\frac{h(s)}{4\left[\int_0^s \frac{h}{\tilde{\omega}}\,\mathrm{d}t + \frac{\langle h/\tilde{\omega}\rangle}{h(S)-1}\right]}, \qquad h(s) := \exp\left(-\int_0^s \frac{2\hat{\mathbf{N}} \cdot \mathbf{f}_\zeta}{\tilde{\omega}}\right), \tag{4.116}$$

where we define the angle-bracket notation by

$$\langle \cdot \rangle := \int_0^S (\cdot)\,\mathrm{d}s. \tag{4.117}$$

We note that $\phi_0 < 0$ as required. This follows from the fact that $\tilde{\omega} > 0$ and $\hat{\mathbf{N}} \cdot \mathbf{f}_\zeta < 0$.

Next, we return to the amplitude equation in (4.110). We will only need the leading-order behaviour of Q for the linear stability analysis in the following section, so we expand Q in a regular asymptotic series as

$$Q(\zeta, s) \sim Q_0(\zeta, s) + \varepsilon Q_1(\zeta, s) + \dots. \tag{4.118}$$

Collecting powers of ε in (4.110), we obtain the following governing equation for Q_0

$$2\left(Q_{0\zeta}\phi_\zeta + \frac{Q_{0s}\phi_s}{1-\zeta\kappa}\right) + Q_0\nabla^2\phi - \hat{\mathbf{N}} \cdot (\mathbf{f}Q_0)_\zeta - \frac{\hat{\mathbf{T}}}{1-\zeta\kappa} \cdot (\mathbf{f}Q_0)_s = 0. \tag{4.119}$$

Since n^* is exponentially localised, we only need the local behaviour of Q_0 near $\zeta = 0$ for a leading-order solution. As such, we look for a solution in the form of a regular power series as

$$Q_0(\zeta, s) = a_0(s) + a_1(s)\zeta + \dots, \tag{4.120}$$

where we will need only the first two terms. Standard power series methods yield the following ODEs for a_0 and a_1:

$$-\hat{\mathbf{T}}\cdot\mathbf{f}a_0' + \left(2\phi_0 - \hat{\mathbf{N}}\cdot\mathbf{f}_\zeta - \hat{\mathbf{T}}\cdot\mathbf{f}_s\right)a_0 = 0, \tag{4.121a}$$

$$\begin{aligned}-\hat{\mathbf{T}}\cdot\mathbf{f}a_1' + \left(6\phi_0 - 2\hat{\mathbf{N}}\cdot\mathbf{f}_\zeta - \hat{\mathbf{T}}\cdot\mathbf{f}_s\right)a_1 = &\Big(- 6\phi_1 + 2\kappa\phi_0 + \hat{\mathbf{T}}\cdot\mathbf{f}_{s\zeta} + \kappa\hat{\mathbf{T}}\cdot\mathbf{f}_s \\ &+ \hat{\mathbf{N}}\cdot\mathbf{f}_{\zeta\zeta}\Big)a_0 + \left(\hat{\mathbf{T}}\cdot\mathbf{f}_\zeta + \kappa\hat{\mathbf{T}}\cdot\mathbf{f}\right)a_0'.\end{aligned} \tag{4.121b}$$

Both equations are linear and first order and can in principle be solved. The solution for a_0 is

$$a_0(s) = \frac{A}{\varepsilon^{1/2}}\exp\left[-\int_0^s \frac{\hat{\mathbf{N}}\cdot\mathbf{f}_\zeta - \tilde{\omega}' - 2\phi_0}{\tilde{\omega}}\,\mathrm{d}t\right], \tag{4.122}$$

where the $\mathcal{O}(\varepsilon^{-1/2})$ scaling is introduced for convenience so that the normalisation constant A is $\mathcal{O}(1)$ as seen in (4.127) below. We omit the formula for a_1 for brevity. The integral in (4.122) can be evaluated indirectly by rearranging the Riccati ODE (4.112) and integrating to obtain

$$\frac{1}{2}\log\left|\frac{\phi_0(s)}{\phi_0(0)}\right| = \int_0^s \frac{2\phi_0 - \hat{\mathbf{N}}(t;c^*)\cdot\mathbf{f}_\zeta(t,0,c^*)}{\tilde{\omega}(t;c^*)}\,\mathrm{d}t. \tag{4.123}$$

Hence (4.122) simplifies to

$$a_0(s) = \frac{A}{\tilde{\omega}(s;c^*)}\sqrt{\frac{|\phi_0(s)|}{\varepsilon}}. \tag{4.124}$$

Since ϕ_0 is known in principle, a_0 is now also known.

Overall, we have the leading order steady-state solution given by

$$n^*(\zeta,s) = \frac{A}{\varepsilon^{1/2}}\left(\frac{|\phi_0(s)|^{1/2}}{\tilde{\omega}(s;c^*)} + \mathcal{O}(\varepsilon)\right)\exp\left(\frac{\phi_0(s)\zeta^2}{\varepsilon}\right), \tag{4.125}$$

with ϕ_0 given in (4.116). The normalisation constant A is determined from

$$\rho^* = \int_{\mathbb{R}^2_+} n^*(\mathbf{u})\,\mathrm{d}\mathbf{u} = \int_0^S\int_{-\zeta_0}^{\zeta_0} n^*(\zeta,s)(1-\zeta\kappa)\,\mathrm{d}\zeta\mathrm{d}s + \text{E.S.T.}, \tag{4.126}$$

where ζ_0 is an $\mathcal{O}(1)$ constant such that $\zeta_0 < 1/|\kappa(s;c^*)|$ for all s. The domain of integration has been truncated in order to express the integral in arc-length coordinates. The error in doing so is exponentially small as n^* is exponentially localised to

$\zeta = 0$. Next, we use the version of Laplace's method in Eq. (A.9) of Appendix A to approximate the integral over ζ, leading to

$$A = \frac{\rho^*}{\sqrt{\pi}} \left\langle \frac{1}{\tilde{\omega}(s; c^*)} \right\rangle^{-1} + \mathcal{O}(\varepsilon). \tag{4.127}$$

Evaluating the integral over s requires explicitly knowing the functional dependence of $\tilde{\omega}(s; c^*)$ and $\phi_0(s)$ on s.

The last step in our steady-state analysis is to determine c^* from the steady version of (4.73b). Changing to arc-length coordinates, we have

$$c^* = \frac{1}{\beta} \int_{\mathbb{R}^2_+} \alpha(\mathbf{u}) n^*(u) \, \mathrm{d}\mathbf{u} = \int_0^S \int_{-\zeta_0}^{\zeta_0} \alpha(\zeta, s) n^*(\zeta, s)(1 - \zeta\kappa) \, \mathrm{d}\zeta \mathrm{d}s + \text{E.S.T.} \tag{4.128}$$

We again approximate the integral over ζ using Laplace's method and obtain

$$c^* = \frac{\rho^*}{\beta} \frac{\langle \alpha(0, s)/\tilde{\omega}(s; c^*) \rangle}{\langle 1/\tilde{\omega}(s; c^*) \rangle} + \mathcal{O}(\varepsilon). \tag{4.129}$$

Since $\tilde{\omega}$ depends on c^* in general, the leading order terms in the above constitute a nonlinear algebraic equation for c^*. In principle it can be solved, so we hereafter take c^* as a known quantity. The leading order steady-state is given by (4.125) and (4.129).

4.3.2.2 Onset of Synchronous Oscillations

The steady-state given in (4.125) and (4.129) represents an asynchronous system. To understand this intuitively, we observe that the distribution of internal states at the continuum level is constant in time and localised to the limit cycle. However, the internal states at the cell level are non-steady because the reaction kinetics $\mathbf{f}$ have no linearly stable steady-states. This implies that the oscillating internal states of the population are spread out over the limit cycle in such a way that the full distribution is steady. We now seek to determine whether the internal states can synchronise by performing a linear stability analysis around the asynchronous state.

The change of variables to arc-length coordinates in (4.101) was crucial in our analysis of the steady system. The same change of coordinates is not as helpful in the time-dependent system because c depends on time and we have defined the limit cycle of $\dot{\mathbf{u}} = \mathbf{f}(\mathbf{u}, c)$ for constant c. However, we can still make use of the same transformation if used at the correct point in the analysis.

We begin by introducing perturbations to the asynchronous steady-state (4.125) and (4.129), but crucially in the original Cartesian coordinate system. Hence, we seek solutions in the form

$$n(\mathbf{u},t) = n^*(\mathbf{u}) + \eta(\mathbf{u})e^{\sigma t}, \tag{4.130a}$$

$$c(t) = c^* + Ce^{\sigma t}, \tag{4.130b}$$

where η and C are the perturbations and σ is the growth rate. Substituting (4.130) into the governing equations (4.73) and retaining up to linear terms in η and C yields

$$\sigma\eta = \varepsilon\nabla^2\eta - \nabla\cdot\left[\mathbf{f}(\mathbf{u},c^*)\eta\right] - C\nabla\cdot\left[\mathbf{f}_c(\mathbf{u},c^*)n^*(\mathbf{u})\right], \tag{4.131a}$$

$$\sigma C = -\beta C + \int_{\mathbb{R}^2_+}\alpha(\mathbf{u})\eta(u)\,\mathrm{d}\mathbf{u}, \tag{4.131b}$$

with the boundary conditions

$$\left[\varepsilon\nabla_{\mathbf{u}}\eta - \mathbf{f}(\mathbf{u},c^*)\eta\right]\cdot\mathbf{N}_u \to 0, \mathbf{u}\in\partial\mathbb{R}^2_+, \quad |\mathbf{u}|\to\infty. \tag{4.131c}$$

After linearising to obtain (4.131), we observe that the kinetic terms depend on c^*, rather than c. It is therefore now appropriate to introduce arc-length coordinates. We use (4.101) in (4.131a) and obtain

$$\begin{aligned}\sigma\eta =&\varepsilon\left(\frac{\partial^2\eta}{\partial\zeta^2} + \frac{1}{(1-\zeta\kappa)^2}\frac{\partial^2\eta}{\partial s^2} - \frac{\kappa}{1-\zeta\kappa}\frac{\partial\eta}{\partial\zeta} + \frac{\zeta\kappa'}{(1-\zeta\kappa)^3}\frac{\partial\eta}{\partial s}\right)\\ &- \hat{\mathbf{N}}\cdot\frac{\partial}{\partial\zeta}\left[\mathbf{f}(\zeta,s,c^*)\eta\right] - \frac{1}{1-\zeta\kappa}\hat{\mathbf{T}}\cdot\frac{\partial}{\partial s}\left[\mathbf{f}(\zeta,s,c^*)\eta\right]\\ &- C\left[\hat{\mathbf{N}}\cdot\frac{\partial}{\partial\zeta}\left(\mathbf{f}_c(\zeta,s,c^*)n^*\right) + \frac{1}{1-\zeta\kappa}\hat{\mathbf{T}}\cdot\frac{\partial}{\partial s}(\mathbf{f}_c(\zeta,s,c^*)n^*)\right].\end{aligned} \tag{4.132}$$

Similar to the steady-state, we impose that the perturbation η is exponentially small for $\zeta = \mathcal{O}(1)$ and periodic in s. Since n^* is exponentially localised, we expect the same to be true of η. We therefore seek a WKBJ solution of the form

$$\eta(\zeta,s) = \varepsilon^{-3/2}q(\zeta,s)\exp\left(\frac{\phi(\zeta,s)}{\varepsilon}\right), \tag{4.133}$$

where the phase ϕ is the same as the steady-state in (4.125). Next, we substitute (4.133) and our WKBJ solution for the steady-state (4.108) into (4.132). The terms at $\mathcal{O}(\varepsilon^{-1})$ determine the phase ϕ; they read

$$\phi_\zeta^2 + \frac{\phi_s^2}{(1-\zeta\kappa)^2} - \left(\hat{\mathbf{N}}\cdot\mathbf{f}\right)\phi_\zeta - \frac{\hat{\mathbf{T}}\cdot\mathbf{f}\phi_s}{1-\zeta\kappa} = 0, \tag{4.134}$$

which, as expected, is identical to the phase equation (4.109) for the steady state. The remaining terms constitute a governing equation for the amplitude q:

$$\varepsilon\nabla^2 q + \left(2\phi_\zeta - \hat{\mathbf{N}}\cdot\mathbf{f}\right) q_\zeta + \left(\frac{2\phi_s}{1-\zeta\kappa} - \hat{\mathbf{T}}\cdot\mathbf{f}\right)\frac{q_s}{1-\zeta\kappa} + \left(\nabla^2\phi - \hat{\mathbf{N}}\cdot\mathbf{f}_\zeta - \frac{\hat{\mathbf{T}}\cdot\mathbf{f}_s}{1-\zeta\kappa} - \sigma\right) q$$
$$= C\left[\varepsilon\nabla\cdot(\mathbf{f}_c Q) + Q\mathbf{f}_c\cdot\left(\hat{\mathbf{N}}\phi_\zeta + \frac{\hat{\mathbf{T}}\phi_s}{1-\zeta\kappa}\right)\right]. \tag{4.135}$$

Our goal now is to determine q from (4.135) to a sufficient level of accuracy for a leading order evaluation of the integral in (4.131b). To this end, we expand q in a regular asymptotic series of the form

$$q(\zeta, s) = q_0(\zeta, s) + \varepsilon q_1(\zeta, s) + \mathcal{O}(\varepsilon^2). \tag{4.136}$$

Now we insert (4.136) into (4.135), and obtain at $\mathcal{O}(1)$

$$\left(2\phi_\zeta - \hat{\mathbf{N}}\cdot\mathbf{f}\right) q_{0\zeta} + \left(\frac{2\phi_s}{1-\zeta\kappa} - \hat{\mathbf{T}}\cdot\mathbf{f}\right)\frac{q_{0s}}{1-\zeta\kappa} + \left(\nabla^2\phi - \hat{\mathbf{N}}\cdot\mathbf{f}_\zeta - \frac{\hat{\mathbf{T}}\cdot\mathbf{f}_s}{1-\zeta\kappa} - \sigma\right) q_0$$
$$= CQ_0\mathbf{f}_c\cdot\left(\hat{\mathbf{N}}\phi_\zeta + \frac{\hat{\mathbf{T}}\phi_s}{1-\zeta\kappa}\right), \tag{4.137a}$$

and at $\mathcal{O}(\varepsilon)$

$$\left(2\phi_\zeta - \hat{\mathbf{N}}\cdot\mathbf{f}\right) q_{1\zeta} + \left(\frac{2\phi_s}{1-\zeta\kappa} - \hat{\mathbf{T}}\cdot\mathbf{f}\right)\frac{q_{1s}}{1-\zeta\kappa} + \left(\nabla^2\phi - \hat{\mathbf{N}}\cdot\mathbf{f}_\zeta - \frac{\hat{\mathbf{T}}\cdot\mathbf{f}_s}{1-\zeta\kappa} - \sigma\right) q_1$$
$$= -\nabla^2 q_0 + C\left[\nabla\cdot(\mathbf{f}_c Q_0) + Q_1\mathbf{f}_c\cdot\left(\hat{\mathbf{N}}\phi_\zeta + \frac{\hat{\mathbf{T}}\phi_s}{1-\zeta\kappa}\right)\right]. \tag{4.137b}$$

We remark that the term Q_1 from the steady-state expansion (4.118) appears in the RHS of (4.137b) above, but will not contribute to the final result as we later flag. Since η is exponentially localised, we expand q_0 and q_1 in regular power series centred at $\zeta = 0$ as

$$q_0(\zeta, s) = \frac{1}{\tilde{\omega}}\left[c_0^{(0)}(s) + c_0^{(1)}(s)\zeta + c_0^{(2)}(s)\zeta^2 + \mathcal{O}(\zeta^3)\right], \tag{4.138a}$$
$$q_1(\zeta, s) = \frac{1}{\tilde{\omega}}\left[c_1^{(0)}(s) + \mathcal{O}(\zeta)\right], \tag{4.138b}$$

where the factors of $\tilde{\omega}^{-1}$ are introduced to simplify (4.139) below. In (4.138) we show only the terms required for a leading-order evaluation of the integral in (4.131b). As with the steady-state solution, we cannot expand the amplitudes in (4.138) with

respect to the arc-length coordinate s without introducing an $\mathcal{O}(1)$ error. We must therefore determine the full s-dependence in the coefficients $c_j^{(\ell)}$. To this end, we substitute (4.138) into (4.137) and Taylor expand the kinetic terms with respect to ζ only. This results in the following recursive system of ODEs for the coefficients $c_j^{(\ell)}$

$$\tilde{\omega}\frac{dc_0^{(0)}}{ds} + \left(\sigma + \hat{\mathbf{N}}\cdot\mathbf{f}_\zeta - 2\phi_0\right)c_0^{(0)} = CP_0^{(0)}(s) + R_0^{(0)}(s), \tag{4.139a}$$

$$\tilde{\omega}\frac{dc_0^{(1)}}{ds} + \left(\sigma + 2\hat{\mathbf{N}}\cdot\mathbf{f}_\zeta - 6\phi_0\right)c_0^{(1)} = CP_0^{(1)}(s) + R_0^{(1)}(s), \tag{4.139b}$$

$$\tilde{\omega}\frac{dc_0^{(2)}}{ds} + \left(\sigma + 3\hat{\mathbf{N}}\cdot\mathbf{f}_\zeta - 10\phi_0\right)c_0^{(2)} = CP_0^{(2)}(s) + R_0^{(2)}(s), \tag{4.139c}$$

$$\tilde{\omega}\frac{dc_1^{(0)}}{ds} + \left(\sigma + \hat{\mathbf{N}}\cdot\mathbf{f}_\zeta - 2\phi_0\right)c_1^{(0)} = CP_1^{(0)}(s) + R_1^{(0)}(s), \tag{4.139d}$$

where $P_j^{(\ell)}$ and $R_j^{(\ell)}$ are inhomogeneous contributions from steady-state quantities and recursion terms, respectively. They are given explicitly by

$$P_0^{(0)} = 0, \tag{4.140a}$$

$$P_0^{(1)} = 2A|\phi_0|^{3/2}\hat{\mathbf{N}}\cdot\mathbf{f}_c, \tag{4.140b}$$

$$P_0^{(2)} = -\tilde{\omega}\left[a_0\left(3\hat{\mathbf{N}}\cdot\mathbf{f}_c\phi_1 + 2\hat{\mathbf{N}}\cdot\mathbf{f}_{c\zeta}\phi_0 + \hat{\mathbf{T}}\cdot\mathbf{f}_c\phi_0'\right) + 2a_1\hat{\mathbf{N}}\cdot\mathbf{f}_c\phi_0\right], \tag{4.140c}$$

$$P_1^{(0)} = -\tilde{\omega}\left[a_1\hat{\mathbf{N}}\cdot\mathbf{f}_c + a_0'\hat{\mathbf{T}}\cdot\mathbf{f}_c + a_0\left(\hat{\mathbf{N}}\cdot\mathbf{f}_{\zeta c} + \hat{\mathbf{T}}\cdot\mathbf{f}_{sc}\right)\right], \tag{4.140d}$$

$$R_0^{(0)} = R_0^{(1)} = 0, \tag{4.140e}$$

$$R_0^{(2)} = \left(12\phi_1 - \frac{3}{2}\hat{\mathbf{N}}\cdot\mathbf{f}_{\zeta\zeta} - 2\kappa\phi_0 - \hat{\mathbf{T}}\cdot\mathbf{f}_{s\zeta}\right)c_0^{(1)} - \hat{\mathbf{T}}\cdot\mathbf{f}_\zeta\frac{dc_0^{(1)}}{ds}, \tag{4.140f}$$

$$R_1^{(0)} = \left(2c_0^{(2)} - \kappa c_0^{(1)}\right), \tag{4.140g}$$

where we have simplified the above using the fact that $c_0^{(0)}$ will turn out to be zero. We note that the contribution from Q_1 in (4.137b) does not appear in (4.139)–(4.140) above, as expected. Since the perturbation η must be periodic in s, the same must be true for the coefficients in $c_j^{(\ell)}$.

Our next task is to solve the ODEs in (4.139)–(4.140). We consider $c_0^{(0)}$ first. The general solution of (4.139a) is

$$c_0^{(0)}(s) = \text{const.} \times |\phi_0|^{1/2}\exp\left[-\int_0^s \frac{\hat{\mathbf{N}}\cdot\mathbf{f}_\zeta - 2\phi_0 + \sigma}{\tilde{\omega}}\,\mathrm{d}t\right], \tag{4.141}$$

where the integration constant is determined from imposing periodicity. Using the identity (4.123), we find

$$c_0^{(0)}(s) = B_0^{(0)}|\phi_0(s)|^{1/2}\exp\left[-\int_0^s \frac{\sigma}{\tilde{\omega}}\,\mathrm{d}t\right], \tag{4.142}$$

where $B_0^{(0)}$ is a new integration constant. Since $\tilde{\omega} > 0$, periodicity of $c_0^{(0)}$ requires that either $\sigma = 0$ or $B_0^{(0)} = 0$. In order to detect linear instabilities, we focus on the case case $B_0^{(0)} = 0$; hence $c_0^{(0)} = 0$ as expected. We solve the remaining ODEs in (4.139)–(4.140) with a similar procedure to obtain

$$c_j^{(\ell)}(s) = \frac{|\phi_0(s)|^{\frac{\ell+1}{2}}}{\nu_\ell(s)} \left[\int_0^s \frac{\nu_\ell(t)}{\tilde{\omega}(t)|\phi_0(t)|^{\frac{\ell+1}{2}}} \left(CP_j^{(\ell)}(t) + R_j^{(\ell)}(t) \right) \mathrm{d}t + B_j^{(\ell)} \right], \quad (4.143a)$$

where the integrating factors ν_ℓ are given by

$$\nu_\ell(s) := \exp\left[\int_0^s \frac{\sigma - 2\ell\phi_0(t)}{\tilde{\omega}(t)} \, \mathrm{d}t \right], \quad (4.143b)$$

while the constants $B_j^{(\ell)}$, determined by enforcing periodicity, are given by

$$B_j^{(\ell)} := \frac{\left\langle \frac{\nu_\ell}{\tilde{\omega}} |\phi_0|^{\frac{-\ell+1}{2}} \left(CP_j^{(\ell)} + R_j^{(\ell)} \right) \right\rangle}{\nu_\ell(S) - 1}. \quad (4.143c)$$

Since $R_j^{(\ell)}$ depends on the lower order coefficient $c_j^{(\ell-1)}$ or $c_{j-1}^{(\ell)}$, Eq. (4.143) recursively determines the coefficients $c_j^{(\ell)}$, with the first coefficient being $c_0^{(0)} = 0$.

We can now partially evaluate the integral in (4.131b). Rewriting in arc-length coordinates, it reads

$$\int_{\mathbb{R}^2_+} \alpha(\mathbf{u})\eta(u) \, \mathrm{d}\mathbf{u} = \int_0^S \int_{-\zeta_0}^{\zeta_0} \alpha(\zeta, s)\eta(\zeta, s)(1 - \zeta\kappa) \, \mathrm{d}\zeta \mathrm{d}s + \text{E.S.T.}, \quad (4.144)$$

where $\zeta_0 < 1/|\kappa|$ and we use the shorthand $\alpha(\zeta, s) = \alpha(\mathbf{u}(\zeta, s))$. As before, the exponentially small errors are due to truncating the domain of integration. Another application of Laplace's method yields

$$\sigma + \beta = \frac{\sqrt{\pi}}{C} \int_0^S \frac{1}{|\phi_0|^{1/2}} \left[\left(\frac{3\phi_1 - 2\kappa|\phi_0|}{2\phi_0^2} c_0^{(1)} + \frac{c_0^{(2)}}{|\phi_0|} + 2c_1^{(0)} \right) \frac{\alpha^*}{\tilde{\omega}} + \frac{\alpha_\zeta^*}{\tilde{\omega}|\phi_0|} c_0^{(1)} \right] \mathrm{d}s + \mathcal{O}(\varepsilon), \quad (4.145)$$

where $\alpha^* := \alpha(0, s)$ and $\alpha_\zeta^* := \partial\alpha/\partial\zeta|_{\zeta=0}$. The integral over s cannot be evaluated without fixing the kinetics. We note from (4.139) that all coefficients $c_j^{(\ell)}$ are proportional to C. Therefore, C drops out from (4.145).

Eq. (4.145) is a transcendental equation for the eigenvalue σ. This is because the coefficients $c_j^{(\ell)}$ depend transcendentally on σ through ν_ℓ in (4.143b). In principle, our linear stability analysis is finished in the general case since (4.145) is an algebraic equation for σ in terms of the original model parameters. In order to illustrate the theory, we consider a simple, but non-trivial example where (4.145) simplifies.

4.3.3 Example: Modified Normal Form Kinetics

We illustrate the theory with the following modified normal form for the reaction kinetics:

$$\mathbf{f}(\mathbf{u}, c) = \begin{pmatrix} (\mu(c) - \tilde{u}^2 - \tilde{v}^2)\tilde{u} - \omega(\tilde{\mathbf{u}}, c)\tilde{v} \\ (\mu(c) - \tilde{u}^2 - \tilde{v}^2)\tilde{v} + \omega(\tilde{\mathbf{u}}, c)\tilde{u} \end{pmatrix}, \tag{4.146}$$

where we allow the (positive) kinetic parameters μ and ω to depend on c to simulate QS. The shifted variables $(\tilde{u}, \tilde{v}) := (u - u_0, v - v_0)$ are used so that the internal concentrations are positive on and near the limit cycle. We additionally allow ω to depend on $\mathbf{u}$ in order to break axial symmetry in state space[4]. The limit cycles that appear in many biologically relevant reaction kinetics do not admit axial symmetry, e.g. Fitzhugh-Nagumo and Sel'kov [46].

For simplicity we impose the additional restriction on ω that when expressed in arc-length coordinates, it is a function of s only. This is equivalent to $\omega = \omega(\theta; c)$ in polar coordinates. Non-uniqueness of ω at the origin is not problematic since n is exponentially small there. This assumption significantly simplifies the analysis, but is not strictly necessary.

We begin by simplifying the steady-state. To this end, we rewrite the components of $\mathbf{f}$ and $\mathbf{f}_c$ in arc-length coordinates

$$\mathbf{f}(\zeta, s, c^*) = \begin{pmatrix} \zeta\left(\sqrt{\mu^*} - \zeta\right)\left(\sqrt{\mu^*} - \zeta\right)\cos\left(\frac{s}{\sqrt{\mu^*}}\right) - \omega^*\left(\sqrt{\mu^*} - \zeta\right)\sin\left(\frac{s}{\sqrt{\mu^*}}\right) \\ \zeta\left(\sqrt{\mu^*} - \zeta\right)\left(\sqrt{\mu^*} - \zeta\right)\sin\left(\frac{s}{\sqrt{\mu^*}}\right) - \omega^*\left(\sqrt{\mu^*} + \zeta\right)\cos\left(\frac{s}{\sqrt{\mu^*}}\right) \end{pmatrix}, \tag{4.147a}$$

$$\mathbf{f}_c(\zeta, s, c^*) = \begin{pmatrix} \left(\mu_c^*\cos\left(\frac{s}{\sqrt{\mu^*}}\right) - \omega_c^*\sin\left(\frac{s}{\sqrt{\mu^*}}\right)\right)\left(\sqrt{\mu^*} - \zeta\right) \\ \left(\mu_c^*\sin\left(\frac{s}{\sqrt{\mu^*}}\right) + \omega_c^*\cos\left(\frac{s}{\sqrt{\mu^*}}\right)\right)\left(\sqrt{\mu^*} - \zeta\right) \end{pmatrix}, \tag{4.147b}$$

where '$*$' denotes evaluation at the steady-state $c = c^*$. We additionally compute the following quantities

$$\hat{\mathbf{T}}(s, c^*) = \left(-\sin\left(\frac{s}{\sqrt{\mu^*}}\right), \cos\left(\frac{s}{\sqrt{\mu^*}}\right)\right)^T, \tag{4.148a}$$

$$\hat{\mathbf{N}}(s, c^*) = -\left(\cos\left(\frac{s}{\sqrt{\mu^*}}\right), \sin\left(\frac{s}{\sqrt{\mu^*}}\right)\right)^T, \tag{4.148b}$$

$$\tilde{\omega}(s, c^*) := \hat{\mathbf{T}} \cdot \mathbf{f}\big|_{\zeta=0} = \sqrt{\mu^*}\omega^*, \tag{4.148c}$$

$$\kappa(s; c^*) = (\mu^*)^{-1/2}. \tag{4.148d}$$

[4]The limit cycle itself is circular, but the instantaneous 'speed' at which the orbit is traversed is non-constant.

We obtain the coefficients of the phase ϕ from (4.116) and (4.113), which turn out to be constants:

$$\phi_0 = -\mu^*, \quad \phi_1 = \sqrt{\mu^*}. \tag{4.149}$$

We note that the exact phase can be obtained directly from the full phase equation (4.109), with ϕ independent of s. It is the same as for our toy example in (4.81), but with $r = \sqrt{\mu^*} - \zeta$. The coefficients of the leading-order (in ε) steady-state amplitude Q_0 can be obtained from (4.124) and (4.121b). The first coefficient a_0 turns out to be an exact solution for Q_0 in (4.119), so we have

$$Q_0(s) = \frac{\rho^*}{\sqrt{\pi\varepsilon}} \frac{1/\omega^*}{\langle 1/\omega^* \rangle}, \tag{4.150}$$

where (4.127) has been used to fix the normalisation constant. The steady-state n^* is therefore, from (4.125),

$$n^*(\zeta, s) = \frac{A}{\varepsilon^{1/2}\omega^*} \exp\left[-\frac{\zeta^2}{4}\left(\zeta - 2\sqrt{\mu^*}\right)^2\right], \quad A = \frac{\rho^*}{\sqrt{\pi}\,\langle 1/\omega^* \rangle} + \mathcal{O}(\varepsilon), \tag{4.151a}$$

where c^* is determined from the algebraic equation

$$\beta c^* = \frac{\rho^*}{\beta} \frac{\langle \alpha(0,s)/\omega^* \rangle}{\langle 1/\omega^* \rangle} + \mathcal{O}(\varepsilon). \tag{4.151b}$$

Next, we simplify the algebraic equation for the eigenvalue σ in (4.145). We calculate the coefficients from (4.143) and find

$$c_0^{(0)} = 0, \tag{4.152a}$$

$$c_0^{(1)} = -\frac{2AC(\mu^*)^2\mu_c^*}{\sigma + 2\mu^*}, \tag{4.152b}$$

$$c_0^{(2)} = \frac{5AC(\mu^*)^{3/2}\mu_c^* + 3\sqrt{\mu^*}c_0^{(1)}}{\sigma + 4\mu^*}, \tag{4.152c}$$

$$c_1^{(0)} = \frac{1}{\sigma}\left[c_0^{(2)} - \frac{c_0^{(1)}}{\sqrt{\mu^*}} - 2A\mu_c^*\sqrt{\mu^*}\right] - \frac{2A\mu^*}{\nu_0(s)}\left[\frac{\langle \nu_0 \left(\omega_c^*/\omega^*\right)_s \rangle}{(\nu_0(S) - 1)} + \int_0^s \nu_0 \left(\frac{\omega_c^*}{\omega^*}\right)_t \mathrm{d}t\right], \tag{4.152d}$$

where

$$\nu_0(s) = \exp\left[(\mu^*)^{-1/2} \int_0^s \frac{\sigma}{\omega(t)}\,\mathrm{d}t\right]. \tag{4.152e}$$

We see that the only non-constant coefficient is $c_1^{(0)}$, and it involves only two layers of integration. Finally, substituting the coefficients and steady-state quantities into

the integral term in (4.145), and writing arc-length in terms of the polar angle θ as $s = \sqrt{\mu^*}\theta$, leads to

$$\sigma + \beta = \frac{\rho^*}{\langle 1/\omega^* \rangle} \left[\frac{\sqrt{\mu^*}\mu_c^*}{\sigma + 2\mu^*} \left\langle \frac{\alpha_r}{\omega^*} \right\rangle + g(\sigma) \right], \tag{4.153a}$$

$$g(\sigma) := \left\langle \frac{\nu_0(\theta;\sigma)\omega_c^*(\theta)}{(\omega^*)^2(\theta)} \int_0^\theta \frac{\alpha_\theta(\sqrt{\mu^*},t)}{\nu_0(t;\sigma)}\,\mathrm{d}t \right\rangle - \frac{\nu_0(2\pi;\sigma)}{\nu_0(2\pi;\sigma)-1} \left\langle \frac{\nu_0\omega_c^*}{(\omega^*)^2} \right\rangle \left\langle \frac{\alpha_\theta}{\nu_0} \right\rangle, \tag{4.153b}$$

where $\alpha_r := \frac{\partial \alpha}{\partial r}$ and $\alpha_\theta := \frac{\partial \alpha}{\partial \theta}$. Here, we have written $\nu_0(\theta) = \nu_0(\theta;\sigma)$ to explicitly show the dependence on σ. Eq. (4.153) is a transcendental equation that has three layers of nested integrals (the innermost layer is in ν_0, as seen from (4.152e)). We obtain numerical solutions in Section 4.4.2 and apply a winding number argument to detect solutions lying in the right half-plane $\mathrm{Re}(\sigma) > 0$, signifying a linear instability.

4.4 Numerical Results and Discussion

We now investigate the emergent patterning that arises from the linear instabilities predicted from our asymptotic theory in Sections 4.1 and 4.3. We accomplish this by obtaining full numerical solutions of the governing equations (4.1)–(4.2) and (4.73)–(4.74). The numerics for the two-component kinetics with spatial dependence in Section 4.2 are significantly more computationally intensive due to the extra dimension in **u**-space and exponentially localised solution structure. We therefore omit numerical calculations for (4.33)–(4.34), but emphasize that the predictions of our analytical theory can still be compared to the predictions of the IMF model, which we postpone until Chapter 5. This section is divided into two parts: first we consider the one-component kinetics from Section 4.1 and then the oscillatory kinetics from Section 4.3.

4.4.1 One-Component Kinetics

To facilitate the numerical calculations, we begin by fixing the reaction kinetics $f(u,c)$ and secretion rate $\alpha(u)$. We consider an illustrative example for convenience, but we expect the emergent behaviour to be qualitatively similar for other one-component kinetics with multiple equilibria.

We fix the reaction kinetics as

$$f(u,c) = -\gamma(u - g_-(c))(u - u_0)(u - g_+(c)), \tag{4.154a}$$

where we define the functions $g_\pm$ by

$$g_\pm(c) = a_\pm + \frac{L_\pm c}{K_\pm + c}, \tag{4.154b}$$

and also impose the following form for α

$$\alpha(u) = \alpha_0 u, \tag{4.154c}$$

where $\alpha_0 > 0$ is a parameter. The quantities γ, u_0, $a_\pm$, $L_\pm$, and $K_\pm$ are positive parameters which we choose such that $g_-(c) < u_0 < g_+(c)$ at the uniform steady-state. The form (4.154) is convenient for several reasons. First, it is clear that $f(u, c) = 0$ has only three solutions for a given c, one of which can be discarded since it corresponds to a local maximum of F in (4.6). There are then only two possible steady-state concentrations u^* and since F is easily calculated analytically, it is straightforward to determine which of the two possibilities is a global minimum of F. Secondly, the form (4.154) ensures that the algebraic equation (4.32) for the eigenvalue σ does not reduce to a version of its counterpart from Chapter 3 in Eq. (3.25). This would happen if, for example, g_- was chosen as a constant since this would lead to $f_c^- = 0$ in Eq. (4.32).

Next, we determine the quasi-steady concentrations $u_\pm$ and c_q. From (4.18b)–(4.18c), we have

$$u_\pm = g_\pm(c_q), \tag{4.155a}$$

$$\beta c_q = \alpha_0 \left(g_-(c_q)\rho_- + g_+(c_q)\rho_+ \right). \tag{4.155b}$$

Since Eq. (4.155b) can be rearranged into a cubic equation for c_q, there are three possible values of c_q. We obtain these values numerically, but in principle they can be determined exactly by invoking the cubic formula. Since $u_\pm$ are uniquely determined from (4.155a) once c_q is fixed, the distinct positive solutions for c_q correspond to three distinct quasi-steady states. For simplicity, we restrict our attention to parameter regimes where there is a unique positive solution. Once c_q and $u_\pm$ are known, we can calculate n_q from (4.18b), which we plot in Figure 4.3.

For a true steady-state, all of the cells are in either the '+' state or the '−' state. This is because $n^*(u)$ in (4.9) is exponentially localised around a single point u^*. Thus either $u^* = g_-(c^*)$ or $u^* = g_+(c^*)$, whichever is consistent with u^* being the global minimum of F. With the benefit of hindsight, we try the latter which gives

$$\beta c^* = \alpha_0 \rho^* g_+(c^*). \tag{4.156}$$

This is a quadratic equation for c^* with one positive solution. We verify that u^* is a global minimum by computing $F(u, c^*)$ from (4.6). We plot the result in Figure 4.3

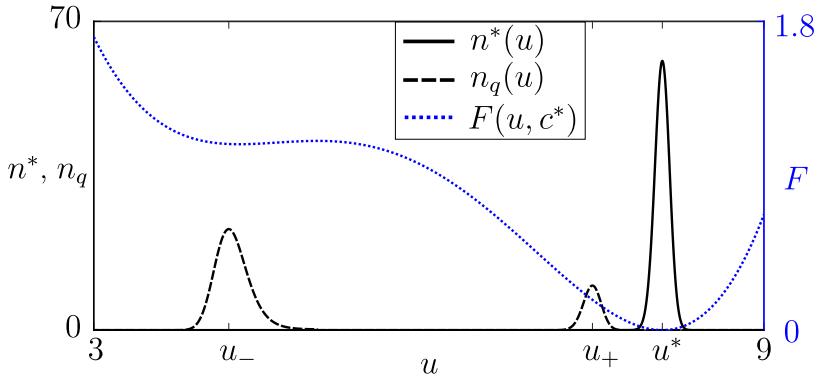

Figure 4.3: Steady-state n^* and quasi-steady state n_q as given in Eqs. (4.9) and (4.18)–(4.19), along with $F(u, c^*)$ from (4.6) and (4.154a). For the quasi-steady state, we calculate $u_- \approx 4.2$, $u_+ \approx 7.5$, and $c_q \approx 4.9$ from (4.155) with $\rho_- = 8$ and $\rho_+ = 2$. For the steady-state, we find from $u^* = g_+(c^*)$ and Eq. (4.156) that $u^* = c^* \approx 8.1$. The plot of $F(u, c^*)$ shows that u^* is indeed a global minimum of F. We use $\varepsilon = 0.005$ while all other parameters values here and the rest of this subsection are given in Table D.2 of Appendix D. Note that the exponentially small discontinuity in $n_q(u)$ at $u = u_0 = 5$ is indistinguishable from zero.

along with $n^*(u)$. If we had instead guessed $u^* = g_-(c^*)$, then we would find that u^* is not a global minimum, implying that our guess was incorrect.

It will be convenient in this section to identify slow variations in the fraction of the population in the '$\pm$' states. To this end, we extend our definition of the cell

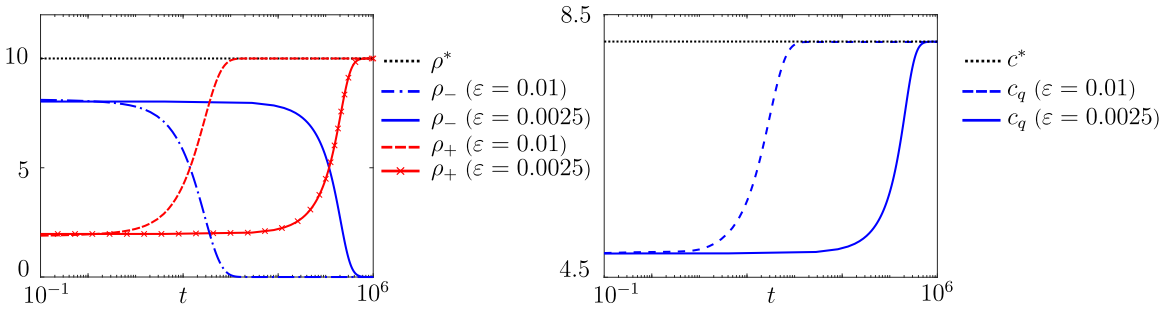

Figure 4.4: Numerical solution of the governing equations (4.1)–(4.2) and (4.154) showing the time evolution of the quasi-steady uniform state towards the uniform steady-state. The variations in $\rho_\pm$ and c_q occur over longer timescales as ε is decreased (note the logarithmic t-axis). The initial condition for n is the quasi-steady state n_q shown in Figure 4.3.

densities $\rho_\pm$ in (4.20) to the non-uniform case as

$$\rho_-(x,t) := \int_0^U n(x,u,t)\,\mathrm{d}u, \tag{4.157a}$$

$$\rho_+(x,t) := \int_U^\infty n(x,u,t)\,\mathrm{d}u. \tag{4.157b}$$

We also define the average cell density in both states as

$$\bar{\rho}_\pm(t) := \frac{1}{\mathcal{L}_x}\int_0^{\mathcal{L}_x} \rho_\pm(x,t), \tag{4.158}$$

where $\mathcal{L}_x$ is the length of the domain. Clearly $\bar{\rho}_\pm = \rho_\pm$ when n is spatially uniform.

We expect that the quasi-steady states vary slowly towards the true steady-state when the system is stable to spatial perturbations. In particular, the quantities $\rho_\pm$ should be slow functions of time (and independent of x). To verify this, we obtain numerical solutions of the governing equations (4.1)–(4.2) with $\mathcal{D} = \text{const}$. We then calculate $\rho_\pm$ from our numerical solution using (4.157) and Simpson's rule. We plot the results in Figure 4.4 where we see that the timescale over which $\rho_\pm$ vary increases rapidly as ε is decreased.

We now consider the effect of gene-regulated motility on the population, represented mathematically by non-constant diffusion coefficient $\mathcal{D}(u)$. For simplicity, we select a piecewise linear function. Since we must have $\mathcal{D} > 0$, our formula depends on the signs of $\mathcal{D}'_\pm$, but when both are negative we use

$$\mathcal{D}(u) = \begin{cases} \mathcal{D}'_-(u-u_-) + \mathcal{D}_-, & 0 \le u < u_{c1}, \\ \mathcal{D}'_m(u-u_{c2}) + \mathcal{D}_m, & u_{c1} \le u < u_{c2}, \\ \mathcal{D}'_+(u-u_+) + \mathcal{D}_+, & u_{c2} \le u < u_{c3}, \\ \mathcal{D}_\infty, & u_{c3} \le u, \end{cases} \tag{4.159}$$

where the quantities u_{cj}, $\mathcal{D}_m$ and $\mathcal{D}_\infty$ are parameters chosen such that $\mathcal{D}$ is continuous. We emphasize that the important parameters in (4.159) are $\mathcal{D}'_\pm$ and $\mathcal{D}_\pm$ since they affect the stability of the spatially uniform state. The signs of $\mathcal{D}'_\pm$ indicate whether motility is repressed or promoted in each state.

When QS sufficiently represses motility in both states, we expect that instabilities in the spatially uniform state lead to motility-induced phase separation. The onset of instability on an $\mathcal{O}(1)$ timescale is signified by $\mathrm{Re}(\sigma) = 0$ in (4.32), with the other four roots satisfying $\mathrm{Re}(\sigma) < 0$. By calculating the roots numerically, we find that simply setting $\sigma = 0$ in (4.32) gives the correct instability condition (but only when $\mathcal{D}'_\pm$ are both negative). In particular, we find

$$D_c k^2 + \beta = \alpha_0 \sum_{j=\pm} \left[\rho_j f_c \frac{\mathcal{D} - u\mathcal{D}'}{\mathcal{D}\left(\mathcal{D}k^2 - f_u\right)} \right]\Bigg|_{u=u_j}, \tag{4.160}$$

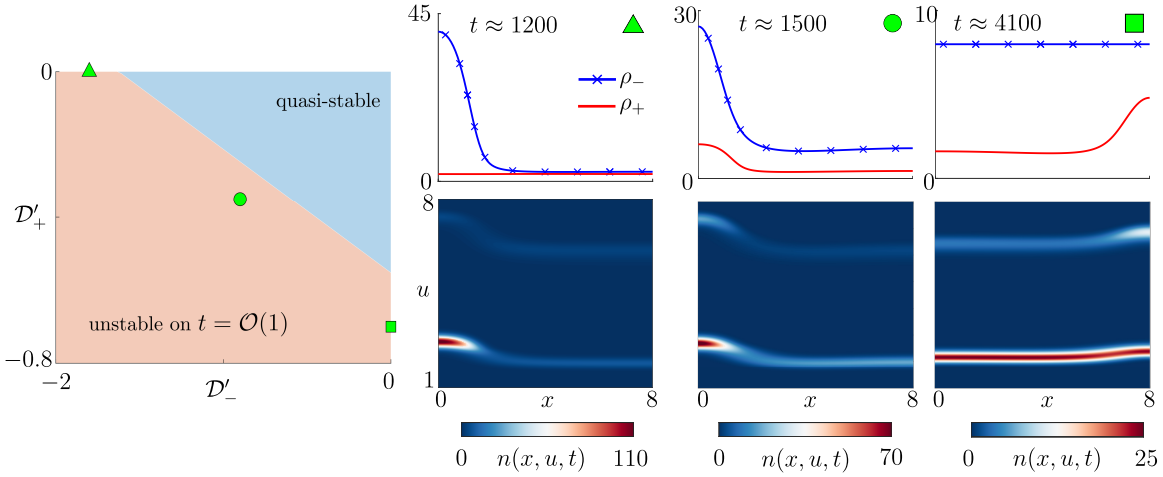

Figure 4.5: Instability region in parameter space, as computed from (4.160), with numerical results marked (left). A snapshot of the numerical solution of (4.1)–(4.2) and (4.154) is shown for three points in parameter space (right panels). When $\mathcal{D}'_- = 0$ cells in u_- do not phase separate, and similarly when $\mathcal{D}'_+ = 0$. Even in the constant density states, the distribution of internal chemical can be spatially heterogeneous due to non-uniform AI concentrations (not shown). Note that in the quasi-stable region, the timescale of variation is on the order of 10^4.

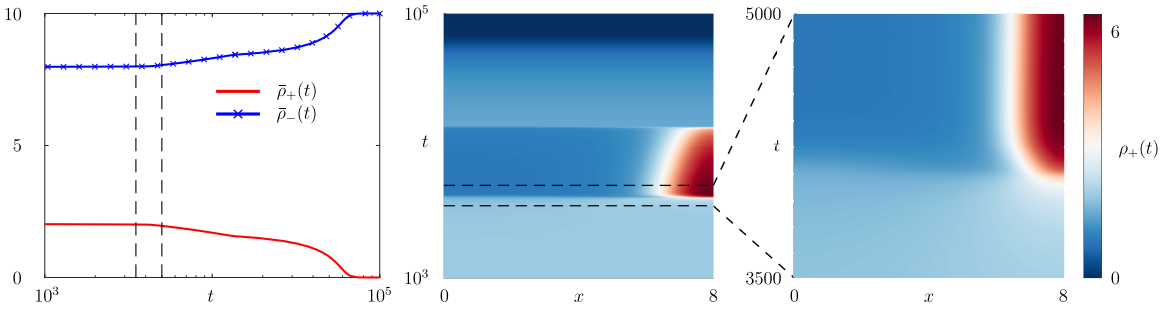

Figure 4.6: Numerical solution of (4.1)–(4.2) and (4.154) showing transient phase separation in the cell density $\rho_+(x,t)$. The final steady-state is spatially uniform with all cells in the '+' state (note that different parameters are used in Figure 4.4). The values of $\bar{\rho}_\pm$ are roughly unchanged from their initial values during phase separation. The profile of ρ_- (not shown) is nearly spatially uniform over the entire calculation while the profile for $c(x,t)$ is omitted since it is qualitatively similar to $\rho_+(x,t)$. A magnified view of the phase separation is shown in the region delineated by black dashed lines. The calculation is performed for the point in parameter space denoted by the green square in Figure 4.5. The phase separated state is also transient for the green circle, but the green triangle has a phase separated steady-state.

which defines a straight line in $(\mathcal{D}'_-, \mathcal{D}'_+)$ parameter space, as shown in Figure 4.5. We perform numerical simulations within the unstable region and observe phase separation on timescales over which $\bar{\rho}_\pm$ are nearly constant. Snapshots of the phase separation are also shown in Figure 4.5. A complete simulation for one of these snapshots is shown in Figure 4.6, along with the temporal evolution of $\bar{\rho}_\pm$.

The mechanism for MIPS in the canonical LuxIR system is similar to the mechanism here, except that it applies separately to cells in the '$\pm$' states. This implies that if QS repression of motility is weak in one of the two states, then phase separation will only occur in the other state. We illustrate this situation in Figure 4.5 with two calculations corresponding to $\mathcal{D}'_+ = 0$ and $\mathcal{D}'_- = 0$ (green triangle and green square, respectively) . If $\mathcal{D}'_- = 0$, then cells in the '$-$' state effectively experience constant diffusion, and therefore remain spatially uniform. However, cells in the '$+$' state can still phase separate if motility is sufficiently repressed. Even though the density ρ_- is spatially uniform, the internal state of cells in the '$-$' population can vary in space. This occurs because the entire population responds to the spatially dependent AI concentration c through the GRN reaction kinetics. A similar argument applies when instead $\mathcal{D}'_+ = 0$. In contrast, when both $\mathcal{D}'_-$ and $\mathcal{D}'_+$ are negative and not near zero, then cells in both states form clusters, as seen in Figure 4.5 (green circle).

Our numerical simulations show that the phase separated states exhibit variations on timescales much longer than the initial instability. This leads to situations where the phase separated state is transient. In order to detect these variations, we track $\bar{\rho}_\pm$ over time. For the example in Figure 4.6, phase separation occurs in the '$+$' state at a relatively early time where $\bar{\rho}_\pm$ are nearly unchanged from their initial values. The phase separated state gradually looses cells to the spatially uniform '$-$' state over a long timescale. This represents transitions in state space between the '$-$' and '$+$' states due to noise in the GRN kinetics (represented by finite ε). Eventually the '$+$' state loses enough cells for the cluster to disperse and the system returns to a spatially uniform quasi-steady state. The system then evolves towards the spatially uniform steady-state where the entire population is in the '$-$' state.

The slow variations in $\rho_\pm$ can lead to delayed phase separation due to slow passage through a bifurcation [62]. This occurs because the stable and unstable regions in parameter space change as $\rho_\pm$ vary in time. As we show in Figure 4.7, there are regions in parameter space that are initially stable on $\mathcal{O}(1)$ timescales, but become unstable after an exponentially long time. We obtain a numerical solution for the marked point in parameter space in order to observe the delay. Snapshots of the solution, as well as variations in $\bar{\rho}_+$ are shown in Figure 4.8 (we recall that $\bar{\rho}_\pm = \rho_\pm$ for uniform solutions).

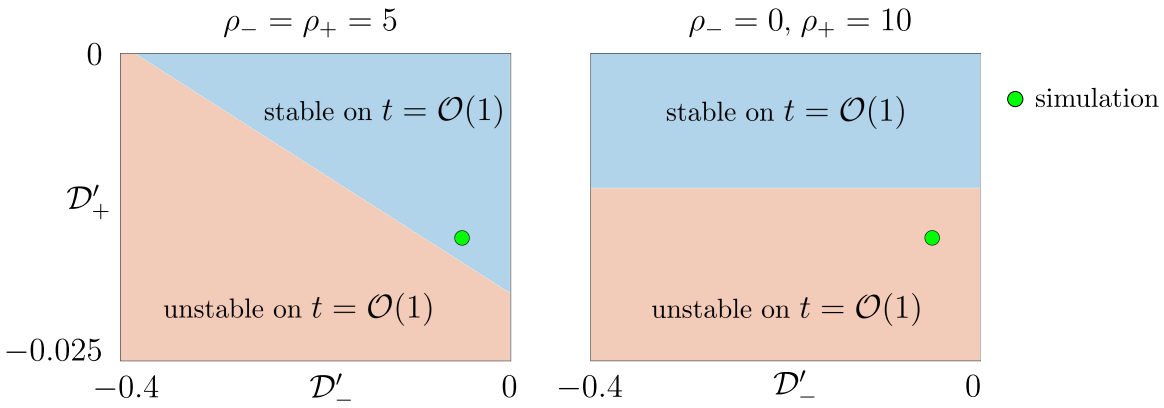

Figure 4.7: Instability regions in parameter space, as calculated from (4.160), for $\rho_+ = \rho_- = 5$ (left panel) and $\rho_+ = 10$, $\rho_- = 0$ (right panel). The boundary of the unstable region changes exponentially slowly in time due to variations in $\rho_\pm$. An initially quasi-stable uniform state (green circle) can become unstable to spatial perturbations on an $\mathcal{O}(1)$ timescale. A numerical calculation for the green circle is shown in Figure 4.8.

The quasi-steady uniform state becomes unstable after an exponentially long time, but the instability is significantly delayed as expected. Our asymptotic theory can therefore predict whether MIPS occurs over short $\mathcal{O}(1)$ timescales or exponentially long timescales.

We remark that the calculation of the stability boundaries as $\rho_\pm$ vary is somewhat non-intuitive. This is because changes in $\rho_\pm$ induce change in $u_\pm$ and c_q, which in turn affect several quantities in the eigenvalue equation (4.32), including $\mathcal{D}_\pm$, f_c and f_u. The amount that $\mathcal{D}_\pm$ change depends on their derivatives $\mathcal{D}'_\pm$. Hence the shift in the stability boundary becomes a function of $\mathcal{D}'_\pm$, and the boundaries therefore become curved. At steady-state however, either $\rho_- = 0$ or $\rho_+ = 0$, so the boundary eventually returns to being a straight line.

We now consider situations where QS can promote motility in either of the two states, represented mathematically by one or both of $\mathcal{D}'_\pm$ positive. Stability boundaries in parameter space are shown in Figure 4.9 where we distinguish between real-valued and complex-valued dominant eigenvalues. The boundaries between the blue and green regions correspond to Hopf bifurcations, and we expect a limit cycle near these boundaries (on $\mathcal{O}(1)$ timescales). Such a limit cycle is shown in Figure 4.9 for a very small value of ε so that $\bar{\rho}_\pm$ are effectively constant. We observe standing wave-like patterns in ρ_+, and smaller amplitude oscillations in ρ_-. The full cell density $\rho_- + \rho_+$ is therefore qualitatively similar to the spatio-temporal oscillations observed for the canonical LuxIR circuit.

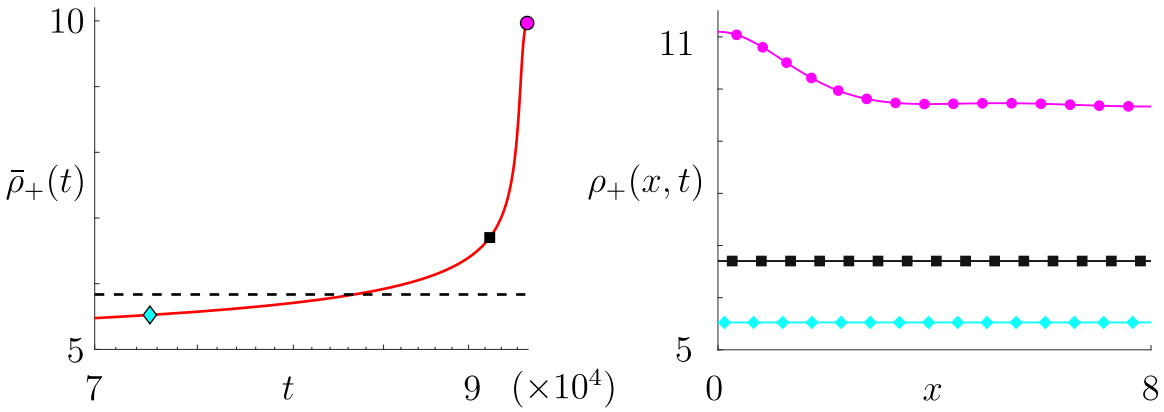

Figure 4.8: Numerical solution of (4.1)–(4.2) and (4.154) with a quasi-stable uniform initial condition that eventually becomes unstable to spatial perturbations. Left: slow evolution of $\bar{\rho}_+$. The dashed line denotes the value of $\bar{\rho}_+$ where the spatially uniform state becomes unstable according to (4.32). Right: snapshots of $\rho_+(x,t)$ for the points marked with the corresponding symbol and colour on the left. The solution exhibits the expected delayed instability, as seen from the final snapshot. We calculate the numerical solution up to $t \approx 10^5$ to clearly identify the delayed instability.

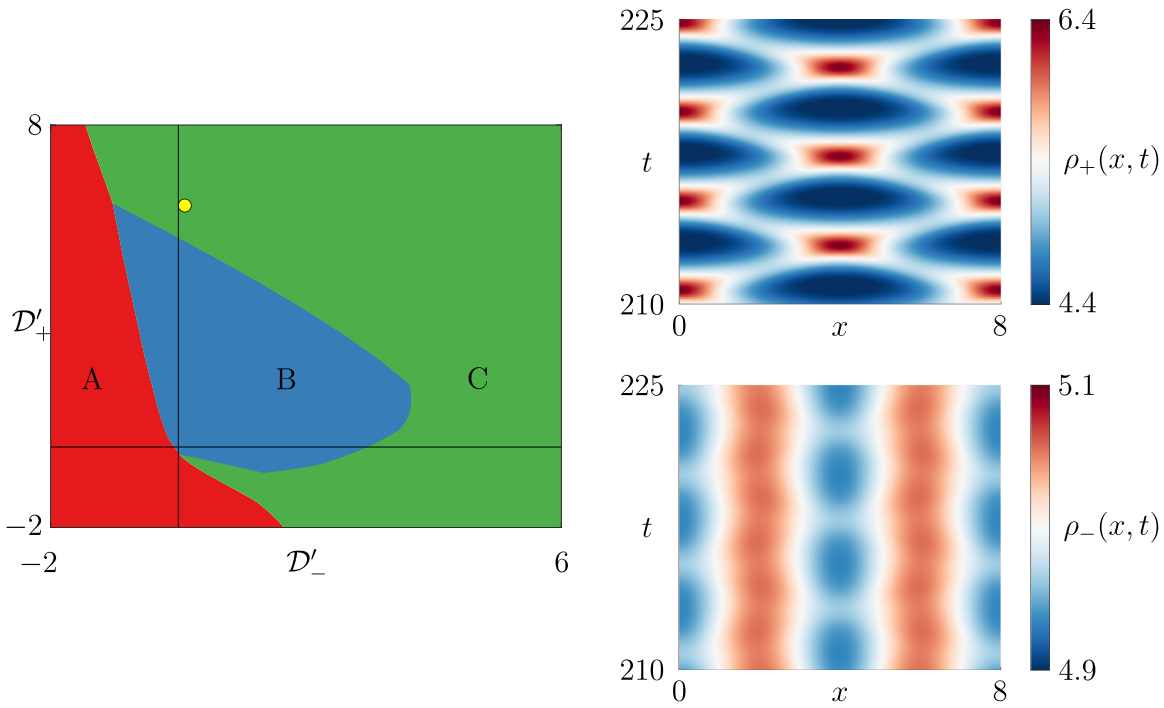

Figure 4.9: Left: Instability regions in parameter space on $\mathcal{O}(1)$ timescales, as calculated from (4.32). Blue regions (B) are quasi-stable while green (C) and red (A) are unstable. The dominant eigenvalue is real-valued in the red region and complex-valued in the green region. Blue-green boundaries correspond to Hopf bifurcations. Right: Example patterning for the point in parameter space denoted by a yellow circle, showing quasi-periodic behaviour. Snapshots are obtained from a numerical solution of (4.1)–(4.2) and (4.154).

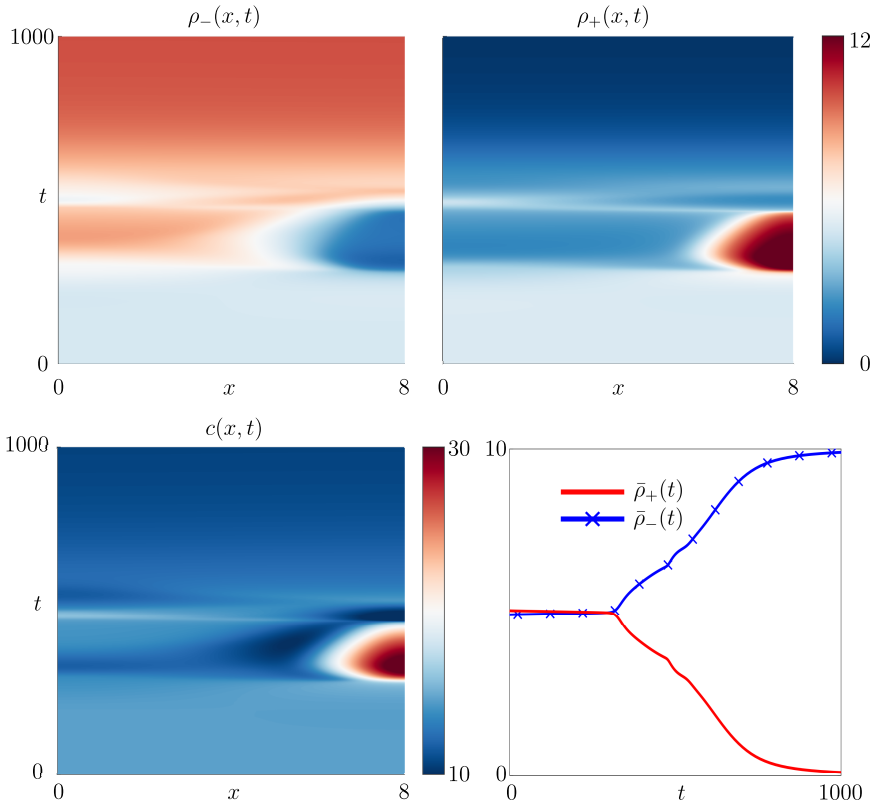

Figure 4.10: Numerical solution of (4.1)–(4.2) and (4.154) showing emergent patterning following the instability when QS promotes motility in the '−' state and represses motility in the '+' state. Initially, the cells in the repressing state cluster on the right, while the cells in the promoting state deplete. Overall, more cells accumulate on the right, leading to locally higher AI concentrations, which favours clustering. Over time $\bar{\rho}_+(t)$ slowly decreases, and eventually the cluster disperses and gives way to decaying oscillations. The steady-state is spatially uniform.

We remark that the numerical calculations when both $\mathcal{D}'_\pm > 0$ are significantly more challenging than when both are negative. This is because oscillating solutions inherently require a short timestep throughout the calculation, whereas clustering behaviour only requires short timesteps during cluster formation. We therefore do not investigate the effect of exponentially long variations in $\bar{\rho}_\pm$ when $\mathcal{D}'_\pm$ can be positive. We expect that the system will evolve towards a state where either $\bar{\rho}_+ = 0$ or $\bar{\rho}_- = 0$. The oscillations may persist throughout the process, or they may be transient. Similarly, we also expect that delayed Hopf bifurcations are possible.

When QS promotes motility in one state and represses it in the other, the instabilities give rise to a combination of oscillation and clustering. Figure 4.10 shows an example where initially the population clusters, but oscillates at later times. To understand this qualitatively, let us suppose that there is a region of locally higher

AI concentration c. This causes larger internal concentrations u for cells in both states. By the mechanism described in Chapter 3 for the LuxIR circuit, cells in the repressing state tend to cluster in this region, but cells in the promoting state tend to disperse. This affects the secretion rate of AI. The net effect depends on whether overall cells locally accumulate or deplete. If cells accumulate in the repressing state faster than they deplete in the promoting state, then overall the cell density $\rho_- + \rho_+$ increases. This leads to a local increase in the AI concentration, which further reinforces clustering. In contrast, if cells in the promoting state deplete faster than cells in the repressing state accumulate, then the AI concentration will decrease, which favours oscillations. For the case in Figure 4.10, clustering in the '+' state dominates depletion in the '−' state. Therefore, the overall cell density and AI concentration increase locally, leading to clustering. The fraction of the population in the '+' state decreases over long timescales. This eventually causes the cluster to disperse and give way to small amplitude (decaying) oscillations.

4.4.2 Oscillatory Kinetics

We now investigate synchronisation in spatially uniform populations with oscillatory kinetics. We obtain numerical solutions of the governing equations in (4.73) with the GRN kinetics in (4.146), which we repeat here for convenience

$$\mathbf{f}(\mathbf{u}, c) = \begin{pmatrix} (\mu(c) - \tilde{u}^2 - \tilde{v}^2)\tilde{u} - \omega(\tilde{\mathbf{u}}, c)\tilde{v} \\ (\mu(c) - \tilde{u}^2 - \tilde{v}^2)\tilde{v} + \omega(\tilde{\mathbf{u}}, c)\tilde{u} \end{pmatrix}. \tag{4.161}$$

We recall that the shift $\tilde{\mathbf{u}} := \mathbf{u} - \mathbf{u}_0$ ensures that the internal concentrations are positive. Our goal is to determine whether the linear instabilities in the asynchronous state lead to QS-induced synchronous oscillations.

For concreteness, we fix convenient forms for ω and μ in the GRN kinetics, and secretion rate α. Specifically, we choose

$$\omega(\theta, c) = \frac{1}{2 + \cos(\theta - c)}, \tag{4.162a}$$

$$\mu(c) = \frac{1}{4} + \frac{c}{1 + c}, \tag{4.162b}$$

$$\alpha(\mathbf{u}) = \alpha_0 u^2, \tag{4.162c}$$

where θ is the polar angle in the shifted coordinates $\tilde{\mathbf{u}}$. We note that u is not shifted in the definition of α. The fact that ω is not defined at the origin is not problematic since n is exponentially small there for all of our calculations. Although we consider the specific system (4.162), we expect that our results hold more generally.

We recall that linear instabilities occur when there are solutions of (4.153) in the right half-plane $\mathrm{Re}(\sigma) > 0$. In order to detect instabilities, we rewrite (4.153) as $G(\sigma) = 0$, where

$$G(\sigma) := \sigma + \beta - \frac{\rho^*}{\langle 1/\omega^* \rangle} \left[\frac{\sqrt{\mu^*}\mu_c^*}{\sigma + 2\mu^*} \left\langle \frac{\alpha_r}{\omega^*} \right\rangle + g(\sigma) \right], \tag{4.163a}$$

$$g(\sigma) := \left\langle \frac{\nu_0(\theta;\sigma)\omega_c^*(\theta)}{(\omega^*)^2(\theta)} \int_0^\theta \frac{\alpha_\theta(\sqrt{\mu^*},t)}{\nu_0(t;\sigma)}\,\mathrm{d}t \right\rangle - \frac{\nu_0(2\pi;\sigma)}{\nu_0(2\pi;\sigma)-1} \left\langle \frac{\nu_0\omega_c^*}{(\omega^*)^2} \right\rangle \left\langle \frac{\alpha_\theta}{\nu_0} \right\rangle, \tag{4.163b}$$

$$\nu_0(s) := \exp\left[(\mu^*)^{-1/2} \int_0^s \frac{\sigma}{\omega(t)}\,\mathrm{d}t \right]. \tag{4.163c}$$

Since G is a meromorphic function on $\mathbb{C}$ (as shown below), the number of zeros N of G lying inside a closed contour Γ in the complex plane is given by

$$N = w(G(\Gamma)) + P. \tag{4.164}$$

Here, P is the number of poles of G inside Γ while $G(\Gamma)$ is the image of Γ under G and $w(G(\Gamma))$ its winding number. The closed contour Γ must not pass through any zeros or poles of G, but is otherwise arbitrary. As we show below, all of the (infinitely many) poles of G lie on the imaginary axis, except one at $\sigma = -2\mu^* < 0$. We therefore detect roots of G in the right half-plane using (4.164) with a shifted semicircular contour Γ, given by

$$\Gamma := \left\{ \delta + i\xi \,\middle|\, -R < \xi < R \right\} \cup \left\{ \delta + Re^{i\xi} \,\middle|\, -\frac{\pi}{2} \le \xi \le \frac{\pi}{2} \right\}, \tag{4.165}$$

where δ and R are fixed positive numbers. Thus $P = 0$ in (4.164) and N is equal to the winding number of $G(\Gamma)$. If there is at least one root in the right half-plane, then it can be detected by taking sufficiently small δ and sufficiently large R. An example contour Γ and its image $G(\Gamma)$ are shown in Figure 4.11. We automate the winding number calculation using the algorithm in [4]. We also remark that similar winding number methods have been used previously (see, e.g., [46]).

Near a bifurcation, the roots of G are close to the imaginary axis, so the winding number method can be inaccurate unless δ is very small. We therefore supplement the winding number method with a direct numerical solution of $G(\sigma) = 0$ using Newton iteration. We take the global density ρ^* as a bifurcation parameter and perform pseudo arc-length continuation using the `Matcont` package [32] for `Matlab` to detect bifurcations. Pseudo arc-length continuation is a numerical method for solving systems of algebraic equations that depend on a parameter [55]. Broadly, the method

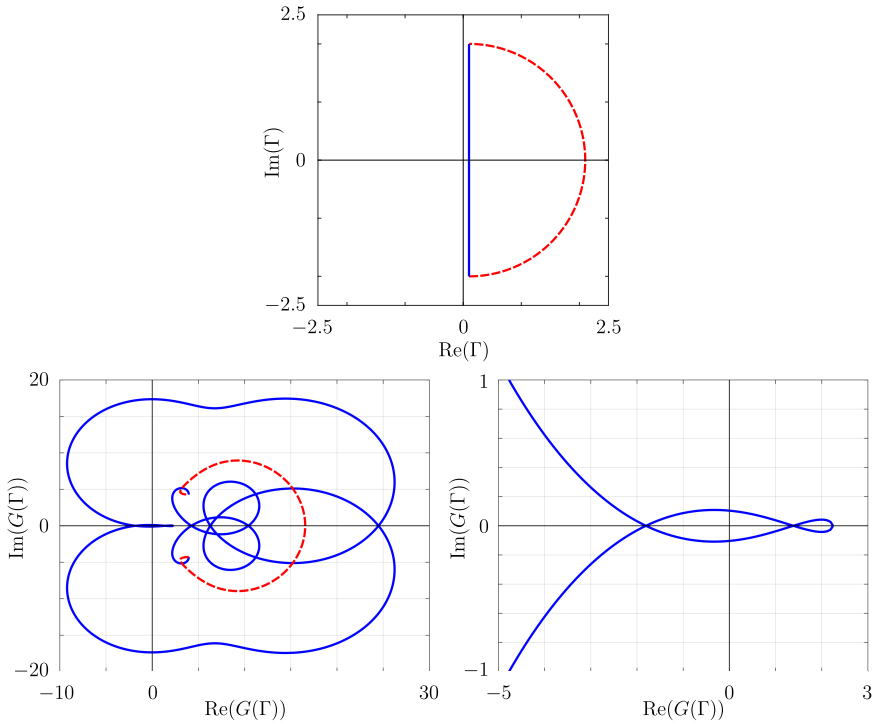

Figure 4.11: Semicircular contour Γ (top panel) and its image $G(\Gamma)$ computed from (4.163) (bottom panels). The solid blue and dashed red segments in $G(\Gamma)$ are images of the corresponding segments of Γ. The number of zeros of G inside Γ is equal to the winding number of $G(\Gamma)$, which in this case is 2. The spatially uniform steady-state is therefore linearly unstable. We use a relatively small semicircle and large δ for the purpose of illustration. There are at least 26 additional unstable eigenvalues that lie outside Γ as shown in Figure 4.12. We use $\rho^* = 360$ with the remaining parameter values henceforth given by $\mu_0 = 0.25$, $\alpha_0 = 0.1$, and $\beta = 1.0$.

works by parametrising the solution curve in terms of arc-length and using Newton iteration to compute points that are approximately evenly spaced in arc-length.

We now show that G is meromorphic and that all but one of its infinitely many poles lie on the imaginary axis. From (4.163a), we see that G has one pole at $\sigma = -2\mu^*$, and all other poles of G must also be poles of g. The only quantity in the definition of g in (4.163b) that depends on σ is ν_0. From the definition of $\nu_0(s;\sigma)$ in (4.163c), we see that it is holomorphic on $\mathbb{C}$ with respect to σ for all fixed s. As long as α and ω are continuously differentiable, the integrals involving ν_0 are also holomorphic functions with respect to σ. We note that the integral over s is always non-singular since ω cannot vanish (as otherwise the limit cycle would pass through a steady-state). Since ν_0 is holomorphic and does not vanish, g can only have poles where the denominator $\nu_0(2\pi;\sigma) - 1$ vanishes. This occurs when

$$\sigma = \frac{2\pi i\sqrt{\mu^*}}{\langle 1/\omega^* \rangle} j, \tag{4.166}$$

where j is an integer. Thus G is meromorphic on $\mathbb{C}$ with infinitely many poles of order one along the imaginary axis. We note that $G(\sigma) = \bar{G}(\bar{\sigma})$, where $\bar{\cdot}$ denotes complex conjugation, so the eigenvalues appear in complex-conjugate pairs.

Using a combination of the techniques above, we determine the linear stability of the steady-state in terms of the global density ρ^*. We find that there can be a large number of eigenvalues in the right half-plane, many of which are very close to the imaginary axis. To show this, we plot the first 14 eigenvalues nearest the origin (excluding conjugate pairs) for two different values of ρ^* in Figure 4.12. Using pseudo arc-length continuation, we track the eigenvalues as ρ^* is varied and plot three of the resulting curves in Figure 4.12. Each eigenvalue exhibits instability 'bands' in parameter space. Since these bands do not completely overlap across different eigenvalues, we observe that there is an eigenvalue with positive real part for nearly all values of ρ^* in Figure 4.12. There is an extremely narrow parameter regime near $\rho^* = 30$ where there appears to be no unstable eigenvalues. We remark that the eigenvalue structure for larger values of ρ^* and further from the origin is quite complicated since solutions of $G(\sigma) = 0$ tend to undergo bifurcations, so the number of eigenvalues is non-constant as ρ^* varies.

We expect that a synchronised population should oscillate periodically with a highly localised distribution of internal states. To determine if the population synchronises, we obtain full numerical solutions of the governing equations in (4.73) in the unstable regime. A typical example is shown in Figure 4.13. The instability leads to a distribution of internal states that is more localised than for the steady-state,

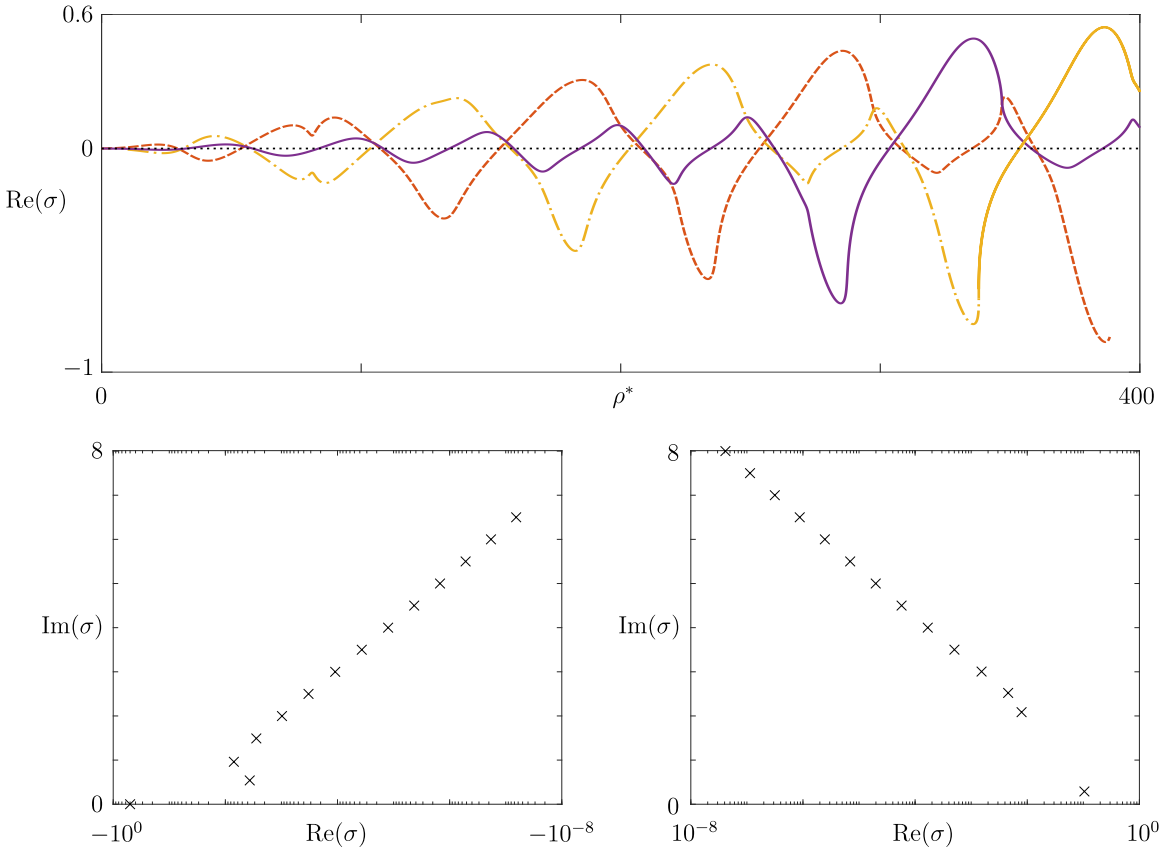

Figure 4.12: Eigenvalue structure for oscillatory kinetics computed from numerical solutions of (4.163). Top: Three solutions of $G(\sigma) = 0$ in terms of the global density ρ^* showing that the system is unstable for nearly all ρ^*, except for a small band at $\rho^* = 30$. Bottom left: First 14 eigenvalues nearest the origin when $\rho^* = 30$ (excluding conjugate pairs in $\mathrm{Im}(\sigma) < 0$). Right: First 14 unstable eigenvalues nearest the origin when $\rho^* = 360$.

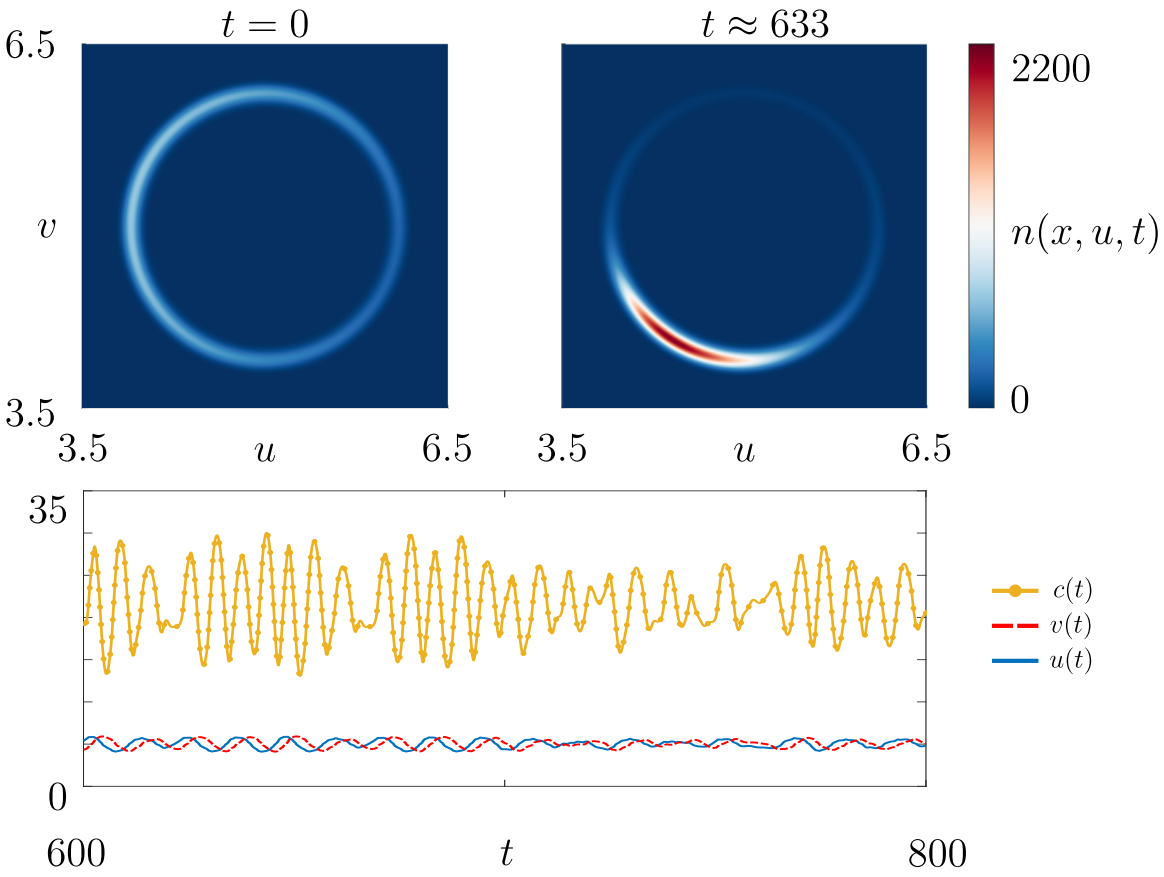

Figure 4.13: Numerical solution of the governing equations (4.73)–(4.74) with GRN kinetics given in (4.161)–(4.162) showing partially synchronised oscillations. Top left: steady-state initial condition (asynchronous state). Top right: snapshot showing a more localised distribution of internal states. Bottom: temporal evolution showing no apparent periodic structure. Here $\mathbf{u}(t) := (u(t), v(t))^T$ are the mean internal concentrations, calculated from $\mathbf{u}(t) = (1/\rho^*) \int_{\mathbb{R}^2_+} \mathbf{u}\, n(\mathbf{u}, t)\, \mathrm{d}\mathbf{u}$.

but is clearly not localised to a single point. This somewhat localised distribution of internal states indicates an incomplete or partial synchronisation. Additionally, there is no apparent periodic structure over long times; we expect a completely synchronised population to have periodic dynamics (as we show at the end of Chapter 5). We have run several simulations over long time intervals and different parameter sets and observe qualitatively similar behaviour to that show in Figure 4.13. We have also verified numerically that the steady-states are stable in the narrow parameter regime near $\rho^* = 30$ in Figure 4.12, and unstable just outside this regime. Overall, we conclude that QS can trigger emergent partial synchronisation from an initially asynchronous population. Even though synchronisation occurs over a wide parameter regime, the population does not synchronise completely.

Chapter 5

Motility-Induced Pattering in the IMF Model

So far in this thesis we have analysed motility-induced patterning for various classes of reaction kinetics using our structured modelling framework. In this chapter, we compare the predictions of our structured model with those for the internal mean-field (IMF) model that we derived in Chapter 2. From a mathematical modelling perspective, the IMF model is an attractive choice since it takes the form of a reaction-diffusion system and is therefore simpler to analyse (both numerically and analytically) compared to structured model. However, the IMF model is an approximation of the structured model since it assumes that locally (in space) all cells have identical internal concentrations. The IMF model additionally assumes that there is no noise term in the reaction kinetics (i.e. $\varepsilon = 0$). We seek to understand the implications of these assumptions on motility-induced patterning as well as for oscillator synchronisation.

To tackle this challenge, we determine criteria for motility-induced patterning for the IMF model, analogous to our analytical results for the structured model. We then compare full numerical solutions for both models to identify quantitative and qualitative differences in emergent patterning. Broadly, we find that on $\mathcal{O}(1)$ timescales, the IMF model has almost the same steady-states and linear stability properties as the structured model (in the limit $\varepsilon \to 0$) whenever the reaction kinetics have stable steady-states. The models predict quantitative, but not qualitative, differences in the spatially non-uniform states. We find more significant differences between the two models in the long time behaviour of the quasi-steady solutions of the structured model, which we analysed in Section 4.1. However, if the reaction kinetics have a stable limit cycle, then the predictions differ both quantitatively and qualitatively.

We additionally perform a detailed comparison of the two models for the canonical LuxIR circuit.

The rest of this Chapter is divided into three sections. First, we characterise linear instabilities in the spatially uniform state of the IMF model for two broad classes of reaction kinetics. Next, we perform an in-depth analysis of the canonical LuxIR circuit for the IMF model. Finally, we compare theoretical and numerical predictions of both models, with focus on the canonical LuxIR circuit.

5.1 Model Setup for One and Two Sub-populations

Our general IMF model is given in (2.36) and (2.38), which we restate here for convenience

$$\frac{\partial \rho_\pm}{\partial t} = \nabla_{\mathbf{x}}^2 \left[\mathcal{D}(\mathbf{u}_\pm)\rho_\pm\right], \tag{5.1a}$$

$$\frac{\partial}{\partial t}\left(\rho_\pm \mathbf{u}_\pm\right) = \nabla_{\mathbf{x}}^2 \left[\mathcal{D}(\mathbf{u}_\pm)\mathbf{u}_\pm\rho_\pm\right] + \mathbf{f}(\mathbf{u}_\pm, c)\rho_\pm, \tag{5.1b}$$

$$\frac{\partial c}{\partial t} = D_c \nabla_{\mathbf{x}}^2 c - \beta c + \sum_{j=\pm} \alpha(\mathbf{u}_j)\rho_j. \tag{5.1c}$$

We recall that the '+' and '−' subscripts denote sub-populations of cells that have internal concentrations or states $\mathbf{u}_-$ and $\mathbf{u}_+$ and cell densities ρ_- and ρ_+. Eqs. (5.1a)–(5.1c) constitute a system of $2M + 3$ equations, where M is the number of internal chemicals (i.e. the number of components of $\mathbf{u}_\pm$). For the analysis that follows, it will be useful to eliminate the time-derivative of $\rho_\pm$ from (5.1b) using (5.1a). This leads to

$$\rho_\pm \frac{\partial \mathbf{u}_\pm}{\partial t} = \rho_\pm \mathcal{D}(\mathbf{u}_\pm)\nabla_{\mathbf{x}}^2 \mathbf{u}_\pm + 2\nabla_{\mathbf{x}}\left(\mathcal{D}(\mathbf{u}_\pm)\rho_\pm\right) \cdot \nabla_{\mathbf{x}} \mathbf{u}_\pm + \rho_\pm f(\mathbf{u}_\pm, c). \tag{5.1d}$$

The no-flux boundary conditions in (2.37) and (2.39) read

$$\nabla_{\mathbf{x}} \rho_\pm \cdot \mathbf{N}_{\mathbf{x}} = \nabla_{\mathbf{x}} c \cdot \mathbf{N}_{\mathbf{x}} = 0, \qquad \mathbf{x} \in \partial\Omega, \tag{5.1e}$$

$$\nabla_{\mathbf{x}} \left(\mathbf{u}_\pm\right) \mathbf{N}_{\mathbf{x}} = \mathbf{0}, \qquad \mathbf{x} \in \partial\Omega. \tag{5.1f}$$

Eqs. (5.1a), (5.1c), and (5.1d), together with the no-flux conditions in (5.1e)–(5.1f) constitute our mathematical model for a colony consisting of two sub-populations or states.

There are two situations where we can reduce the two-state model to a one-state model. The first situation occurs when $\mathbf{u}_-(\mathbf{x}, t) = \mathbf{u}_+(\mathbf{x}, t) := \mathbf{u}(\mathbf{x}, t)$. We can see this by summing the two equations for $\rho_\pm$ in (5.1a), as well as the two equations for $\mathbf{u}_\pm$

in (5.1b). Then after defining $\rho = \rho_- + \rho_+$ and simplifying, we obtain the following system

$$\frac{\partial \rho}{\partial t} = \nabla_{\mathbf{x}}^2 \left[\mathcal{D}(\mathbf{u})\rho\right], \tag{5.2a}$$

$$\rho\frac{\partial \mathbf{u}}{\partial t} = \rho\mathcal{D}(\mathbf{u})\nabla_{\mathbf{x}}^2\mathbf{u} + 2\nabla_{\mathbf{x}}\left(\mathcal{D}(\mathbf{u})\rho\right)\cdot\nabla_{\mathbf{x}}\mathbf{u} + \rho f(\mathbf{u}, c), \tag{5.2b}$$

$$\frac{\partial c}{\partial t} = D_c\nabla_{\mathbf{x}}^2 c - \beta c + \alpha(\mathbf{u})\rho. \tag{5.2c}$$

In other words, if the sub-populations have the same internal state, then it is redundant to keep track of the '$-$' and '$+$' quantities separately. The second situation occurs when either $\rho_+ = 0$ or $\rho_- = 0$ at $t = 0$ (but not both). If $\rho_+ = 0$ initially, then since (5.1a) are conservation equations for ρ_- and ρ_+, we have that

$$\int_\Omega \rho_\pm(\mathbf{x}, t)\,\mathrm{d}\mathbf{x} = \text{const.}, \tag{5.3}$$

for all times t. This implies that $\rho_+ = 0$ for all future times and Eq. (5.1d) for $\mathbf{u}_+$ is trivially satisfied, so $\mathbf{u}_+$ is arbitrary. In other words, if one of the two sub-populations has no cells, then effectively there is only one sub-population. The one-state model (5.2a)–(5.2c) has only $M + 2$ governing equations. As we will see in our steady-state analysis below, the one-state model (5.2) is appropriate when the reaction kinetics $\mathbf{f}$ admit only one equilibrium, while the two-state model (5.1) is appropriate when the kinetics admit two equilibria.

We seek to compare the predictions of the IMF model with the structured model. Since we have found spatially uniform solutions of the structured model and analysed their linear stability properties, our next task is to do the same for the IMF model.

5.1.1 Steady-States

We begin by finding spatially uniform solutions, which we denote with superscript '$*$.' For the two-state model, these satisfy

$$\rho_\pm^* = \text{const.}, \tag{5.4a}$$

$$\mathbf{f}(\mathbf{u}_\pm^*, c^*) = \mathbf{0}, \tag{5.4b}$$

$$\beta c^* = \sum_{j=\pm}\alpha_j\rho_j^*, \tag{5.4c}$$

where $\alpha_\pm := \alpha(\mathbf{u}_\pm^*)$. We take $\rho_\pm^*$ as additional model parameters since (5.3) implies that they are determined by the initial condition. If the only solutions of (5.4) have

$\mathbf{u}_-^* = \mathbf{u}_+^* := \mathbf{u}^*$, then (5.4) effectively reduces to the steady-state system of the one-state model in (5.2) since, after summing (5.2a), we obtain

$$\rho^* := \rho_-^* + \rho_+^* = \text{const.}, \tag{5.5a}$$

$$\mathbf{f}(\mathbf{u}^*, c^*) = \mathbf{0}, \tag{5.5b}$$

$$\beta c^* = \rho^* \alpha_*. \tag{5.5c}$$

Here $\alpha_* := \alpha(\mathbf{u}^*)$ and we recall that ρ^* is the global cell density.

Next, we perform linear stability analyses around the spatially uniform steady-states in (5.4) and (5.5) as two separate cases. Although it is possible in principle to unify these analyses while retaining general M, our purpose here is to compare the results with their counterparts for the structured model. We therefore divide our analysis into two cases: 1) two internal chemicals ($M = 2$) and one internal state ($\mathbf{u}_+ = \mathbf{u}_-$) and 2) one internal chemical ($M = 1$) with two internal states. The two cases respectively correspond to our analysis in Sections 4.2 and 4.1. In the following section, we also consider a subcase of 2) for which we use the canonical LuxIR reaction kinetics in Chapter 3. For this subcase, we also perform a weakly nonlinear analysis in order to characterise the type of bifurcation, just as we did for the structured model in Section 3.3.

5.1.2 Linear Stability Case 1: Two Chemicals, One State

In our first case we have $\mathbf{u}_- = \mathbf{u}_+ := \mathbf{u} := (u_1, u_2)^T$ and $\mathbf{f} := (f_1, f_2)^T$. Here it is sufficient to only keep track of the sum $\rho_- + \rho_+$, rather than the individual values of $\rho_\pm$. The steady-states ρ^*, $\mathbf{u}^*$, and c^* satisfy (5.5).

We begin by introducing small perturbations of the form

$$\rho(\mathbf{x}, t) = \rho^* + Pe^{i\mathbf{k}\cdot\mathbf{x}+\sigma t}, \quad \mathbf{u}(\mathbf{x}, t) = \mathbf{u}^* + \mathbf{U}e^{i\mathbf{k}\cdot\mathbf{x}+\sigma t}, \quad c(\mathbf{x}, t) = c^* + Ce^{i\mathbf{k}\cdot\mathbf{x}+\sigma t}, \tag{5.6}$$

where $\mathbf{U} := (U_1, U_2)^T$ and $|P|$, $|\mathbf{U}|$, $|C| \ll 1$. The quantities σ and $\mathbf{k}$ are the usual growth rate and wavenumber of the perturbation. Next, we substitute (5.6) into the governing equations for the one-state model (5.2) and retain up to linear terms in the perturbations. This leads to the following linear system

$$\begin{pmatrix} -\mathcal{D}_* k^2 - \sigma & -\rho^* \mathcal{D}_{u_1}^* k^2 & -\rho^* \mathcal{D}_{u_2}^* k^2 & 0 \\ 0 & -\mathcal{D}_* k^2 + \mu_{11} - \sigma & \mu_{12} & \frac{\partial f_1^*}{\partial c} \\ 0 & \mu_{21} & -\mathcal{D}_* k^2 + \mu_{22} - \sigma & \frac{\partial f_2^*}{\partial c} \\ \alpha_* & \alpha_{u_1}^* \rho^* & \alpha_{u_2}^* \rho^* & -D_c k^2 - \beta - \sigma \end{pmatrix} \begin{pmatrix} P \\ U_1 \\ U_2 \\ C \end{pmatrix} = \mathbf{0}, \tag{5.7}$$

where we define

$$\mathcal{D}^*_{u_j} := \frac{\partial \mathcal{D}}{\partial u_j}(\mathbf{u}^*), \quad \alpha_{u_j} := \frac{\partial \alpha}{\partial u_j}(\mathbf{u}^*), \quad \mu_{ij} := \frac{\partial f_i}{\partial u_j}(\mathbf{u}^*, c^*), \quad i,j = 1,2. \tag{5.8}$$

Eq. (5.7) constitutes a matrix eigenvalue problem for the eigenvalue σ and eigenvector $(P, U_1, U_2, C)^T$. A non-trivial solution for the perturbations therefore requires the determinant of the LHS matrix to vanish. After rearranging, this requirement yields

$$\sigma + D_c k^2 + \beta = \frac{\rho^* \left(R_{\pi/2}\mathbf{f}^*_c\right)^T \left[(\sigma + \mathcal{D}_* k^2) I_2 - \mathbf{J}\right] R_{\pi/2} \left[(\sigma + \mathcal{D}_* k^2)\nabla_{\mathbf{u}}\alpha_* - \alpha_* \nabla_{\mathbf{u}} \mathcal{D}^* k^2\right]}{(\sigma + \mathcal{D}_* k^2)(\sigma + \mathcal{D}_* k^2 - \lambda^-_{\mathbf{J}})(\sigma + \mathcal{D}_* k^2 - \lambda^+_{\mathbf{J}})}, \tag{5.9}$$

where the Jacobian matrix $\mathbf{J}$ has entries μ_{ij} and eigenvalues $\lambda^{\pm}_{\mathbf{J}}$, the matrix $R_{\pi/2}$ is an anti-clockwise rotation by $\pi/2$ in the plane, while I_2 is the 2×2 identity matrix, and finally $\mathbf{f}^*_c := \partial \mathbf{f}/\partial c(\mathbf{u}^*, c^*)$. Crucially, Eq. (5.9) is identical to its counterpart for the structured model (to leading order in ε) in (4.72). We therefore deduce that the uniform steady–states in (5.5) have the same linear stability properties as the uniform steady-states in the structured model, up to $\mathcal{O}(\varepsilon)$ corrections.

5.1.3 Linear Stability Case 2: One Chemical, Two States

For this case, we have $M = 1$, so we denote $\mathbf{u}_{\pm} := u_{\pm}$. As before, we perturb the steady-state as

$$\rho_{\pm}(\mathbf{x}, t) = \rho^*_{\pm} + P_{\pm} e^{i\mathbf{k}\cdot\mathbf{x} + \sigma t}, \quad u_{\pm}(\mathbf{x}, t) = u^*_{\pm} + U_{\pm} e^{i\mathbf{k}\cdot\mathbf{x} + \sigma t}, \quad c(\mathbf{x}, t) = c^* + C e^{i\mathbf{k}\cdot\mathbf{x} + \sigma t}, \tag{5.10}$$

where the perturbations $|P_{\pm}|$, $|U_{\pm}|$, $|C| \ll 1$. Substituting (5.10) into the governing equations (5.1a), (5.1c), and (5.1d), and linearising yields the eigenvalue problem

$$\mathcal{M}\mathbf{V} = \sigma \mathbf{V}, \tag{5.11a}$$

where $\mathcal{M}$ and $\mathbf{V}$ are given by

$$\mathcal{M} := \begin{pmatrix} -\mathcal{D}_- k^2 & 0 & -\rho_- \mathcal{D}'_- k^2 & 0 & 0 \\ 0 & -\mathcal{D}_+ k^2 & 0 & -\rho_+ \mathcal{D}'_+ k^2 & 0 \\ 0 & 0 & -\mathcal{D}_- k^2 + f^-_u & 0 & f^-_c \\ 0 & 0 & 0 & -\mathcal{D}_+ k^2 + f^+_u & f^+_c \\ \alpha_- & \alpha_+ & \alpha'_- \rho^*_- & \alpha'_+ \rho^*_+ & -(D_c k^2 + \beta) \end{pmatrix}, \quad \mathbf{V} := \begin{pmatrix} P_- \\ P_+ \\ U_- \\ U_+ \\ C \end{pmatrix}. \tag{5.11b}$$

Here we define

$$f^{\pm}_u := \frac{\partial f}{\partial u}(u_{\pm}, c^*), \quad f^{\pm}_c := \frac{\partial f}{\partial c}(u_{\pm}, c^*), \quad \alpha_{\pm} := \alpha(u_{\pm}), \quad \mathcal{D}_{\pm} := \mathcal{D}(u_{\pm}), \tag{5.12}$$

and similarly for the derivatives $\alpha'_{\pm}$ and $\mathcal{D}'_{\pm}$.

Eq. (5.11) has a non-trivial solution if, and only if, σ is an eigenvalue of $\mathcal{M}$. We therefore require

$$\det(\mathcal{M} - \sigma I) = 0. \tag{5.13}$$

After some algebra, we find that this can be rewritten as

$$\sigma + D_c k^2 + \beta = \sum_{j=\pm} \left[\rho_j f_c \frac{\alpha' \left(\sigma + \mathcal{D}k^2\right) - \alpha \mathcal{D}' k^2}{\left(\sigma + \mathcal{D}k^2\right)\left(\sigma + \mathcal{D}k^2 - f_u\right)} \right] \Bigg|_{u=u_j}. \tag{5.14}$$

Similar to Case I above, this is precisely the leading order result from the linear stability analysis of the structured model in Eq. (4.32). We therefore conclude that the spatially uniform states in the two models have exactly the same linear stability properties, up to an $\mathcal{O}(\varepsilon)$ correction. We emphasize here that the equivalence between the two models applies only on an $\mathcal{O}(1)$ timescale. This is because the uniform states for the structured model are only quasi-steady, as shown in Section 4.1.

5.2 Detailed Analysis for Canonical LuxIR Kinetics

We now perform a detailed analysis for the canonical LuxIR circuit in order to compare with our linear and weakly nonlinear results for the structured model in Chapter 3. The reaction kinetics and secretion rate from Chapter 3 are given by

$$f(u,c) = a + \frac{Lc}{K+c} - \lambda u, \quad \alpha(u) = \alpha_0 u. \tag{5.15}$$

This system can be viewed as a special case of either Case 1 or Case 2 above, but it is more convenient to use Case 2 since Eq. (5.14) for the eigenvalue σ is simpler than Eq. (5.9). We therefore set $\mathbf{u}_- = \mathbf{u}_+ = u$ with $\rho := \rho_- + \rho_+$ in the two-state model (5.1a), (5.1c), and (5.1d). We additionally work in one spatial dimension for simplicity. For concreteness, we state the governing equations for this special case here

$$\frac{\partial \rho}{\partial t} = \frac{\partial^2}{\partial x^2}\big(\mathcal{D}(u)\rho\big), \tag{5.16a}$$

$$\rho \frac{\partial u}{\partial t} = \rho \mathcal{D}(u) \frac{\partial^2 u}{\partial x^2} + 2 \frac{\partial u}{\partial x} \frac{\partial}{\partial x}\big(\mathcal{D}(u)\rho\big) + \rho f(u,c), \tag{5.16b}$$

$$\frac{\partial c}{\partial t} = D_c \frac{\partial^2 c}{\partial x^2} - \beta c + \alpha_0 u \rho. \tag{5.16c}$$

The no-flux boundary conditions (5.1e)–(5.1f) for one internal chemical in 1D reduce to

$$\frac{\partial \rho}{\partial x} = \frac{\partial c}{\partial x} = \frac{\partial u}{\partial x} = 0, \quad x = 0, \mathcal{L}_x, \tag{5.17}$$

where $\mathcal{L}_x$ is the length of the domain. The steady-states satisfy

$$f(u^*, c^*) = 0, \quad \beta c^* = \alpha_0 \rho^* u^*, \quad \rho^* = \text{const.}, \tag{5.18}$$

and (5.14) reduces to

$$\sigma + D_c k^2 + \beta - \alpha_0 f_c^* \rho^* \frac{\sigma + (\mathcal{D}_* - u^* \mathcal{D}'_*)\, k^2}{(\sigma + \mathcal{D}_* k^2)\,(\sigma + \mathcal{D}_* k^2 + \lambda)} = 0. \tag{5.19}$$

Eq. (5.19) is exactly the algebraic equation for the eigenvalue σ that we found for the structured model in Eq. (3.25)[1].

So far we have found that the IMF model reproduces the leading order linear stability theory from the structured model. We now determine if the type of bifurcation and the local branch of non-uniform steady states is also the same. To accomplish this, we perform a weakly nonlinear analysis near the 'MIPS' bifurcation corresponding to $\sigma = 0$ in (5.19).

As in Chapter 3, we take $\mathcal{D}'_*$ as a bifurcation parameter. We therefore introduce a perturbation to $\mathcal{D}'_*$ in the form

$$\mathcal{D}(u) = \mathcal{D}_0 + \delta^2 d(u), \tag{5.20}$$

where $d(u)$ is a perturbing function and $0 < \delta \ll 1$ measures the distance from the bifurcation point. The unperturbed diffusion coefficient $\mathcal{D}_0$ is such that it exactly satisfies (5.19) with $\sigma = 0$, in particular

$$\frac{\mathcal{D}'_{0*}}{\mathcal{D}_{0*}} = -\frac{1}{u^*}\left[\frac{(D_c k^2 + \beta)\,(\mathcal{D}_* k^2 + \lambda)}{\alpha_0 \rho^* f_c^*} - 1\right] < 0. \tag{5.21}$$

Here we take k to be the critical wavenumber $k = \pi/|\Omega|$, where $|\Omega| = \mathcal{L}_x$ is now the length of the domain Ω. As we showed in Section 3.2, this mode is the first to lose stability as $\mathcal{D}'_{0*}$ is decreased from zero. We also impose

$$d(u^*) = 0, \tag{5.22}$$

so that (5.20) perturbs $\mathcal{D}'_*$, but not $\mathcal{D}_*$. Thus

$$\mathcal{D}'_* = \mathcal{D}'_{0*} + \delta^2 d'_*. \tag{5.23}$$

[1]Eq. (5.19) can also can be obtained from (5.11). This is because the '$-$' and '$+$' quantities in $\mathcal{M}$ are equal, so the eigenvectors are of the form $(P, P, U, U, C)^T$. Hence the first equation is a copy of the second, and the third equation is a copy of the fourth.

From our analysis of the structured model, we anticipate that the instability will correspond to a pitchfork bifurcation. For convenience, we have therefore fixed the $\mathcal{O}(\delta^2)$ scaling in the perturbation (5.21) and additionally rescale time as

$$t = \delta^{-2}\tau, \tag{5.24}$$

where τ is slow time. These scalings are the same as for the structured model in Section 3.3 (cf. Eqs.(3.65) and (3.67) where we later deduced $r = p = 2$).

Next, we seek solutions of the governing equations (5.16) in the form

$$\rho(x,\tau) = \rho^* + \sum_{j=1}^{3} \rho_j(x,\tau)\delta^j + \mathcal{O}(\delta^4), \tag{5.25a}$$

$$u(x,\tau) = u^* + \sum_{j=1}^{3} u_j(x,\tau)\delta^j + \mathcal{O}(\delta^4), \tag{5.25b}$$

$$c(x,\tau) = c^* + \sum_{j=1}^{3} c_j(x,\tau)\delta^j + \mathcal{O}(\delta^4), \tag{5.25c}$$

where we show only the terms that will be required in our analysis. Since the governing equation for ρ in (5.2a) conserves mass, we require that the perturbations ρ_j satisfy

$$\int_\Omega \rho_j(x,\tau)\,\mathrm{d}x = 0, \tag{5.26}$$

for all τ. This ensures that the expansion (5.25a) does not introduce small perturbations to the parameter ρ^*.

We now obtain governing equations for ρ_j, u_j, c_j by substituting the expansions (5.25), (5.20), and (5.24) into the governing equations and equating coefficients of powers of δ.

The $\mathcal{O}(1)$ terms yield the steady-state problem in (5.18) for ρ^*, u^*, and c^*. At $\mathcal{O}(\delta)$, we obtain

$$\mathcal{L}\begin{pmatrix}\rho_1\\ u_1\\ c_1\end{pmatrix} := \begin{pmatrix}\mathcal{D}_{0*}\frac{\partial^2\rho_1}{\partial x^2} + \rho^*\mathcal{D}'_{0*}\frac{\partial^2 u_1}{\partial x^2}\\ \mathcal{D}_{0*}\frac{\partial^2 u_1}{\partial x^2} - \lambda u_1 + f_c^* c_1\\ D_c\frac{\partial^2 c_1}{\partial x^2} - \beta c_1 + \alpha_0\left(u^*\rho_1 + \rho^* u_1\right)\end{pmatrix} = \mathbf{0}. \tag{5.27}$$

Next, we seek separated solutions of the form

$$\rho_1(x,\tau) = P(\tau)\cos(kx), \quad u_1(x,\tau) = U(\tau)\cos(kx), \quad c_1(x,\tau) = C(\tau)\cos(kx), \tag{5.28}$$

where k is the critical wavenumber of the instability. Substituting (5.28) into (5.27) leads to the linear system

$$\mathcal{M}(k)\begin{pmatrix} P \\ U \\ C \end{pmatrix} = \mathbf{0}, \quad \mathcal{M}(k) := \begin{pmatrix} -\mathcal{D}_{0*}k^2 & -\rho^*\mathcal{D}'_{0*}k^2 & 0 \\ 0 & -\mathcal{D}_{0*}k^2 - \lambda & f_c^* \\ \alpha_0 u^* & \alpha_0\rho^* & -D_c k^2 - \beta \end{pmatrix}, \tag{5.29}$$

where we explicitly show the dependence of $\mathcal{M}$ on the wavenumber k for later convenience. A non-trivial solution requires $\det \mathcal{M}(k) = 0$, which is simply a restatement of the bifurcation condition $\sigma = 0$ in (5.13). Hence any non-trivial solution for $(P, U, C)^T$ is proportional to the eigenvector of $\mathcal{M}(k)$ corresponding to the zero eigenvalue, namely

$$\begin{pmatrix} P \\ U \\ C \end{pmatrix} = C(\tau)\begin{pmatrix} -\rho^* \frac{\mathcal{D}'_{0*} f_c^*}{\mathcal{D}_{0*}(\mathcal{D}_{0*}k^2+\lambda)} \\ \frac{f_c^*}{\mathcal{D}_{0*}k^2+\lambda} \\ 1 \end{pmatrix}, \tag{5.30}$$

where $C(\tau)$ is still to be determined.

Eq. (5.27) also admits constant solutions. This is because the first row of $\mathcal{M}(0)$ is all zeros and hence $\mathcal{M}(0)$ has a non-trivial nullspace. Such solutions are proportional to

$$\begin{pmatrix} \rho_1 \\ u_1 \\ c_1 \end{pmatrix} = \begin{pmatrix} \lambda\beta - \alpha_0\rho^* f_c^* \\ \alpha_0 u^* f_c^* \\ \alpha_0 u^* \lambda \end{pmatrix}. \tag{5.31}$$

The general solution of (5.27) is a linear combination of (5.28), with coefficients in (5.30), and the constant solution (5.31). However, we must reject the constant solution since it fails to satisfy the mass constraint in (5.26).

Our task now is to determine $C(\tau)$ in (5.30). To accomplish this, we will need to obtain governing equations for the unknowns at $\mathcal{O}(\delta^2)$ and $\mathcal{O}(\delta^3)$ in (5.25). Since $\mathcal{L}$ has a non-trivial nullspace (spanned by Eqs. (5.28) and (5.31)), we will find that the governing equations at higher order must satisfy certain solvability conditions. We now derive these conditions through consideration of the adjoint operator $\mathcal{L}^*$.

5.2.1 The Adjoint Problem

In order to determine the adjoint operator $\mathcal{L}^*$, we must first define an appropriate inner product. Suppose $\mathbf{v}(x)$, $\mathbf{w}(x) \in \mathbb{R}^3$, then we define

$$(\mathbf{v}, \mathbf{w}) := \int_\Omega \mathbf{v} \cdot \mathbf{w} \, \mathrm{d}x. \tag{5.32}$$

This meets the requirements of an inner product (see, e.g., chapters 6–7 in the book by Axler [8]). Thus the adjoint of $\mathcal{L}$ is uniquely defined through

$$(\mathcal{L}(\mathbf{v}), \mathbf{w}) = (\mathbf{v}, \mathcal{L}^*(\mathbf{w})). \tag{5.33}$$

If the components of $\mathbf{v}$ satisfy no-flux boundary conditions on Ω, then using integration by parts, we deduce from (5.33) and the definition of $\mathcal{L}$ in (5.27) that $\mathcal{L}^*$ is given by

$$\mathcal{L}^*(\mathbf{w}) := \begin{pmatrix} \mathcal{D}_{0*}\frac{\partial^2 w_1}{\partial x^2} + \alpha_0 u^* w_3 \\ \rho^* \mathcal{D}'_{0*}\frac{\partial^2 w_1}{\partial x^2} + \mathcal{D}_{0*}\frac{\partial^2 w_2}{\partial x^2} - \lambda w_2 + \rho^* \alpha_0 w_3 \\ \frac{\partial^2 w_3}{\partial x^2} - \beta w_3 + f_c^* w_2 \end{pmatrix}, \tag{5.34}$$

where w_j, $j = 1, 2, 3$ denote the components of $\mathbf{w}$. In the above calculation, we deduced that $\mathbf{w}$ must also satisfy no-flux boundary conditions so that the boundary terms arising from the integration vanish.

Now suppose that we wish to solve $\mathcal{L}(\mathbf{v}) = \mathbf{g}$ for some function $\mathbf{g}$ not identically zero. The Fredholm alternative states that a solution exists if, and only if, $\mathbf{g}$ satisfies the solvability condition

$$(\mathbf{g}, \mathbf{w}) = 0, \tag{5.35}$$

where $\mathbf{w}$ is a solution of the homogeneous adjoint problem $\mathcal{L}^*(\mathbf{w}) = \mathbf{0}$. In order to write (5.35) in terms of known quantities, we will need to obtain explicit solutions of the homogeneous adjoint problem.

Solutions of $\mathcal{L}^*(\mathbf{w}) = \mathbf{0}$ have the form

$$\mathbf{w}(x) = \tilde{\mathbf{w}} \cos(kx), \tag{5.36}$$

where $\tilde{\mathbf{w}}$ is a solution of

$$\mathcal{M}^*(k)\tilde{\mathbf{w}} = \mathbf{0}. \tag{5.37}$$

Here $\mathcal{M}^*(k)$ is the adjoint of the matrix $\mathcal{M}(k)$ defined in (5.29). Since the nullspace of $\mathcal{M}^*$ is orthogonal to the range of $\mathcal{M}$, the rank-nullity theorem guarantees that the nullspaces of $\mathcal{M}(k)$ and $\mathcal{M}^*(k)$ have the same dimension. Thus the only non-trivial solutions are obtained for the critical wavenumber of the instability and for $k = 0$. In both cases, $\mathcal{M}(k)$ has a one-dimensional nullspace. It follows that $\tilde{\mathbf{w}}$ must be the eigenvector corresponding to the zero eigenvalue of $\mathcal{M}^*$. We therefore have two linearly independent solutions

$$\mathbf{w} = (1, 0, 0)^T, \tag{5.38a}$$

$$\mathbf{w} = \tilde{\mathbf{w}} \cos(kx), \quad \tilde{\mathbf{w}} = \left(\frac{\alpha_0 u^*}{\mathcal{D}_{0*} k^2}, \frac{D_c k^2 + \beta}{f_c^*}, 1 \right)^T, \tag{5.38b}$$

where the (irrelevant) normalisation has been fixed for both solutions. Using (5.35), we find that the corresponding solvability conditions read

$$\int_\Omega g_1(x)\,\mathrm{d}x = 0, \tag{5.39a}$$

$$\tilde{\mathbf{w}} \cdot \left(\int_\Omega \mathbf{g}(x)\cos(kx)\,\mathrm{d}x \right) = 0, \tag{5.39b}$$

where g_1 is the first component of $\mathbf{g}$.

5.2.2 Weakly Nonlinear Analysis

Our next step is to obtain governing equations for the unknowns at $\mathcal{O}(\delta^2)$ in (5.25). Substituting the scalings (5.20) and (5.24), as well as the expansions for ρ, u, and c (5.25) into the governing equations (5.16) and collecting terms at $\mathcal{O}(\delta^2)$ gives

$$\mathcal{L}\begin{pmatrix}\rho_2\\ u_2\\ c_2\end{pmatrix} = \begin{pmatrix} \left(\rho^*\mathcal{D}_{0*}''k^2U + 2\mathcal{D}_{0*}k^2P\right)U\cos(2kx) \\ U\left(\mathcal{D}_{0*}'k^2U + \frac{\mathcal{D}_{0*}k^2}{\rho^*}P\right)\left(3\cos^2(kx)-2\right) + \left(\frac{\lambda}{\rho^*}PU - \frac{f_c^*}{\rho^*}PC - \frac{f_{cc}^*}{2}C^2\right)\cos^2(kx) \\ -\alpha_0 PU\cos^2(kx) \end{pmatrix}, \tag{5.40}$$

where we have used (5.28) to write the above in terms of P, U, and C.

Since (5.40) is of the form $\mathcal{L}(\mathbf{v}) = \mathbf{g}$, the RHS vector must satisfy the solvability conditions in (5.39) for a solution to exist. By writing the RHS as a linear combination of constant terms and terms proportional to $\cos(2kx)$, we find that both solvability conditions are trivially satisfied. Since no secular terms appear on the RHS of (5.40), the assumed $\mathcal{O}(\delta^2)$ scalings in Eqs. (5.20) and (5.24) are appropriate.

Since our analysis at $\mathcal{O}(\delta^2)$ does not yield any useful information about $C(\tau)$, we must proceed to higher order. Before doing so, we must calculate the solutions of (5.40) as they will influence the analysis at next order in δ. To do this, we seek solutions in the form

$$\begin{pmatrix}\rho_2(x,\tau)\\ u_2(x,\tau)\\ c_2(x,\tau)\end{pmatrix} = C^2(\tau)\begin{pmatrix}P_{20}\\ U_{20}\\ C_{20}\end{pmatrix} + C^2(\tau)\cos(2kx)\begin{pmatrix}P_{22}\\ U_{22}\\ C_{22}\end{pmatrix}, \tag{5.41}$$

where the coefficient vectors are unknowns to be determined. Note that a term from the nullspace of $\mathcal{L}$ proportional to $\cos(kx)$ may also be included in the above; such a term does not influence the final result (since it will be orthogonal to the forcing) and is therefore omitted.

Substituting (5.41) into (5.40) leads to the following linear system for P_{20}, U_{20}, and C_{20}

$$\mathcal{M}(0)\begin{pmatrix} P_{20} \\ U_{20} \\ C_{20} \end{pmatrix} = \begin{pmatrix} 0 \\ \frac{f^*_{cc}}{4} - \frac{1}{2}\mathcal{D}'_{0*}k^2\mu^2 \\ -\frac{\alpha_0\rho^*\mathcal{D}'_{0*}\mu^2}{2\mathcal{D}_{0*}} \end{pmatrix}, \tag{5.42a}$$

and a similar system for P_{22}, U_{22}, and C_{22}

$$\mathcal{M}(2k)\begin{pmatrix} P_{22} \\ U_{22} \\ C_{22} \end{pmatrix} = \begin{pmatrix} \rho^*\mu^2k^2\left(\mathcal{D}''_{0*} - 2\frac{(\mathcal{D}'_{0*})^2}{\mathcal{D}_{0*}}\right) \\ -\frac{f^*_{cc}}{4} + \frac{1}{2}\mathcal{D}'_{0*}k^2\mu^2 \\ \frac{\alpha_0\rho^*\mu^2\mathcal{D}'_{0*}}{2\mathcal{D}_{0*}} \end{pmatrix}, \tag{5.42b}$$

where we recall that $\mathcal{M}(k)$ is given in (5.29) and we define the constant μ by

$$\mu := \frac{f^*_c}{\mathcal{D}_{0*}k^2 + \lambda}. \tag{5.42c}$$

We have also used (5.30) to eliminate P and U in favour of C. It follows from (5.42a) and (5.26) that $P_{20} = 0$. Eq. (5.42a) then reduces to a system of two equations (the top row of $\mathcal{M}(0)$ is all zeros), which in principle uniquely determine U_{20} and C_{20}. We omit the lengthy explicit formulas for brevity. Since k is the critical wavenumber, it follows that $\det\mathcal{M}(2k) \neq 0$ in general. Hence (5.42b) uniquely determines P_{22}, U_{22}, and C_{22} (explicit formulas also omitted for brevity). As ρ_2, u_2, and c_2 are now known in terms of C, this concludes our analysis at $\mathcal{O}(\delta^2)$ and we proceed to next (and final) order.

Finally, we substitute the scalings (5.20) and (5.24), as well as the expansions for ρ, u, and c (5.25) into the governing equations (5.16) and collect terms at $\mathcal{O}(\delta^3)$. This yields the following governing equations for ρ_3, u_3, and c_3

$$\mathcal{L}\begin{pmatrix} \rho_3 \\ u_3 \\ c_3 \end{pmatrix} = \mathbf{g}_0\cos(kx)\frac{dC}{d\tau} + \mathbf{g}_1\cos(kx)C(\tau) + \left[\mathbf{g}_2\cos(kx) + \mathbf{g}_3\cos^3(kx)\right]C^3(\tau). \tag{5.43}$$

The quantities $\mathbf{g}_0$ and $\mathbf{g}_1$ are given by

$$\mathbf{g}_0 := \begin{pmatrix} -\frac{\rho^*\mathcal{D}'_{0*}\mu}{\mathcal{D}_{0*}} \\ \mu \\ 1 \end{pmatrix}, \quad \mathbf{g}_1 := d'_*k^2\rho^*\mu\begin{pmatrix} 1 \\ 0 \\ 0 \end{pmatrix}, \tag{5.44a}$$

while $\mathbf{g}_2 := (A_1, A_2, A_3)^T$, $\mathbf{g}_3 := (B_1, B_2, B_3)^T$ are constant vectors whose components are given by

$$A_1 := -\mu k^2 \left[13\mathcal{D}'_{0*} P_{22} + \rho^* (U_{20} - 13U_{22}) \left(\frac{(\mathcal{D}'_{0*})^2}{\mathcal{D}_{0*}} - \mathcal{D}''_{0*} \right) \right] - \rho^* \mu^3 k^2 \left(\mathcal{D}'''_{0*} - 3\frac{\mathcal{D}'_{0*}\mathcal{D}''_{0*}}{\mathcal{D}_{0*}} \right), \tag{5.44b}$$

$$A_2 := -f^*_{cc}(C_{20} - C_{22}) - 8\mathcal{D}_{0*}k^2\mu\frac{P_{22}}{\rho^*} + \frac{\mathcal{D}'_{0*}}{\mathcal{D}_{0*}}\mu\left[(\mathcal{D}_{0*}k^2 - \lambda)U_{20} + (9\mathcal{D}_{0*}k^2 - \lambda)U_{22}\right] + f^*_c\mu(C_{20} - C_{22})\frac{\mathcal{D}'_{0*}}{\mathcal{D}_{0*}} + 2\mu^3k^2\left(2\frac{(\mathcal{D}'_{0*})^2}{\mathcal{D}_{0*}} - \mathcal{D}''_{0*}\right), \tag{5.44c}$$

$$A_3 := \alpha_0\mu\left[P_{22} + \rho^*\frac{\mathcal{D}'_{0*}}{\mathcal{D}_{0*}}(U_{20} - U_{22})\right], \tag{5.44d}$$

$$B_1 := 18k^2\mu\left[P_{22}\mathcal{D}'_{0*} + U_{22}\rho^*\left(\mathcal{D}''_{0*} - \frac{(\mathcal{D}'_{0*})^2}{\mathcal{D}_{0*}}\right)\right] + \frac{3}{2}\mu^3k^2\left(\mathcal{D}'''_{0*} - 3\frac{\mathcal{D}'_{0*}\mathcal{D}''_{0*}}{\mathcal{D}_{0*}}\right), \tag{5.44e}$$

$$B_2 := -\left(2C_{22}f^*_{cc} + \frac{f^*_{ccc}}{6}\right) + 8\mathcal{D}_{0*}k^2\mu\frac{P_{22}}{\rho^*} + 2\mu\frac{\mathcal{D}'_{0*}}{\mathcal{D}_{0*}}U_{22}\left(5\mathcal{D}_{0*}k^2 - \lambda\right) + \left(2f^*_cC_{22} + \frac{f^*_{cc}}{4}\right)\mu\frac{\mathcal{D}'_{0*}}{\mathcal{D}_{0*}} + \frac{5}{2}\mu^3k^2\left(\mathcal{D}''_{0*} - 2\frac{(\mathcal{D}'_{0*})^2}{\mathcal{D}_{0*}}\right), \tag{5.44f}$$

$$B_3 := -2\alpha_0\mu\left(P_{22} - \rho^*U_{22}\frac{\mathcal{D}'_{0*}}{\mathcal{D}_{0*}}\right). \tag{5.44g}$$

In deriving the above, we have used the solution of the $\mathcal{O}(\delta)$ problem in (5.28) and (5.30), as well as the solution of the $\mathcal{O}(\delta^2)$ problem in (5.41). Since U_{20}, C_{20}, P_{22}, U_{22}, and C_{22} are known in terms of the original model parameters, the same is true of the RHS of (5.43).

We require that a solution of (5.43) exists and hence impose the solvability conditions (5.39). Since each term on the RHS is proportional to either $\cos(kx)$ or $\cos^3(kx)$, the first solvability condition (5.39a) is automatically satisfied. The second solvability condition (5.39b) yields

$$\left[\mathbf{g}_0\frac{dC}{d\tau} + \mathbf{g}_1C + \left(\mathbf{g}_2 + \frac{3}{2}\mathbf{g}_3\right)C^3\right]\cdot\tilde{\mathbf{w}} = 0. \tag{5.45}$$

Rearranging and inserting $\mathbf{g}_0$ and $\mathbf{g}_1$ into the linear terms using (5.44a), we find

$$\frac{dC}{d\tau} = -\frac{\alpha_0\rho^*f^*_cu^*\left(\mathcal{D}_{0*}k^2 + \lambda\right)d'_*k^2}{\mathcal{D}_{0*}k^2\left(\mathcal{D}_{0*}k^2 + \lambda\right)^2 + \alpha_0\rho^*f^*_c\left[\mathcal{D}_{0*}k^2 - \left(2\mathcal{D}_{0*}k^2 + \lambda\right)u^*\frac{\mathcal{D}'_{0*}}{\mathcal{D}_{0*}}\right]}C - \frac{\left(\mathbf{g}_2 + \frac{3}{2}\mathbf{g}_3\right)\cdot\tilde{\mathbf{w}}}{\tilde{\mathbf{w}}\cdot\mathbf{g}_0}C^3. \tag{5.46}$$

The above ODE for $C(\tau)$ is the counterpart of (3.123) for the structured model. The linear terms are identical, as expected from the linear stability analysis. When

expressed in terms of the original model parameters, the expressions for the cubic coefficients are very lengthy. We therefore postpone a detailed comparison to the next section where we evaluate the expressions numerically and show that they differ quantitatively. The steady-states of (5.46) determine the local solution structure near the bifurcation point at $d'_* = 0$. We see that the instability occurs through a pitchfork bifurcation. Whenever the coefficients of the linear and nonlinear terms on the RHS have opposite sign, there are non-trivial steady-states given by

$$C = \pm\sqrt{-d'_* \frac{\alpha_0 \rho^* f_c^* u^*}{\mathcal{D}_{0*}\left(\mathcal{D}_{0*}k^2 + \lambda\right)\tilde{\mathbf{w}} \cdot \left(\mathbf{g}_2 + \frac{3}{2}\mathbf{g}_3\right)}}. \tag{5.47}$$

The above can be expressed in terms of the original bifurcation parameter $\mathcal{D}'_*$ using (5.23). We also eliminate C in favour of $\rho(x)$ using the expansion in (5.25a), as well as the solution for the $\mathcal{O}(\delta)$ term in (5.28) and (5.30). This leads to

$$\rho(x) = \rho^* \pm \mathcal{D}'_{0*}\sqrt{-\frac{\alpha_0 u^*(\mathcal{D}'_* - \mathcal{D}'_{0*})}{\tilde{\mathbf{w}} \cdot \left(\mathbf{g}_2 + \frac{3}{2}\mathbf{g}_3\right)}\left(\frac{\rho^* f_c^*}{\mathcal{D}_{0*}\left(\mathcal{D}_{0*}k^2 + \lambda\right)}\right)^3}\cos(kx) + \mathcal{O}(\mathcal{D}'_* - \mathcal{D}'_{0*}). \tag{5.48}$$

Eq. (5.48) describes the spatially non-uniform branch of steady-states that bifurcate from the uniform branch, near the bifurcation point. The counterpart from the structured model is given in (3.127). Eqs. (5.46) and (5.48) are the main results of this section. We compare these results with full numerical solutions of the governing equations in the following section, and find good agreement.

5.3 Comparisons with the Structured Model

In this section, we quantitatively and qualitatively compare the IMF and structured models. First, we provide detailed comparisons for the canonical LuxIR circuit from Chapter 3. We then briefly compare the models when the kinetics have multiple equilibria, as in Section 4.1, or a limit cycle as in Section 4.3.

5.3.1 Canonical LuxIR Kinetics

We consider the reaction kinetics $f(u, c)$ and secretion rate $\alpha(u)$ in (5.15). In order to facilitate numerical calculations, we choose a convenient form for the diffusion coefficient. In particular, we set

$$\mathcal{D}(u) = \mathcal{D}_* - (\mathcal{D}_* - \mathcal{D}_\infty)\tanh\left(\frac{-\mathcal{D}'_*}{\mathcal{D}_* - \mathcal{D}_\infty}(u - u^*)\right). \tag{5.49}$$

This definition ensures that $\mathcal{D}_* := \mathcal{D}(u^*)$ and $\mathcal{D}'_* := \mathcal{D}'(u^*)$ are independent parameters. It also ensures that the steady-states for $\rho(x)$ and $u(x)$ are smooth for the IMF model since there are non-uniform solutions of the form

$$\rho(x) \propto \frac{1}{\mathcal{D}(u(x))}, \tag{5.50}$$

as can be seen from the governing equation (5.16a). If we were to use our piecewise definitions from previous chapters, then either ρ or u (or potentially both) would be non-smooth.

The spatially uniform steady-states for the IMF model in (5.18) are the same as those for the structured model in (3.6)–(3.9), up to an exponentially small correction. In particular, the spatially uniform cell density ρ^* from the structured model is

$$\int_0^\infty n^*(u)\,\mathrm{d}u = \rho^* = \text{const.} \tag{5.51}$$

The mean internal concentration $\bar{u}$ in the structured model is defined by

$$\bar{u}(x,t) := \frac{1}{\rho(x,t)} \int_0^\infty u n(x,u,t)\,\mathrm{d}u, \tag{5.52}$$

which reduces to

$$\bar{u} = \frac{1}{\rho^*} \int_0^\infty u n^*(u)\,\mathrm{d}u = u^* + \text{E.S.T.}, \tag{5.53}$$

for the uniform steady state, where E.S.T. denotes exponentially small terms. Since u^* and c^* for the structured model satisfy (3.7) and (3.9), which read

$$f(u^*, c^*) = 0, \tag{5.54a}$$

$$\beta c^* = \alpha_0 \rho^* u^* + \text{E.S.T.}, \tag{5.54b}$$

the leading order terms are exactly the steady-state system for the IMF model in (5.18). As we showed in the previous section, the linear stability properties of the uniform state are also identical at leading order in ε.

In order to identify significant $\mathcal{O}(1)$ differences between the models, we consider spatially non-uniform solutions. We first discuss the case where QS represses motility, signified by $\mathcal{D}'_* < 0$. We demonstrate that the spatially non-uniform states near the bifurcation, as predicted by our weakly nonlinear analyses, are different for each model. To this end, we write the steady-state system for the locally-defined ODEs in (5.46) and (3.121a) as

$$0 = b_0 C_I + b_I C_I^3, \tag{5.55a}$$

$$0 = b_0 C_S + b_S C_S^3, \tag{5.55b}$$

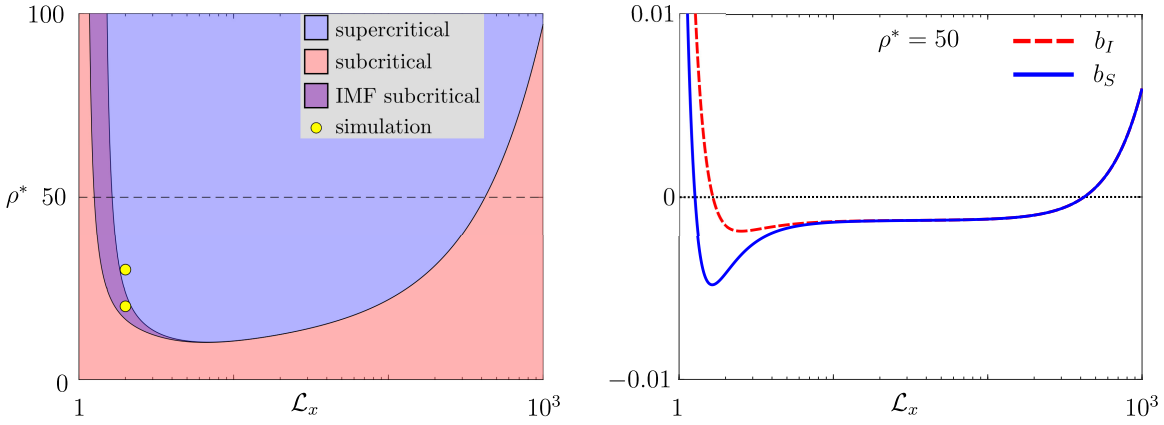

Figure 5.1: Left: Regions in parameter space showing bifurcation types (supercritical or subcritical pitchfork) for both models. The bifurcations are both supercritical (subcritical) in the blue (red) shaded regions. In the purple shaded region the bifurcation in the IMF model is subcritical but is supercritical in the structured model. There are no regions where the reverse occurs (IMF is supercritical and structured is subcritical). Bifurcation diagrams for the points marked with a circle are shown in Figure 5.2. Right: values of the cubic coefficients b_I and b_S in (5.55c) and (5.55d) along the slice $\rho^* = 50$ (dashed line left). The two models agree as the domain length is increased. Parameter values for this chapter are given in Table D.3.

where subscripts I and S denote IMF and structured models, respectively. The coefficients are given by

$$b_I := -\left(\mathbf{g}_2 + \frac{3}{2}\mathbf{g}_3\right) \cdot \tilde{\mathbf{w}}, \tag{5.55c}$$

$$b_S := -\left[\left(c_{20} + \frac{c_{22}}{2}\right) f^*_{cc} + \frac{f^*_{ccc}}{8}\right] I_2 + \left[\left(c_{20} + \frac{c_{22}}{2}\right) f^*_c + \frac{3}{8} f^*_{cc}\right] I_3 + f^*_c \left(I_4 + \frac{I_5}{2}\right), \tag{5.55d}$$

$$b_0 := -\frac{\alpha_0 \rho^* f^*_c u^* d'_*}{\mathcal{D}_{0*}(\mathcal{D}_{0*} k^2 + \lambda)}, \tag{5.55e}$$

where $\tilde{\mathbf{w}}$ and $\mathbf{g}_j$ are given in (5.38b) and (5.44), while c_{20}, c_{22}, and I_j are given in (3.109), (3.117), and (3.121). When expressed in terms of the original model parameters, Eqs. (5.55c)–(5.55d) are quite lengthy, making direct comparison cumbersome. Instead, we compute the boundaries in parameter space defined by $b_I = 0$ and $b_S = 0$, each signifying a transition between supercritical and subcritical pitchfork bifurcations in their respective models. This is accomplished numerically using pseudo arc-length continuation with the software package `Matcont` for `Matlab` [32]. The regions in $(\mathcal{L}_x, \rho^*)$ parameter space where the bifurcation is supercritical and subcritical are shown in Figure 5.1 along with values of b_I and b_S. We recall that $\mathcal{L}_x$ is the domain length.

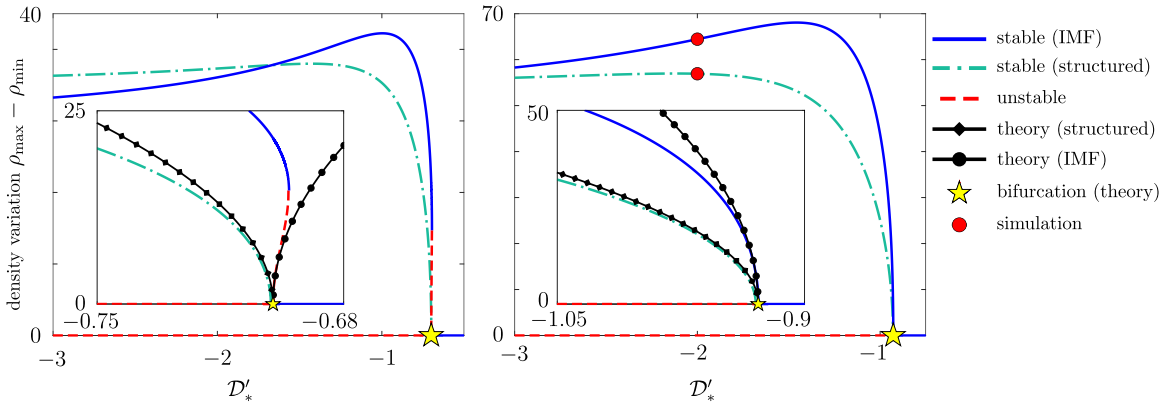

Figure 5.2: Bifurcation diagrams for the structured and IMF models when QS represses motility. Numerical results for the IMF and structured models are obtained from (5.15)–(5.17) and (5.49), and (3.1)–(3.4) and (5.49), respectively. The bifurcation point is given by (3.66) while theoretical solution branches near the bifurcation are given in (3.127) and (5.48). The spatially uniform branches display nearly identical linear stability properties, however the non-uniform branch differs both globally and locally near the bifurcation point. Left: Bifurcation is supercritical for the structured model and subcritical for the IMF model, corresponding to the point $(\mathcal{L}_x, \rho^*) = (2, 20)$ in the left panel of Figure 5.1. Right: Bifurcation is supercritical for both models $(\rho^*, \mathcal{L}_x) = (2, 30)$. Insets show the local behaviour near the bifurcation and agree well with theoretical results from our weakly nonlinear analysis. Red circles denote points where steady-state profiles are shown in Figure 5.3.

As seen in Figure 5.1, there are regions in parameter space where the type of bifurcation differs. We additionally observe that the values of the coefficients b_I and b_S differ in general, but they appear to agree for large domains. This agreement is linked to the fact that the two models agree for spatially uniform systems; the critical wavenumber $k = \pi/\mathcal{L}_x$ tends to zero in the limit of large domain length $\mathcal{L}_x$, which signifies small spatial gradients on solution branches near the bifurcation. Our observation that the two models agree in this limit can be verified analytically by comparing b_I and b_S in the limit of small critical wavenumber k. A straightforward but somewhat lengthy calculation yields

$$\lim_{k\to 0} \frac{b_I}{b_S} = 1, \tag{5.56}$$

where we note that this holds independently of our particular choice of $\mathcal{D}(u)$ in (5.49). In Figure 5.2, we provide example bifurcation diagrams for the points in parameter space marked by circles in Figure 5.1. There are clear differences both near the bifurcation and globally. Theoretical predictions from our linear and weakly nonlinear analysis are also shown to agree well with numerical results.

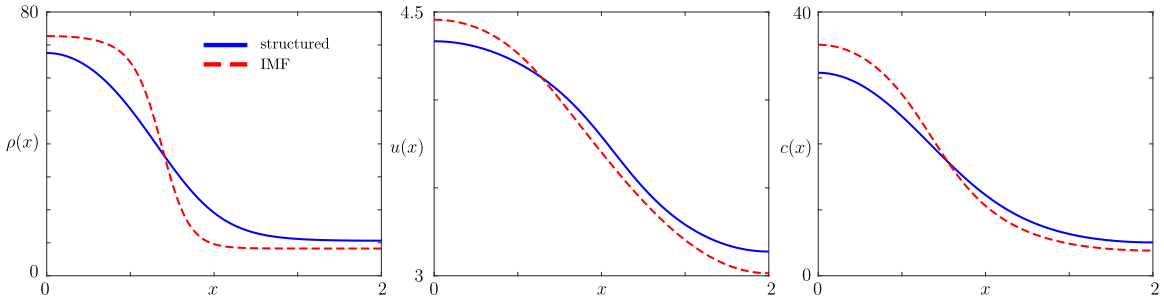

Figure 5.3: Typical steady-state profiles for the IMF and structured models. Results are shown for the points marked with red circles on the bifurcation diagram in Figure 5.2. Profiles for the IMF model are obtained from numerical solutions of (5.15)–(5.17) and (5.49), while profiles for the structured model are obtained from (3.1)–(3.4) and (5.49). Parameter values are given in Table D.3.

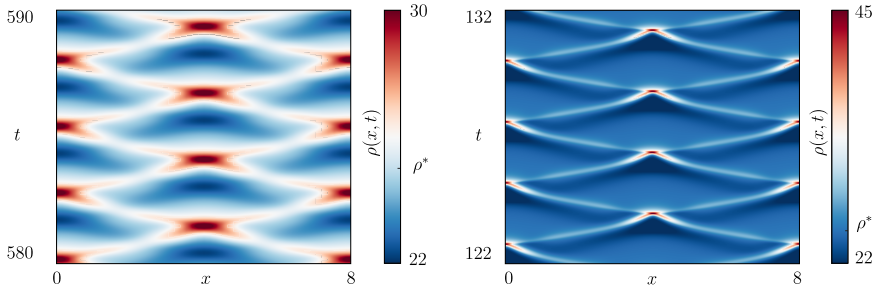

Figure 5.4: Spacetime diagrams of the limit cycles in both models with identical parameter values (as given in Table D.3). Numerical solutions for the IMF model are obtained from (5.15)–(5.17) and (5.49), while numerical solutions for the structured model are obtained from (3.1)–(3.4) and (5.49).

We show typical steady-state profiles for both models in Figure 5.3, showing quantitative, but not qualitative differences. Here we use the shorthand $u(x)$ to denote the mean internal concentration for both models. For the structured model, this is computed from (5.52). The transition layer between the high and low cell density regions is sharper for the IMF model. For the particular parameter set used in Figure 5.3, the IMF model overestimates all quantities in the high density region and underestimates them in the low density region; however, this is not always the case as the left bifurcation diagram in Figure 5.2 shows (e.g. for $\mathcal{D}'_* \in (-3, -2)$).

Finally, we briefly compare the spatio-temporal oscillations in Figure 5.4 when QS promotes motility. The models exhibit qualitatively similar behaviour, but there are clear quantitative differences. The wave patterns for the IMF model are more localised in space with larger amplitude than the structured model. The left- and right- travelling waves are clearly visible for the IMF model. The period of oscillation is similar for both models.

5.3.2 One-Component Kinetics

We now briefly compare the structured and IMF models for the GRN kinetics with two stable equilibria. We use the kinetics f and secretion rate α in (4.154), which we restate here for convenience:

$$f(u,c) = -\gamma(u - g_-(c))(u - u_0)(u - g_+(c)), \tag{5.57a}$$

$$g_\pm(c) = a_\pm + \frac{L_\pm c}{K_\pm + c}, \tag{5.57b}$$

$$\alpha(u) = \alpha_0 u, \tag{5.57c}$$

where the values of the parameters γ, u_0, $a_\pm$, $L_\pm$, $K_\pm$, and α_0 are given in Table D.2. On $\mathcal{O}(1)$ time scales, we expect the differences between the IMF and structured models to be similar to those for the LuxIR circuit in the previous section. The differences over long timescales are more significant as we show below.

First, we show that the steady-states of the IMF model correspond to quasi-steady states of the structured model. To see this, we recall that the quasi-steady states of the structured model are given in (4.18)–(4.19), which we repeat here for convenience

$$n_q(u) = \begin{cases} \rho_-^* \sqrt{\dfrac{f_u^-}{2\pi\varepsilon}} \left[1 + \mathcal{O}(\varepsilon)\right] \exp\left[-\dfrac{F_-(u,c_q)}{\varepsilon}\right] + \text{E.S.T.}, & 0 \le u < U, \\ \rho_+^* \sqrt{\dfrac{f_u^+}{2\pi\varepsilon}} \left[1 + \mathcal{O}(\varepsilon)\right] \exp\left[-\dfrac{F_+(u,c_q)}{\varepsilon}\right] + \text{E.S.T.}, & U \le u < \infty, \end{cases} \tag{5.58a}$$

$$c_q = \frac{1}{\beta}\left(\alpha(u_-)\rho_-^* + \alpha(u_+)\rho_+^*\right) + \mathcal{O}(\varepsilon), \tag{5.58b}$$

$$f(u_\pm, c_q) = 0, \tag{5.58c}$$

where

$$F_\pm(u,c) := -\int_{u_\pm}^{u} f(u,c)\,\mathrm{d}u, \tag{5.59}$$

and we have renamed $\rho_\pm$ to $\rho_\pm^*$ to unify notation with the IMF model. We note that the quasi-steady states of the structured model with either $\rho_-^* = 0$ or $\rho_+^* = 0$ are true steady-states. The steady-states of the IMF model are, from (5.4),

$$\rho_\pm^* = \text{const.}, \tag{5.60a}$$

$$f(u_\pm^*, c^*) = 0, \tag{5.60b}$$

$$\beta c^* = \sum_{j=\pm} \alpha_j \rho_j^*. \tag{5.60c}$$

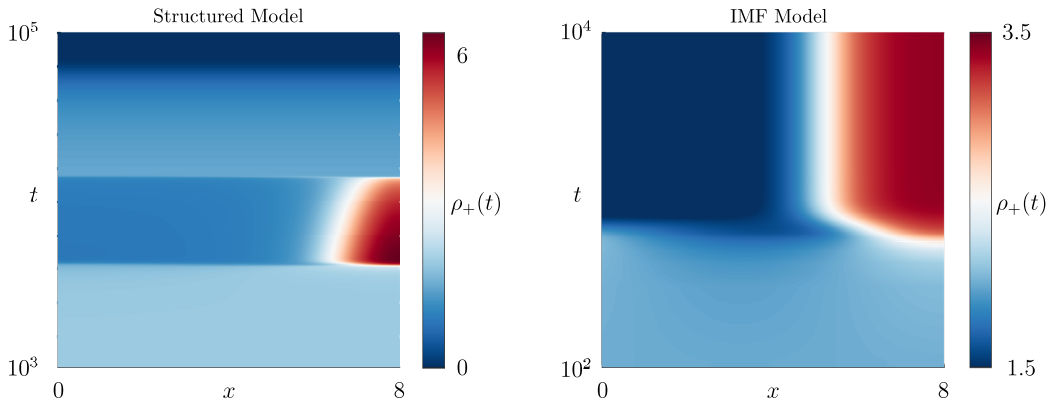

Figure 5.5: Qualitative comparison of MIPS in the structured and IMF models when the GRN kinetics have two equilibria. The IMF model fails to predict that MIPS can be transient. Results are obtained from a numerical solution of (5.1a)–(5.1c) and (5.1e)–(5.1f) for the IMF model (with scalar $\mathbf{u}_\pm = u_\pm$ and one spatial dimension), and (4.1)–(4.2) for the structured model. We use the kinetics f, diffusion coefficient $\mathcal{D}$, and secretion rate α in (4.159) and (5.57) for both models. Parameter values are the same as in Figure 4.6 (see also Table D.2).

Thus the leading order terms in (5.58b)–(5.58c) are the same as (5.60b)–(5.60c). Since $\rho_\pm^*$ in the quasi-steady states (5.58a) vary over exponentially long time scales (see Figure 4.4), we conclude that the uniform states of the two models agree over short $\mathcal{O}(1)$ times.

In terms of spatio-temporal dynamics, we expect that the instabilities in both models lead to qualitatively similar behaviour on $\mathcal{O}(1)$ time scales. We recall that the stability analyses for both models gave the same instability criterion. We also expect the differences in the non-uniform solutions to be qualitatively similar to the differences identified for the canonical LuxIR circuit in the previous section. We therefore focus on a comparison of the MIPS instability over exponentially long timescales.

The IMF model fails to predict delayed MIPS and transient MIPS. Delayed MIPS occurs in the structured model when slow variations in $\rho_\pm^*$ in the uniform state cause the system to transit through a bifurcation from a stable regime to an unstable regime. This situation is not possible in the IMF model since the corresponding uniform states are stable steady-states. Similarly, MIPS transients are not possible in the IMF model. A comparison of the two models for the same parameter set (but with a smooth version of $\mathcal{D}$) is shown in Figure 5.5. The MIPS state is transient in the structured model, but stable in the IMF model. In order for a MIPS transient to occur in the IMF model, the system would need to begin near a spatially uniform state, phase separate, and subsequently return to the same uniform state. Since the

uniform state must be linearly unstable for MIPS to occur, in general the system will not return to the same uniform state after MIPS.

5.3.3 Oscillatory Kinetics

Finally, we briefly compare the (spatially uniform) structured and IMF models when the GRN kinetics have a stable limit cycle. The IMF model here is simply an ODE system given by

$$\frac{d\mathbf{u}}{dt} = \mathbf{f}(\mathbf{u}, c), \tag{5.61a}$$

$$\frac{dc}{dt} = -\beta c + \alpha(\mathbf{u})\rho^*. \tag{5.61b}$$

As a simple but non-trivial example, we use the GRN kinetics and secretion rate given in (4.146) and (4.162), which we restate here as

$$\mathbf{f}(\mathbf{u}, c) = \begin{pmatrix} (\mu(c) - \tilde{u}^2 - \tilde{v}^2)\tilde{u} - \omega(\tilde{\mathbf{u}}, c)\tilde{v} \\ (\mu(c) - \tilde{u}^2 - \tilde{v}^2)\tilde{v} + \omega(\tilde{\mathbf{u}}, c)\tilde{u} \end{pmatrix}, \tag{5.61c}$$

$$\omega(\theta, c) = \frac{1}{2 + \cos(\theta - c)}, \tag{5.61d}$$

$$\mu(c) = \frac{1}{4} + \frac{c}{1 + c}, \tag{5.61e}$$

$$\alpha(\mathbf{u}) = \alpha_0 u^2, \tag{5.61f}$$

where we recall that $\tilde{\mathbf{u}} = \mathbf{u} - \mathbf{u}_0 = (\tilde{u}, \tilde{v})^T$ so that the internal concentrations $\mathbf{u}$ are positive near the limit cycle. We choose parameter values such that the trivial steady-state $\mathbf{u} = \mathbf{u}_0$ is unstable.

Since the IMF model (5.61) assumes that all cells have the same internal state, it cannot represent asynchronous oscillations. More specifically, our derivation in Chapter 2 assumes that the structured density $n(\mathbf{x}, \mathbf{u}, t)$ is exponentially localised at a single point in state space (but may vary in physical space in a non-uniform system). The limit cycle solution of the IMF model shown in Figure 5.6 therefore represents population-wide synchronous oscillations. The population cannot desynchronise according to the IMF model.

In contrast, the structured model retains the full distribution of internal states. Our analysis in Section 4.3 shows that the population has a tendency to slowly desynchronise in the absence of QS. This leads to asynchronous oscillations represented mathematically by a steady-state distribution $n^*(\mathbf{u})$. Accordingly, we defined the limit cycle as a periodic solution of (5.61a) with constant c, which is different than a periodic solution of the full ODE system (5.61) in general.

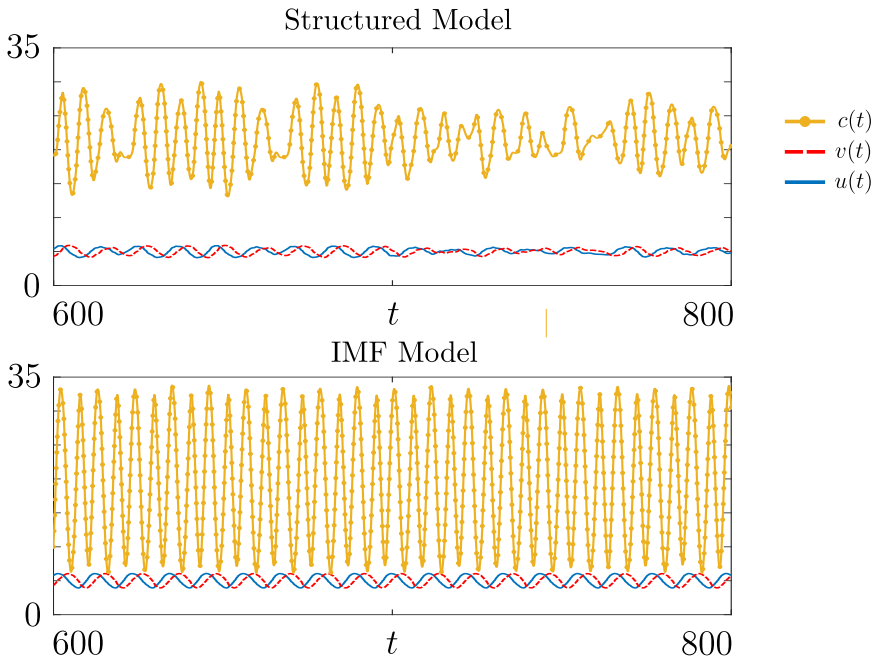

Figure 5.6: Comparison of partially synchronous oscillations in the structured model with synchronous oscillations in the IMF model. Numerical solutions for the IMF model are obtained from (5.61), while numerical solutions for the structured model are obtained from (4.73)–(4.74) and (5.61c)–(5.61f).

The instability in the steady-state of the structured model leads to partial synchronisation as we saw in Section 4.4.2. We compare this behaviour with the limit cycle of the IMF model in Figure 5.6, which shows clear differences. We conclude that the IMF model fails to approximate the structured model qualitatively and quantitatively when the GRN kinetics have a stable limit cycle. We expect even greater differences in spatially non-uniform systems.

Chapter 6

Conclusions and Future Work

6.1 Conclusion

In this thesis, we consider a population of motile bacteria where quorum sensing (QS) regulates motility. We characterise the effect of the gene-regulatory network (GRN) on emergent population-level patterning. We accomplish this through analysis and simulation of two continuum models, referred to as the structured model and the internal mean-field (IMF) model, which we formally upscale from a cell-level model.

Our formal derivation of the continuum models in Chapter 2 sheds light on the hidden assumptions of placing motile QS bacteria within the framework of active matter. Previously, QS interactions in active systems have been modelled by effective inter-particle forces [2, 45, 54]. Here, we show that this carries the assumption of fast chemical timescales compared to the timescale of tumbling or rotation. This scaling assumption is typically not satisfied in real biological systems, implying that living systems are not accurately represented in the framework of classical active matter. We recall our definition of classical active matter as an active system that interacts through physical forces with no QS nor gene-regulated motility. We address this issue in Chapter 2 by incorporating biologically realistic scaling regimes into the derivation of our continuum models.

On large lengthscales and timescales, motility-induced phase separation (MIPS) in classical active matter can only be triggered by variations in self-propulsion speed [20]. Here, we uncover a new route to MIPS on large lengthscales and timescales *via* genetic regulation of tumbling frequency or rotational diffusion. Additionally, when QS promotes motility, our models predict a new physical mechanism underlying the emergence of spatio-temporal oscillations in the cell density. This mechanism is an effective time-delay between variations in cell density and variations in motility. We expect that it has no counterpart in classical active systems since repulsive pairwise

forces act instantaneously and effectively *reduce* motility at the continuum level. We remark that similar spatio-temporal oscillations have been observed previously (see, e.g., [34,64,95]), but the mechanism is based on non-reciprocal interactions instead of an effective time-delay. We discuss possible future work on this front in the next section. We conclude that the new route to MIPS and the time-delay instability cannot be captured within the framework of classical active matter without incorporating the effect of QS and the GRN.

The effect of the GRN on emergent behaviour in active systems is not well-understood in general. Our work throughout this thesis addresses this issue by characterising emergent behaviour in an active system for various classes of GRN reaction kinetics. In general, the onset of emergent behaviour depends on the details of the GRN, which we have quantified through our instability criteria in Chapters 3–4. For relatively simple reaction kinetics with one steady-state, the population either phase separates or oscillates depending on whether QS represses or promotes motility. For more complicated GRNs with multiple steady-states, the transitions between steady-states due to noise in the GRN can lead to transient or delayed phase separation over long timescales. Additionally, QS can promote motility in some states and repress motility in others. This can lead to combinations of clustering and spatio-temporal oscillations. Overall, our work in this thesis links emergent population level behaviour with specific classes of cell-level GRNs.

Reaction-diffusion systems provide an attractive framework for modelling motile signalling bacteria. Such models have been used in previous studies [99]. However, the assumptions underlying these phenomenological models are not well-understood. Our work in this thesis characterises situations when a reaction-diffusion (IMF) model is appropriate, and when it fails. Broadly, if the GRN kinetics admit stable steady-states, then the IMF model can be qualitatively accurate; but if the GRN kinetics admit stable limit cycles, then the IMF model is qualitatively and quantitatively inaccurate. We discuss these two cases in more detail below.

When the GRN kinetics admit stable steady-states (e.g. the LuxIR circuit), then the IMF model is qualitatively accurate on $\mathcal{O}(1)$ timescales near a spatially uniform steady-state. It correctly predicts the uniform steady-states and the onset of emergent patterning. However, our weakly nonlinear analysis of the structured and IMF models demonstrates that the IMF model can mischaracterise bifurcations for small and intermediate-sized spatial domains. On longer timescales the structured model predicts delayed instabilities and transient phase separation, which the IMF model fails to capture.

When the GRN kinetics admit stable limit cycles (e.g. Fitzhugh-Nagumo kinetics), then the IMF model is inaccurate even for spatially uniform systems. The fundamental reason for this is that the IMF model effectively replaces the distribution of internal chemical states in the structured model with an 'average' state. Consequently, the population in the IMF model is inherently synchronised; it is unable to desynchronise. It therefore cannot reproduce the QS-induced partial synchronisation that we observe for the structured model. We expect that the differences between the two models will be even greater for spatially non-uniform systems. One possible remedy for the IMF model is to use more internal states so that asynchronous oscillations can be represented.

6.2 Future Work

A clear generalisation of the work in Section 4.3 is to consider spatially non-uniform populations. As a first step, it would be interesting to consider constant diffusion coefficients, representing the case where motility is not gene-regulated. It may be that this diffusion further destabilizes the uniform state, similar to a Turing instability [86]. From a theoretical perspective, this analysis is a straightforward generalisation of the current work. Next, we could consider gene-regulated motility in order to characterise motility-induced patterning. The key difference in this analysis would be in the solution of the recursive ODE system (4.139) in the linear stability analysis. Each equation would contain an additional term of the form $\mathcal{D}(s)k^2c_j^{(\ell)}(s)$, where $\mathcal{D}(s)$ is the gene-regulated diffusion coefficient evaluated on the limit cycle and k is a constant wavenumber. Although the equations are still exactly solvable with this extra term, it complicates the determination of the eigenvalues. It may be prudent to consider a truncated Fourier series representation of $\mathcal{D}$ and/or the coefficients $c_j^{(\ell)}$ in order to simplify the eigenvalue calculations.

It may also be interesting to investigate whether the orientational dynamics have a significant affect on motility-induced patterning, or if new types of patterning emerge. To accomplish this, we could modify the upscaling in Chapter 2 to retain the orientation field $\mathbf{p}(\mathbf{x}, \mathbf{u}, t)$ from (2.11) in the governing equations. The resulting structured model would include an additional equation for $\mathbf{p}$, and it is straightforward to generalise the IMF model. If we restrict our analysis to GRN kinetics with stable equilibria and consider only $\mathcal{O}(1)$ timescales, then the (much simpler) IMF model would be appropriate. Our analytical techniques should remain valid for both models (see the Supplemental Material of [77]).

The main challenge with the above generalisations is that numerical solution of the structured governing equations would be computationally intensive. Because solutions are typically exponentially localised, it may be possible to speed up the calculations using adaptive mesh refinement (AMR). This would require a new method for handling the non-local (in $\mathbf{u}$) secretion term (see Appendix C). The `oomph-lib` library contains several built-in routines for AMR that may be applicable to our system [1, 49]. It may therefore be possible to modify our current implementation with `oomph-lib` to incorporate AMR.

In terms of biological extensions, our model could be generalised to include multiple types of AI signalling molecules or multiple bacterial species. This extension is motivated by the experimental setup in [23], which shows patterning in a population consisting of two different strains of engineered *E. coli* with mutual motility regulation. This system is an example of active matter with non-reciprocal interactions since each strain responds differently to chemical signals. Non-reciprocal active systems have been shown to exhibit a range of novel dynamical behaviour when the interactions consist of steric repulsion or volume exclusion [34,64,95]. It may be worthwhile to investigate whether there are significant differences when the interactions are mediated by QS. It is also well-known that bacteria use multiple 'channels' of communication *via* secretion of multiple types of AI, even within the same species [6, 70]. Some studies have investigated the effect of this on QS behaviour [71, 72]. It would be interesting to study the effect of multiple AI signals on motility-induced patterning.

Real populations of bacteria reproduce through cell division and die. A simple way of including these effects in our model is to include an *ad hoc* logistic growth term to the density equation (2.14a). The model would still admit a spatially uniform state and our analysis techniques would remain applicable. In principle, such a model should be capable of reproducing the experimentally observed concentric ring patterns in [58].

In this work we ignore the effect of steric interactions between cells, but it would be interesting to investigate its role in emergent patterning. We expect this effect to be significant at large volume fractions of cells. One way to tackle this challenge would be to adapt the upscaling approaches from [13, 16]. Intuitively, it is reasonable to assume that steric interaction does not directly depend on QS (and *vice versa*). We therefore expect the strategies for handling pairwise interactions to remain valid when QS interactions are present.

Appendix A

Laplace's Method

Laplace's method is a technique for approximating integrals. In its simplest form, it applies to integrals of the form (see e.g. [50], Ch. 3)

$$I := \int_{t_-}^{t_+} g(t) \exp\left(\frac{\phi(t)}{\varepsilon}\right) \mathrm{d}t, \tag{A.1}$$

where $\varepsilon \ll 1$ and the quantities $g(t)$, $\phi(t)$, t_-, and t_+ do not depend on ε. This technique is essential in our steady-state, linear, and weakly nonlinear analyses in Chapters 3–4. In this appendix, we derive and list several variants and generalisations of the method that are used in the main text.

A.1 Single-Variable Versions

We begin with the standard Laplace's method for a single variable. For the cases required in the main text, $\phi(t)$ and $g(t)$ are smooth functions on (t_-, t_+), where $t_\pm$ may be infinite. We additionally assume that $\phi(t)$ has a global maximum at some $t_* \in (t_-, t_+)$ and we assume that $\phi(t_*) = 0$ without loss of generality since any non-zero value can be absorbed into g. We additionally assume that t_* is not near the boundary, i.e. $|t - t_\pm| \gg \varepsilon^{1/2}$. Thus $\phi(t)$ is locally quadratic near t_* and the integrand is exponentially small for $|t - t_*| \gg \mathcal{O}(\varepsilon^{1/2})$. We therefore write (A.1) as

$$I = \left(\int_{t_-}^{t_*-\delta} + \int_{t_*-\delta}^{t_*+\delta} + \int_{t_*+\delta}^{t_+}\right) g(t) \exp\left(\frac{\phi(t)}{\varepsilon}\right) \mathrm{d}t, \tag{A.2}$$

where $\varepsilon^{1/2} \ll \delta \ll 1$. The integrands for the first and last terms are exponentially small. Their contribution to I is also exponentially small even if $t_- = -\infty$ and/or $t_+ = \infty$ (we assume that I is finite).

The dominant contribution to I is the middle term in (A.2) since the integrand is $\mathcal{O}(1)$ when $t - t_* = \mathcal{O}(\varepsilon^{1/2})$. Since $\delta \ll 1$, we can Taylor expand g and ϕ as

$$g(t) = g_* + (t-t_*)g'_* + \frac{1}{2!}(t-t_*)g''_* + \mathcal{O}((t-t_*)^3), \tag{A.3a}$$

$$\phi(t) = \frac{1}{2!}(t-t_*)^2\phi''_* + \frac{1}{3!}(t-t_*)^3\phi'''_* + \frac{1}{4!}(t-t_*)^4\phi''''_* + \mathcal{O}((t-t_*)^5), \tag{A.3b}$$

where subscript '$*$' denotes evaluation at t_*. Enough terms are retained in the Taylor series for a two-term asymptotic expansion of I. Inserting (A.3) into (A.2) and using the change of variables

$$y = (t-t_*)\sqrt{\frac{|\phi''_*|}{2\varepsilon}}, \tag{A.4}$$

leads to

$$\begin{aligned} I =& \sqrt{\frac{2\varepsilon}{|\phi''_*|}} \int_{y_-}^{y_+} \left[g_* + g'_* \sqrt{\frac{2\varepsilon}{|\phi''_*|}} y + \frac{g''_* y^2}{|\phi''_*|}\varepsilon + \mathcal{O}(\varepsilon^{3/2}y^3) \right] e^{-y^2} \\ & \times \exp\left[\frac{\phi'''_*}{3!} \left(\frac{2}{|\phi''_*|} \right)^{3/2} y^3 \varepsilon^{1/2} + \frac{\phi''''_*}{4!} \left(\frac{2}{|\phi''_*|} \right)^2 y^4 \varepsilon + \mathcal{O}(\varepsilon^{3/2}y^5) \right] \mathrm{d}y, \end{aligned} \tag{A.5}$$

where

$$y_\pm := \pm\delta \sqrt{\frac{|\phi''_*|}{2\varepsilon}}, \tag{A.6}$$

and we have used the fact that $\phi''_* < 0$ for a local maximum at t_*.

So far we have assumed that δ satisfies $\varepsilon^{1/2} \ll \delta \ll 1$. The next step is to restrict this range so that the terms in the second exponential in (A.5) are small. Since the maximum absolute value of y is $|y_\pm| = \mathcal{O}(\delta/\sqrt{\varepsilon})$, we impose $\varepsilon^{1/2} \ll \delta \ll \varepsilon^{1/3}$. Taylor expanding this exponential, we obtain

$$\begin{aligned} I =& \sqrt{\frac{2\varepsilon}{|\phi''_*|}} \int_{y_-}^{y_+} \left[g_* + g'_* \sqrt{\frac{2\varepsilon}{|\phi''_*|}} y + \frac{g''_* y^2}{|\phi''_*|}\varepsilon + \mathcal{O}(\varepsilon^{3/2}y^3) \right] e^{-y^2} \\ & \times \left[1 + \frac{\phi'''_*}{3!} \left(\frac{2}{|\phi''_*|} \right)^{3/2} \varepsilon^{1/2} y^3 + \frac{\phi''''_*}{3!|\phi''_*|^2}\varepsilon y^4 + \frac{4(\phi'''_*)^2}{(3!)^2|\phi''_*|^3}\varepsilon y^6 + \mathcal{O}(\varepsilon^{3/2}y^5) \right] \mathrm{d}y. \end{aligned} \tag{A.7}$$

Since $|y_\pm| \gg 1$, the integrand is exponentially small for $|y| \geq y_\pm$. We can therefore replace the limits of integration $y_\pm$ with $\pm\infty$ at the cost of introducing an exponentially small error. The integral can then be evaluated explicitly using the identity

$$\int_{-\infty}^{\infty} y^{2n} e^{-y^2} \, \mathrm{d}y = \sqrt{\pi} \frac{(2n-1)!!}{2^n}, \tag{A.8}$$

where n is a positive integer. After some algebra, we obtain a two-term asymptotic expansion for I:

$$I = \sqrt{\frac{2\pi\varepsilon}{|\phi_*''|}}\left[g_* + \frac{\varepsilon}{2|\phi_*''|}\left(g_*'' + \frac{g_*'\phi_*'''}{|\phi_*''|} + \frac{g_*\phi_*''''}{4|\phi_*''|} + \frac{5!!g_*(\phi_*''')^2}{(3!)^2|\phi_*''|^2}\right) + \mathcal{O}(\varepsilon^2)\right]. \tag{A.9}$$

Eq. (A.9) is the first main result of this Appendix. We note that the leading order term in (A.9) can be found in standard texts on asymptotic analysis (see e.g. [50], Ch. 3).

Next, we derive a three-term asymptotic expansion for I in the case where $\phi(t)$ is a quadratic. This result is needed for our weakly nonlinear analysis in Chapter 3. To derive this result, we must retain terms in the Taylor series of $g(t)$ in (A.3a) up to quartic order. This leads to a version of (A.5) where the second exponential is equal to one (because ϕ is exactly quadratic), so there is no need to further restrict δ. The terms inside the first set of brackets now contain terms up to y^4. Replacing the limits with $\pm\infty$ and integrating term-by-term yields

$$I = \sqrt{\frac{2\pi\varepsilon}{|\phi_*''|}}\left[g_* + \frac{g_*''}{2|\phi_*''|}\varepsilon + \frac{g_*''''}{8(\phi_*'')^2}\varepsilon^2 + \mathcal{O}(\varepsilon^3)\right], \tag{A.10}$$

which is the second main result of this Appendix.

A.2 Two-Variable Versions

Next, we consider a two-dimensional generalisation of (A.1) of the form

$$I = \int_\Omega g(\mathbf{t})\exp\left(\frac{\phi(\mathbf{t})}{\varepsilon}\right)\,\mathrm{d}\mathbf{t}, \tag{A.11}$$

where $\Omega \subset \mathbb{R}^2$ and ϕ is a quadratic. This integral is needed in the analysis of the two-component kinetics in Section 4.2. We assume that ϕ has a global maximum at $\mathbf{t} = \mathbf{0}$ and that $\phi(0) = 0$ without loss of generality.

We begin by rewriting I as

$$I = \left(\int_{\Omega/\mathcal{D}} + \int_{\mathcal{D}}\right) g(\mathbf{t})\exp\left(\frac{\phi(\mathbf{t})}{\varepsilon}\right)\,\mathrm{d}\mathbf{t}, \tag{A.12}$$

where

$$\mathcal{D} := [-\delta, \delta]^2 \subset \Omega, \tag{A.13}$$

and $\varepsilon^{1/2} \ll \delta \ll 1$. This is possible as long as $\mathbf{t} = \mathbf{0}$ is an $\mathcal{O}(1)$ distance from the boundary, which is true for the cases considered in the main text. The dominant

contribution to I is from the second term in (A.12). Since ϕ is quadratic and vanishes at the origin, we write

$$\phi(\mathbf{t}) = (t_1, t_2)^T \Phi(t_1, t_2), \quad \Phi := \begin{pmatrix} \phi_1 & \phi_2 \\ \phi_2 & \phi_3 \end{pmatrix}, \tag{A.14}$$

where $\mathbf{t} = (t_1, t_2)^T$. Next, we make the change of variables

$$\mathbf{t} = \frac{\mathbf{v}_-}{\sqrt{-\lambda_-}} x + \frac{\mathbf{v}_+}{\sqrt{-\lambda_+}} y, \tag{A.15}$$

where $(\lambda_j, \mathbf{v}_j)$ are eigenpairs of Φ. The matrix Φ must be negative definite for a local maximum at the origin (and for I to be finite), so both eigenvalues are negative. Note that Φ is real symmetric so the eigenvectors $\mathbf{v}_\pm$ can be chosen orthonormal. Thus (A.12) becomes

$$I = \frac{1}{\sqrt{\det \Phi}} \int_{\tilde{\mathcal{D}}} g(\mathbf{x}) \exp\left(-\frac{|\mathbf{x}|^2}{\varepsilon}\right) \mathrm{d}\mathbf{x}, \tag{A.16}$$

where $\mathbf{x} = (x, y)^T$ and $\tilde{\mathcal{D}}$ is the image of $\mathcal{D}$ under the transformation (A.15). For convenience, we use the shorthand $g(\mathbf{x}) = g(\mathbf{t}(x, y))$. Next, we Taylor expand g up to quadratic terms and replace $\tilde{\mathcal{D}}$ with $\mathbb{R}^2$ at the cost of introducing an exponentially small error. Then integrating (A.16) term-by-term, we obtain

$$I = \frac{\pi\varepsilon}{\sqrt{\det \Phi}} \left(g + \frac{\varepsilon}{4} \nabla_{\mathbf{x}}^2 g + \mathcal{O}(\varepsilon^2)\right)\Big|_{\mathbf{t}=\mathbf{0}}. \tag{A.17a}$$

The Laplacian term is taken with respect to the transformed variables x and y, so changing back to the original $\mathbf{t}$ variable, we have

$$\begin{aligned} \nabla_{\mathbf{x}}^2 g = &- \left[\frac{(v_{1-})^2}{\lambda_-} + \frac{(v_{1+})^2}{\lambda_+}\right] \frac{\partial^2}{\partial {t_1}^2} - 2\left(\frac{v_{1-}v_{2-}}{\lambda_-} + \frac{v_{1+}v_{2+}}{\lambda_+}\right) \frac{\partial^2}{\partial t_1 \partial t_2} \\ &- \left[\frac{(v_{2-})^2}{\lambda_-} + \frac{(v_{2+})^2}{\lambda_+}\right] \frac{\partial^2}{\partial {t_2}^2}, \end{aligned} \tag{A.17b}$$

where $v_{j\pm}$ are the components of $\mathbf{v}_\pm$. Eq. (A.17) is the third result of this Appendix.

Even though we have assumed that ϕ is globally quadratic in deriving (A.17), the leading order term is valid even if ϕ is only locally quadratic. To see this, we Taylor expand ϕ in (A.12) and make the change of variables

$$\mathbf{t} = \varepsilon^{1/2} \left(\frac{\mathbf{v}_-}{\sqrt{-\lambda_-}} x + \frac{\mathbf{v}_+}{\sqrt{-\lambda_+}} y\right). \tag{A.18}$$

This yields

$$I = \frac{\varepsilon}{\sqrt{\det \Phi}} \int_{\tilde{\mathcal{D}}} \left[g(0) + \mathcal{O}(|\mathbf{x}\varepsilon^{1/2}|)\right] \exp\left[-|\mathbf{x}|^2 + \mathcal{O}(|\mathbf{x}|^3 \varepsilon^{3/2})\right] \mathrm{d}x\mathrm{d}y, \tag{A.19}$$

where now $\tilde{\mathcal{D}}$ is the image of $\mathcal{D}$ under (A.18). From (A.13) and (A.18), the maximum value of $|\mathbf{x}|$ on $\tilde{\mathcal{D}}$ is of order $\mathcal{O}(\delta\varepsilon^{-1/2})$, so we can Taylor expand the exponential provided that $\delta \ll \varepsilon^{1/3}$ (in addition to the original restriction $\varepsilon^{1/2} \ll \delta$). Retaining only the leading order term gives

$$I = \frac{\varepsilon}{\sqrt{\det \Phi}} g(0) \int_{\tilde{\mathcal{D}}} \big(1 + \mathcal{O}(\varepsilon|\mathbf{x}|^2)\big) e^{-|\mathbf{x}|^2} \, \mathrm{d}x\mathrm{d}y. \tag{A.20}$$

Finally, replacing $\tilde{\mathcal{D}}$ with $\mathbb{R}^2$, we obtain the fourth (and final) key result of this appendix:

$$I = \frac{\pi\varepsilon}{\sqrt{\det \Phi}} g(0) + \mathcal{O}(\varepsilon^2), \tag{A.21}$$

where we note that the leading order term agrees with the case where ϕ is globally quadratic (A.17).

Appendix B

Analysis of the Phase Equation for Two Internal Chemicals

In Section 4.2, we obtained a nonlinear PDE for the phase ϕ in our WKBJ approximation. By performing a local expansion, we found that the quadratic coefficients ϕ_1, ϕ_2, and ϕ_3 satisfy a coupled system of quadratic equations. They read

$$2\phi_1^2 + 2\phi_2^2 - \mu_{11}\phi_1 - \mu_{21}\phi_2 = 0, \tag{B.1a}$$

$$4\phi_2(\phi_1 + \phi_3) - \mu_{12}\phi_1 - (\mu_{11} + \mu_{22})\phi_2 - \mu_{21}\phi_3 = 0, \tag{B.1b}$$

$$2\phi_2^2 + 2\phi_3^2 - \mu_{12}\phi_2 - \mu_{22}\phi_3 = 0, \tag{B.1c}$$

where μ_{ij} are constants that satisfy

$$\operatorname{Tr}\mathbf{J} < 0, \quad \det\mathbf{J} > 0, \quad \mathbf{J} := \begin{pmatrix} \mu_{11} & \mu_{12} \\ \mu_{21} & \mu_{22} \end{pmatrix}. \tag{B.2}$$

The purpose of this Appendix is to argue that there is only one real-valued solution of (B.1) with $\det\Phi \neq 0$, where

$$\Phi := \begin{pmatrix} \phi_1 & \phi_2 \\ \phi_2 & \phi_3 \end{pmatrix}. \tag{B.3}$$

Bézout's theorem implies that there are eight solutions of (B.1), some of which may be complex. One non-trivial solution can be obtained by seeking a solution in the form $2\operatorname{Tr}\phi = \operatorname{Tr}\mathbf{J}$. This leads to the solution in Eq. (4.44) considered in the main text. The other solutions are found by solving (B.1a) and (B.1c) for ϕ_1 and ϕ_3 in terms of ϕ_2, which yields

$$\phi_1 = \frac{\mu_{11}}{4} \pm \frac{1}{2}\sqrt{\frac{\mu_{11}^2}{4} - 4\phi_2^2 + \mu_{21}\phi_2}, \tag{B.4a}$$

$$\phi_3 = \frac{\mu_{22}}{4} \pm \frac{1}{2}\sqrt{\frac{\mu_{22}^2}{4} - 4\phi_2^2 + \mu_{12}\phi_2}. \tag{B.4b}$$

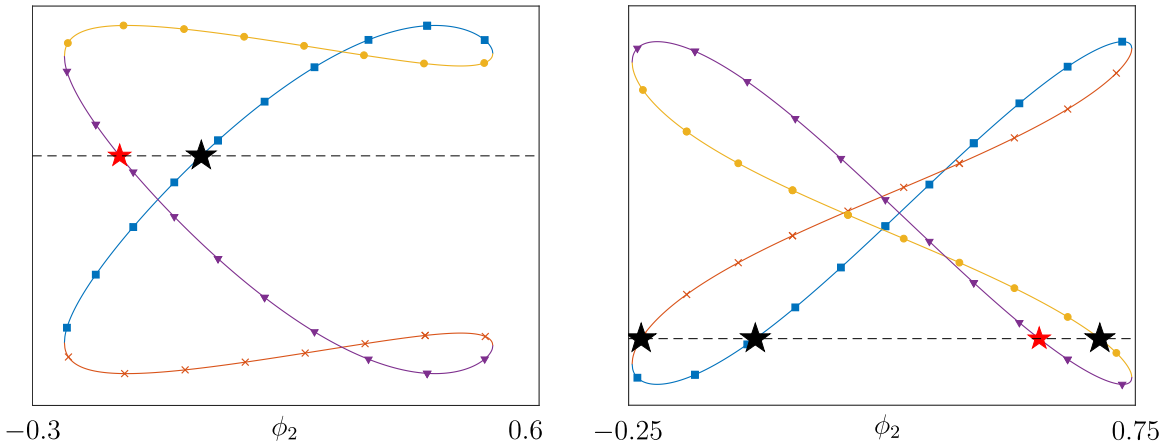

Figure B.1: Plots of the LHS of (B.5a) for two different parameter sets. The four combinations of $\pm$ are shown as different linestyles. Real solutions are denoted by stars, with the small red star corresponding to the solution in (4.44) of the main text. The solutions denoted by black stars have $|\det \Phi| < 10^{-16}$, which we take as evidence that $\det \Phi$ vanishes for the exact solutions. We use $\mu_{11} = -5$, $\mu_{12} = 1$, $\mu_{21} = -5$, and $\mu_{22} = -1.7$ for left panel and $\mu_{11} = -5$, $\mu_{12} = 1$, $\mu_{21} = 1.5$, and $\mu_{22} = -1.7$ for the right panel. Both parameter sets satisfy (B.2).

Substituting into (B.1b), we obtain

$$\pm\left(2\phi_2 - \frac{\mu_{12}}{2}\right) a(\phi_2) \pm \left(2\phi_2 - \frac{\mu_{21}}{2}\right) b(\phi_2) - \frac{\mu_{12}\mu_{11} + \mu_{21}\mu_{22}}{4} = 0, \tag{B.5a}$$

$$a(\phi_2) := \sqrt{\frac{\mu_{11}^2}{4} - 4\phi_2^2 + 2\mu_{21}\phi_2}, \tag{B.5b}$$

$$b(\phi_2) := \sqrt{\frac{\mu_{22}^2}{4} - 4\phi_2^2 + 2\mu_{12}\phi_2}, \tag{B.5c}$$

where any of the (four) combinations of $\pm$ signs can be taken. Thus (B.5) constitutes four independent equations for ϕ_2. We solve each numerically with a combination of binary searches and Newton iteration. We note for real-valued solutions, the terms inside the square roots in (B.4) must be positive. This restricts the range of ϕ_2 to a finite interval, so it is straightforward to exactly determine the number of real-valued solutions for a given parameter set. This is illustrated in Figure B.1 showing a plot of the LHS of (B.5a).

We solve (B.5) for a number of parameter sets satisfying (B.2). In some cases, we find only the trivial solution and the solution with $2\,\mathrm{Tr}\,\Phi = \mathrm{Tr}\,\mathbf{J}$. For some parameter sets, we find two additional solutions, but we observe numerically that they always satisfy $\det \Phi = 0$ with a high degree of accuracy. We therefore argue that the only real-valued solution having $\det \Phi \neq 0$ is the one considered in the main text.

Appendix C

Description of Numerical Methods

In this appendix we describe the general implementation of the numerical solution of the governing equations for the structured and IMF models. For all calculations, we use the open-source finite-element library `oomph-lib` for C++ [49]. The `oomph-lib` package has built-in implementations for many standard PDEs. Our model equations do not fit exactly into any of these implementations, so we develop custom codes that still use the `oomph-lib` framework. This involves reformulating the governing equations in weak form and explicitly discretising the problem. Broadly, we use a Galerkin finite element method with quadratic Lagrange elements and a BDF2 time-stepping scheme. We describe the details below.

To illustrate the process, we describe the method for the structured model with one internal chemical and one spatial dimension. The governing equations in this case are

$$\frac{\partial n}{\partial t} = \mathcal{D}(u)\frac{\partial^2 n}{\partial x^2} + \varepsilon\frac{\partial^2 n}{\partial u^2} - \frac{\partial}{\partial u}\left[f(u,c)n\right], \quad x \in \Omega, \quad u \in \mathbb{R}_+, \tag{C.1a}$$

$$\frac{\partial c}{\partial t} = D_c\frac{\partial^2 c}{\partial x^2} - \beta c - \int_0^\infty \alpha(u)n\,\mathrm{d}u, \quad x \in \Omega, \tag{C.1b}$$

where $\Omega := (0, \mathcal{L})$. The boundary conditions are

$$\varepsilon\frac{\partial n}{\partial u} - f(u,c)n \to 0, \quad u \to 0, \infty, \tag{C.2a}$$

$$\frac{\partial n}{\partial x} = \frac{\partial c}{\partial x} = 0, \quad x = 0, \mathcal{L}. \tag{C.2b}$$

We discretise in time first, and space second (Rothe's method). In the following we use the notation $\Delta(\cdot)/\Delta t$ to denote the discretised time derivative. The temporal discretising is done using the (implicit) BDF2 method, so

$$\frac{\partial n}{\partial t} \approx \frac{\Delta n_j}{\Delta t} = \frac{3}{2\Delta t}\left(n_j - \frac{4}{3}n_{j-1} + \frac{1}{3}n_{j-2}\right), \tag{C.3}$$

where the subscript j denotes evaluation at $t = t_j$. Since this scheme requires two history values, we must provide an initial condition at $t_0 = 0$ and a solution at the first time-step $t = t_1$. Here we simply choose a small value of t_1 and provide the same initial condition for the first two time levels, each polluted with different realisations of small amplitude noise. All of our simulations in this thesis begin from a spatially uniform state, so the noise is added to excite as many modes as possible.

In all simulations, we use an adaptive time-step with a specified level of accuracy. For most of our simulations, we impose a relative error of no more than 10^{-5} per time-step. Our rule of thumb in choosing the relative error is to make it small enough that the numerically computed bifurcation points do not change significantly as the time-step is decreased. We also ensure that the total mass in the solution remains constant in time up to the precision with which the solution is recorded (recall that (C.1a) conserves the integral of n over the composite domain $\bar{\Omega} := \Omega \times \mathbb{R}_+$).

The temporal error estimate is computed with built-in `oomph-lib` functions. According to the documentation (see [1]), a predictor-corrector method is used in which a lower-order explicit time-stepping scheme is used to calculate a prediction on each node in the spatial mesh (see below for the spatial discretisation). Then the error is estimated using the difference between this prediction and the actual value computed using the implicit BDF2 scheme. The global error, defined as the RMS of the errors at each node, is used to control the size of the time-step.

In order to derive a weak form of (C.1), we multiply (C.1a) by a test function ψ and integrate over the composite domain $\bar{\Omega}$. We then use integration by parts to rewrite the second derivatives, as well as the boundary conditions (C.2) to eliminate the boundary terms. Inserting the BDF2 discretisation (C.3), we obtain the weak form: find $n_j(x,u) \in H^1(\bar{\Omega})$ such that n_j satisfies

$$\int_{\bar{\Omega}} \psi \frac{\Delta n_j}{\Delta t} d\xi + \varepsilon \int_{\bar{\Omega}} \frac{\partial \psi}{\partial u} \frac{\partial n_j}{\partial u} d\xi + \int_{\bar{\Omega}} \mathcal{D}(u) \frac{\partial \psi}{\partial x} \frac{\partial n_j}{\partial x} d\xi - \int_{\bar{\Omega}} \frac{\partial \psi}{\partial u} f(u, c_j) n_j d\xi = 0, \quad \text{(C.4a)}$$

for all test functions $\psi \in H^1(\bar{\Omega})$ with compact support. Here $H^1(\bar{\Omega})$ is the (Sobolev) space of functions such that the function and its weak first derivatives have finite L^2 norm on $\bar{\Omega}$. Similarly, for (C.1b) we have the weak formulation: find $c_j \in H^1(\bar{\Omega})$ such that it satisfies

$$\int_{\bar{\Omega}} \psi \frac{\Delta c_j}{\Delta t} d\xi + D_c \int_{\bar{\Omega}} \frac{\partial \psi}{\partial x} \frac{\partial c_j}{\partial x} d\xi + \beta \int_{\bar{\Omega}} \psi c_j d\xi - \int_{\bar{\Omega}} \psi \bar{\alpha}_j d\xi = 0, \quad \text{(C.4b)}$$

for all test functions $\psi \in H^1(\bar{\Omega})$ with compact support. Here we define $\bar{\alpha}_j$ as

$$\bar{\alpha}_j(x) := \int_{\mathbb{R}_+} \alpha(u) n_j(x,u) du. \quad \text{(C.4c)}$$

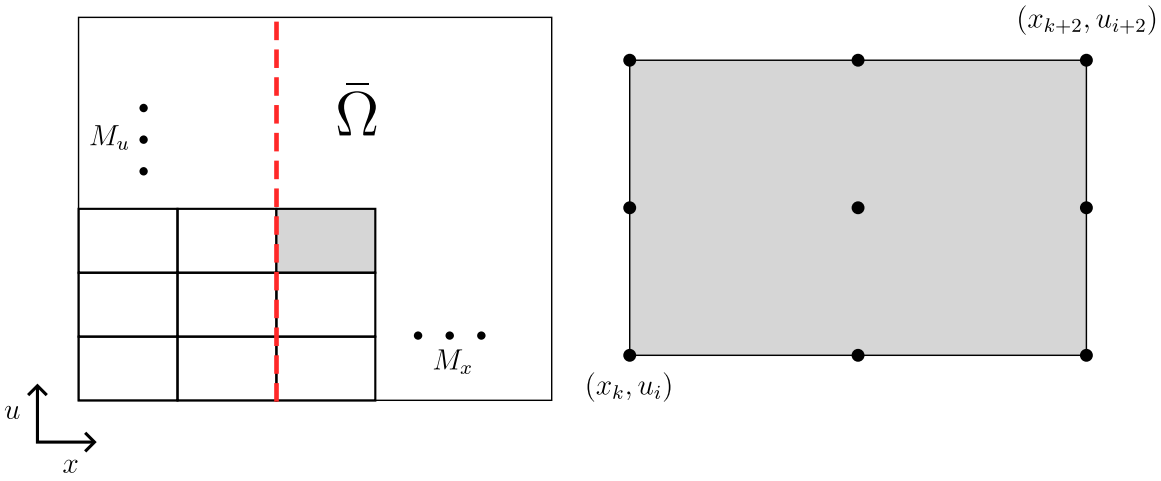

Figure C.1: Left: Mesh of rectangular elements on $\bar{\Omega}$. For n_j, we use M_u elements in the u direction and M_x in the x direction. For c_j, we use only 1 element in u and M_x in x. The red dashed line denotes an example integration path for computing $\bar{\alpha}_j(x_k)$ in (C.6d); it passes through the (equally spaced) nodes at x_k. Right: Individual rectangular element. We use Lagrange elements with piecewise quadratic basis functions (9 nodes per element).

We have extended the domain of (C.1b) to include both u and x. Given our mathematical system, we are only interested in solutions where $c_j = c_j(x)$ is independent of u. As long as we ensure that the initial conditions c_0 and c_1 are independent of u, the solution c_j will remain independent of u for all j. We also verify *a posteriori* for all calculations that this is the case.

Next, we discretise the weak form (C.4). Since $\bar{\Omega}$ is semi-infinite, we truncate the domain in the u-coordinate at a sufficiently large value of u. The error in doing so is very small since n decays rapidly at large u. To ease notation, we hereafter use $\bar{\Omega}$ to denote the truncated domain. We discretise space by replacing the infinite dimensional space $H^1(\bar{\Omega})$ with a finite dimensional subspace. Since we seek solutions for which c_j is independent of u, it is efficient from a computational perspective to use different finite dimensional solution spaces for n_j and c_j. This approach is called a multi-domain method. Let us denote these finite dimensional subspaces as V_n and V_c. Thus we now seek a solution $n_j \in V_n$ that satisfies (C.4a) for all test functions $\psi \in V_n$, and a solution $c_j \in V_c$ satisfying (C.4b) for all test functions $\psi \in V_c$.

A multi-domain approach enables us to use different meshes for n_j and c_j. For reasons that will become apparent below, we select meshes consisting of rectangular Lagrange elements (see Figure C.1). For n_j, we use a mesh with $M_x \times M_u$ elements, where M_x and M_u are the number of elements in the x and u directions. For c_j, we instead use $M_x \times 1$ elements since c_j must be independent of u. We fix V_n and V_c as

spaces of continuous piecewise quadratics on the meshes. The solutions n_j and c_j can be expressed as

$$n_j(x,u) = \sum_{i=1}^{K_n} N_i^j \psi_i^n(u,x), \tag{C.5a}$$

$$c_j(x,u) = \sum_{i=1}^{K_c} C_i^j \psi_i^c(u,x), \tag{C.5b}$$

where ψ_i^n and ψ_i^c form a basis of V_n and V_c, respectively, which have dimension $K_n = (2M_u+1)(2M_x+1)$ and $K_c = 2M_x+1$ (each element has 3×3 nodes, so both meshes have $2M_x+1$ nodes in the x-direction). Each basis function is a piecewise quadratic with compact support such that it is equal to unity at exactly one node in the mesh, and zero at all others.

Lastly, we determine the coefficients N_i^j and C_i^j in (C.5). When discretised as described above, Eq. (C.4) must hold for all test functions ψ in the discretised spaces. Thus we have

$$R_k(n_j^1,\ldots,n_j^{K_n},c_j^1,\ldots,c_j^{K_c}) = 0, \quad k = 1,\ldots,N_n+N_c, \tag{C.6a}$$

where

$$R_k = \int_{\bar{\Omega}} \psi_k^n \frac{\Delta n_j}{\Delta t} + \varepsilon \frac{\partial n_j}{\partial u}\frac{\partial \psi_k^n}{\partial u} + \mathcal{D}(u)\frac{\partial \psi_k^n}{\partial x}\frac{\partial n_j}{\partial x} - \frac{\partial \psi_k^n}{\partial u} f(u,c_j) n_j \,\mathrm{d}\xi, \tag{C.6b}$$

for $k = 1,\ldots,K_n$,

$$R_{K_n+k} = \int_{\bar{\Omega}} \psi_k^c \frac{\Delta c_j}{\Delta t} + D_c \frac{\partial \psi_k^c}{\partial x}\frac{\partial c_j}{\partial x} + \beta \psi_k^c c_j - \psi_k^c \bar{\alpha}_j \,\mathrm{d}\xi, \tag{C.6c}$$

for $k = 1,\ldots,K_c$, and

$$R_{K_n+K_c+k} = \bar{\alpha}_j(x_k) - \int_0^{\mathcal{U}} \alpha(u) n_j(x_k,u)du, \tag{C.6d}$$

for $k = 1,\ldots,K_c$, where $[0,\mathcal{U}]$ is our truncation of $\mathbb{R}_+$. Inserting (C.5) into (C.6) yields a system of $K_n + 2K_c$ nonlinear algebraic equations for the coefficients N_i^j, C_i^j, and $\bar{\alpha}_j(x_k)$.

The reason we use rectangular meshes with quadratic basis functions is to simplify the calculation of $\bar{\alpha}_j$ in (C.6d). The integral in (C.6d) is along a line in (x,u)-space that exactly passes through the nodes at constant x in the mesh for n_j (see Figure C.1). We evaluate the integral using Simpson's composite rule where the evaluation points coincide with nodes of the rectangular elements (where n_j is simply equal to

one of the coefficients N_j^i). If we had chosen (say) triangular elements, then the domain of integration in (C.6d) in general would not pass through any nodes, so an additional interpolation step would be needed. We would also need to divide the domain of integration into segments on which n_j is smooth (n_j is continuous but non-smooth across element boundaries).

We solve the system (C.6) with Newton iteration using `oomph-lib`'s built-in routines. In order to do this, we must calculate the Jacobian of the residuals R_k with respect to the unknown coefficients. Typically we compute the entries numerically. When we perform calculations near a bifurcation, then an analytical Jacobian is used as it gives better convergence rates in the Newton iteration. To speed up the calculation, we parallelise the implementation using OpenMPI. We typically use between 32 and 200 threads depending on the number of elements needed.

When computing bifurcation diagrams, it is much faster to solve the steady-state problem directly. In addition to setting the time-derivatives to zero, one additional modification is needed. This is because the steady-state problem itself is not fully determined without a normalisation condition. Mathematically, this manifests as N_i^j in (C.5)–(C.6) being determined only up to a multiplicative constant. Thus (C.6) has one redundant equation. To resolve this issue, we replace one of the equations (say the $k = 1$ equation) with another equation that imposes the constraint

$$\rho^* |\Omega| = \int_{\Omega \times \mathbb{R}_+} n(x, u) \, \mathrm{d}x \mathrm{d}u, \tag{C.7}$$

where ρ^* is given and $|\Omega|$ is the length (area in 2D) of Ω. To calculate roughly evenly spaced points when computing bifurcation diagrams, we use pseudo arc-length continuation with respect to the bifurcation parameter. The `oomph-lib` package provides a routine to automate this calculation, so we only need to calculate the residuals for the steady-state problem and specify the bifurcation parameter.

Appendix D

Parameter Values

In this Appendix, we provide lists of parameter values for the numerical simulations used throughout this thesis. Parameter values are listed here unless given in the relevant figure caption.

Symbol	Description	Value (QS represses motility)	Value (QS promotes motility)
$\mathcal{D}_*$	Effective diffusion coefficient in the uniform state (bifurcation parameter)	0.5	0.5
$\mathcal{D}'_*$	Motility response in the uniform state	Variable $(-5, -0.19)$, see Figure 3.2	Variable $(3, 16)$, see Figure 3.6
$\mathcal{D}_0$	Effective diffusion coefficient at zero internal concentration	–	0.1
$\mathcal{D}_\infty$	Effective diffusion coefficient at large internal concentrations	0.1	–
ε	Strength of stochasticity in the gene-regulatory network (GRN) reaction kintetics	0.001–0.04	0.001
a	Base production rate of internal chemical in GRN kinetics	0.3	0.3
L	Saturation production rate of positive feedback in GRN kinetics	10	15
K	Threshold activation concentration of positive feedback in GRN kinetics	10 (subcritical), 5 (supercritical)	15
λ	Decay rate of transcription factor	2	1
D_c	Diffusion coefficient of autoinducer (AI)	0.4	0.4
β	Decay rate of AI	4	5
α_0	Secretion rate of AI	12.5	6.25
ρ_*	Global cell density	1	1

Table D.1: List of parameters and their values used in Chapter 3.

Symbol	Value (Figs. 4.3 – 4.4)	Value (Figs. 4.5 – 4.6)	Value (Figs. 4.7 – 4.8)	Value (Fig. 4.9)	Value (Fig. 4.10)
$\mathcal{D}_-$	0.5	0.5	0.5	0.1	0.1
$\mathcal{D}_+$	0.5	0.2	0.1	0.5	0.5
$\mathcal{D}'_-$	0	variable	variable	0.1	1
$\mathcal{D}'_+$	0	variable	variable	6	-1
ε	0.0025–0.01	0.02	0.02	5×10^{-5}	0.0025
a_-	3.5	1	0.1	0.1	0.1
a_+	5	5	0.1	0.1	0.1
L_-	1	2	10	10	10
L_+	5	3	20	20	20
K_-	2	2	10	10	10
K_+	5	3	15	20	20
u_0	5	5	8	7.5	7.5
γ	0.1	0.1	0.1	0.1	0.04
$\rho_-\ (t=0)$	8	8	5	5	5
$\rho_+\ (t=0)$	2	2	5	5	5
D_c	0.4	0.1	0.1	0.1	0.1
β	5	5	2	2	2
α_0	0.5	0.5	0.4	0.4	0.4

Table D.2: List of parameters and their values used for the general one-component kinetics in Chapters 4 and 5.

Symbol	Value (Fig. 5.1)	Value (Fig. 5.2)	Value (Fig. 5.3)	Value (Fig. 5.4)
$\mathcal{D}_*$	0.5	0.5	0.5	0.5
$\mathcal{D}'_*$	bifurcation condition ($\mathcal{D}_{0*}$ in Eq. (5.21))	variable	-2	10
$\mathcal{D}_\infty$	-	0.1	0.1	0.1
ε	-	0.001	0.001	0.001
a	0.3	0.3	0.3	0.3
L	10	10	10	15
K	5	5	5	15
λ	2	2	2	1
D_c	0.4	0.4	0.4	0.4
β	4	4	4	5
α_0	0.5	0.5	0.5	0.25
ρ^*	variable	variable (20–30)	30	25

Table D.3: List of parameters and their values used in Chapter 5. Both IMF and structured models use the same parameters, except ε which only appears in the structured model.

Bibliography

[1] oomph-lib: Main Page. https://oomph-lib.github.io/oomph-lib/doc/html/index.html. Accessed: 2023-20-02.

[2] C. Abaurrea Velasco, M. Abkenar, G. Gompper, and T. Auth. Collective behavior of self-propelled rods with quorum sensing. *Physical Review E*, 98:022605, 2018.

[3] J. Agudo-Canalejo and R. Golestanian. Active Phase Separation in Mixtures of Chemically Interacting Particles. *Physical Review Letters*, 123(1):018101, 2019.

[4] D. Alciatore and R. Miranda. A Winding Number and Point-in-Polygon Algorithm. *Glaxo Virtual Anatomy Project Research Report, Department of Mechanical Engineering, Colorado State University*, 1995.

[5] N. Anesiadis, H. Kobayashi, W. R. Cluett, and R. Mahadevan. Analysis and Design of a Genetic Circuit for Dynamic Metabolic Engineering. *ACS Synthetic Biology*, 2(8):442–452, 2013.

[6] S. Atkinson and P. Williams. Quorum sensing and social networking in the microbial world. *Journal of The Royal Society Interface*, 6(40):959–978, 2009.

[7] S. Auschra, V. Holubec, N. A. Söker, F. Cichos, and K. Kroy. Polarization-density patterns of active particles in motility gradients. *Physical Review E*, 103:062601, 2021.

[8] S. Axler. *Linear Algebra Done Right*. Springer, 2015.

[9] N. J. Bainton, B. W. Bycroft, S. R. Chhabra, P. Stead, L. Gledhill, P. J. Hill, C. E. Rees, M. K. Winson, G. P. Salmond, G. S. Stewart, and P. Williams. A general role for the *lux* autoinducer in bacterial cell signalling: control of antibiotic biosynthesis in *Erwinia*. *Gene*, 116(1):87–91, 1992.

[10] C. Bechinger, R. D. Leonardo, H. Löwen, C. Reichhardt, G. Volpe, and G. Volpe. Active particles in complex and crowded environments. *Reviews of Modern Physics*, 88:045006, 11 2016.

[11] H. C. Berg. *Random Walks in Biology*. Princeton University Press, Princeton, 1984.

[12] H. C. Berg. *E. coli in Motion*. Springer, 2004.

[13] J. Bialké, H. Löwen, and T. Speck. Microscopic theory for the phase separation of self-propelled repulsive disks. *Europhysics Letters*, 103(3):30008, 2013.

[14] J. Bialké, T. Speck, and H. Löwen. Active colloidal suspensions: Clustering and phase behavior. *Journal of Non-Crystalline Solids*, 407:367–375, 2015.

[15] A. Boo, R. L. Amaro, and G.-B. Stan. Quorum sensing in synthetic biology: A review. *Current Opinion in Systems Biology*, 28:100378, 2021.

[16] M. Bruna, M. Burger, A. Esposito, and S. M. Schulz. Phase Separation in Systems of Interacting Active Brownian Particles. *SIAM Journal on Applied Mathematics*, 82(4):1635–1660, 2022.

[17] I. Buttinoni, J. Bialké, F. Kümmel, H. Löwen, C. Bechinger, and T. Speck. Dynamical Clustering and Phase Separation in Suspensions of Self-Propelled Colloidal Particles. *Physical Review Letters*, 110:238301, 2013.

[18] T. Bäuerle, A. Fischer, T. Speck, and C. Bechinger. Self-organization of active particles by quorum sensing rules. *Nature Communications*, 9:3232, 12 2018.

[19] M. E. Cates and J. Tailleur. When are active Brownian particles and run-and-tumble particles equivalent? Consequences for motility-induced phase separation. *Europhysics Letters*, 101(2):20010, 2013.

[20] M. E. Cates and J. Tailleur. Motility-Induced Phase Separation. *Annual Review of Condensed Matter Physics*, 6(1):219–244, 2015.

[21] J.-B. Caussin, A. Solon, A. Peshkov, H. Chaté, T. Dauxois, J. Tailleur, V. Vitelli, and D. Bartolo. Emergent Spatial Structures in Flocking Models: A Dynamical System Insight. *Physical Review Letters*, 112(14):148102, 2014.

[22] S. Chapman, J. King, and K. Adams. Exponential asymptotics and Stokes lines in nonlinear ordinary differential equations. *Proceedings of the Royal Society of London. Series A: Mathematical, Physical and Engineering Sciences*, 454(1978):2733–2755, 1998.

[23] A. Curatolo, N. Zhou, Y. Zhao, C. Liu, A. Daerr, J. Tailleur, and J. Huang. Cooperative pattern formation in multi-component bacterial systems through reciprocal motility regulation. *Nature Physics*, 16(11):1152–1157, 2020.

[24] M. P. Dalwadi and J. R. King. A Systematic Upscaling of Nonlinear Chemical Uptake Within a Biofilm. *SIAM Journal on Applied Mathematics*, 80(4):1723–1750, 2020.

[25] M. P. Dalwadi and P. Pearce. Emergent robustness of bacterial quorum sensing in fluid flow. *Proceedings of the National Academy of Sciences*, 118(10):e2022312118, 2021.

[26] M. P. Dalwadi and P. Pearce. Universal dynamics of biological pattern formation in spatio-temporal morphogen variations. *Proceedings of the Royal Society A*, 479(2271):20220829, 2023.

[27] R. Daniels, J. Vanderleyden, and J. Michiels. Quorum sensing and swarming migration in bacteria. *FEMS Microbiology Reviews*, 28(3):261–289, 2004.

[28] T. Danino, O. Mondragón-Palomino, L. Tsimring, and J. Hasty. A synchronized quorum of genetic clocks. *Nature*, 463(7279):326–330, 2010.

[29] T. R. de Kievit and B. H. Iglewski. Bacterial Quorum Sensing in Pathogenic Relationships. *Infection and Immunity*, 68(9):4839–4849, 2000.

[30] D. S. Dean. Langevin equation for the density of a system of interacting Langevin processes. *Journal of Physics A: Mathematical and General*, 29(24):L613, 1996.

[31] A. Deutsch, P. Friedl, L. Preziosi, and G. Theraulaz. Multi-scale analysis and modelling of collective migration in biological systems. *Philosophical Transactions of the Royal Society B*, 375(1807):20190377, 2020.

[32] A. Dhooge, W. Govaerts, Y. A. Kuznetsov, H. G. E. Meijer, and B. Sautois. New features of the software MatCont for bifurcation analysis of dynamical systems. *Mathematical and Computer Modelling of Dynamical Systems*, 14(2):147–175, 2008.

[33] J. D. Dockery and J. P. Keener. A Mathematical Model for Quorum Sensing in *Pseudomonas aeruginosa*. *Bulletin of Mathematical Biology*, 63(1):95–116, 2001.

[34] Y. Duan, J. Agudo-Canalejo, R. Golestanian, and B. Mahault. Phase coexistence in nonreciprocal quorum-sensing active matter. *arXiv preprint arXiv:2411.05465*, 2024.

[35] R. Erban and S. J. Chapman. *Stochastic Modelling of Reaction-Diffusion Processes*. Cambridge Texts in Applied Mathematics. Cambridge University Press, 2020.

[36] R. Erban and H. G. Othmer. From individual to collective behavior in bacterial chemotaxis. *SIAM Journal on Applied Mathematics*, 65(2):361–391, 2004.

[37] F. Farrell, M. Marchetti, D. Marenduzzo, and J. Tailleur. Pattern Formation in Self-Propelled Particles with Density-Dependent Motility. *Physical Review Letters*, 108(24):248101, 2012.

[38] Y. Fily and M. C. Marchetti. Athermal Phase Separation of Self-Propelled Particles with No Alignment. *Physical Review Letters*, 108:235702, 2012.

[39] A. Fischer, A. Chatterjee, and T. Speck. Aggregation and sedimentation of active Brownian particles at constant affinity. *The Journal of Chemical Physics*, 150(6):064910, 2019.

[40] A. Fischer, F. Schmid, and T. Speck. Quorum-sensing active particles with discontinuous motility. *Physical Review E*, 101:012601, 2020.

[41] H. Z. Ford, A. Manhart, and J. R. Chubb. Controlling periodic long-range signalling to drive a morphogenetic transition. *eLife*, 12:e83796, 2023.

[42] L. Fung, R. N. Bearon, and Y. Hwang. A local approximation model for macroscale transport of biased active Brownian particles in a flowing suspension. *Journal of Fluid Mechanics*, 935:A24, 2022.

[43] D. T. Gillespie. The chemical Langevin equation. *The Journal of Chemical Physics*, 113(1):297–306, 2000.

[44] D. T. Gillespie, A. Hellander, and L. R. Petzold. Perspective: Stochastic algorithms for chemical kinetics. *The Journal of Chemical Physics*, 138(17):170901, 2013.

[45] N. Gnan and C. Maggi. Critical behavior of quorum-sensing active particles. *Soft Matter*, 18(39):7654–7661, 2022.

[46] J. Gou and M. J. Ward. An Asymptotic Analysis of a 2-D Model of Dynamically Active Compartments Coupled by Bulk Diffusion. *Journal of Nonlinear Science*, 26:979–1029, 2016.

[47] A. Gupta, I. M. B. Reizman, C. R. Reisch, and K. L. J. Prather. Dynamic regulation of metabolic flux in engineered bacteria using a pathway-independent quorum-sensing circuit. *Nature Biotechnology*, 35(3):273–279, 2017.

[48] B. K. Hammer and B. L. Bassler. Quorum sensing controls biofilm formation in *Vibrio cholerae*. *Molecular Microbiology*, 50(1):101–104, 2003.

[49] M. Heil and A. L. Hazel. oomph-lib–an *O*bject-*O*riented *M*ulti-*P*hysics Finite-Element *L*ibrary. In *Bungartz, H. J., Schäfer, M. (eds) Fluid-Structure Interaction*, volume 53, pages 19–49. Springer (Lecture Notes on Computational Science and Engineering), 2006.

[50] E. J. Hinch. *Perturbation Methods*. Cambridge University Press, Cambridge, 1991.

[51] E. J. Hinch and L. G. Leal. Constitutive equations in suspension mechanics. Part 2. Approximate forms for a suspension of rigid particles affected by Brownian rotations. *Journal of Fluid Mechanics*, 76(1):187–208, 1976.

[52] R. Hu, S. Seager, and S. Yasuda. Effects of internal dynamics on chemotactic aggregation of bacteria. *Physical Biology*, 18:066001, 9 2021.

[53] S. A. Iyaniwura and M. J. Ward. Synchrony and Oscillatory Dynamics for a 2-D PDE-ODE Model of Diffusion-Mediated Communication between Small Signaling Compartments. *SIAM Journal on Applied Dynamical Systems*, 20(1):438–499, 2021.

[54] F. Jose, S. K. Anand, and S. P. Singh. Phase separation of an active colloidal suspension *via* quorum-sensing. *Soft Matter*, 17(11):3153–3161, 2021.

[55] H. B. Keller. Numerical solution of bifurcation and nonlinear eigenvalue problems. *Applications of Bifurcation Theory (Proc. Advanced Sem., Univ. Wisconsin, Madison, Wis., 1976)*, pages 359–384, 1977.

[56] H. Kobayashi, M. Kaern, M. Araki, K. Chung, T. S. Gardner, C. R. Cantor, and J. J. Collins. Programmable cells: interfacing natural and engineered gene networks. *Proceedings of the National Academy of Sciences*, 101(22):8414–8419, 2004.

[57] B. Liebchen, D. Marenduzzo, I. Pagonabarraga, and M. E. Cates. Clustering and Pattern Formation in Chemorepulsive Active Colloids. *Physical Review Letters*, 115(25):258301, 2015.

[58] C. Liu et al. Sequential establishment of stripe patterns in an expanding cell population. *Science*, 334:238–241, 2011.

[59] M. J. Lynch, S. Swift, D. F. Kirke, C. W. Keevil, C. E. R. Dodd, and P. Williams. The regulation of biofilm development by quorum sensing in *Aeromonas hydrophila*. *Environmental Microbiology*, 4(1):18–28, 2002.

[60] F. R. Macfarlane, T. Lorenzi, and K. J. Painter. The Impact of Phenotypic Heterogeneity on Chemotactic Self-Organisation. *Bulletin of Mathematical Biology*, 84(12):143, 2022.

[61] B. Mahault, P. Godara, and R. Golestanian. Emergent organization and polarization due to active fluctuations. *Physical Review Research*, 5(2):L022012, 2023.

[62] P. Mandel and T. Erneux. The slow passage through a steady bifurcation: Delay and memory effects. *Journal of Statistical Physics*, 48:1059–1070, 1987.

[63] A. Manela and I. Frankel. Generalized Taylor dispersion in suspensions of gyrotactic swimming micro-organisms. *Journal of Fluid Mechanics*, 490:99–127, 2003.

[64] J. Mason, R. L. Jack, and M. Bruna. Dynamical patterns in active-passive particle mixtures with non-reciprocal interactions: Exact hydrodynamic analysis. *arXiv preprint arXiv:2408.03932*, 2024.

[65] P. Melke, P. Sahlin, A. Levchenko, and H. Jönsson. A Cell-Based Model for Quorum Sensing in Heterogeneous Bacterial Colonies. *PLoS Computational Biology*, 6(6):1–12, 2010.

[66] J. D. Murray. *Mathematical Biology. I, An Introduction.* Interdisciplinary Applied Mathematics; 17. Springer, New York; London, 3rd ed. edition, 2002.

[67] S. Nakamura and T. Minamino. Flagella-Driven Motility of Bacteria. *Biomolecules*, 9(7):279, 2019.

[68] A. Olde Daalhuis, S. Chapman, J. King, J. Ockendon, and R. Tew. Stokes phenomenon and matched asymptotic expansions. *SIAM Journal on Applied Mathematics*, 55(6):1469–1483, 1995.

[69] M. Paoluzzi, M. Leoni, and M. C. Marchetti. Information and motility exchange in collectives of active particles. *Soft Matter*, 16(27):6317–6327, 2020.

[70] K. Papenfort and B. L. Bassler. Quorum sensing signal–response systems in Gram-negative bacteria. *Nature Reviews Microbiology*, 14(9):576–588, 2016.

[71] M. Pelz and M. J. Ward. The emergence of spatial patterns for compartmental reaction kinetics coupled by two bulk diffusing species with comparable diffusivities. *Philosophical Transactions of the Royal Society A*, 381(2245):20220089, 2023.

[72] M. Pelz and M. J. Ward. Symmetry-breaking bifurcations for compartmental reaction kinetics coupled by two bulk diffusing species with comparable diffusivities in 2-D. *Frontiers in Applied Mathematics and Statistics*, 9:1110497, 2023.

[73] V. Piskovsky and N. M. Oliveira. Bacterial motility can govern the dynamics of antibiotic resistance evolution. *Nature Communications*, 14(1):5584, 2023.

[74] A. Prindle, J. Selimkhanov, H. Li, I. Razinkov, L. S. Tsimring, and J. Hasty. Rapid and tunable post-translational coupling of genetic circuits. *Nature*, 508(7496):387–391, 2014.

[75] E. M. Purcell. Life at Low Reynolds Number. In *Physics and Our World*, pages 47–67. World Scientific, 2014.

[76] M. Rein, N. Heinß, F. Schmid, and T. Speck. Collective Behavior of Quorum-Sensing Run-and-Tumble Particles under Confinement. *Physical Review Letters*, 116:058102, 2016.

[77] W. J. M. Ridgway, M. P. Dalwadi, P. Pearce, and S. J. Chapman. Motility-Induced Phase Separation Mediated by Bacterial Quorum Sensing. *Physical Review Letters*, 131(22):228302, 2023.

[78] D. Saintillan and M. J. Shelley. Theory of Active Suspensions. In *Spagnolie, S. (eds) Complex Fluids in Biological Systems: Experiment, Theory, and Computation*, pages 319–355. Springer New York, New York, NY, 2015.

[79] E. E. Sel'Kov. Self-Oscillations in Glycolysis 1. A Simple Kinetic Model. *European Journal of Biochemistry*, 4(1):79–86, 1968.

[80] H. Smith, C. J. Dorman, G. Dougan, D. W. Holden, G. Dougan, P. Williams, P. Williams, M. Camara, A. Hardman, S. Swift, D. Milton, V. J. Hope, K. Winzer, B. Middleton, D. I. Pritchard, and B. W. Bycroft. Quorum sensing and the population-dependent control of virulence. *Philosophical Transactions of the Royal Society of London. Series B: Biological Sciences*, 355(1397):667–680, 2000.

[81] T. Speck, A. M. Menzel, J. Bialké, and H. Löwen. Dynamical mean-field theory and weakly non-linear analysis for the phase separation of active Brownian particles. *The Journal of Chemical Physics*, 142(22):224109, 2015.

[82] V. Sperandio, A. G. Torres, and J. B. Kaper. Quorum sensing *Escherichia coli* regulators B and C (QseBC): a novel two-component regulatory system involved in the regulation of flagella and motility by quorum sensing in *E. coli*. *Molecular Microbiology*, 43(3):809–821, 2002.

[83] J. Stenhammar, A. Tiribocchi, R. J. Allen, D. Marenduzzo, and M. E. Cates. Continuum Theory of Phase Separation Kinetics for Active Brownian Particles. *Physical Review Letters*, 111:145702, 2013.

[84] J. Tailleur and M. E. Cates. Statistical mechanics of interacting run-and-tumble bacteria. *Physical Review Letters*, 100(21):218103, 2008.

[85] S. P. Thampi, R. Golestanian, and J. M. Yeomans. Vorticity, defects and correlations in active turbulence. *Philosophical Transactions of the Royal Society A*, 372(2029):20130366, 2014.

[86] A. M. Turing. The chemical basis of morphogenesis. *Philosophical Transactions of the Royal Society of London. Series B, Biological Sciences*, 237(641):37–72, 1952.

[87] T. Vicsek, A. Czirók, E. Ben-Jacob, I. Cohen, and O. Shochet. Novel Type of Phase Transition in a System of Self-Driven Particles. *Physical Review Letters*, 75(6):1226–1229, 1995.

[88] N. Wadhwa and H. C. Berg. Bacterial motility: machinery and mechanisms. *Nature Reviews Microbiology*, 20(3):161–173, 2022.

[89] J. P. Ward, J. R. King, A. J. Koerber, P. Williams, J. M. Croft, and R. E. Sockett. Mathematical modelling of quorum sensing in bacteria. *Mathematical Medicine and Biology: A Journal of the IMA*, 18:263–292, 2001.

[90] C. M. Waters and B. L. Bassler. Quorum Sensing: Cell-to-Cell Communication in Bacteria. *Annual Review of Cell and Developmental Biology*, 21(1):319–346, 2005.

[91] L. E. Weiss, J. P. Badalamenti, L. J. Weaver, A. R. Tascone, P. S. Weiss, T. L. Richard, and P. C. Cirino. Engineering motility as a phenotypic response to LuxI/R-dependent quorum sensing in *Escherichia coli*. *Biotechnology and Bioengineering*, 100:1251–1255, 8 2008.

[92] M. Whiteley, S. P. Diggle, and E. P. Greenberg. Progress in and promise of bacterial quorum sensing research. *Nature*, 551(7680):313–320, 2017.

[93] P. Williams, K. Winzer, W. C. Chan, and M. Cámara. Look who's talking: communication and quorum sensing in the bacterial world. *Philosophical Transactions of the Royal Society B: Biological Sciences*, 362(1483):1119–1134, 2007.

[94] X. Xue, C. Xue, and M. Tang. The role of intracellular signaling in the stripe formation in engineered *Escherichia coli* populations. *PLOS Computational Biology*, 14:e1006178, 6 2018.

[95] Z. You, A. Baskaran, and M. C. Marchetti. Nonreciprocity as a generic route to traveling states. *Proceedings of the National Academy of Sciences*, 117(33):19767–19772, 2020.

[96] J. Zhang, R. Alert, J. Yan, N. S. Wingreen, and S. Granick. Active phase separation by turning towards regions of higher density. *Nature Physics*, 17(8):961–967, 2021.

[97] X. Zhang and N. Mitarai. Finite response time in stripe formation by bacteria with density-suppressed motility. *arXiv preprint arXiv:1905.02933*, 2019.

[98] H. Zhao, A. Košmrlj, and S. S. Datta. Chemotactic Motility-Induced Phase Separation. *Physical Review Letters*, 131(11):118301, 2023.

[99] A. Ziepke, I. Maryshev, I. S. Aranson, and E. Frey. Multi-scale organization in communicating active matter. *Nature Communications*, 13(1):6727, 2022.